UNIVERSITY OF CAPE TOWN
Department of Mechanical Engineering
Rondebosch, Cape Town, South Africa

THE EFFECT OF STAND-OFF DISTANCE ON THE FAILURE OF THIN PLATES SUBJECTED TO BLAST LOADS

Neville Jacob

2005

Submitted to the University of Cape Town in partial fulfillment of the degree of MSc in Mechanical Engineering

Declaration

I, Neville Jacob, declare that this dissertation is essentially my own work. It is being submitted in partial fulfillment of the requirements for the Masters of Science in Engineering degree at the University of Cape Town and has not been submitted in this or any other form for a degree at any other university.

Neville Jacob
August 2005

Abstract

This investigation examines the effect of stand-off distance on the response of fully clamped circular plates subjected to blast loads.

The experimental procedure consists of creating a blast load using disc shaped plastic explosive mounted onto a tube of required length. The length of the tube is the stand-off distance. Different lengths of tubes are used ranging from 25mm to 300mm. The internal diameter of the tube is 106mm. The dimension of the circular test plate is governed by the internal diameter of the tube. Hence all tests are conducted on 106mm diameter circular plates of thickness 1.9mm. The test plate is clamped between two clamping plates. The tube is screwed onto one of the clamping plates.

The plate responses range from large inelastic deformation to complete tearing at the plate boundary. The deformed plate profile is dependent on stand-off distance. For stand-off distances ranging from 13mm to 40mm an inner dome atop a larger global dome is observed. In the case of stand-off distances ranging from 50mm to 300mm the deformed plate profile resembles a large global dome.

The results show that mid-point deflection decreases with increasing stand-off distance for a given charge mass. The mid-point deflection drops rapidly from stand-off distance of 13mm to 50mm, from stand-off distance of 75mm to 300mm the mid-point deflection asymptotes with similar values measured for a given charge mass. The results show two distinct loading regimes that occur depending on the stand-off distance between the explosive charge and the plate. At stand-off distances less than the plate radius of 53mm (13mm to 40mm), the blast load is considered to be focused. This type of loading is referred to as localised loading. For stand-off distances greater than the plate radius (100mm to 300mm), the loading is said to be uniformly distributed over the entire plate area. At stand-off distances of 50mm to 75mm, the plate deformations exhibit a transition phase from localised loading to uniform loading.

Theoretical and empirical analysis using Jones damage number, Nurick and Martin damage number and strain energy analysis to predict mid-point deflection of the deformed plate is performed. Appropriate modifications are made to above mentioned damages numbers and strain energy analysis to account for the effect of

stand-off distance on plate deformation. The modified analyses show satisfactory correlation with experimental results.

Table of Contents

List of Figures

List of Tables

Notation

A	Plate area ($A = \pi(D/2)^2$)
A_0	Loaded area
B	Plate half width
D	Plate diameter
H	Plate thickness
I	Impulse
L	Plate half length
M_0	$\sigma_0 H^2/4$
P_s	Peak overpressure
R	Plate radius
R_0	Charge radius
S	Stand-off distance
v_{det}	Detonation velocity
V_0	Initial velocity
U_{def}	Deformation strain energy
U	shock velocity
u	Particle velocity
$U_{rarefaction}$	Rarefaction velocity
Z	Scaled distance
b	Plate width (2B)
h	Charge height
l	Plate length (2L)
α	Johnson damage number
λ	Jones dimensionless number
Φ_q	Nurick dimensionless number (quadrangular plates)
Φ_c	Nurick dimensionless number (circular plates)
ζ_c	Loading parameter (circular plates)
ζ_{ql}	Loading parameter (quadrangular plates)
μ	Mass per unit area (ρH)
β	Aspect ratio
δ	Mid point deflection
ρ	Material density
σ_0	Static yield stress of material
σ_0^1	Dynamic yield stress of material

Acknowledgement

I would like to take this opportunity to thank all the people without whose assistance, this report could not be written.

Sincere thanks go to:

Prof. GN Nurick, my supervisor for his continuous and precious help and advice throughout the course of my studies at the University of Cape Town.

Dr. Genevieve Langdon, my co supervisor for always being helpful with all my queries and proof reading this report.

Mr. Steeve Chung Kim Yuen, for his assistance during the experiments and photographing the experimental rig and test specimens.

Mr. G. Newins and Mr. L Watkins, as well as the entire workshop staff for their continuous support throughout the course my work.

Mrs. Penny Park-Ross, for her assistance in using the Zwick tensile test machine.

I would also like to thank Mrs Val Atkinson and all the members of the Blast Impact and Survivability Research Unit (BISRU) for their support during the course of my MSc.

Last but not least my parents Mr. and Mrs. Jacob and my sister Clarine, who have always been supportive and given much encouragement.

1 Introduction

Investigations into the failure of thin plates subjected to impulsive loads have been going on for some years as reported by Nurick and Martin [1, 2]. Understanding the way plates fail under blast loading lends itself to improved designs capable of resisting blast damage.

Previous experimental work at the University of Cape Town has concentrated on uniform and localised loading of mild steel plates at a given stand-off distance between the explosive and test plate in order to investigate plate geometry, tearing at the boundary [3, 4, 5] and in the central area of the plate [6, 7, 8], different boundary fixations [3, 9] and the effect of plate thickness [7, 8].

Other experimental works include the study into structural response of plates subjected to air pressure generated from explosive devices. Jacinto et al [10] report experiments conducted using two quadrangular un-stiffened plates with different boundary conditions (one clamped in the soil and another clamped along the four edges). The experiments were carried out to validate numerical modelling. The effect of explosive stand-off distance on square plates is reported by Akus and Yildirim [11]. The test were carried out using C4 plastic explosives of different masses (131g to 654.8g) at stand-off distances ranging from 200mm to 600mm.

This thesis reports on the results of experimental investigation into the inelastic response of circular plates subjected to blast loads at various stand-off distances.

The purpose of this investigation is to ascertain the influence of stand-off distance between the explosive and a fully clamped circular plate mounted on a ballistic pendulum. The response of the circular plate is described by its deflection resulting from the blast load applied by the explosive.

In the experiments described in this report, the stand-off distance is varied using 106mm internal diameter mild steel tubes of different lengths. A tube of required stand-off distance is screwed onto a clamping plate. The test plate is sandwiched between the tube and a second clamping plate. The explosive mounted on a polystyrene pad is placed at the open end of the tube. The test rig is then attached

onto a ballistic pendulum. The impulse applied by the explosive on the test plate is measured from the oscillation of the ballistic pendulum. The final mid-point deflection of the plate is measured using a digital height gauge.

The objectives of this thesis are to:

- Investigate the effect of different stand off distances between the explosive and test plate.
- Compare experimental results with previously reported analytical and empirical relations developed to predict mid-point deflection of plates subjected to blast loads.
- Incorporate appropriate modifications to analytical and empirical relations if required.
- Investigate the effect of polystyrene on plate deformation and applied impulse.
- Draw conclusions and recommendations based on the findings.

The scope of the investigation was limited to 1.9mm thick circular plates of diameter 106mm subjected to blast loading using explosive charge of diameter 34mm.

The thesis is based on experiments conducted in the blast laboratory of the Blast Impact and Survivability Research Unit (**BISRU**) at the University of Cape Town.

Chapter 2 details a literature review that covers background into blast loading, theoretical work and experimental results. Past experimental results are used for comparison with results from this investigation.
The experimental details are described in Chapter 3, along with material properties of mild steel plates used in the experiments.
Experimental observations are described in Chapter 4, including tables containing the experimental data recorded from the tests.
Analysis of the experimental results is presented in Chapter 5 including graphs and results of theoretical analysis performed.
Conclusions are drawn and recommendations made based on the findings in Chapters 6 and 7 respectively.

2 Literature review

A blast load is generated by detonating explosives which interact with any objects in its path causing widespread damage and represent major disaster (Kinney [12]). The blast load is generally expressed in terms of its pressure – time history. In reality the pressure – time history of a blast event is very complex, hence simplified models are often used in numerical modelling of structures subjected to blast loads. A blast load is considered impulsive if the duration is significantly lower than the natural frequency of the structure, as reported by the Steel Construction Institute [13]. This means that the structure does not have time to fully react to the blast load.

2.1 Defining an explosion

Baker [14] defines explosion as the generation of a pressure wave of finite amplitude in air by a rapid release of energy. Hence an explosion forms a blast wave. Kinney [12], states that the source of the sudden release of energy is irrelevant, for example it could be from gun powder or wheat flour dust. However, the nature of the energy release is important. The release of energy must be sudden and an accumulation of energy must occur at the region near the source. This accumulation of energy is then rapidly dissipated in various ways; the most pertinent one is in the form of a blast wave.

2.1.1 Blast phenomena

A detonation initiated at the centre of an explosive material will result in a rapid and stable chemical reaction which propagates through the un-reacted explosive. A detonation wave is created that travels at supersonic speeds (in the order of several thousand metres per second) depending on the density of the explosive, as shown in Figure 2.1. In general the detonation velocity is higher for denser explosives. The detonation wave quickly converts the explosive material into a very hot, dense and high pressure gas. This volume of gas is the source of the subsequent strong blast waves in air. The pressures behind a detonation front vary from 10GPa to 30GPa. However, only a third of the total chemical energy available is released during the detonation process for most high explosives. The remaining two-thirds of the chemical energy are released more slowly in chemical reactions as the detonation

products mix with air and burn. This secondary release of energy has little effect on the blast wave property since it is a much slower process (TM5-1300 [15]).

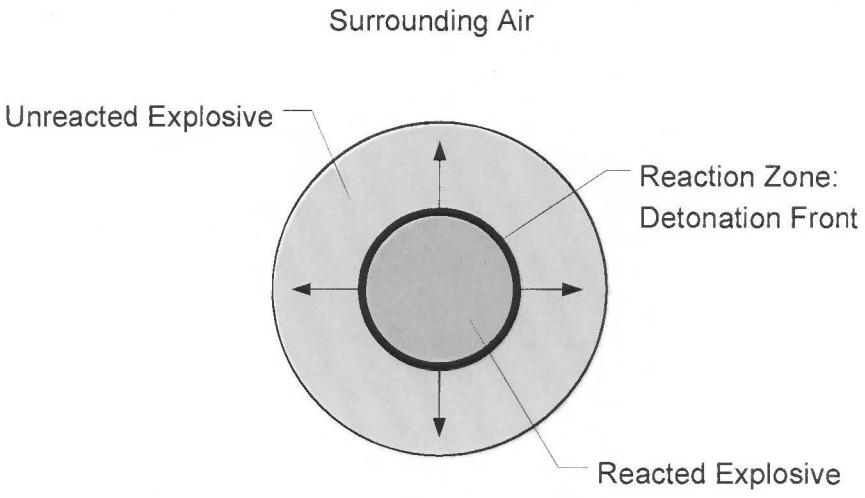

Figure 2.1: Illustration of detonation front propagating within the explosive

The blast effect of the explosion comprises a shock wave composed of a high intensity shock front created by gases from the chemical reaction during detonation. A compressed layer of air is formed in front of the expanding gases that contain most of the energy of the explosion, as shown in Figure 2.2. The shock front expands outward from the surface of the explosive into the surrounding air. This is called the blast wave. The blast wave speed is much slower than the detonation wave [15].

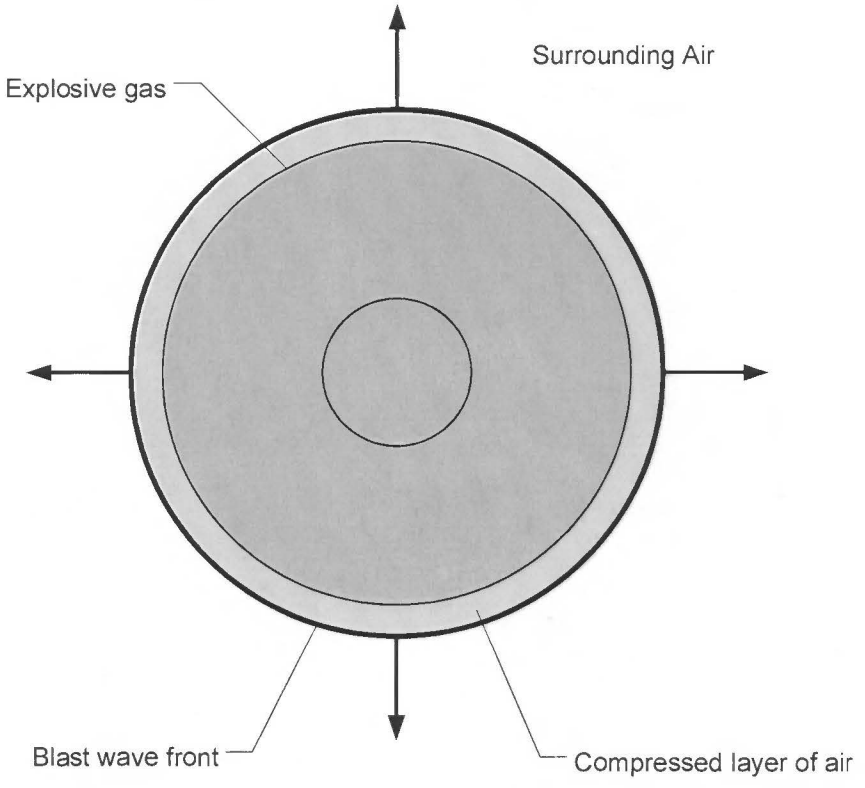

Figure 2.2: Illustration of expanding explosive gases and blast wave front

The expanding blast wave interacts with structures it comes in contact with along its path. The magnitude and distribution of the blast load is dependant on the following factors [15]:

- Explosive properties
  - Type of explosive
  - Energy output of the explosive
  - Charge mass
- Location of structure relative to the explosive charge
- Magnitude and reinforcement of blast pressure by its interaction with the structure

2.1.2 Types of explosives

Explosives are divided into two categories, namely

Initiating/Primary explosives – these are very sensitive materials that can be easily detonated by friction, spark or impact. An example of primary explosive is Lead Azide.

Lead Azide – the major initiating explosive used in most detonators and blasting caps. It is extremely sensitive to sparks, friction and impact leading to initiation of the explosive. Lead Azide has excellent storage characteristics and is stable up to almost 270°C.

Properties:

Density – 4.38gcm^{-3}

Detonation velocity – 5500ms^{-1}

Secondary explosives – these have higher energy content than initiating explosives but are stable and insensitive. Detonation is only possible through sudden and intense shock delivered using blasting caps or purpose built detonators. TNT and RDX are common examples of secondary explosives.

TNT – this is the most commonly produced military explosive. It is relatively insensitive to sparks, friction and impact. TNT requires a detonator for initiation. TNT is only slightly soluble in water, hence can be used underwater without water proofing.

Properties:

Density – 1.62gcm^{-3}

Detonation velocity – 7045ms^{-1}

RDX – this explosive is stable and less sensitive to spark, friction and impact. RDX requires a detonator for initiation. It is only slightly soluble in water and is non-hygroscopic.

Properties:

Density – 1.767gcm^{-3}

Detonation velocity – 8639ms^{-1}

2.1.3 Detonation

Rinehart and Pearson [16] describe detonation as the decomposition of explosive material into hot gases. The detonation front travels through the unused part of the explosive at speeds of the order of several thousands of metres per second leaving in its wake gases at high temperature and pressure.

In an ideal case detonation can be viewed as a sharp discontinuity travelling through an explosive at a constant velocity, referred to as the detonation velocity (v_{det}) as shown in Figure 2.3.

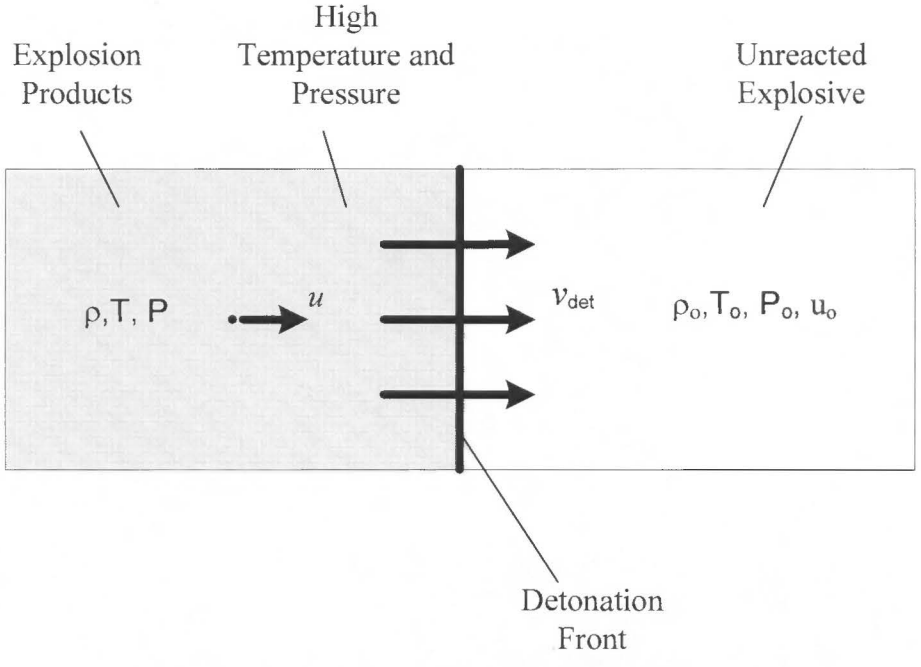

Figure 2.3: Idealised Detonation Process Parameters [16]

The initial condition of the explosive is shown in Figure 2.3 in front of the detonation front, characterised by its density ρ_o and temperature T_o. The explosive is assumed to be completely reacted behind the detonation front. The hot gases that are released from the explosive reaction fill the volume behind the detonation front at high

temperature, T, and high pressure, P, compressing the hot gases to density, ρ, that is higher than the initial explosive density (ρ_o) of the unreacted part of the explosive ahead of the detonation front and imparting a particle streaming velocity of *u* towards the unreacted part of the explosive.

2.1.4 Reaction zone

In section 2.1.3, it is assumed that conversion of the solid explosive to gaseous products happens instantaneously during detonation. In reality, this is not feasible as all chemical reactions occur over a finite time. Therefore the boundary between the reacted and unreacted parts of the explosive is not sharp but rather of finite thickness, as shown in Figure 2.4.

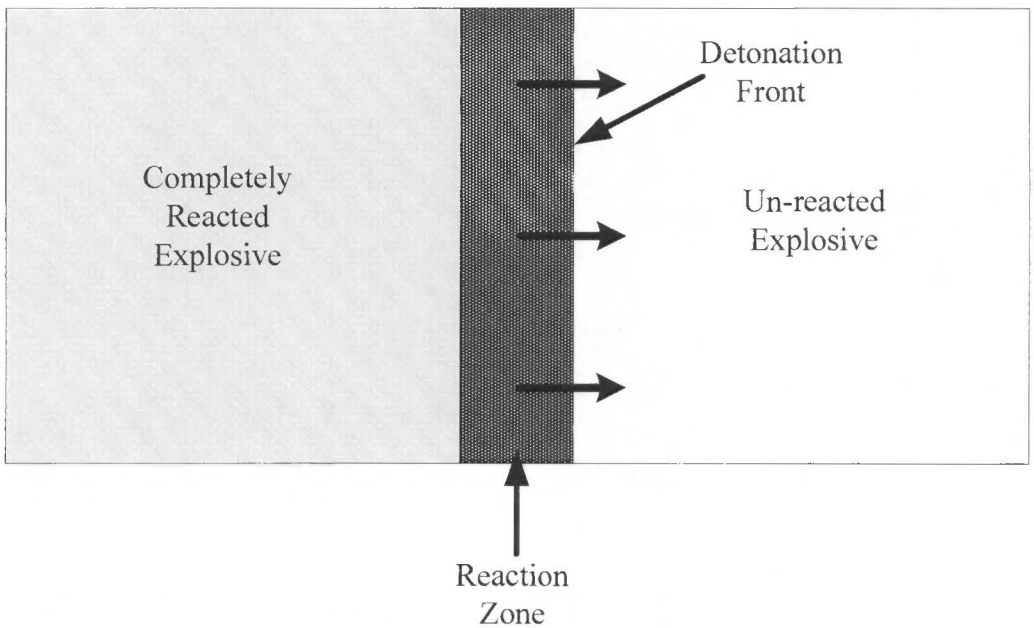

Figure 2.4: Schematic view of the reaction zone in an explosive [16]

The size of the reaction zone has an important influence on the geometry of the explosive charge. In unconfined explosive charges the gaseous products can expand laterally and literally blow away un-reacted explosive before the completion of the reaction. In the case of very thin sheet or elongated cylinder (charge length much greater than charge diameter) shaped explosive as shown in Figure 2.5 (a) and (b), this could result in incomplete detonation due to dissipation of energy due to mechanical dispersion of un-reacted explosive, [16].

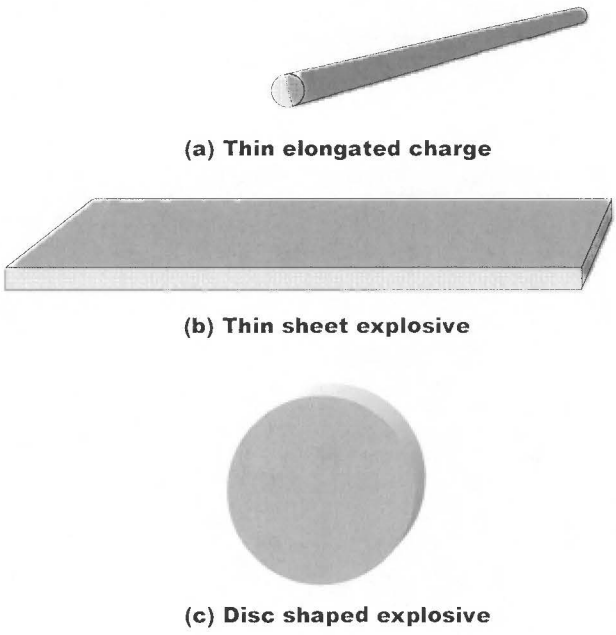

Figure 2.5: Illustration of elongated cylindrical, thin sheet and disc shaped explosive

The combination of reaction zone size and mechanical dispersion of un-reacted explosive contribute to the choice of charge geometry. In the case of disc shaped explosive (charge diameter is greater than charge height) as shown in Figure 2.5 (c), detonated at the centre of the charge diameter, the explosive thickness (charge height) must be larger than the size of the reaction zone for that particular explosive.

2.1.5 Shock waves

The shock front of a blast wave is described by Cooper and Kurowski [17] as a high pressure disturbance travelling through a material. The disturbance is not smooth but discontinuous as shown in Figure 2.6. The shock pressure can stress a structure beyond its elastic limit thus deforming it permanently.

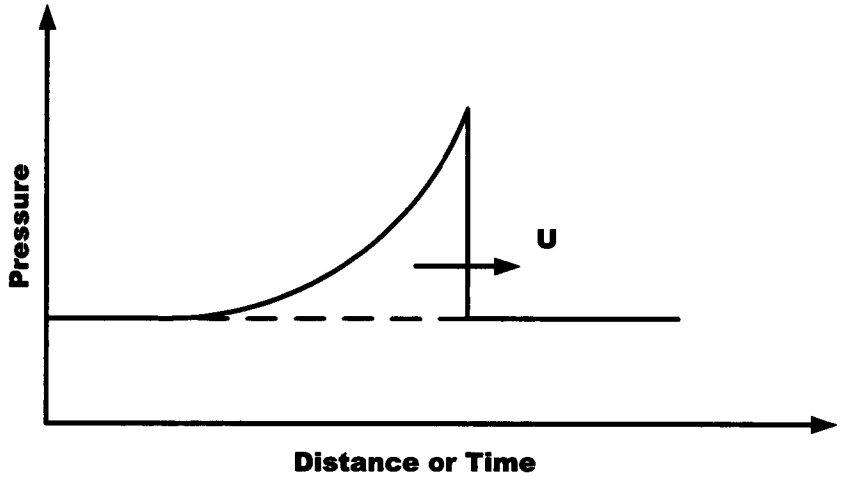

Figure 2.6: Structure of shock wave [17]

2.1.5.1 Rankine-Hugoniot jump equations for shock waves

As the shock front travels through a material, the mass, momentum and energy are conserved across the shock front. This implies that neither energy nor mass is created or destroyed by the shock process. The motion of the particles in front of the shock is due to the particles bumping into them from just behind the shock.
The conservation of mass, momentum and energy leads to three equations which describe the shock process referred to as *Rankine-Hugoniot Jump Equations*, [17].

Conservation of mass:

$$\frac{\rho_1}{\rho_o} = \frac{U - u_o}{U - u_1} \qquad \text{(eq. 2.1)}$$

Conservation of momentum:

$$P_1 - P_o = \rho_o (u_1 - u_o)(U - u_o) \qquad \text{(eq. 2.2)}$$

Conservation of energy:

$$e_1 - e_o = \frac{P_1 u_1 - P_o u_o}{\rho_o (U - u_o)} - \frac{1}{2}\left(u_1^2 - u_o^2\right) \qquad \text{(eq. 2.3)}$$

Where, P – shock pressure (GPa), U – shock velocity (km/s), u – particle velocity (km/s), ρ – density (g/cm^3), e – internal energy

Note: the subscripts 0 and 1 in the Rankine-Hugoniot jump equations refer to the un-shocked and shocked part of the material respectively.

The above expressions are further simplified if the un-shocked material is at rest and at low ambient pressure. In this case, u_o= 0 and the pressure of the un-shocked material is so small that it can be assumed to be zero (P_o = 0). Hence the equations can be rewritten as follows,

Conservation of mass:

$$\frac{\rho_1}{\rho_o} = \frac{U}{U - u_1} \qquad \text{(eq. 2.4)}$$

Conservation of momentum:

$$P_1 = \rho_o u_1 U \qquad \text{(eq. 2.5)}$$

Conservation of energy:

$$e_1 - e_o = \frac{1}{2} P_1 \left(\frac{1}{\rho_o} - \frac{1}{\rho_1} \right) \qquad \text{(eq. 2.6)}$$

2.1.5.2 Attenuation of shock waves

The shock wave not only loses energy but also the shock pressure decreases with time and distance travelled. This loss in pressure is attributed to the rarefaction wave that follows a shock wave and eventually overtakes it. A simple example is illustrated in Figure 2.7 for an assumed square-wave pulse. In this case the front of the shock wave is travelling at a velocity U, which is determined by the density, ρ_o of un-shocked region and shock pressure P. The trailing rarefaction wave is travelling through the shocked and compressed material at velocity $U_{rarefaction}$. The velocity of the rarefaction wave is determined by density ρ, pressure P and particle velocity u, of the material behind and in front of it. The rarefaction wave is travelling through shocked and compressed material with density,ρ which is higher than the density, ρ_o, through which the shock wave is travelling, thus velocity, $U_{rarefaction}$ is greater than U. As the rarefaction wave travels further into the square region, the shock wave is attenuated, and its shape changes, as shown in Figure 2.8. After this change in shape the shock front pressure starts to drop until the shock wave is transformed into sound wave. The loss in pressure results in a corresponding decrease in shock velocity.

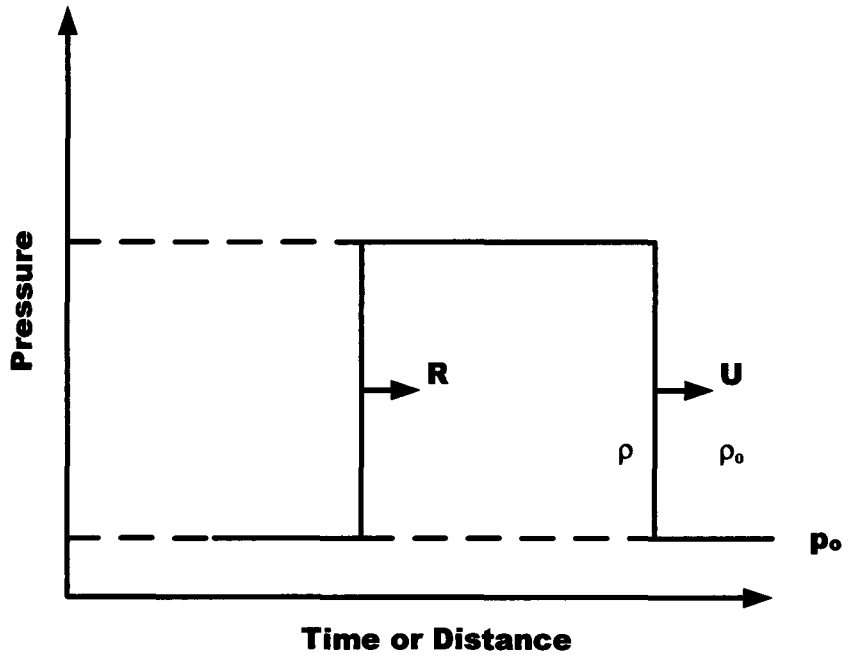

Figure 2.7: Square shock wave pulse [17]

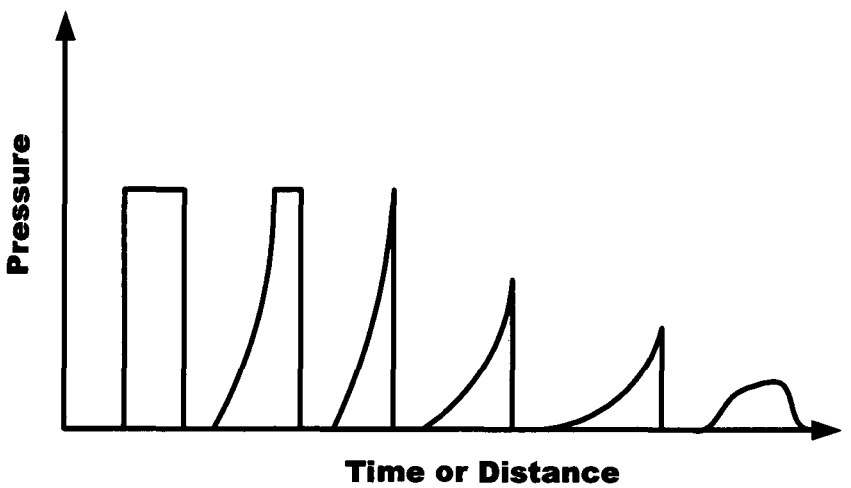

Figure 2.8: Attenuation of a square shock wave [17]

2.1.6 Detonation wave

A detonation wave is a shock wave travelling within the explosive material where the chemical reaction is carried out in the shock front. The chemical reaction continuously adds energy to the shock and compensates for energy losses. The detonation wave achieves a constant velocity v_{det}, when the energy added to the detonation wave front from the chemical reaction is in equilibrium with the energy lost through work and expansion of the detonation product gases. This is referred to as steady state detonation, (Cooper and Kurowski [17]).

A steady state detonation wave does not attenuate and retains its structure until the entire explosive is consumed. A graphical representation of the structure of the detonation wave is shown in Figure 2.9. The front of the wave is travelling at detonation velocity, v_{det}. The explosive reaction is initiated by the spike at the front end of the detonation wave, called the *Von Neuman spike* as shown in Figure 2.9. The chemical reaction of the explosion process occurs in the reaction zone immediately behind the wave front. The end of the reaction zone is called the Chapman-Jouget (C-J) plane. The pressure, density, particle and shock velocity within the C-J plane is characteristic of the particular explosive material at a given initial unreacted density. Behind the C-J plane the product gases from the chemical reactions expand. However the expansion is governed by the boundary conditions surrounding the explosive. The coupling of the energy from the explosion into another material (for example, air) occurs during this gas expansion. A decrease in pressure occurs during expansion of the hot product gases, called the Taylor wave [17].

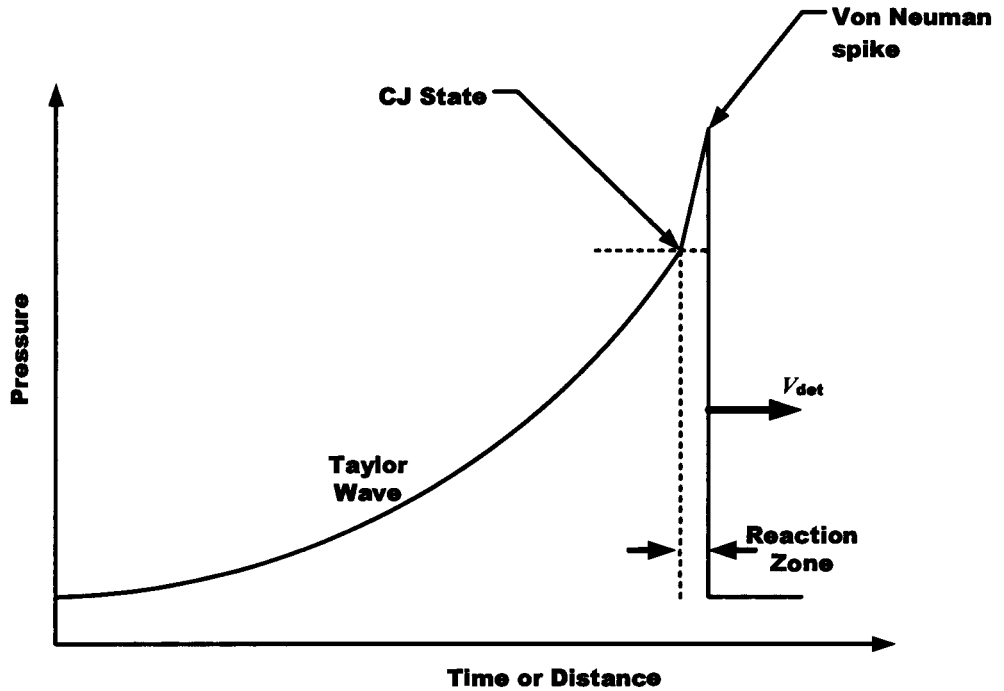

Figure 2.9: Structure of a detonation wave [17]

2.1.6.1 *Rankine-Hugoniot jump equations for detonation waves*

The Rankine-Hugoniot jump equations for shockwaves (as described in Section 2.1.5.1) apply across the detonation front. However in this case the shock pressure is replaced by the C-J pressure, P_{cj}, the shock particle velocity by u_{cj}, the shock density by ρ_{cj}, and the shock velocity by the detonation velocity, v_{det}, [17].

Mass balance:

$$\frac{\rho_{cj}}{\rho_o} = \frac{v_{det}}{v_{det} - u_{cj}} \qquad \text{(eq. 2.7)}$$

Momentum balance:

$$p_{cj} = \rho_o u_{cj} v_{det} \qquad \text{(eq. 2.8)}$$

Where, P_{cj} – C-J pressure (GPa), v_{det} – detonation velocity (km/s), u_{cj} – particle velocity at the C-J state (km/s), ρ_o – density of unreacted explosive (g/cm^3), ρ_{cj} – density in the C-J state (g/cm^3)

An approximation for determining the C-J pressure is obtained from the simplification of the momentum equation (2.8). Equation (2.9) predicts the C-J pressure for a particular explosive within an accuracy of 7% for most explosives, [17].

$$p_{cj} = \rho_o \, v_{det}^2 / 4 \qquad \text{(eq. 2.9)}$$

2.2 Blast wave phenomena

Smith and Hetherington [18] describe the blast wave phenomena as a sequence of events that follow the initiation of an explosive. The rapid release of energy from the detonation converts an explosive charge into very high pressure gas (10 – 30GPa) at very high temperature (3000 – 4000°C). The gases expand violently and the surrounding air is forced out from the volume it occupies. A layer of compressed air at high pressure is formed in front of the expanding gases which contain most of the energy from the explosion. This pressure front is referred to as the blast wave as shown in Figure 2.10, [18].

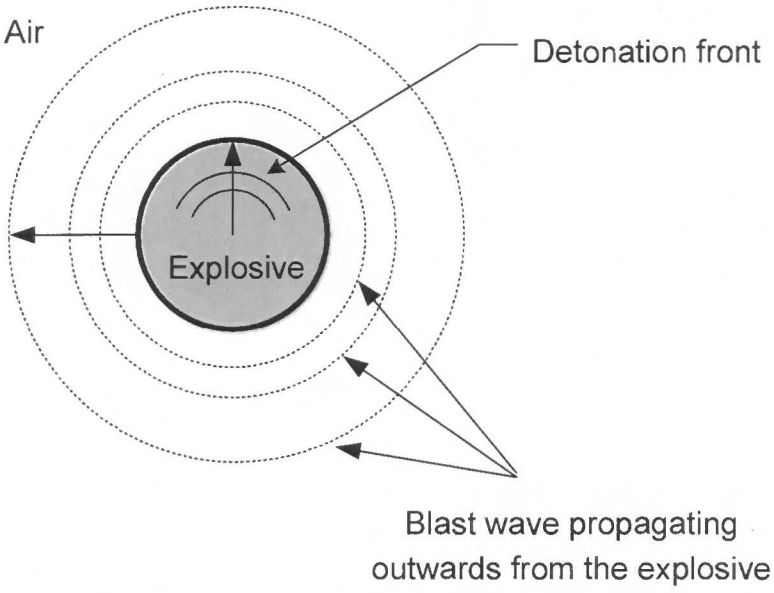

Figure 2.10: A simplified figure of detonation front propagating through an explosive and the blast wave propagating from the explosion

As the explosive gases expand the pressure drops to atmospheric pressure as the blast wave travels outwards from the source. Similarly, the pressure of the compressed air at the blast front also falls with increasing distance. As the explosive gases expand they cool and their pressure drops slightly below ambient pressure. This is because the gas molecules have mass and are moving. It takes some time and further distance of travel before their momentum is zero. The gases are now 'over-expanded' and the result is a reversal of flow towards the source driven by the small pressure differential between atmospheric conditions and the pressure of the gases. This drop in pressure is referred to as the under pressure [18].

2.2.1 Blast loading categories

The description of different blast loads described in this section is a summary of discussion in TM5-1300 [15].
Blast loads can be classified into two categories,

2.2.1.1 Unconfined explosions

This type of blast loading occurs above the surface of the ground, either in free air (free air blast), a certain distance above the ground (air burst) or a surface blast (explosive placed on the ground).

- ***Free air blast*** – In this case, the explosive is detonated in air sufficiently away from the ground such that shock waves propagate away from the centre of the explosive and arrives at the target without intermediate amplification of the wave as shown in Figure 2.11.

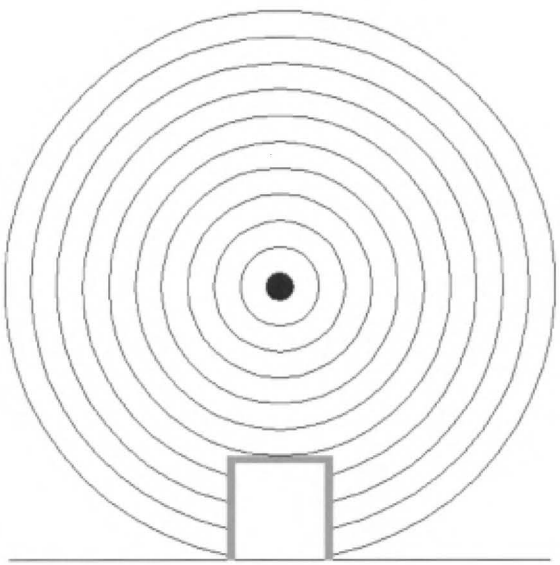

Figure 2.11: Schematic of free air blast

Above ground – in this case, the explosive is placed at a predetermined distance above the ground such that the shock wave is reflected off the ground before arriving at the target as shown in Figure 2.12.

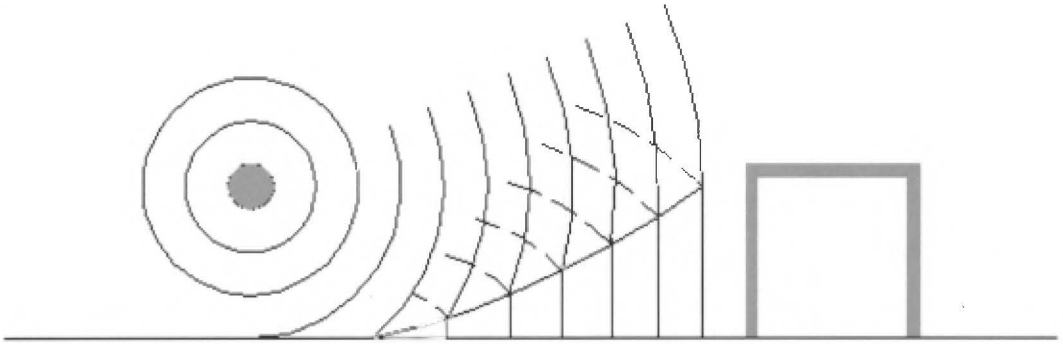

Figure 2.12: Schematic of above ground blast

- ***Surface blast*** – in this case, the explosive is placed near or on the ground. When detonation is initiated the subsequent shock wave moves from the centre of the explosive and is amplified by ground reflections, as shown in Figure 2.13.

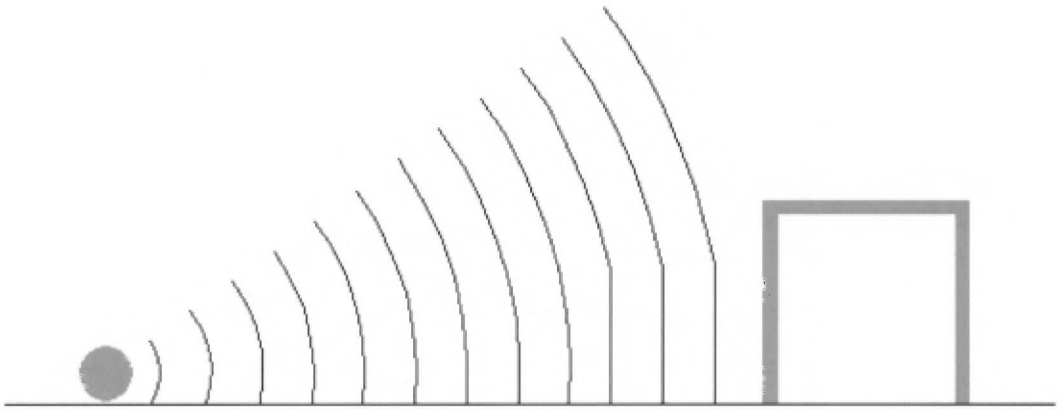

Figure 2.13: Schematic of surface blast

2.2.1.2 *Confined explosions*

This type of blast loading occurs in cases where the explosive is placed in a confined space. The level of confinement is described as follows,

- ***Fully vented*** – this type of blast loading will be produced near a barrier or confinement. The resulting shock wave is amplified by the rigid surfaces of the barrier or confining structure. The products of detonation are vented completely into the open air creating a shock wave moving away from the structure. An example is a cubicle as shown in Figure 2.14.

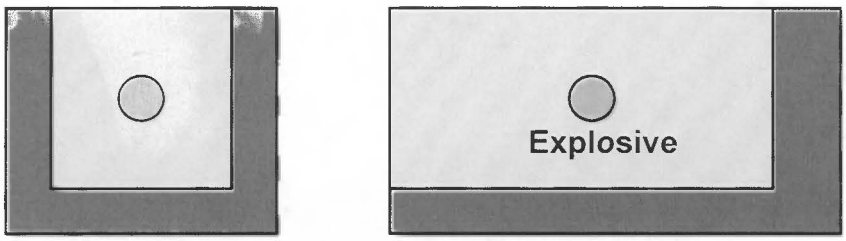

Figure 2.14: Illustration of fully vented blast loading

- ***Partially vented*** – in this type of blast loading the explosion occurs within a confining structure with limited opening to allow venting as shown in Figure 2.15. The initial shock wave is amplified by the rigid surfaces of the structure. The products of detonation are able to vent but only after a finite period of time. The confinement of detonation products results in the accumulation of high temperature and gaseous products. This is associated with a build up of gaseous pressure. This pressure has longer time duration compared to shock wave duration.

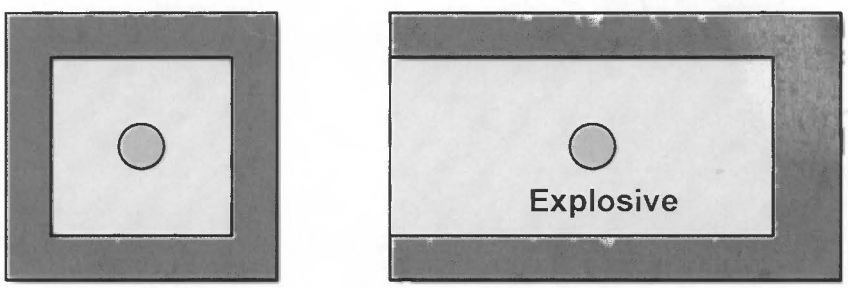

Figure 2.15: Illustration of partially vented blast loading

- ***Fully confined*** – A fully confined explosion occurs when the explosive is detonated inside a completely enclosed structure as shown in Figure 2.16. In this case the internal blast load consists of the un-vented shock wave and long duration gaseous products which is a function of the degree of confinement.

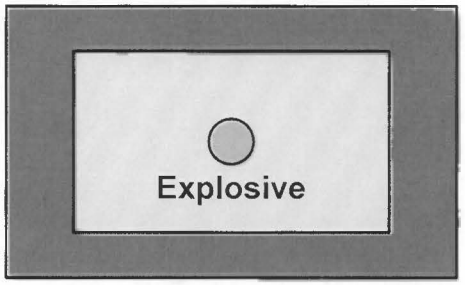

Figure 2.16: Illustration of fully confined blast loading

2.2.1.3 Effect of confinement

When an explosion is confined within a structure, the associated shock wave pressure is very high and amplified by multiple reflections within the structure. The products of detonation, (the gaseous products from the chemical reaction involved in the detonation) exert additional pressure and substantially increase the load duration. The combination of these factors leads to larger loads applied on the structure. A typical pressure-time curve for a confined explosion is shown in Figure 2.17. The initial incident and reflected blast waves are followed by several reverberating blast waves whose amplitudes are attenuated by the irreversible thermodynamic process of detonation.

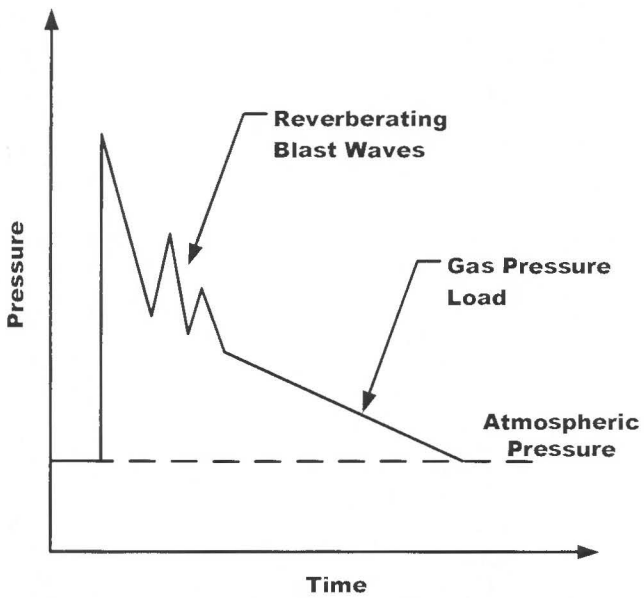

Figure 2.17: Pressure-time history for a confined explosion

2.2.2 Description of blast load

The blast load is generally expressed in terms of its pressure-time history. The specific impulse of the blast load is represented by the area under the pressure-time graph from the arrival time, t_a (as shown in Figure 2.18) is given by,

$$I_o = \int_{t_a}^{t_a+T} P(t)dt \qquad \text{(eq. 2.10)}$$

The impulse depends on the peak over-pressure, duration and the rate of decay. It is normal practice to consider the positive over-pressure only as it is larger than the under-pressure.

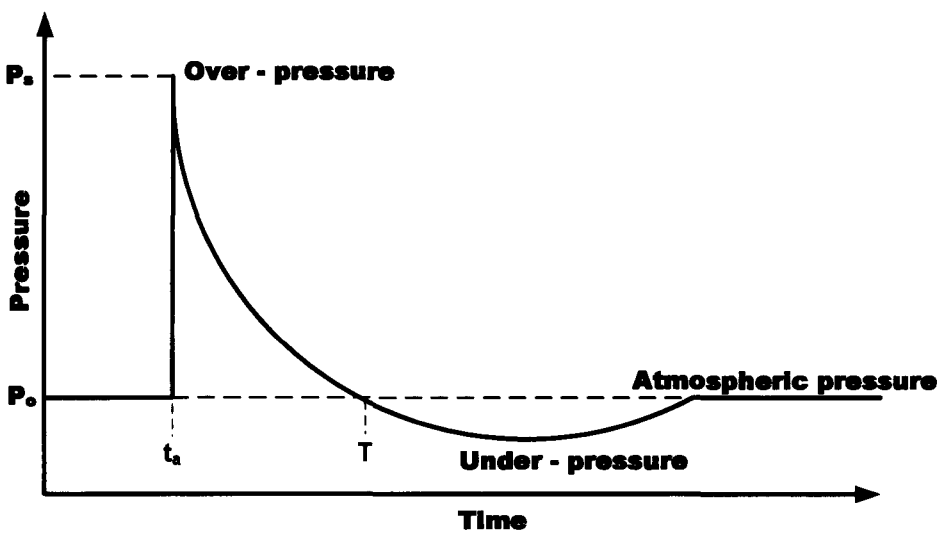

Figure 2.18: Pressure time history [13]

2.2.3 Idealised blast pressure-time history

The pressure-time history is described by exponential functions such as the Friedlander equation (eq 2.11), [14, 18].

$$P(t) = P_s\left[1 - \frac{t}{T}\right]e^{-\left(\frac{at}{T}\right)} \qquad \text{(eq. 2.11)}$$

Where, a – waveform parameter, P_s – peak overpressure, T – blast duration, t - time

However approximations of the pressure-time history are regularly used and have been found satisfactory [18] and linear decay is often used in design. In the case of conservative design approach the impulse is overestimated by assuming a pressure-time history, marked case I, in Figure 2.19. Conversely, case II, is adopted in cases

where it is desirable to preserve the impulse. It should be noted that different approximations of the pressure-time history are used other than that shown in Figure 2.18. The Steel Construction Institute [13] suggests several alternatives that are commonly used, as shown in Figure 2.20.

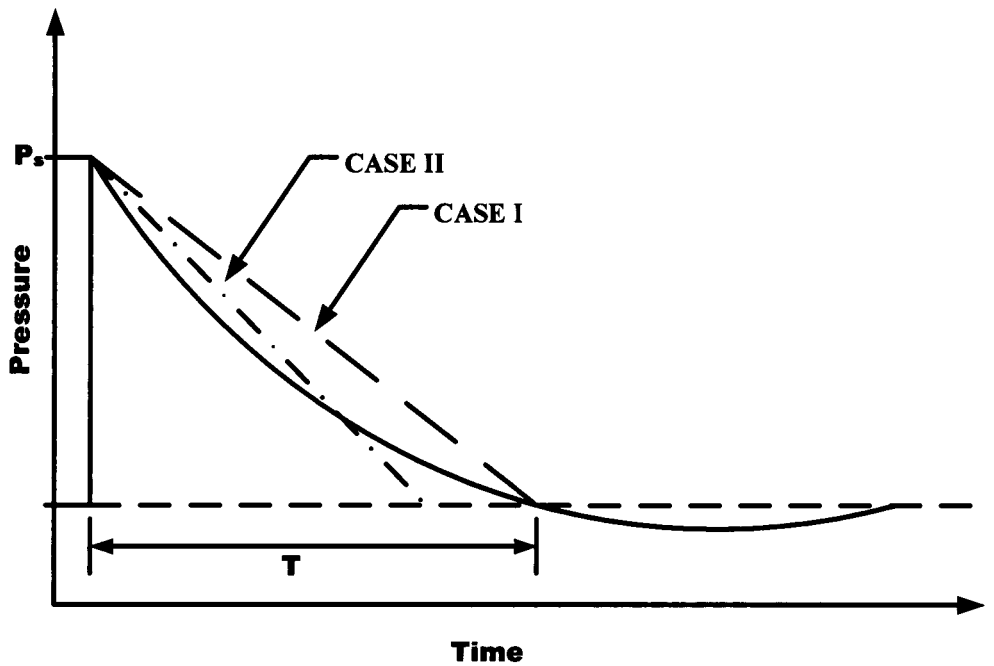

Figure 2.19: Idealization of the pressure-time history [18]

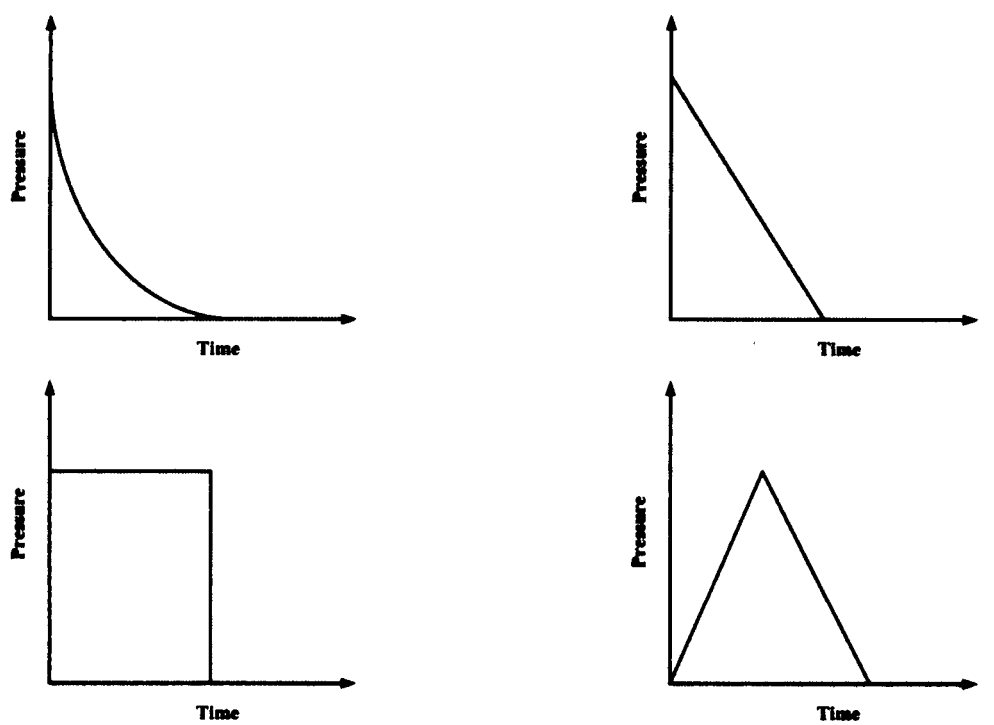

Figure 2.20: Simplified pressure – time histories [13]

2.2.4 Blast scaling

Experimental studies of large scale blast wave phenomena are expensive and difficult to perform, thus many investigators have attempted to develop models and scaling laws to describe blast wave characteristics, namely blast pressure, impulse, stand off distance and duration.

2.2.4.1 Hopkinson-Cranz scaling

The scaling law developed independently during World War I by Hopkinson and Cranz in 1915 [14, 18, 19] is the most widely known and used. The law states that "self similar blast waves are produced at identical scaled distance when two explosive charges of similar geometry and same explosive, but different size, are detonated in the same atmosphere".

The scaling law can be illustrated as follows,

Consider two charge masses W_1 and W_2 of diameter d_1 and d_2 respectively as shown in Figure 2.21.

The respective volumes of the two charges are given by

$$Volume(\text{charge1}) = \frac{\pi}{6} d_1^3 \qquad \text{(eq.2.12)}$$

$$Volume(\text{charge2}) = \frac{\pi}{6} d_2^3 \qquad \text{(eq.2.13)}$$

The charge masses W_1 is proportional to Volume (charge1) and W_2 is proportional to Volume (charge2) such that

$$W_1 \propto d_1^3 \qquad \text{(eq.2.14)}$$

$$W_2 \propto d_2^3 \qquad \text{(eq.2.15)}$$

If the charges are of the same explosive material it follows that

$$\left(\frac{d_1}{d_2}\right)^3 = \frac{W_1}{W_2} \qquad \text{(eq.2.16)}$$

$$\frac{d_1}{d_2} = \left(\frac{W_1}{W_2}\right)^{1/3} \qquad \text{(eq.2.17)}$$

The ratio of the charge diameters can be written as

$$\frac{d_1}{d_2} = \omega \qquad \text{(eq.2.18)}$$

Therefore, if the same overpressure P_s is to be produced from the two charges the ratio of the ranges at which the particular pressure is developed will also be ω. Hence the ranges at which a given overpressure is produced can be calculated from the results of equation (2.19),

$$\frac{R_1}{R_2} = \left(\frac{W_1}{W_2}\right)^{1/3} \Rightarrow \frac{R_1}{W_1^{1/3}} = \frac{R_2}{W_2^{1/3}} = Z \qquad \text{(eq.2.19)}$$

Where R_1 is the range at which a given overpressure is produced by charge W_1 and R_2 is the range at which the same overpressure is generated by charge W_2.

The Hopkinson-Cranz approach leads to the concept of scaled distance Z ($= R/W^{1/3}$). It is evident that Z is the constant of proportionality in relationships such as equations (2.17). The implication being that, an observer located at a distance R_1, from an explosive source of characteristic dimension d_1 is subjected to peak over pressure P and blast duration T. The positive blast impulse is defined by equation (2.10). The Hopkinson Scaling law then states that if an observer is positioned at a distance ZR_1 (R_2) from the centre of the explosive source of characteristic dimension Zd_1 (d_2) detonated in the same atmosphere, a blast wave of similar form with the same peak over pressure P, scaled blast duration ZT, and scaled impulse ZI is observed. All characteristic times are scaled by the same factor as the length scale factor Z. Blast peak pressure and velocities are not scaled in homologous times, (Baker [14]).

Hopkinson Scaling law applies over wide range of distance and explosive source energies.

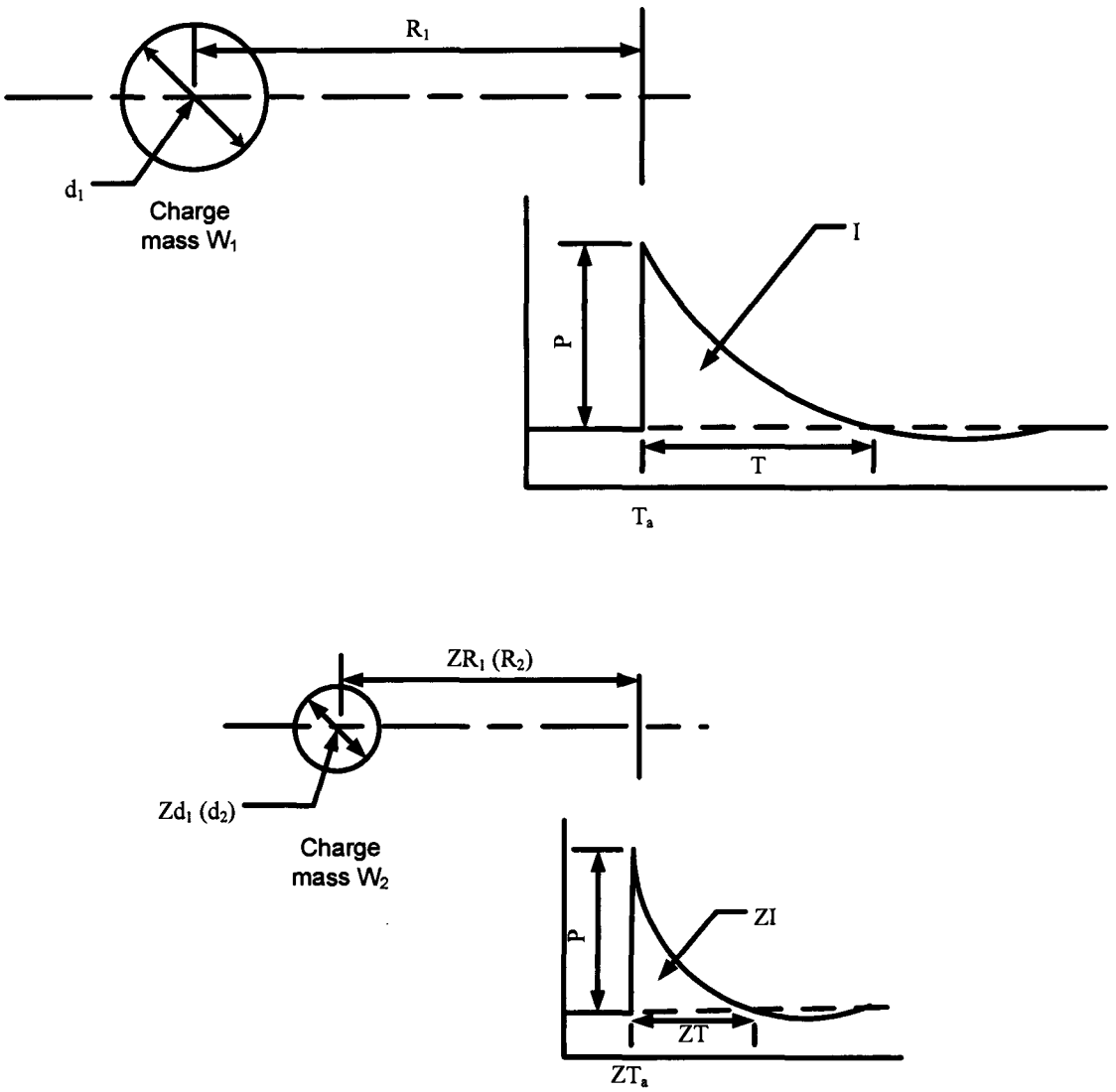

Figure 2.21: Hopkinson blast wave scaling

2.2.4.2 Sach's scaling

Another widely used scaling law was developed by Sachs [14, 19], which facilitates predictions for different ambient conditions. Sach's law states that dimensionless overpressure and impulse can be expressed as unique functions of a dimensionless scaled distance. The dimensionless parameters include quantities that include the ambient condition prior to the explosion.

2.2.5 Equations for predicting blast peak overpressure

The blast peak overpressure (P_s) and the duration of the positive pressure load (t_s) are determined as a function of scaled distance (Z) from equations developed experimentally and analytically. The analysis due to Brode [18] provides the following equations for calculating the peak overpressure, classified as near field (where P_s is greater than 10Bar) and far field (P_s between 0.1 and 10Bar).

Near Field (p_s >10 Bar)

$$P_s = \frac{6.7}{Z^3} + 1 \text{ (Bar)} \qquad \text{(eq. 2.22)}$$

Medium and Far Field (0.1<p_s<10 Bar)

$$P_s = \frac{0.975}{Z} + \frac{1.455}{Z^2} + \frac{5.85}{Z^3} - 0.019 \text{ (Bar)} \qquad \text{(eq. 2.23)}$$

Henrych proposed three equations for blast over pressure classified according to ranges of scaled stand-off distances (Z); the equations are derived from TNT explosions [18].

For range 0.05 < Z < 0.3(m/kg$^{1/3}$)

$$P_s = \frac{14.072}{Z} + \frac{5.540}{Z^2} - \frac{0.357}{Z^3} + \frac{0.00625}{Z^4} \text{ (Bar)} \qquad \text{(eq. 2.24)}$$

For range 0.3 < Z < 1.0(m/kg$^{1/3}$)

$$P_s = \frac{6.194}{Z} - \frac{0.326}{Z^2} + \frac{2.132}{Z^3} \text{ (Bar)} \qquad \text{(eq. 2.25)}$$

For range 1 < Z < 10(m/kg$^{1/3}$)

$$P_s = \frac{0.662}{Z} + \frac{4.05}{Z^2} + \frac{3.288}{Z^3} \text{ (Bar)} \qquad \text{(eq. 2.26)}$$

Kinney and Graham proposed the equation (eq. 2.27) for peak overpressure and (eq. 2.28) for blast duration derived from the relationship between the Mach number of the shock front and ambient pressure [10].

Ratio of peak overpressure to ambient pressure

$$\frac{P_s}{P_o} = \frac{808\left(1+\left(\frac{Z}{4.5}\right)^2\right)}{\sqrt{1+\left(\frac{Z}{0.02}\right)^2}\sqrt{1+\left(\frac{Z}{0.32}\right)^2}\sqrt{1+\left(\frac{Z}{1.35}\right)^2}} \qquad \text{(eq. 2.27)}$$

Blast duration

$$\frac{t_s}{W^{1/3}} = \frac{980\left[1+\left(\frac{Z}{0.54}\right)^{10}\right]}{\left[1+\left(\frac{Z}{0.02}\right)^{3}\right]\left[1+\left(\frac{Z}{0.74}\right)^{6}\right]\sqrt{1+\left(\frac{Z}{6.9}\right)^{2}}} \qquad \text{(eq. 2.28)}$$

Example:

Comparing peak overpressures calculated using the equations (2.22 – 2.27).

Assume a 1kg of TNT sphere detonated at the centre. Determine the blast peak overpressure at 1m from the charge.

Scaled distance Z is given by

$$Z = \frac{R}{W^{1/3}} = \frac{1m}{(1kg)^{1/3}} = 1mkg^{-1/3}$$

Using Brode equations for Z = 1m (equations 2.22 and 2.23)

Near Field (p_s >10 Bar) (2.22)

$$P_s = \frac{6.7}{Z^3} + 1 = \frac{6.7}{1^3} + 1$$

$P_s = 7.7$ (Bar) = <u>0.77MPa</u>

Medium and Far Field (0.1<p_s<10 Bar) (eq. 2.23)

$$P_s = \frac{0.975}{Z} + \frac{1.455}{Z^2} + \frac{5.85}{Z^3} - 0.019 = \frac{0.975}{1} + \frac{1.455}{1^2} + \frac{5.85}{1^3} - 0.019$$

$$P_s = 0.975 + 1.455 + 5.85 - 0.019$$

$P_s = 8.26$ (Bar) = <u>0.83MPa</u>

Using Henrych equations for Z = 1m (equations 2.25 and 2.26)

For range 0.3 < Z < 1.0(m/kg$^{1/3}$) (eq. 2.25)

$$P_s = \frac{6.194}{Z} - \frac{0.326}{Z^2} + \frac{2.132}{Z^3} = \frac{6.194}{1} - \frac{0.326}{1^2} + \frac{2.132}{1^3}$$

$$P_s = 6.194 - 0.326 + 2.132$$

$P_s = 8$ (Bar) = <u>0.80MPa</u>

For range 1 < Z < 10(m/kg$^{1/3}$) (eq. 2.26)

$$P_s = \frac{0.662}{Z} + \frac{4.05}{Z^2} + \frac{3.288}{Z^3} = \frac{0.662}{1} + \frac{4.05}{1^2} + \frac{3.288}{1^3}$$

$$P_s = 0.662 + 4.05 + 3.288$$

$P_s = 8$ (Bar) = <u>0.80MPa</u>

Using Kinney and Graham equation for Z = 1m (equation 2.27)

$$\frac{P_s}{P_o} = \frac{808\left(1+\left(\frac{Z}{4.5}\right)^2\right)}{\sqrt{1+\left(\frac{Z}{0.02}\right)^2}\sqrt{1+\left(\frac{Z}{0.32}\right)^2}\sqrt{1+\left(\frac{Z}{1.35}\right)^2}} = \frac{808\left(1+\left(\frac{1}{4.5}\right)^2\right)}{\sqrt{1+\left(\frac{1}{0.02}\right)^2}\sqrt{1+\left(\frac{1}{0.32}\right)^2}\sqrt{1+\left(\frac{1}{1.35}\right)^2}}$$

$$\frac{P_s}{P_o} = 9.96$$

Where P_o – atmospheric pressure (0.101MPa)

Therefore,

$P_s = 1010\,\text{KPa}$ = 1.01MPa

The peak overpressure at a distance of 1m from the charge calculated using Brode's equation for near field (equation (2.22)) is lower than that determined using the equation for medium to far field (equation (2.23)). The peak overpressure obtained using equations proposed by Henrych (equations (2.25 and 2.26)) and Kinney and Graham (equation (2.27)) are similar to that determined using Brode's equation for medium and far field. The values for peak overpressure calculated using the different equations range from 0.80MPa to 1.01MPa. Hence, it is important that the correct equation is used to determine the peak overpressure. Care must also be taken to ensure that the equation is applied within its specified range of validity.

2.2.6 Blast curves

The use of scaled distance (Z) in blast curves as shown in Figure 2.22, [18], and those presented in TM-5-1300 [15] allows for a compact and convenient representation of blast wave data. It should be noted that some of these charts (as shown in Figure 2.22) are based on results from experiments using spherical charges of TNT detonated in air.

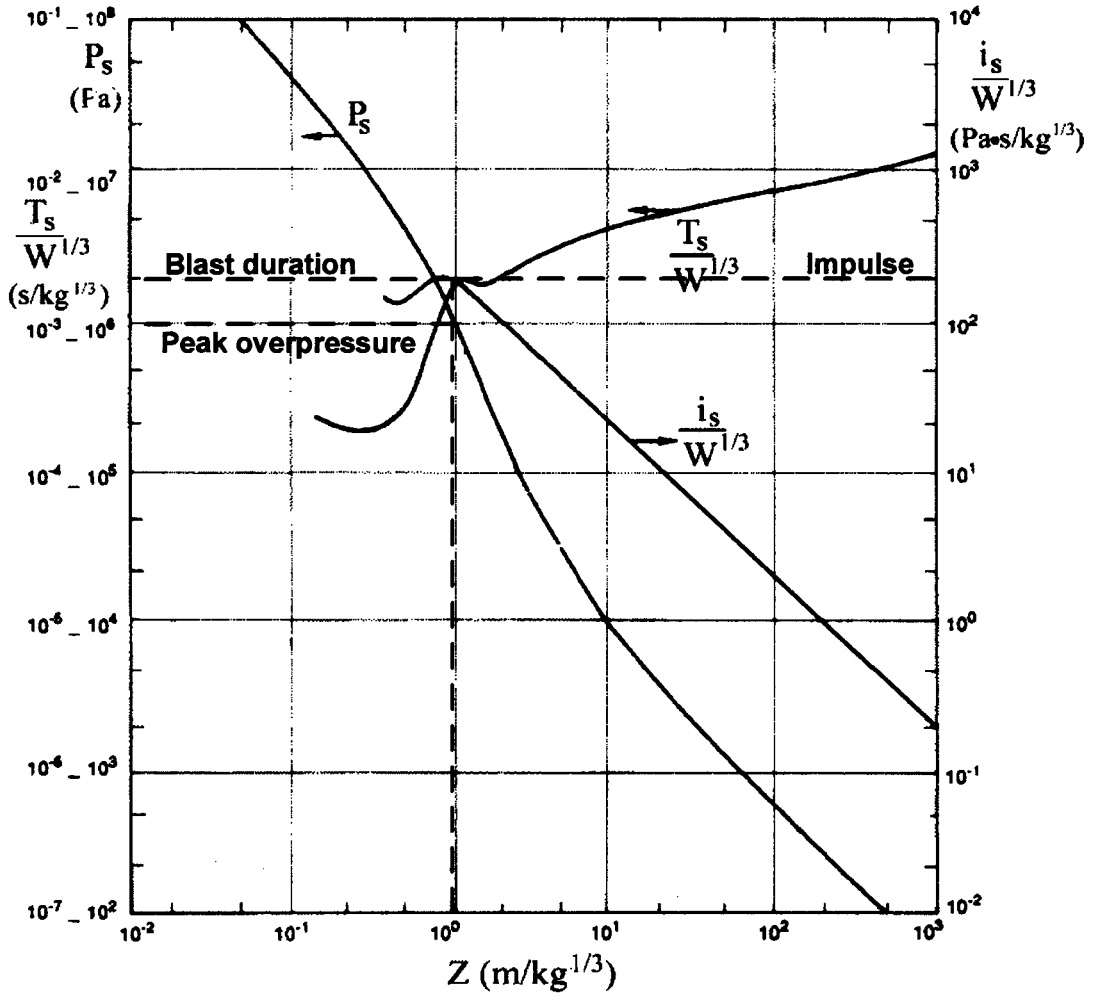

Figure 2.22: Peak overpressure (Ps) for spherical charges of TNT detonated in air [18]

An example of using blast curves is as follow,

Assume 1kg of TNT sphere detonated at the centre. Determine the blast peak overpressure, duration and impulse at a distance of 1m from the explosive.

Scaled distance Z is given by

$$Z = \frac{R}{W^{1/3}} = \frac{1m}{(1kg)^{1/3}} = 1mkg^{-1/3}$$

From the chart shown in Figure 2.22 (dashed lines are used as guides for the reader), the peak pressure, duration and impulse are interpolated,

Peak pressure – 10^6Pa = 1.00MPa,

Blast duration – 0.002sec = 2ms

Specific Impulse – 200Pa.sec

The peak overpressure magnitude determined using the blast curves is similar to that obtained using the blast overpressure equations described in Section 2.2.5.

2.2.7 Reflected pressure

When blast waves encounter a solid surface denser than air it will reflect from it. The simplest case is that of an infinitely large rigid surface onto which the blast wave impinges upon at zero angle of incidence. In this case the incident blast wave front travelling at velocity U undergoes reflection when the forward moving air molecules in the blast wave are brought to rest and further compressed by the following air molecules. This induces a reflected overpressure on the wall which has a greater magnitude than the incident overpressure as shown in Figure 2.23.

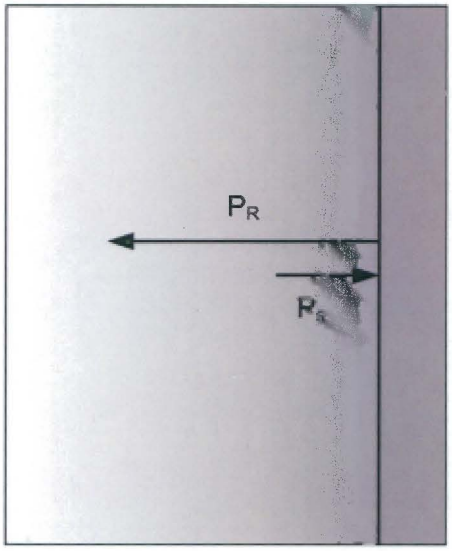

Figure 2.23: Illustration of incident and reflected pressure

The equation for the reflected pressure is given by eq. 2.29, [18].

$$P_r = \frac{2P_s(710+4P_s)}{710+P_s} \text{ (KPa)} \qquad \text{(eq. 2.29)}$$

Where, P_r – reflected pressure, P_s – incident overpressure (KPa)

Following the example from Section 2.26 of a 1kg TNT spherical charge detonated at the centre. The charge is placed 1m from a rigid wall. The incident peak overpressure is 1.00MPa. The reflected pressure is calculated using equation (2.29)

$$P_r = \frac{2P_s(710+4P_s)}{710+P_s} = \frac{2\times1000(710+4\times1000)}{710+1000}$$

Therefore,

P_r = 5508.77KPa = 5.51MPa

The value of the reflected pressure is 5.5 times greater than the incident pressure calculated in Section 2.2.6.

2.2.8 Shock waves in tubes

2.2.8.1 Shock tubes

The response of structures subjected to shock loading has been studied for many years using shock tubes. It enables researchers with a simple and efficient way of subjecting structures to shockwaves. A shock tube consists of a high pressure and low pressure section separated by a diaphragm as shown in Figure 2.24. The driver section is pressurised with gas

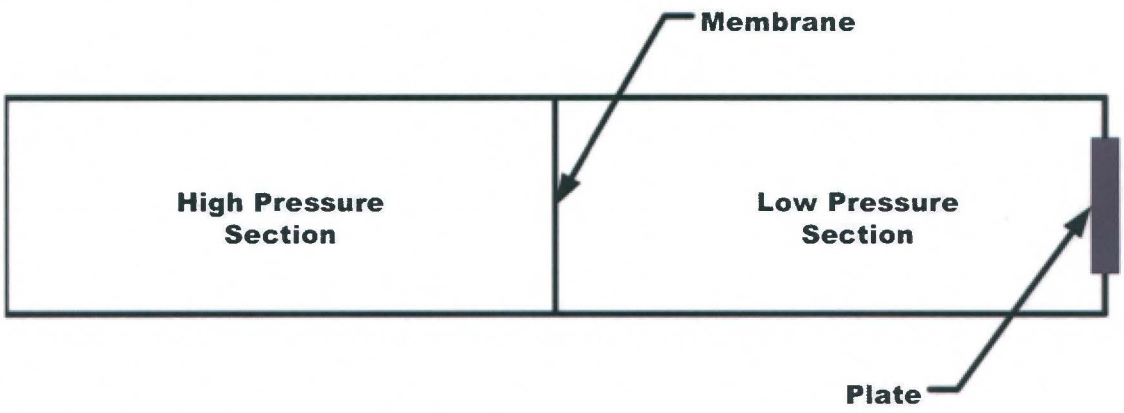

Figure 2.24: Principle of the shock tube, [20]

The high pressure chamber is filled with gas until the membrane is ruptured. A shock wave travels through the low pressure chamber and loads the test plate fixed on the end of the shock tube imparting a high pressure pulse. The pressure-time history of

the load is measured using piezoelectric transducer placed along the length of the shock tube, (Stoffel, [20]).

Shock tubes are designed for different requirements. Kosing and Skews [21] report liquid filled shock tubes used for high speed forming of plates. The pressure energy is used to form metal plates to the desired shape. The liquid shock allows for controlled delivery of the required energy for deformation. A typical pressure-time history for a shock wave travelling down the length of a liquid shock tube is shown in Figure 2.25. The figure shows the pressure-time history of the shock wave at three points along the length of the shock tube. The difference in peak pressure between the top and middle graph is attributed to small loses within the tube. The bottom graph (transducer closest to the plate) shows a sudden drop in pressure due to deformation of the plate. It should be noted that no reflections are observed. This is attributed to complete absorption of pressure energy by the plate deformation process [6].

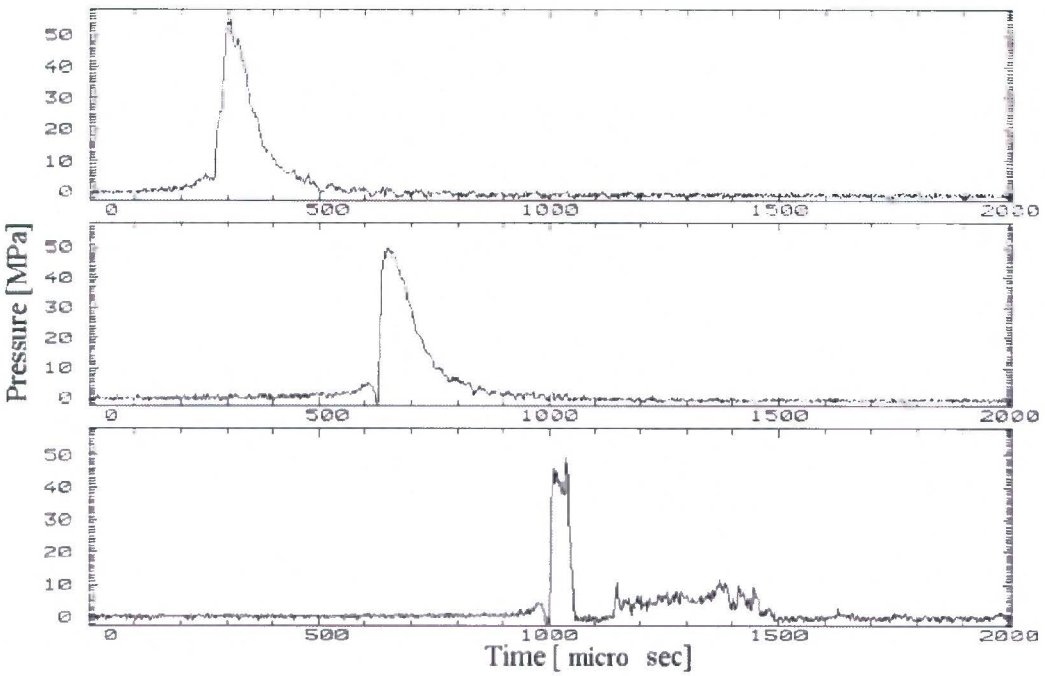

Figure 2.25: Pressure-time history of a shock wave travelling down a shock tube measured at three different locations on the shock tube [21]

2.3 Structural response of plates subjected blast loading

The response of fully clamped metal plates subjected to uniform and localised blast loads has been studied for many years. Experimental work on beams, plates and shells has been widely reported. Nurick and Martin [1, 2] present an overview of theoretical and experimental work conducted in this field pre 1990's. Uniformly distributed impulsive loads were considered. In subsequent years, mild steel plates subjected to circular localised blast loads are reported by Nurick et al [6 – 8].

2.3.1 Impulsive loading – experimental methods

Understanding the response of structures to impulsive loads requires that input and response parameters are well defined and consistent [24]. The following experimental methods are widely used to simulate the response of structures to impulsive loading,

- Air pressure waves generated from explosive devices,
- Impulsive loading using plastic explosives mounted directly, and
- Pressure pulse created using pressure differential between two air chambers.

2.3.1.1 Air pressure generated from explosive devices

An explosive device is detonated in air and structures to be investigated are secured using clamping frames and placed in the path of the pressure wave. Jacinto et al [10] investigated quadrangular steel plates 0.95mm and 2.1mm thick subjected to blast loads using this method. The experimental setup used by Jacinto et al is shown in Figure 2.27. The plate dimensions were 0.95 x 0.95m and 1.0m x 1.5m. The explosive used was Gelamon VF80, with a TNT equivalency of 80%.

Figure 2.27: Photograph of experimental set up used for air pressure generated from explosive devices [10]

The pressure time history of the blast load was recorded using Honeywell 180PC pressure sensors. A typical pressure time history is shown in Figure 2.28. The dynamic response of the plates was measured using accelerometers placed on the plates.

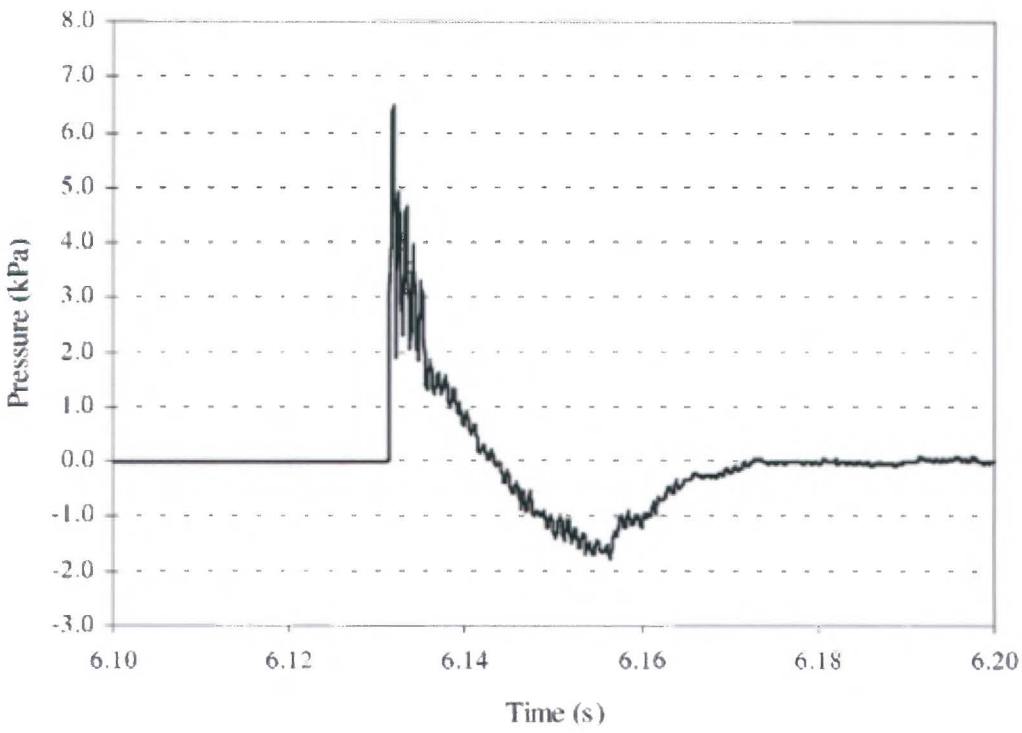

Figure 2.28: Typical pressure time history for air pressure generated from explosive devices [10]

2.3.1.2 *Impulsive loading using plastic explosive mounted directly*

A known mass of plastic explosive is shaped to the required geometry and placed onto polystyrene pads, as shown in Figure 2.29. The polystyrene pad attached to the test specimen is clamped onto a ballistic pendulum as shown in Figure 2.30. The impulse applied by the explosive is measured from the oscillation of the pendulum. This method has been used by Nurick et al. [2 - 8] for uniform and localised blast loading of mild steel plates of different geometries and thicknesses.

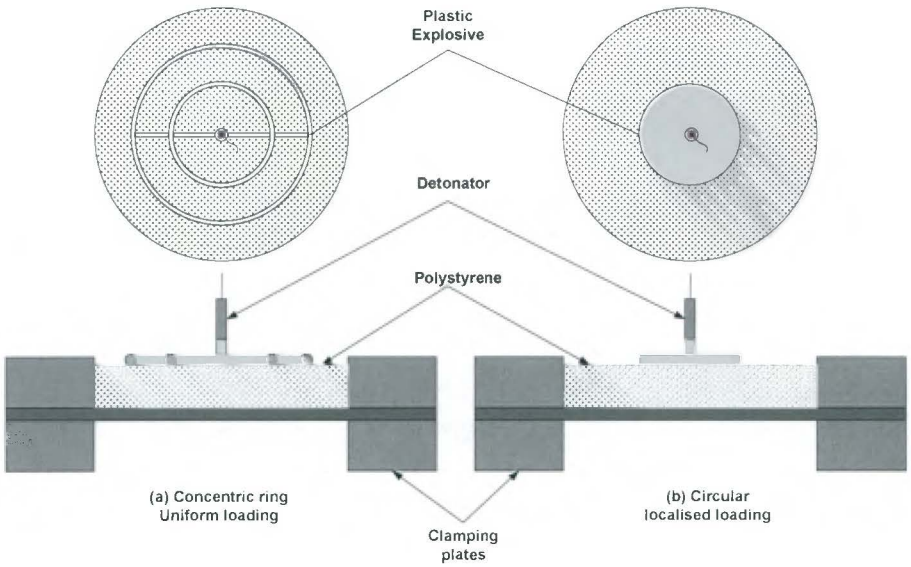

Figure 2.29: Schematic diagram of two different explosive geometries

Figure 2.30: Photograph of experimental set up for impulsive loading using plastic explosive mounted directly

a) *Uniform impulsive loading using plastic explosive mounted directly*

The plastic explosive is laid out in concentric annuli of the shape of the plate, as shown in Figure 2.31 (a) and (b) connected by a cross-leader of explosive. The use of concentric annuli as opposed to using explosive spread over the entire plate area is necessitated by the explosive failing to detonate if charge thickness is less than 2.0mm, as reported by Nurick and Martin [25] using sheet explosive Metabel. This imposes a restriction on the charge mass that can be used, as charge thickness is a function of charge mass and exposed plate area. The arrangement of the concentric annuli is such that there is on average a uniform distribution of explosive mass over the plate [25]. A polystyrene pad is placed between the explosive and plate to prevent spallation of the test plate.

This method was used by Nurick et al [2 - 5].

The concentric annuli are set out as follows:

Circular: $r_1 = 0.41R$; $r_2 = 0.82R$

Square: $l_1 = 0.49L$; $l_2 = 0.84L$

Rectangular: $w_1 = 0.50W$; $w_2 = 0.87W$; $b_1 = 0.50B$; $b_2 = 0.87B$

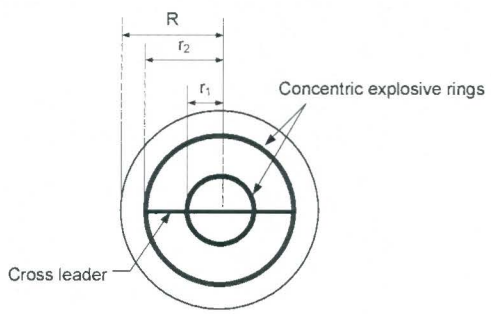

(a) Explosive concentric ring layout for circular plates

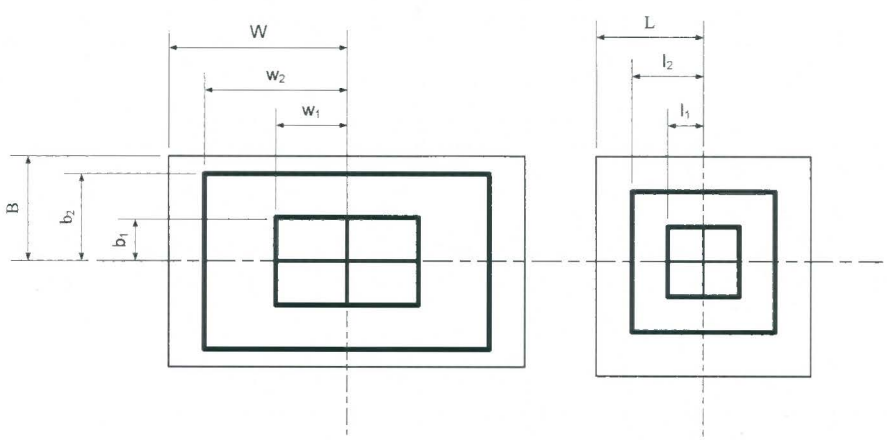

(b) Explosive concentric ring layout for quadrangular plates

Figure 2.31: Explosive layout for uniformly loaded circular and quadrangular plates

b) Localised loading using plastic explosive mounted directly

A disc shaped explosive is laid on a polystyrene pad ranging in thickness from 12mm to 16mm. The explosive height and diameter is based on the loading required [6 - 8]. The polystyrene is attached onto the test plate which is clamped between two clamping plates and fixed onto the ballistic pendulum. The general layout of localised loading is shown in Figure 2.32.

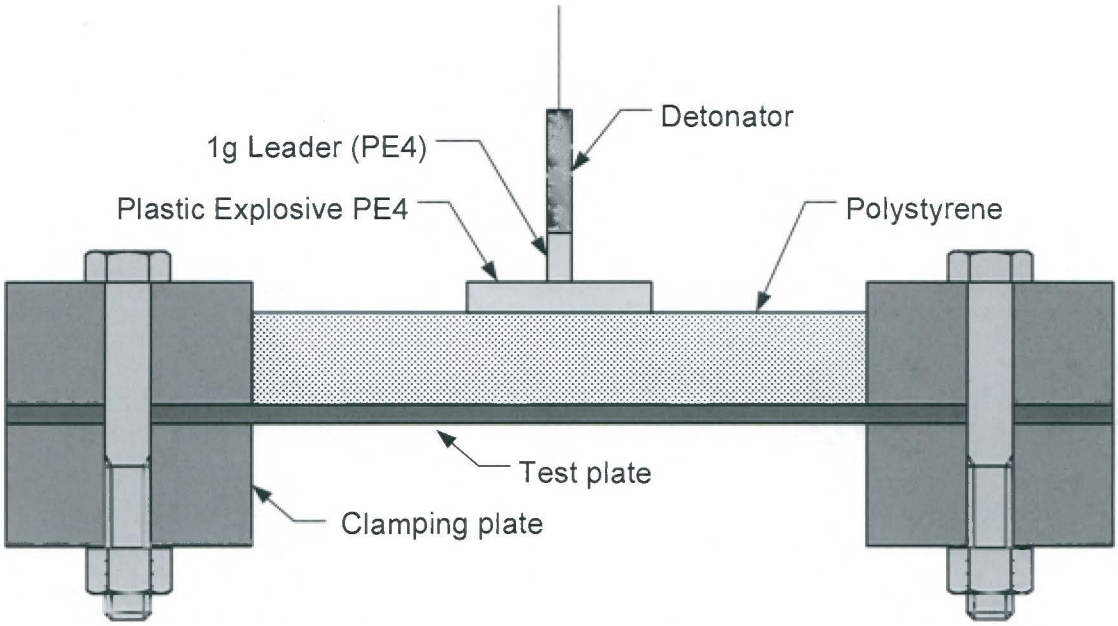

Figure 2.32: Explosive layout for circular localised blast loads

2.3.1.3 *Pressure pulse created using pressure differential between two air chambers*

This method uses pressure differential between two air chambers to impart dynamic load onto the test specimen clamped between the two air chambers via the timed blow-down of the chambers. This method has been shown to produce uniform load distribution across the structure (Langdon [24] and Schleyer et al [26]). The experimental test rig is shown in Figure 2.33. A typical pressure time history of the load is shown in Figure 2.34.

Figure 2.33: Photograph of pressure pulse loading rig [24]

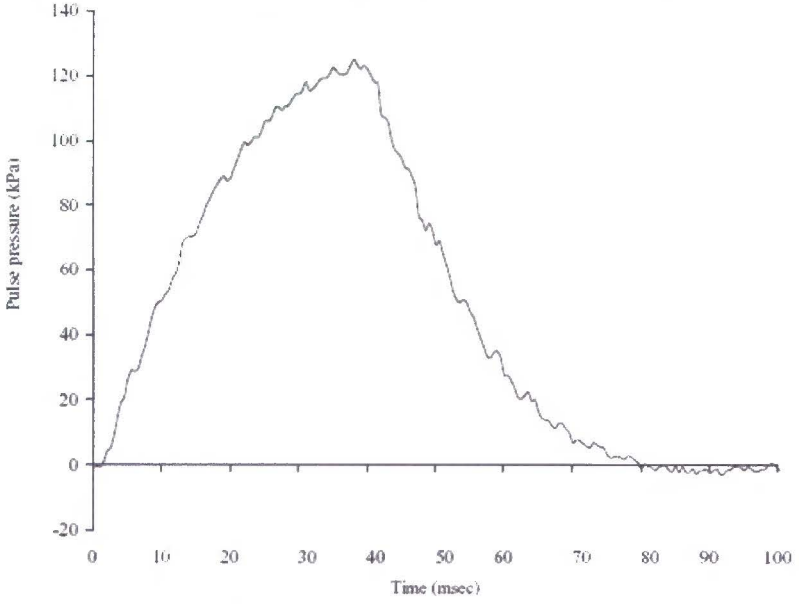

Figure 2.34: Typical pressure time history using pressure pulse loading test rig [26]

2.3.2 Uniformly loaded plates

The studies of impulsive loads on thin disc or circular plates were first conducted during World War II; a review of different experimental work in this field is reported by Nurick and Martin [1].

2.3.2.1 Thin plates subjected to uniform blast load

Experiments on thin mild steel plates subjected to uniform blast loads have been reported by Nurick et al, [2 - 5]. Nurick and Martin, [2] report the development of dimensionless impulse numbers for the different plate geometry (circular and quadrangular) and empirically derived equations for predicting large permanent transverse displacement of the centre of the plate. The failure of circular plates was investigated by Teeling-Smith and Nurick, [5]. The effect of increasing impulse on plate mid-point deflection is reported. It is stated that plate deflection increases with increasing impulse resulting in thinning at the boundary. Further increase in impulse leads to partial tearing along the boundary, followed by complete tearing. The mid-point deflection decreases as impulse is further increased beyond the threshold of complete tearing at the boundary as the failure tends towards complete shear. Figure 2.35 shows the transition in plate deformation reported by Teeling-Smith and Nurick [5]. Analysis was performed to formulate an energy balance equation in terms of input energy and deformation, tearing and disc energy.

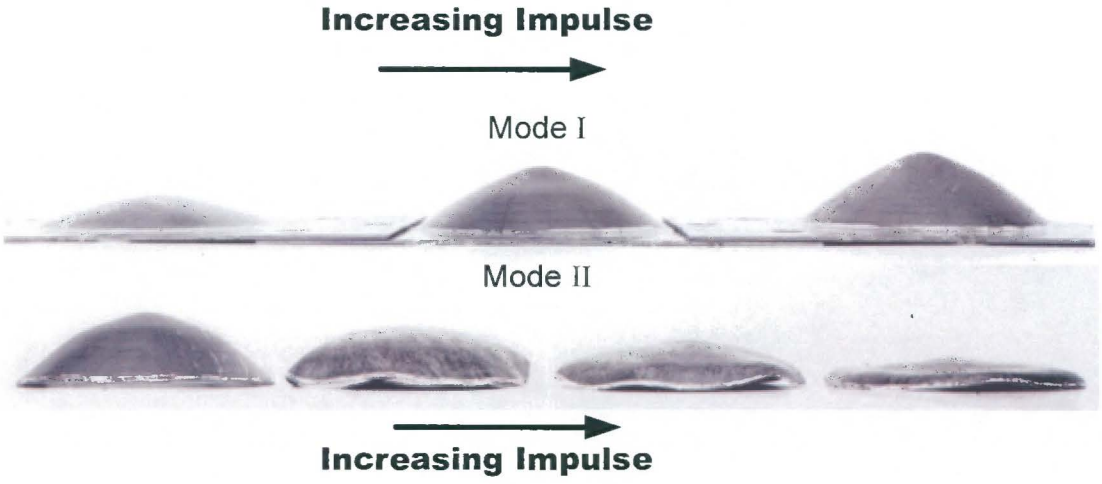

Figure 2.35: Changing mid-point deflection for increasing Impulse (uniformly loaded circular plates) [5]

Experiments on uniformly loaded square plates are reported by Nurick and Shave, [4]. Different failure mechanisms were investigated ranging from large inelastic deformation to partial tearing at the boundary to complete shear. Plate deformations are similar to those reported by Teeling-Smith and Nurick [5] for uniformly loaded circular plates. The mid-point deflection increases for increasing impulse until partial tearing initiates at the middle of one or more sides of the square plate as shown in Figure 2.36. Further increase in impulse results in complete tearing on all sides of the plate with increasing mid-point deflection followed by decreasing mid-point deflection as the plate failure tends towards complete shear at the boundary with no significant mid-point deflection as shown in Figure 2.37.

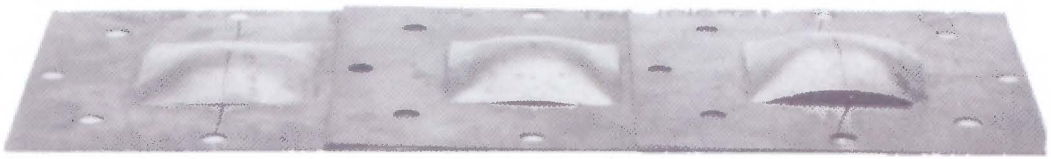

Figure 2.36: Increasing mid-point deflection for increasing impulse with partial tearing along plate boundary [4]

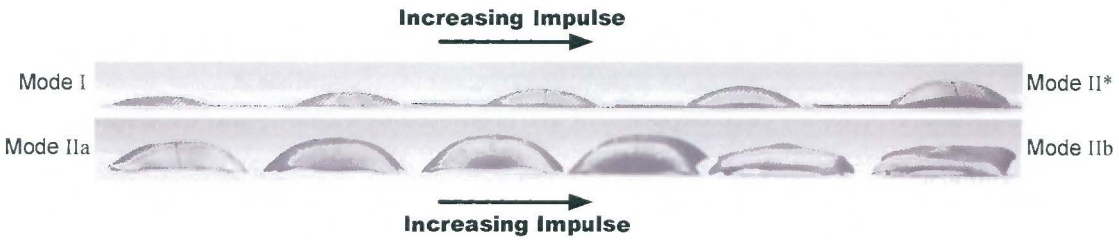

Figure 2.37: Changing mid-point deflection for increasing Impulse (uniformly loaded square plates) [4]

2.3.2.2 *Effect of boundary fixation on thin plates subjected to uniform blast load*

The effect of different plate edge fixations is reported by Thomas and Nurick [9]. Fully clamped plates used by Nurick et al [2, 4, 5] were compared to built-in plates machined from 20mm thick mild steel plates to approximate thickness at the test area of 1.6mm, as shown in Figure 2.38. The results showed that, in the case of large inelastic deformation with no tearing at the boundary the mid-point deflection of clamped circular plates and built-in circular plates are generally within ±1 deflection – thickness ratio as shown in Figure 2.39. However it is noted that curvature of the plate deformation near the boundary starts within the clamped region for fully clamped plates. In the case of built-in plates the curvature of plate deformation begins at the boundary as shown in Figure 2.40. Partial tearing along the boundary occurred at lower impulses for built-in plates compared to clamped plates. It is further stated that clamped plates do not fully prevent in-plane movement of the plate during impulsive loading. This behaviour is also reported by Schleyer et al [26] for pulse pressure loaded mild steel plates.

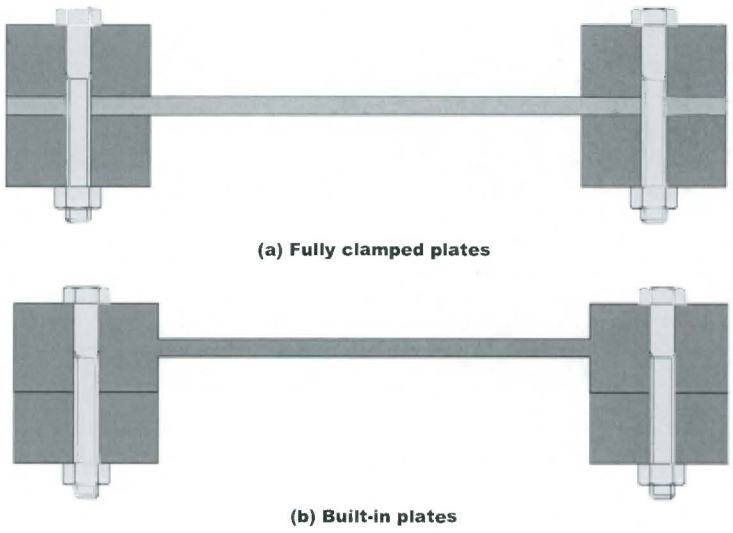

Figure 2.38: Schematic of different plate boundary fixations [9]

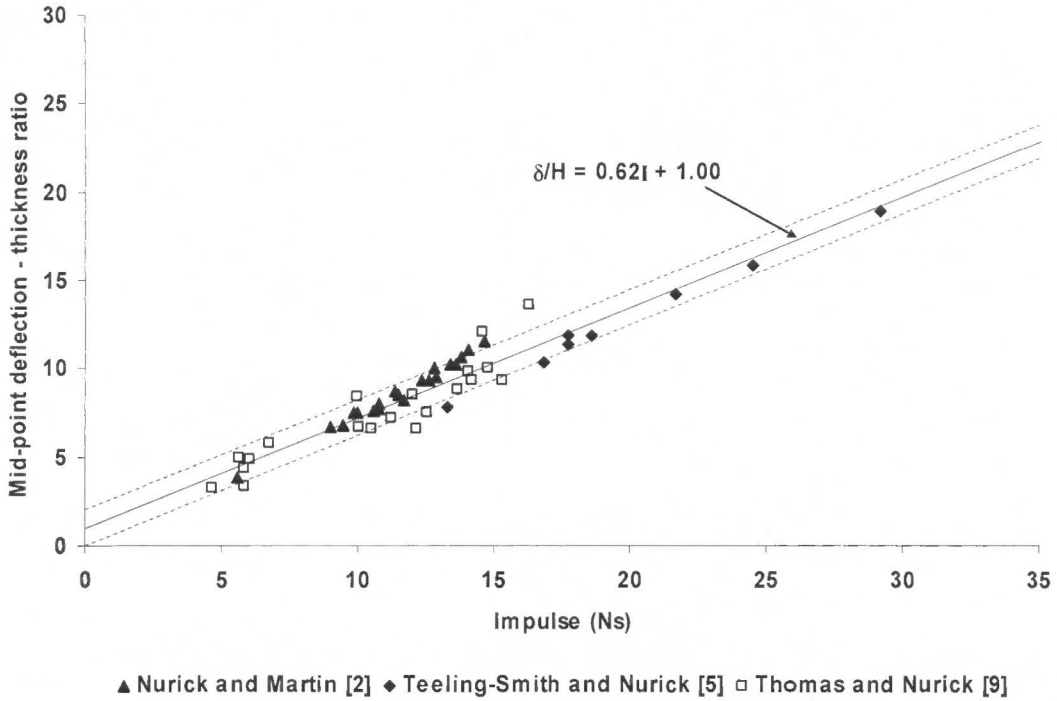

Figure 2.39: Graph of mid-point deflection - thickness ratio versus impulse for large inelastic deformation (Mode I) of fully clamped circular plates [2, 5] and built-in circular plates [9]

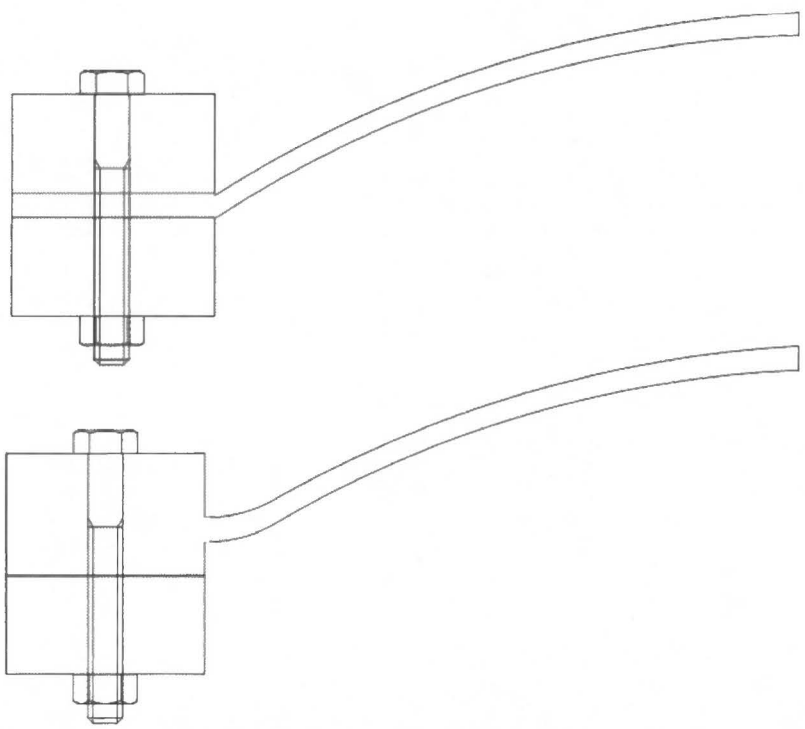

Figure 2.40: Schematic of difference in plate deformation curvature near the boundary for fully clamped and built-in plates [9]

Nurick et al [3] investigated the onset of thinning for different diameter circular mild steel plates clamped between two thicker clamping plates with different edge conditions, as shown in Figure 2.41. The clamps featured sharp edge or fillet radii of 1.5mm or 3.2mm. Observations from the experiments showed that thinning occurred for all plate diameters with sharp edged clamps, however, plates secured using clamping plates with fillets showed larger deflection before the onset of thinning and tearing. The necking at the boundary observed for sharp edged clamps exhibit sharp indentation due to the clamp followed thereafter by stretching and thinning. In the case of curved edge boundary the thinning is similar to that observed in a uniaxial tensile test.

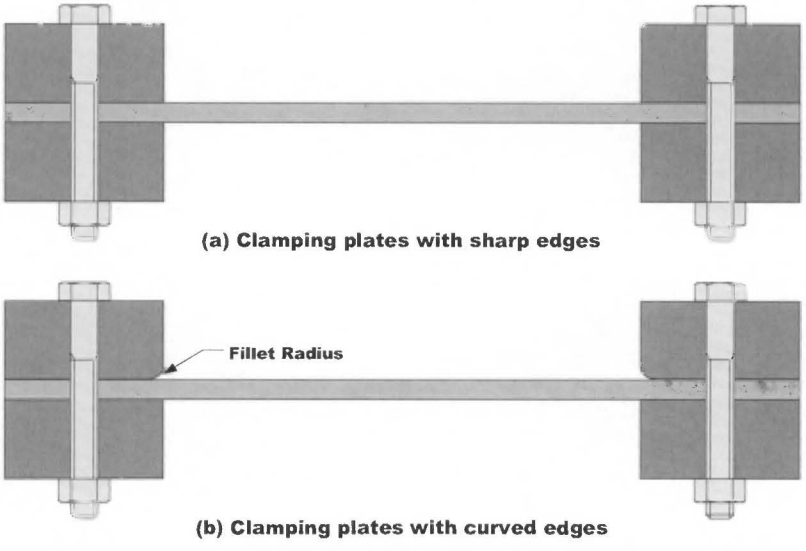

Figure 2.41: Schematic of edge boundary conditions for fully clamped plates [3]

2.3.2.3 Effect of stiffeners on thin plates subjected to uniform blast load

Nurick et al [27, 28] report experiments using stiffened plates. The stiffeners and the plate were two separate components clamped together by two support plates. The test plates with the stiffeners were subjected to uniform blast loads. Nurick et al [29] also report on experimental work on built-in stiffened quadrangular plates. The stiffener, plate and boundary are machined from 12mm thick plate as shown in Figure 2.42. Chung Kim Yuen and Nurick [30] report an experimental investigation into the influence of different stiffener configurations as shown in Figure 2.43. The results indicated that for large inelastic deformation there was a general trend of increasing permanent displacement with increasing impulse similar to un-stiffened plates. In case of tearing at the boundary, the behaviour is similar to that of un-

stiffened square plates. The tearing occurs at the middle of the sides and then progresses towards the corners as the impulse increases. Chung Kim Yuen and Nurick [30] report that tearing is not reduced by stiffening the plates. The stiffeners restrict the plate to deform plastically causing tearing to occur at an impulse that would normally cause an un-stiffened plate to deform. Other experimental work has been reported by Langdon et al [31] on stiffened plates subjected to localised blast loads. The results show increased influence of stiffener configuration. A stiffener located along the mid-line of the plate significantly reduced the overall plate deformation. However, premature tearing occurred at the plate – stiffener interface rather than at the boundary as reported by Chung Kim Yuen and Nurick [30] for uniformly loaded stiffened plates.

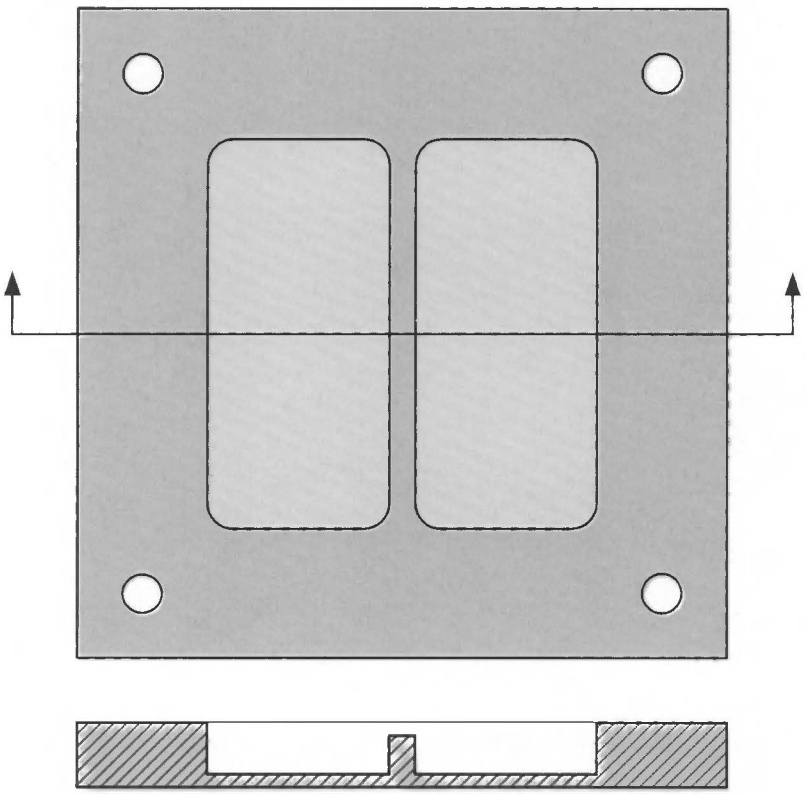

Figure 2.42: Schematic drawing of a built-in plate showing required stiffener configuration machined from 12mm thick mild steel base plate [29]

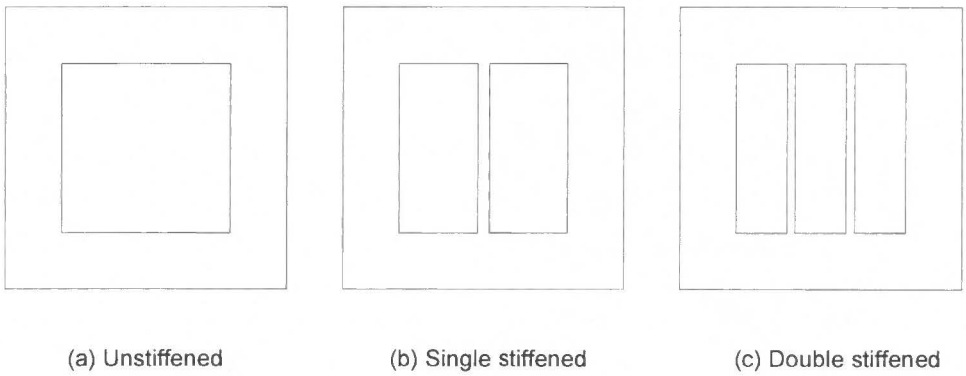

(a) Unstiffened (b) Single stiffened (c) Double stiffened

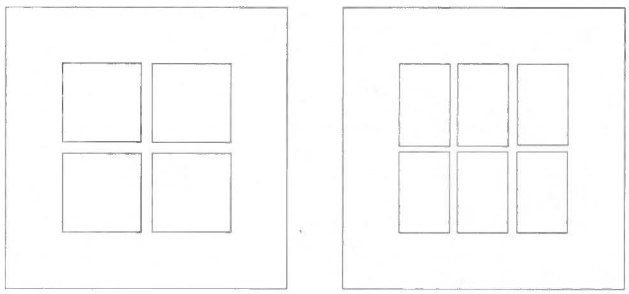

(d) Cross (e) Double cross

Figure 2.43: Schematic drawing of different stiffener configuration [31]

2.3.2.4 *Modes of failure for thin plates subjected to uniform blast loads*

Failure modes of structures were first classified by Menkes and Opat [32], for blast loaded beams.

Mode I – Large inelastic deformation of the entire beam

Mode II – Tearing (tensile failure) of the beam material at the supports

Mode III – Transverse shear failure of the beam material at the supports

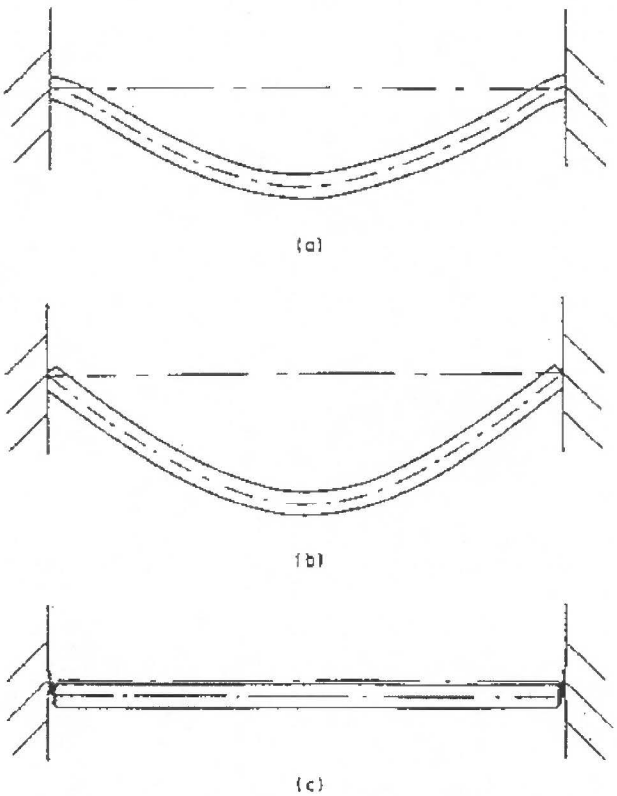

Figure 2.44: Permanent plate deformations (a) Mode I, (b) Mode II and (c) Mode III

Nurick et al [15] further subdivided Mode I failure to describe necking partially and completely around the plate boundary.

Mode Ia – Large inelastic deformation with necking around part of the boundary

Mode Ib – Large inelastic deformation with necking around the entire boundary

The lower bound of Mode Ia is the phase where some part of the boundary exhibits necking. As the load is increased, necking progresses to cover the entire boundary, (upper bound of Mode I) and is designated as Mode Ib failure.

Further increase in load exhibit the transition from Mode I type failure to Mode II. The lower bound of Mode II failure is manifested in the plate as tearing along part of the boundary and is classified as Mode II*. Further classification of the Mode II failure included the case of increasing mid-point deflection for increasing impulse. Further increases in impulse resulted in reduced mid-point deflection similar to those for Mode III failure [4].

Mode II* – Large inelastic deformation with partial tearing around part of the boundary

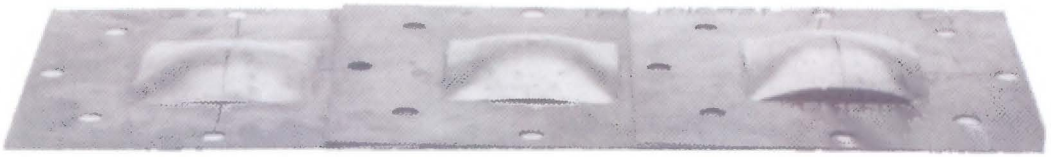

Figure 2.45: Increasing mid-point deflection for increasing impulse with partial tearing along plate boundary [4] (repeated figure)

Mode IIa – Increasing mid-point deflection with increasing impulse with complete tearing at the boundary

Mode IIb – Decreasing mid-point deflection with increasing impulse with complete tearing at the boundary

Figure 2.46: Changing mid-point deflection for increasing impulse (uniformly loaded square plates) [4] (repeated figure)

2.3.3 Localised blast loaded plates

Experiments on circular clamped mild steel plates subjected to localised blast loads are reported by Nurick and Radford, [6]. The test methodology is the same as discussed in Section 2.3.1.2. The plate deformation is characterised by an inner dome superimposed on a larger global dome, as shown in Figure 2.47. This plate deformation shape was later observed by Chung Kim Yuen and Nurick for built-in circular plates, [7] and Jacob et al for quadrangular plates subjected to localised loads, [8].

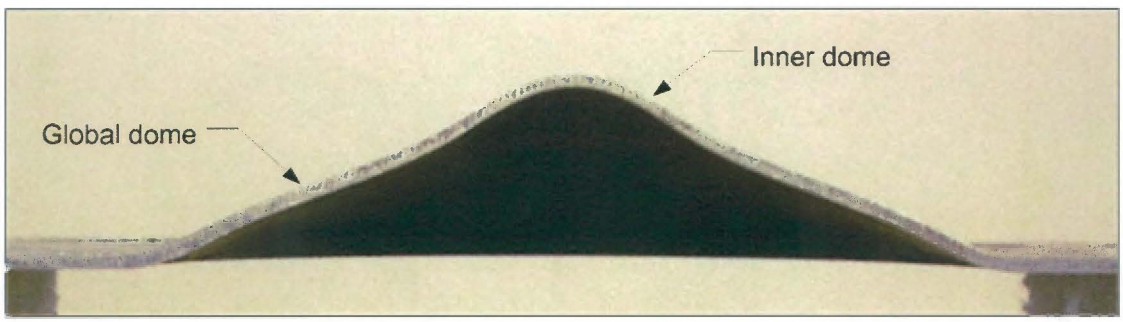

Figure 2.47: Large inelastic deformation for localised blast loaded plate

Modes of failure reported include large inelastic deformations, thinning at the central area and boundary of the plate. Tearing at the central area of the plate occurs with further increase in impulse after the onset of thinning. The tearing observed is characterised by a cap shaped piece tearing away from the plate. Tearing at the boundary is observed for larger load diameter – plate diameter ratios.

It should be noted that the thinning mechanism at the central area and at the boundary are different. In the case of thinning at the boundary, it is defined by the nature of the clamping frames. Sharp edge clamping frames result in plate thinning at the boundary similar to indentation as reported by Nurick et al [3].

2.3.3.1 Modes of failure for thin plates subjected to localised blast loads

The range of plate failure modes observed for localised blast loading are large inelastic deformation (Mode I) to complete tearing at the boundary (Mode II), [6 - 8]. Complete shearing (Mode III) has not been observed. The modes of failure refined by Nurick and Radford [6] to suit plate response for localised blast load are given in Table 2.1

Several modes of failure are obviously common to both uniform and localised blast loading, these are highlighted in Table 2.2 listing a summary of the modes of failure.

Table 2.1: Modes of failure for plates subjected to localised blast loading

	*Mode I – Large Inelastic deformation*		*Mode IIc – Complete tearing in the central area – capping*
	*Mode Itc – Large inelastic deformation with thinning in the central area*		*Mode II – Complete tearing at the boundary*
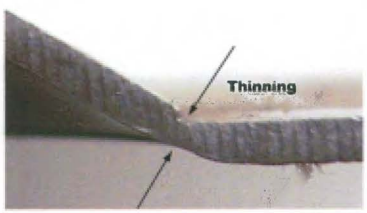	*Mode Ib – Large inelastic deformation with thinning at the boundary*		*Petalling*
	*Mode II*c – Partial tearing in the central area*		

Table 2.2: Summary of modes of failure for plates subjected to uniform and localised blast loads

Modes of Failure	Description	Uniform loading	Localised loading
Mode I	large inelastic deformation	✓	✓
Mode Ia	large inelastic deformation with necking around part of the boundary	✓	
Mode Ib	large inelastic deformation with necking around the entire boundary	✓	✓
Mode Itc	large inelastic deformation with thinning in the central area		✓
Mode II	tensile tearing at the boundary	✓	✓
*Mode II**	large inelastic deformation with partial tearing around part of the boundary	✓	✓
Mode IIa	increasing mid-point deflection with increasing impulse with complete tearing at the boundary	✓	
Mode IIb	decreasing mid-point deflection with increasing impulse with complete tearing at the boundary	✓	
*Mode II*c*	partial tearing in the central area		✓
Mode IIc	Complete tearing in the central area – capping		✓
Mode III	transverse shear failure at the boundary	✓	
Petalling			✓

2.4 Influence of stand-off distance and charge mass on large inelastic deformation of plates

The relationship between stand-off distance and plate deformation due air blast experiments is not widely reported.

Experimental studies using air blast loading to understand the effect of stand-off distance on plate deformation have been reported by Akus and Yildirim [11]. They report experiments using 240 x 240mm steel square plates of 1mm thickness. Experimental parameters are given Table 2.3.

Table 2.3: Experimental set up data, [11]

Charge mass (g)	Charge mass (TNT equivalent) (g)	Stand-off distance (mm)
131	200	200, 225, 250, 300, 400, 500, 600
163.7	250	200, 225, 250, 300, 400, 500
196.4	300	250, 400, 500, 600
261.9	400	250, 400, 500, 600
392.9	600	250, 400, 500, 600
654.8	1000	250, 400, 500, 600

2.4.1 Plate mid-point deflection and stand-off distance [11]

The graph of mid-point deflection versus stand-off distance [11] as shown in Figure 2.48, indicates maximum mid-point deflection at the closest stand-off distance of 200mm followed by a rapid decrease up to stand-off distance of 300mm. The mid-point deflections decrease gradually between stand-off distances of 400mm to 600mm for charge masses ranging from 131g to 261.9g. However, for charge masses 392.9g and 654.8g the mid-point deflection decreases sharply between stand-off distances of 400mm and 600mm. Hence indicating that, the gradual decrease in mid-point deflection with respect to stand-off distance is a function of charge mass.

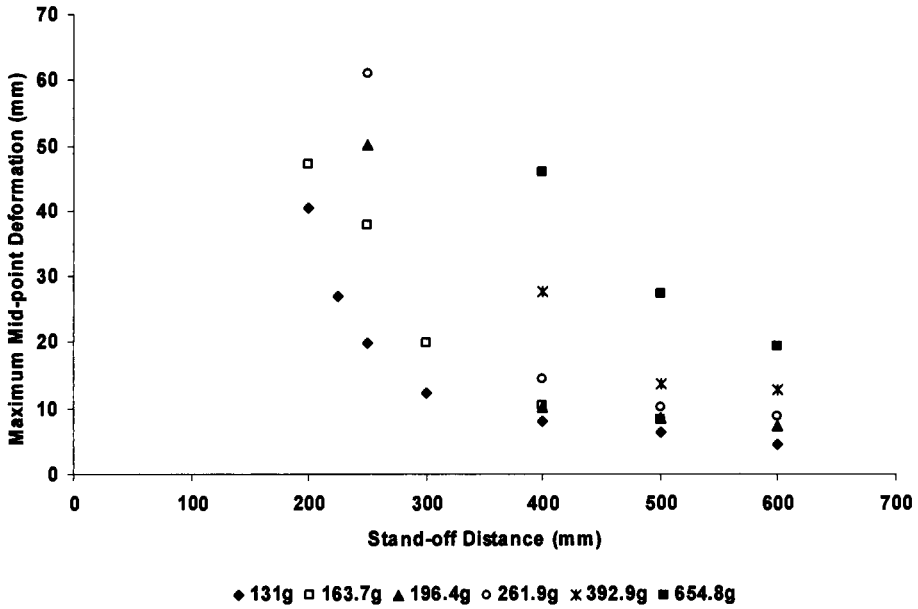

Figure 2.48: Maximum mid-point deformation changing with stand-off distance [11]

2.4.2 Plate mid-point deflection and charge mass

The graph of mid-point deflection versus charge mass [11] as shown in Figure 2.49, indicate that mid-point deflection increases with increasing charge mass for a given stand-off distance. The increase in mid-point deflection is dependent on stand-off distance. At the closest distance the deflection increases rapidly as charge mass is increased. Whilst, moving the explosive further away from the test plate results in a more gradual increase in mid-point deflection for increasing charge mass.

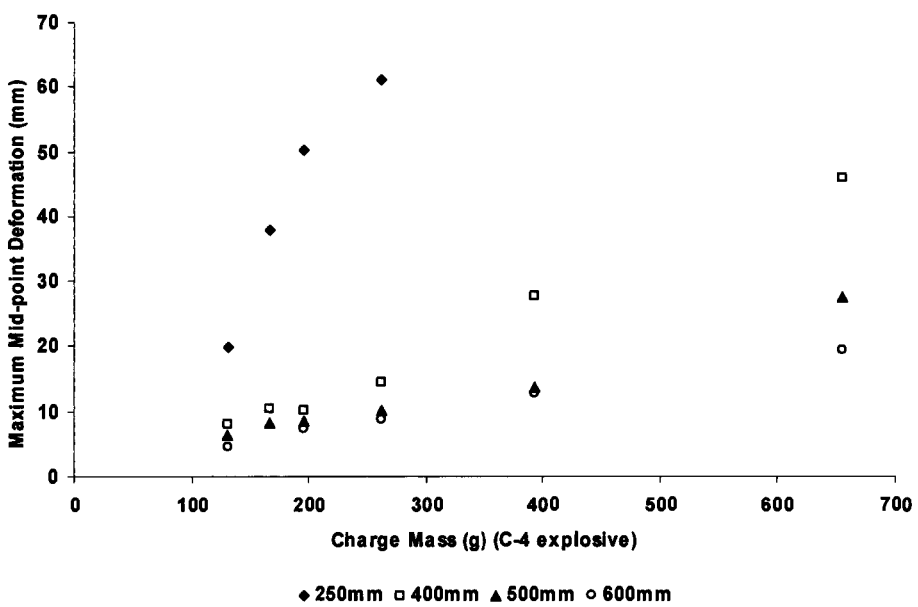

Figure 2.49: Maximum mid-point deformations changing with charge mass [11]

2.4.3 Relationship between stand-off distance on blast loading condition

Marchand and Alfawakhiri [33] suggest a guide for assumption of uniform blast load over a structure. If the charge stand-off exceeds one-half of the structure's width or height (largest dimension), then loads can be reasonably averaged over the structure provided the charge is centred on the structure.

In the case of circular disc shaped explosive charge placed at a certain stand-off distance, S, from a circular metal plate of diameter D. The blast load is said to be applied uniformly over the entire plate area for stand-off greater than plate radius (S ≥ D/2). Conversely, focusing of the blast load occurs at stand-off distance less than plate radius (S ≤ D/2). Hence the plate is subjected to localised blast loads.

An illustration of the ranges of stand-off distance in relation to uniform and localised loading regimes is shown in Figure 2.50.

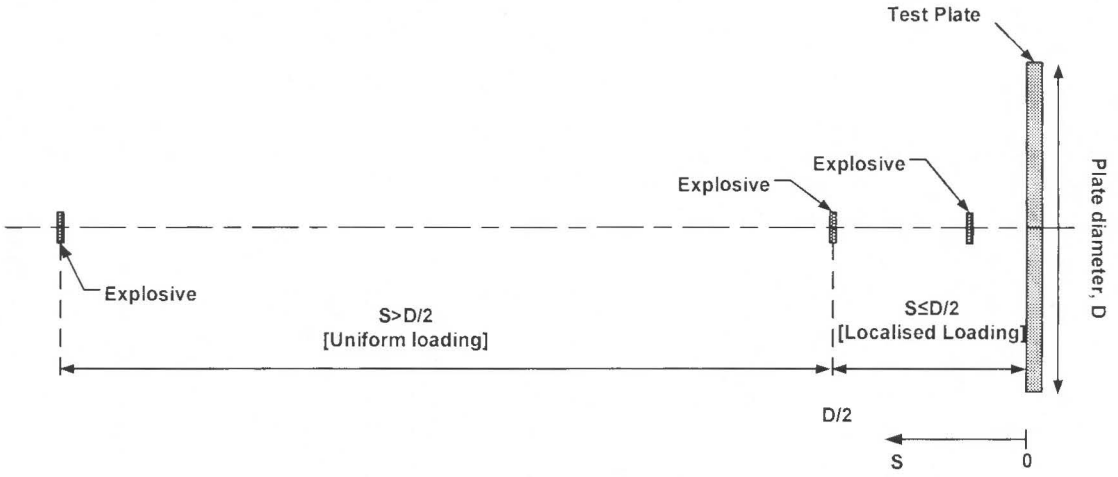

Figure 2.50: Illustration of charge stand-off distance and loading condition

2.5 Theoretical predictions

Theoretical predictions of plates subjected to impulsive loading have been reported for many years, (Nurick and Martin [2]).

2.5.1 Jones damage number for fully clamped rigid circular and Quadrangular plates

2.5.1.1 Jones damage number for circular plates

Jones, [34] proposed a damage number λ to predict large inelastic deformation of fully clamped circular plates loaded impulsively by an uniformly distributed velocity, V_o as shown in Figure 2.51.

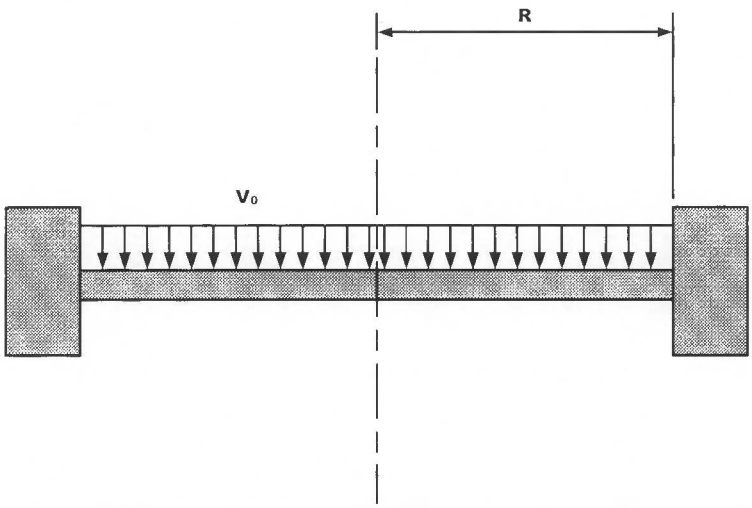

Figure 2.51: Fully clamped circular plate with radius R subjected to a uniformly distributed impulsive velocity Vo, [34]

The damage number λ is a dimensionless initial kinetic energy term,

$$\lambda = \frac{\mu V_o^2 R^2}{M_o H} \qquad \text{(eq. 2.30)}$$

Where, μ - Mass per unit area (ρH), M_0 - $\sigma_0 H^2/4$, V_0 - Initial velocity, R - Plate radius, H - Plate thickness

Jones damage number (equation 2.30) can be written in terms of impulse as follows,

$$\lambda = \frac{\mu V_o R^2}{M_o H} = \frac{(\rho H) V_o^2 R^2}{\left(\frac{\sigma_o H^2}{4}\right) H} = \frac{4\rho V_o^2 R^2}{\sigma_o H^2} \quad \text{(eq. 2.31)}$$

Impulse is given by

$$I = mV_o \quad \text{(eq. 2.32)}$$

Where I – Impulse, m – mass of plate ($\pi R^2 H\rho$)

$$V_o = \frac{I}{m} \quad \text{(eq. 2.33)}$$

$$V_o = \frac{I}{\pi R^2 H\rho} \quad \text{(eq. 2.34)}$$

Substituting equation (2.34) into equation (2.31) and simplifying gives

$$\lambda = \frac{4I^2}{\pi^2 R^2 H^4 \rho\sigma_o} \quad \text{(eq. 2.35)}$$

Where, ρ – plate density, σ_o – static yield stress

The large permanent transverse displacement of the centre of the plate is given by

$$\delta/H = \frac{\left[1 + 2\lambda/3\right]^{1/2} - 1}{2} \quad \text{(eq. 2.36)}$$

Where, δ – permanent transverse displacement

2.5.1.2 *Jones damage number for quadrangular plates*

Jones damage number for quadrangular plate is given as

$$\lambda = \mu V_0^2 L^2 / M_0 H \quad \text{(eq. 2.37)}$$

Written in terms of impulse as follows,

$$\lambda = 4I^2 L^2 / A_0^{\,2} \rho\sigma_0 H^4 \quad \text{(eq. 2.38)}$$

Where L – plate half length, A_o – loaded area (in this case, A_o = 2B x 2L)

The large permanent transverse displacement of the centre of the plate is given by

$$\delta/H = \frac{(3-\xi_0)\left\{\left[1+\frac{1}{6}\lambda\xi_0{}^2\left(1-\xi_0+\frac{1}{2-\xi_0}\right)\right]^{1/2}-1\right\}}{\{2[1+(\xi_0-1)(\xi_0-2)]\}} \qquad \text{(eq. 2.39)}$$

Where, B – plate half width, $\xi_0 = B/L \tan\phi$ and $\tan\phi = -B/L + \left[3+(B/L)^2\right]^{1/2}$

For example, the mid-point deflection of square and rectangular plates is determined as follows,

a) Square plate of half – width to half – length ratio (B/L) equal to one, as shown in Figure 2.51(a).

$$\tan\phi = -B/L + \left[3+(B/L)^2\right]^{1/2} = -1+\left[3+1^2\right]^{1/2} = 1$$

and

$$\xi_0 = B/L \tan\phi = 1$$

Therefore, equation (2.39) simplifies to:

$$\delta/H = \frac{(3-1)\left\{\left[1+\frac{1}{6}\lambda 1^2\left(1-1+\frac{1}{2-1}\right)\right]^{1/2}-1\right\}}{2[1+(1-1)(1-2)]} = \underline{\sqrt{1+\lambda/6}-1}$$

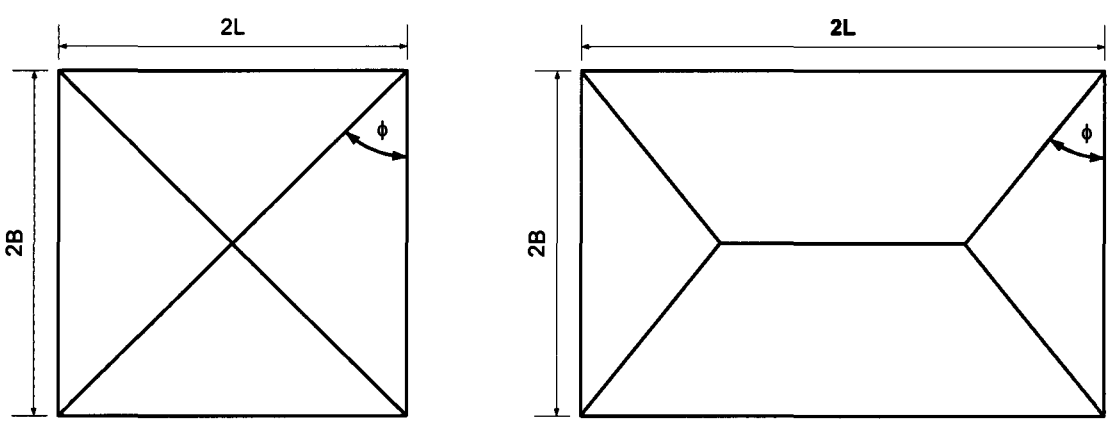

(a) Square plate (B/L = 1) (b) Rectangular plate (B/L = 0.5)

Figure 2.52: Schematic of uniformly loaded square and rectangular plates showing plan view of plastic hinge lines

b) Rectangular plate of half – width to half – length ratio (B/L) equal to 0.5, as shown in Figure 2.51(b).

Hence L = 2B

$$\tan\phi = -B/L + \left[3 + (B/L)^2\right]^{1/2} = -B/2B + \left[3 + (B/2B)^2\right]^{1/2} = -1/2 + \left[3 + (1/2)^2\right]^{1/2} = 1.3$$

and

$$\xi_0 = B/L \tan\phi = 1.3(B/2B) = 0.65$$

Therefore, equation (2.39) simplifies to:

$$\delta/H = \frac{(3-0.65)\left\{\left[1+\frac{1}{6}\lambda(0.65)^2\left(1-0.65+\frac{1}{2-0.65}\right)\right]^{1/2}-1\right\}}{2[1+(0.65-1)(0.65-2)]}$$

Thus,

$$\delta/H = \underline{0.80\left[\sqrt{1+0.13\lambda}-1\right]}$$

2.5.2 Nurick and Martin damage number for uniform and localised loaded circular and quadrangular plates

Nurick and Martin [2] proposed modified dimensionless damage numbers for quadrangular and circular plates loaded impulsively based on Johnson's damage number, given as

$$\alpha = \frac{\rho v^2}{\sigma_d} \qquad \text{(eq. 2.40)}$$

Where, ρ – material density, v – impact velocity, σ_d – damage stress

However, Johnson's damage number does not consider method of impact, target geometry or boundary conditions.

Johnson's damage number can be written in terms of impulse as follows

$$I = mv \qquad \text{(eq. 2.41)}$$

Where, I – Impulse, m – mass of plate ($A_o H \rho$)

$$v = \frac{I}{m} \qquad \text{(eq. 2.42)}$$

$$v = \frac{I}{A_o H \rho} \qquad \text{(eq. 2.43)}$$

Where, A_o – load area, H – plate thickness

Thus substituting equation (2.43) into equation (2.40) gives

$$\alpha = \frac{I^2}{A_o^2 H^2 \rho \sigma_d} = \frac{I_o^2}{H^2 \rho \sigma_d} \qquad \text{(eq. 2.44)}$$

Where, I_o – impulse per area (I/A_o)

Nurick and Martin introduced a geometrical damage number

$$\psi = \left[\beta \alpha \left(\frac{A_o}{A} \right)^2 \right]^{1/2} \qquad \text{(eq. 2.45)}$$

Where, β – geometry number (plate length, l to plate width, b ratio), A – plate area

A relationship between the distance from plate centre to the nearest boundary and plate thickness was introduced (termed Aspect ratio, λ)

For circular plate

$$\lambda = \frac{R}{H} \qquad \text{(eq. 2.46)}$$

For quadrangular plate

$$\lambda = \frac{b}{2H} \qquad \text{(eq. 2.47)}$$

A loading parameter in terms of loading area per total plate area was introduced for circular plates only.

$$\zeta = 1 + \ln\left(\frac{R}{R_o}\right) \qquad \text{(eq. 2.48)}$$

Where, R – Plate radius, R_o – radius of the loaded area

This implies that as R_o tends to R, ζ tends to a value of one. Thus the plate is uniformly loaded over the entire test area. A schematic illustration is shown in Figure 2.53.

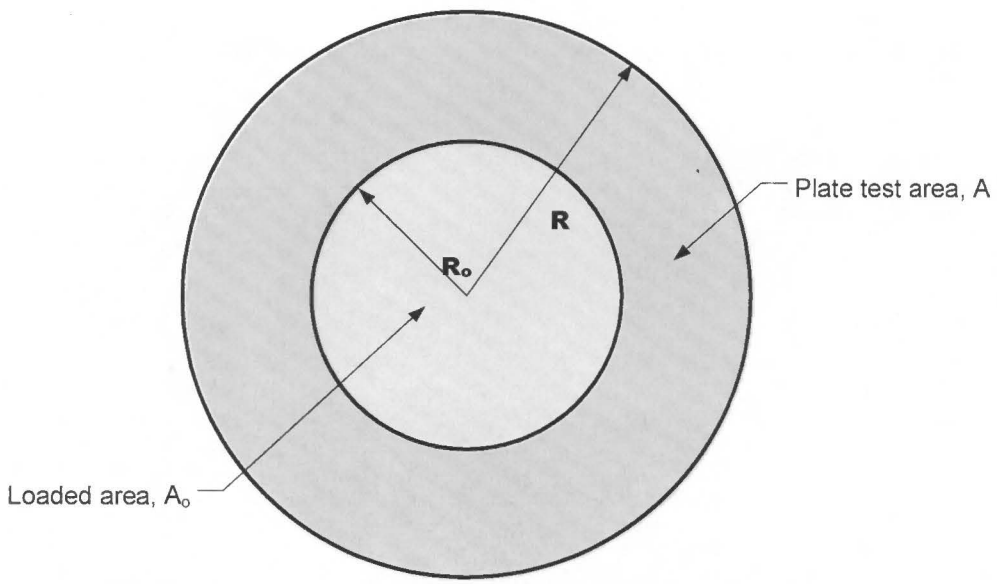

Figure 2.53: Schematic of loading condition for circular plates

Combining equations 2.45 to 2.48 results in a modified damage number which incorporates dimensions and loading:

$$\phi = \psi\lambda\zeta \qquad \text{(eq. 2.49)}$$

For circular plate (uniform impulsive load, ζ=1)

$$\phi_c = \frac{I}{\pi R H^2 (\rho\sigma_0)^{1/2}} \qquad \text{(eq. 2.50a)}$$

For circular plate (localised impulsive load)

$$\phi_c = \frac{I\left(1+\ln\frac{R}{R_0}\right)}{\pi R H^2 (\rho\sigma_0)^{1/2}} \qquad \text{(eq. 2.50b)}$$

For quadrangular plate (uniform impulsive load)

$$\phi_q = \frac{I}{2H^2 (bl\rho\sigma_0)^{1/2}} \qquad \text{(eq. 2.51)}$$

It should be noted that damage stress is replaced by static yield stress, σ_o.

For quadrangular plate (localised impulsive load)

A modification to damage number ϕ_q is reported by Jacob et al [8] for quadrangular plates subjected to localised blast loading. A loading parameter ζ_{ql} similar in form to equation (2.48) is incorporated into ϕ_q (eq. 2.51). The loading parameter is a function of plate area and load (charge) area written as,

$$\zeta_{ql} = 1+\ln\left(\frac{lb}{\pi R_0^{\,2}}\right) \qquad \text{(eq. 2.52)}$$

The modified damage is written as

$$\phi_{ql} = \phi_q \zeta_{ql} \qquad \text{(eq. 2.53)}$$

$$\phi_{ql} = \frac{I\left(1+\ln\left(\frac{lb}{\pi R_0^{\,2}}\right)\right)}{2H^2 (bl\rho\sigma)^{1/2}} \qquad \text{(eq. 2.54)}$$

The difference between loading parameter ζ (equation (2.48)) and ζ_{ql} (equation (2.52)) is the geometrical similarity between the charge shape and plate in the case of circular plates subjected to blast loads using circular disc shaped explosives, hence the ratio of radii of the plate and charge is used. Whilst in the case of quadrangular plate subjected to blast loads using circular disc shaped explosives,

there is no geometrical similarity, as a result the ratio of areas of plate and charge is used.

An empirical relationship between permanent plate mid point deflection-thickness ratio and damage number is reported [2] for circular and quadrangular plates as follows

For circular plates

$$\frac{\delta}{H} = 0.425\phi_c \qquad \text{(eq. 2.55)}$$

For quadrangular plates

$$\frac{\delta}{H} = 0.48\phi_q \qquad \text{(eq. 2.56)}$$

2.5.3 Deformation strain energy analysis

Impulsive loading of plates are accompanied by large plastic deformation at high strain rates. Therefore it is necessary to compute the strain energy of plastic deformation of test specimens. The following is a summary of discussion given by Ezra [35].

The stress-strain relations are an important element in the calculation of the strain energy. At high strain rates the strain energy can be substantially different from values obtained from static or slow strain rate tests. In the case of plates subjected to explosive blast loading, high strain rates occur during the initial stages of deformation and decrease rapidly to zero by the end of the deformation process. Therefore any deviation of the stress-strain relationship from static values would occur during the initial stages of deformation and hence would not necessarily affect the computation of plastic strain energy appreciably.

The strain energy per unit volume dU_{strain}, which is caused by a small increase in strain, is given by

$$dU_{strain} = \sigma_1 d\varepsilon_1 + \sigma_2 d\varepsilon_2 + \sigma_3 d\varepsilon_3 \qquad \text{(eq. 2.57)}$$

Where, σ_1, σ_2, σ_3 are principal true stresses: ε_1, ε_2, ε_3 are principal true strains. The true stress is defined as the load divided by instantaneous cross-sectional area. The true strain is defined as follows: considering a tensile specimen with initial length l_o, instantaneous length l and instantaneous length increment dl, thus

$$d\varepsilon = \frac{dl}{l} \qquad \text{(eq. 2.58)}$$

Integrating equation (2.58) yields

$$\varepsilon = \int_{l_o}^{l} \frac{dl}{l} = \ln \frac{l}{l_o} \qquad \text{(eq. 2.59)}$$

It is noted that engineering strain defined by the change in length divided by the original length l_o cannot be used when deformations are large.

Using St. Venant's theory of plastic flow based on the assumption that plate material volume does not change during deformation, it follows that equation (2.57) is equivalent to

$$dU_{strain} = \sigma_{eff} d\varepsilon_{eff} \qquad \text{(eq. 2.60)}$$

Where,

$$\sigma_{eff} = \frac{1}{\sqrt{2}}\sqrt{(\sigma_1 - \sigma_2)^2 + (\sigma_2 - \sigma_3)^2 + (\sigma_3 - \sigma_1)^2} \qquad \text{(eq. 2.61)}$$

$$\varepsilon_{eff} = \frac{\sqrt{2}}{3}\sqrt{(\varepsilon_1 - \varepsilon_2)^2 + (\varepsilon_2 - \varepsilon_3)^2 + (\varepsilon_3 - \varepsilon_1)^2} \qquad \text{(eq. 2.62)}$$

For most strain hardening materials the following stress-strain relationship can be used

$$\sigma_{eff} = K\varepsilon_{eff}^{n} \qquad \text{(eq. 2.63)}$$

The values for K (strength coefficient) and *n* (strain hardening exponent) are obtained from uni-axial tensile tests where $\sigma_1=\sigma_{eff}$ and $\varepsilon_1=\varepsilon_{eff}$.

The strain energy per unit volume, U_{strain} for a strain hardening material is obtained by substituting equation (2.63) into (2.60) and integrating,

$$U_{strain} = \frac{K}{n+1}\varepsilon_{eff}^{n+1} \qquad \text{(eq. 2.64)}$$

For non-strain hardening materials with constant yield stress, $\sigma_{eff}=\sigma_o$, the yield stress in a uni-axial tensile test, substituting this into equation (2.60) gives

$$U_{strain} = \sigma_o \varepsilon_{eff} \qquad \text{(eq. 2.65)}$$

Total strain energy per unit volume is obtained by integrating either equation (2.65) or (2.64) over the total volume of the deformed plate.

$$U_T = \int U_{strain} dV \qquad \text{(eq. 2.66)}$$

Where, dV is the elemental volume of the material.

For the case of a circular plate with large deformation consider the case shown in Figure 2.54. A plate deformation in the shape of a circular dome formed due to an explosive charge. Let the initial plate thickness be H_o, δ, the plate mid-point deflection and r, the radius of curvature of the segment of the sphere.

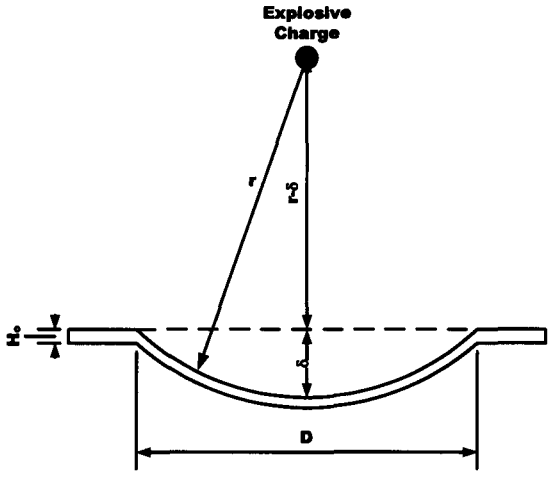

Figure 2.54: Explosively formed dome

From geometric considerations

$$r^2 = \frac{D^2}{4} + (r-\delta)^2 \qquad \text{(eq. 2.67)}$$

Rearranging equation (2.67) yields

$$2r\delta = \frac{D^2}{4} + \delta^2 \qquad \text{(eq. 2.68)}$$

The surface area of the circular dome is given by the integral

$$Area = 2\pi r \int_{r-\delta}^{r} dx = 2\pi r\delta \qquad \text{(eq. 2.69)}$$

Hence the volume of the deformed plate is given by

$$V_{deformed} = 2\pi r\delta H \qquad \text{(eq. 2.70)}$$

Considering the volume of the deformed plate to be constant and unchanged from its initial volume ($V_{initial} = V_{deformed}$). The following relationship is obtained

$$\frac{\pi}{4} D^2 H_0 = 2\pi r H \delta \qquad \text{(eq. 2.71)}$$

Where, H is the final thickness of the plate after deformation, which is uniform according to the basic simplified model. Using equation (2.68) and rearranging equation (2.71) yields

$$\frac{H}{H_o} = \frac{D^2}{4\delta^2 + D^2} \qquad \text{(eq. 2.72)}$$

The thickness strain is given by equation (2.73)

$$\varepsilon_H = \ln\left(\frac{H}{H_o}\right) = \ln\left(\frac{D^2}{4\delta^2 + D^2}\right) = -\ln\left[1 + 4\left(\frac{\delta}{D}\right)^2\right] \quad \text{(eq. 2.73)}$$

From incompressibility of the deformed plate

$$\varepsilon_H + \varepsilon_r + \varepsilon_\theta = 0 \quad \text{(eq. 2.74)}$$

Where ε_r – radial strain, ε_θ – circumferential strain

Based on the assumption of uniform surface strain

$$\varepsilon_r = \varepsilon_\theta \quad \text{(eq. 2.75)}$$

Hence equation (2.74) gives

$$\varepsilon_r = \varepsilon_\theta = -\frac{1}{2}\varepsilon_H \quad \text{(eq. 2.76)}$$

Substituting equation (2.76) in the effective strain equation (2.62)

$$\varepsilon_{eff} = -\varepsilon_H \left(= 2\varepsilon_r = 2\varepsilon_\theta\right) \quad \text{(eq. 2.77)}$$

Thus from equation (2.73)

$$\varepsilon_{eff} = \ln\left[1 + 4\left(\frac{\delta}{D}\right)^2\right] \quad \text{(eq. 2.78)}$$

The strain energy per unit volume, U_{strain}, is obtained by substituting equation (2.78) into (2.64)

$$U_{strain} = \frac{K}{n+1}\left\{\ln\left[1 + 4\left(\frac{\delta}{D}\right)^2\right]\right\}^{n+1} \quad \text{(eq. 2.79)}$$

Therefore the total strain energy for deformation is given by

$$U_{def} = volume_{plate} \times U_{strain} \quad \text{(eq. 2.80)}$$

Hence

$$U_{def} = \frac{\pi}{4} D^2 H_o \frac{K}{n+1}\left\{\ln\left[1 + 4\left(\frac{\delta}{D}\right)^2\right]\right\}^{n+1} \quad \text{(eq. 2.81)}$$

Kosing and Skews [21], report good correlation between predicted mid-point deflections using equation (2.81) and experimental results on copper plates loaded using a liquid shock tube.

If, instead of strain hardening effects, the assumption of constant yield stress, σ_o, the strain energy in the dome shaped plate is obtained by substituting equation 2.78 into equation 2.65,

$$U_{def} = \frac{\pi}{4} D^2 H_o \sigma_o \ln\left[1 + 4\left(\frac{\delta}{D}\right)^2\right] \qquad \text{(eq. 2.82)}$$

2.5.3.1 *Duffey, [5, 36], energy analysis method for rigid-plastic behaviour of plates*

The deformation energy analysis is sensitive to the final deflection shape assumed. For the analysis of experimental results herein the shape function used is given by equation (2.83) to describe the plate deformations. An illustration of the shape of the plate after deformation is shown in Figure 2.55.

$$w = \delta \cos\left(\frac{\pi r}{2R}\right) \qquad \text{(eq. 2.83)}$$

Where, r – Change in plate radius, R – Plate radius, w – Change in plate deflection, δ – Final mid-point deflection

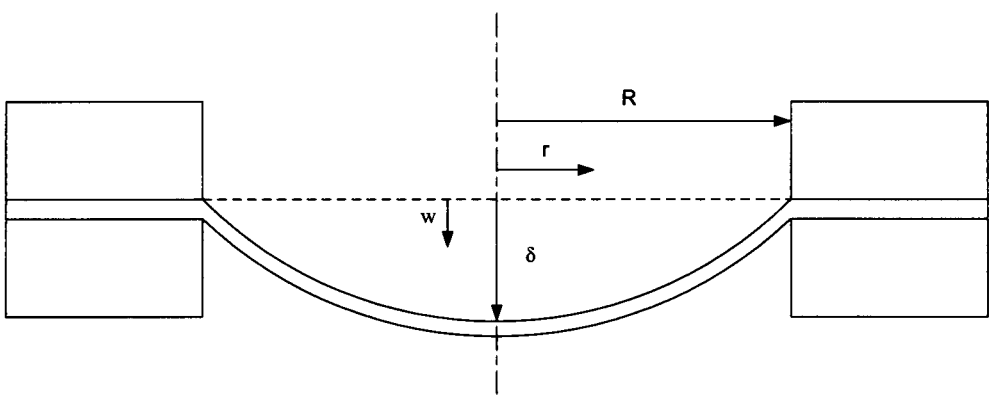

Figure 2.55: Clamped circular plate after deformation

The deformation energy is given by,

$$U_{def} = \pi H \int_0^R \frac{\sigma_0^1}{\left(1 - \nu + \nu^2\right)^{1/2}} \left(\frac{\partial w}{\partial r}\right)^2 r dr \qquad \text{(eq. 2.84)}$$

Where, w is the shape function given by equation (2.83), δ – Mid-point deflection, ν – Poisson's ratio, σ_o^1 – Dynamic yield stress, H – Plate thickness

Substituting equation (2.83) into (2.84) and integrating gives

$$U_{def} = \frac{\pi^3 H \sigma_0^1 \delta^2}{4\left(1 - v + v^2\right)^{1/2}} \left(\frac{1}{4} + \frac{1}{\pi^2}\right) \quad \text{(eq. 2.85)}$$

The mild steel used in experiments is sensitive to strain rate. The material under goes strain hardening during blast loading and therefore as strain rate increases, the value of the dynamic yield stress increases. Teeling-Smith and Nurick [5] use dynamic yield stress calculated using an iterative procedure (equation (2.86)) proposed by Symonds and Wierzbicki [37]

$$\frac{0.05365 I^2}{R^5 H^2 \sqrt{\rho^3 \sigma_o^1}} = 40.4 \left[\frac{\sigma_0^1}{\sigma_0} - 1\right]^5 \quad \text{(eq. 2.86)}$$

Where, R – plate radius, H – plate thickness, I – impulse, ρ – plate density,
σ_0 – static yield stress and σ_0^1 – dynamic yield stress
A simple energy balance is used to define Mode I type failure with large inelastic deformation [5].

$$E_{input} = U_{def} \quad \text{(eq. 2.87)}$$

2.5.3.2 *Input energy for impulsively loaded structures*

The input energy can be simply related to measured impulse using the following methodology for structures with natural period greater than duration of the load. The principle behind this methodology is to acknowledge that when an impulse is delivered to a structure it produces an instantaneous velocity change. As a result the structure gains kinetic energy which is converted to strain energy, (Smith and Hetherington [18]).
Input energy = kinetic energy applied on plate

$$E_{input} = \frac{1}{2} m v^2 \quad \text{(eq. 2.88)}$$

Where, m – Plate mass, v – velocity
Impulse can be written as

$$I = mv \quad \text{(eq. 2.89)}$$

Rewriting equation (2.89) and substituting into equation (2.88)

$$v = \frac{I}{m} \quad \text{(eq. 2.90)}$$

$$E_{input} = \frac{I^2}{2m} \quad \text{(eq. 2.91)}$$

Where, mass = plate density x plate volume

$$m = \pi R^2 H \rho \qquad \text{(eq. 2.92)}$$

Therefore input energy is given by

$$E_{input} = \frac{I^2}{2\pi R^2 H \rho} \qquad \text{(eq. 2.93)}$$

3 Experimental details

This chapter describes the details of blast loading experiments on clamped circular plates manufactured from mild steel.

3.1 Experimental procedure

Disc shaped plastic explosive of radius, R_0, and thickness, h, is used to impart a blast load onto the loaded side of circular test plates. The impulse is measured using a ballistic pendulum. This experimental method has been widely reported by Nurick et al. [6 - 8] and has proven to be reliable and reproducible.

The experiments described herein differ from previous experiments as mild steel tubes of different lengths are used to vary the stand off distance between the explosive load and test plate as shown in Figure 3.1. The aim of these experiments is to understand the influence of varying stand off distances on plate response.

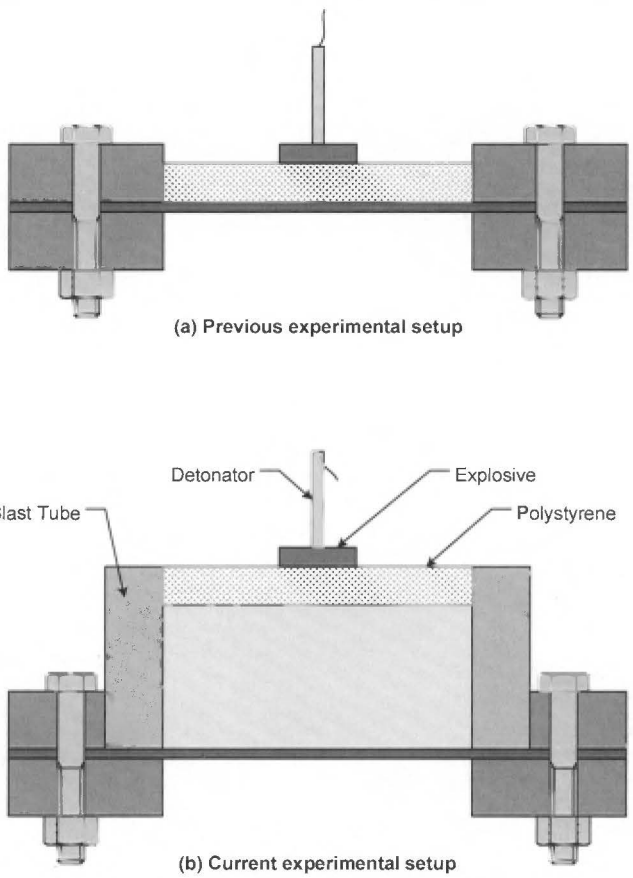

Figure 3.1: Schematic diagram showing blast loading of circular mild steel plates (a) experimental setup used previously and (b) current setup

3.1.1 Experimental arrangement

The apparatus used in these experiments are listed below,

- Ballistic Pendulum – used to measure the applied impulse
- Tubes – 106mm internal diameter used to vary the stand off distance
- Mild steel test specimens, nominal thickness of 1.9mm

3.1.2 Ballistic pendulum

The ballistic pendulum is used to measure the impulse applied to the test plate. The ballistic pendulum consists of a steel I-beam suspended on four spring steel cables. The spring steel cables are attached to the I-beam of the ballistic pendulum by four adjustable screws. The pendulum is levelled by adjusting the screws and verified using a spirit-level. Counter-balancing masses are attached at one end as shown in Figures 3.2 and 3.3. The counter balancing masses are used to counter the mass of the test rig attached on the other end so as to ensure that all four spring steel cables carry the same load. Hence, the impulse generated by the explosion is transmitted through the centroid of the pendulum. A soft tipped recording pen is attached to the pendulum on the same side as the counter balancing masses as shown in Figure 3.3, to record the oscillation amplitude of the pendulum on a sheet of tracing paper. The oscillation relates directly to the impulse generated by the explosion and transmitted to the test specimen. A photograph of the complete experimental set up ready for testing is shown in Figure 3.4. The methodology for calculating the impulse imparted on to the plate by the explosive load is given in Appendix A.

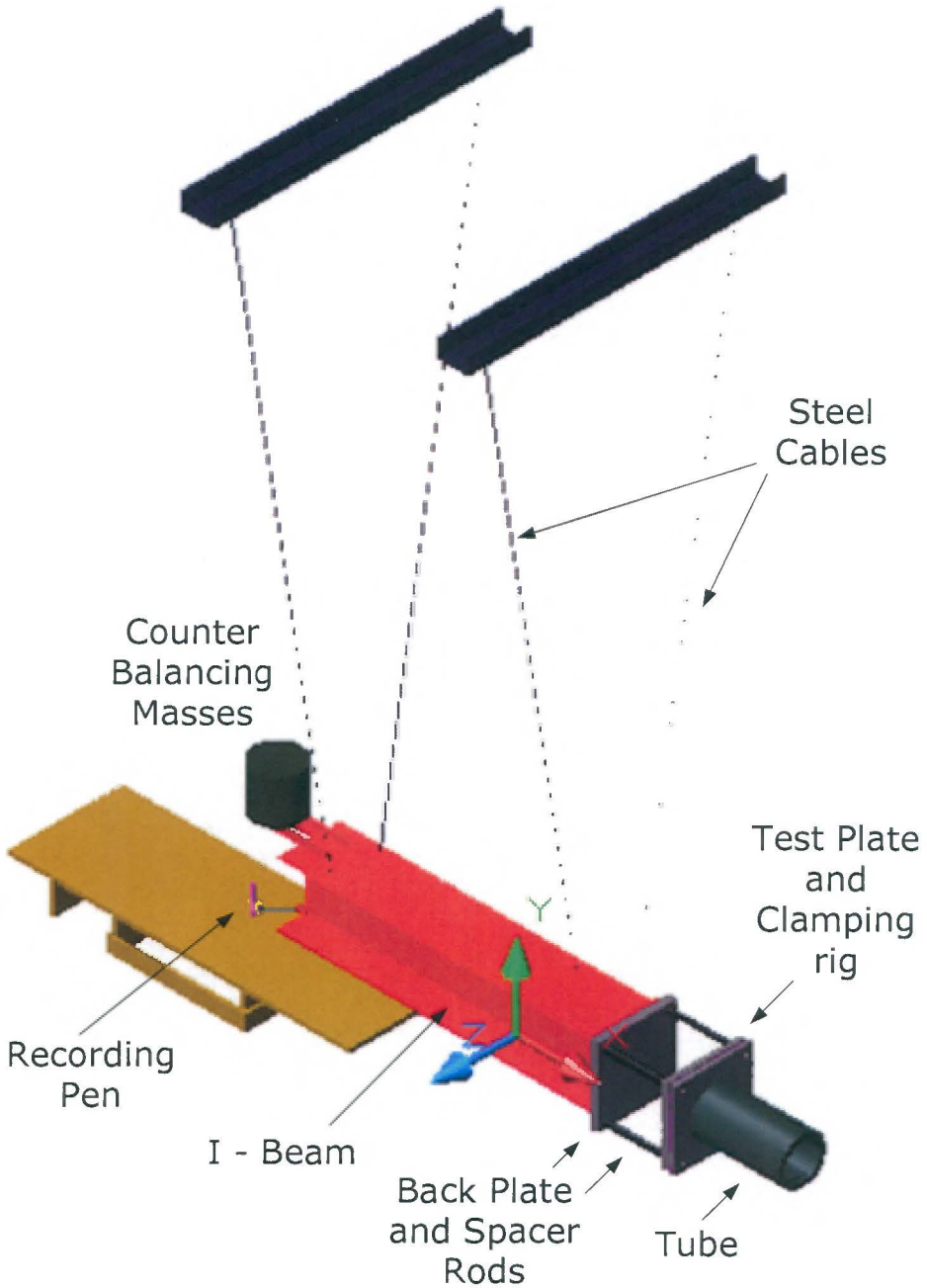

Figure 3.2: 3D rendered view of the ballistic pendulum

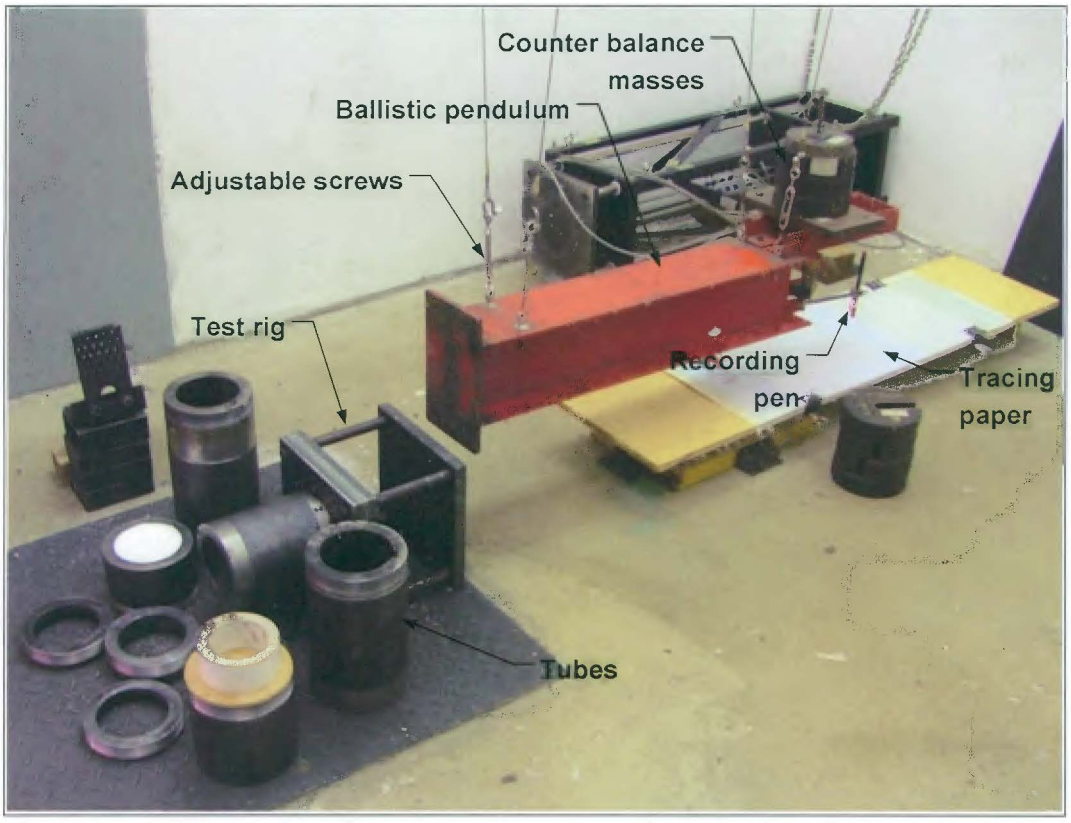

Figure 3.3: Photograph of the test rig with different length tubes and ballistic pendulum

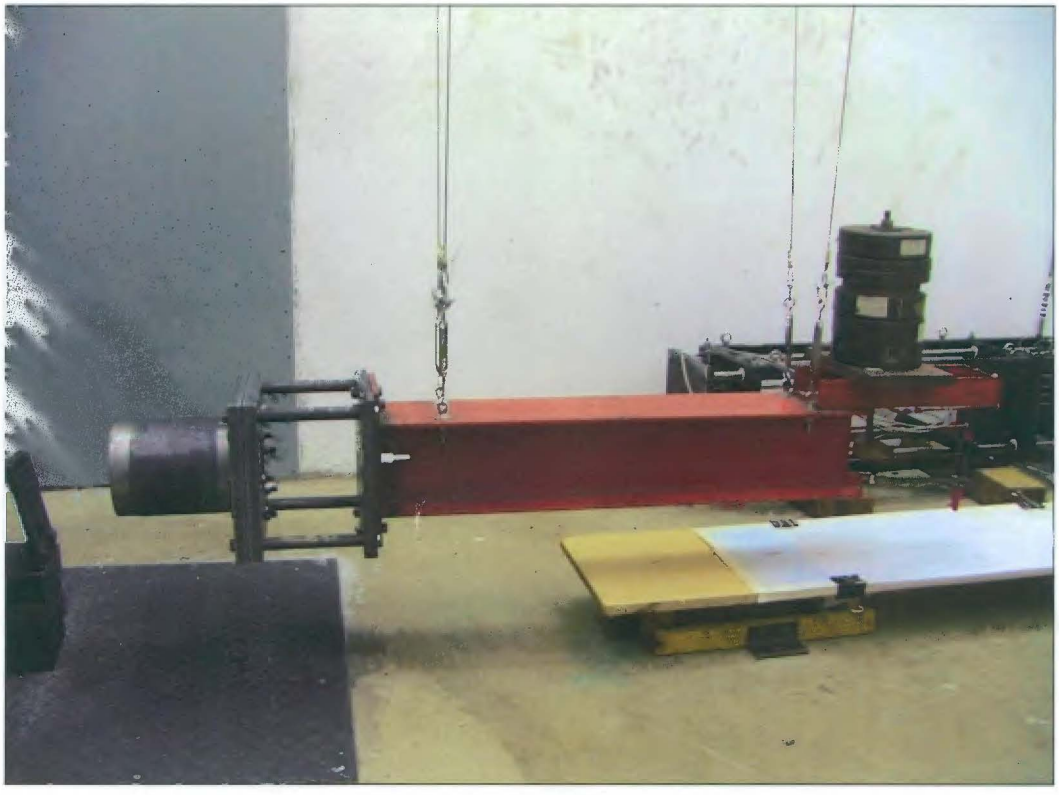

Figure 3.4: Photograph of test rig attached to the ballistic pendulum

3.1.3 Test rig and specimen

The test rig consists of two (244mm x 244mm) clamping frames made from 20mm thick mild steel. A tube of required length selected from the range shown in Figure 3.5 is screwed onto one of the clamping plates and the other clamping plate has a hole machined to 106mm diameter, the same as the internal diameter of the tube as shown in Figure 3.6. The test specimen is sandwiched between the two clamping plates.

The test rig is attached to the ballistic pendulum using four connecting spacer rods. The spacer rods allow the plate to deform without coming in contact with the I-beam of the ballistic pendulum.

Tube specification:

- Internal diameter – 106mm
- Outer diameter – 150mm
- Thickness – 22mm
- Lengths – 25mm, 30mm, 40mm, 50mm, 75mm, 100mm, 150mm, 200mm, 250mm and 300mm

Figure 3.5: Photograph of mild steel tubes used in the experiments

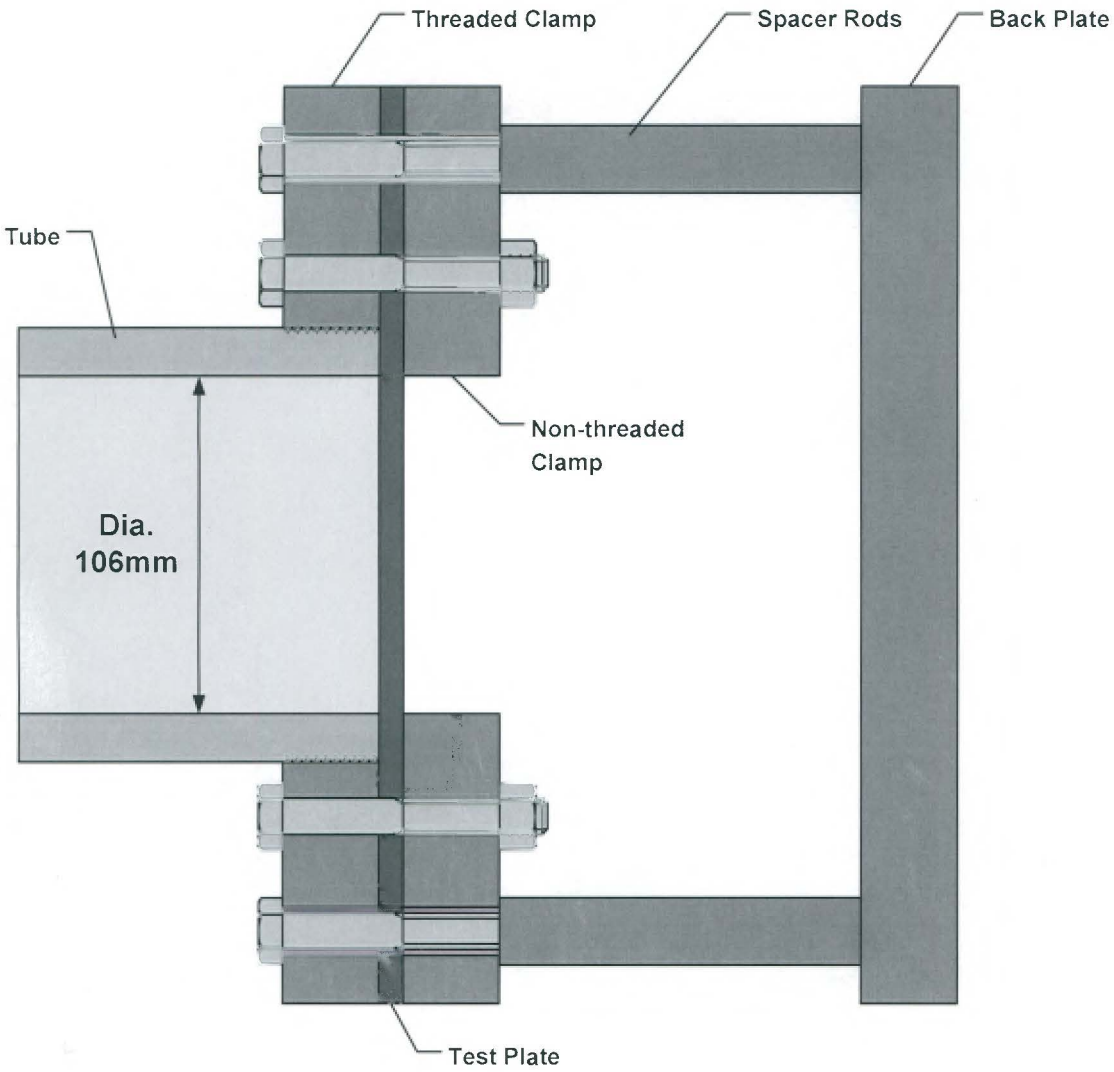

Figure 3.6: Schematic of the experimental test rig

The test specimen is cut to the same outer dimensions as the clamping plates (244mm x 244m) and with nominal plate thickness of 1.9mm. The test specimens are laser cut from three sheets of mild steel.

3.2 Test Specimen material properties

A summary of material properties for the mild steel plates used is presented in Table 3.1. Standard uni-axial flat tensile test specimens are cut from the three mild steel sheets used, labelled A, B and C. The gauge length is 40mm, due to limitation of the extensiometer fitted on the Zwick tensile test machine, which has a maximum extension of 60mm. Three strain rates were selected ($8.33x10^{-4}$, $4.17x10^{-3}$ and $2.08x10^{-2}s^{-1}$) and two specimens from each sheet were tested at the same speed. The results are shown in Table 3.2. The graphs of engineering stress versus engineering strain for the different strain rates are shown in Figures 3.7 – 3.9. The graphs of stress versus strain for each sheet at different strain rates are shown in Figures 3.10 – 3.12. Assuming the mild steel plates to be rigid-viscoplastic, static yield stresses were calculated using the Cowper-Symonds relation:

$$\frac{\sigma_0^1}{\sigma_o} = 1 + \left[\frac{\dot{\varepsilon}}{\dot{\varepsilon}_0}\right]^{1/\eta} \qquad \text{(eq. 3.1)}$$

Where, σ_0^1 - Dynamic yield stress, σ_0 - Static yield stress, $\dot{\varepsilon}$ - Strain rate, $\dot{\varepsilon}_0$ and $\eta$are material constants

Density of mild steel is determined by weighing the test plates and calculating the plate volume.

Table 3.1: Summary of material properties of mild steel test specimens

Density	$7691kgm^{-3}$
$\dot{\varepsilon}_0$ [34]	40.4
η [34]	5
Poisson's ratio	0.33
Average Static Yield Stress	240MPa
K (strength coefficient)	591.23MPa
n (strain hardening exponent)	0.21
Average % Uni-axial strain at failure	41.03

Table 3.2: Uniaxial tensile test results

Specimen number	Specimen thickness mm	Specimen width mm	Test speed mm/min	Strain rate	Dynamic yield stress MPa	Static yield stress MPa	% Strain at failure
A2	1.91	12.50	2	0.00083	266	238	43.0
A10	1.91	12.50	2	0.00083	266	238	44.4
A3	1.90	12.50	10	0.00417	283	244	40.4
A4	1.90	12.55	10	0.00417	292	252	41.9
A5	1.91	12.50	50	0.02083	281	230	40.5
A6	1.91	12.50	50	0.02083	275	225	39.8
					Average	238	41.7

Specimen number	Specimen thickness mm	Specimen width mm	Test speed mm/min	Strain rate	Dynamic yield stress MPa	Static yield stress MPa	% Strain at failure
B1	1.90	12.50	2	0.00083	268	240	42.8
B2	1.91	12.49	2	0.00083	272	244	43.2
B3	1.90	12.52	10	0.00417	291	251	39.4
B4	1.90	12.51	10	0.00417	271	234	40.3
B5	1.90	12.50	50	0.02083	282	231	39.5
B6	1.91	12.50	50	0.02083	299	245	38.5
					Average	241	40.6

Specimen number	Specimen thickness mm	Specimen width mm	Test speed mm/min	Strain rate	Dynamic yield stress MPa	Static yield stress MPa	% Strain at failure
C2	1.91	12.52	2	0.00083	268	240	41.8
C3	1.92	12.50	2	0.00083	270	242	42.6
C4	1.91	12.56	10	0.00417	292	252	39.7
C5	1.91	12.52	10	0.00417	283	244	39.7
C6	1.91	12.50	50	0.02083	291	239	40.9
C7	1.91	12.50	50	0.02083	283	232	40.0
					Average	241	40.8

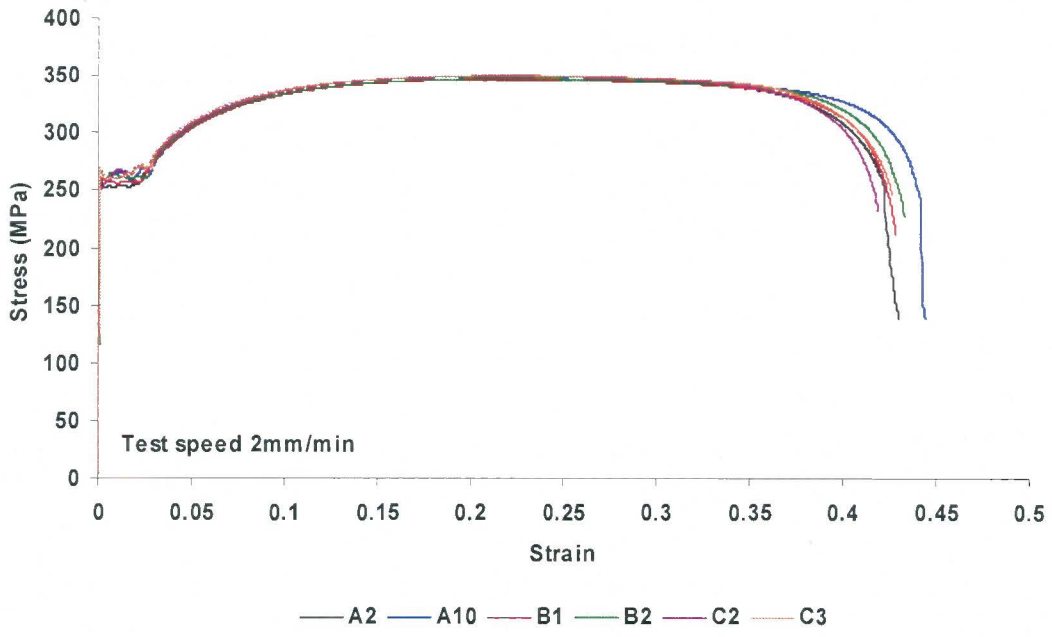

Figure 3.7: Graph of Stress versus Strain for strain rate $8.33 \times 10^{-4} s^{-1}$

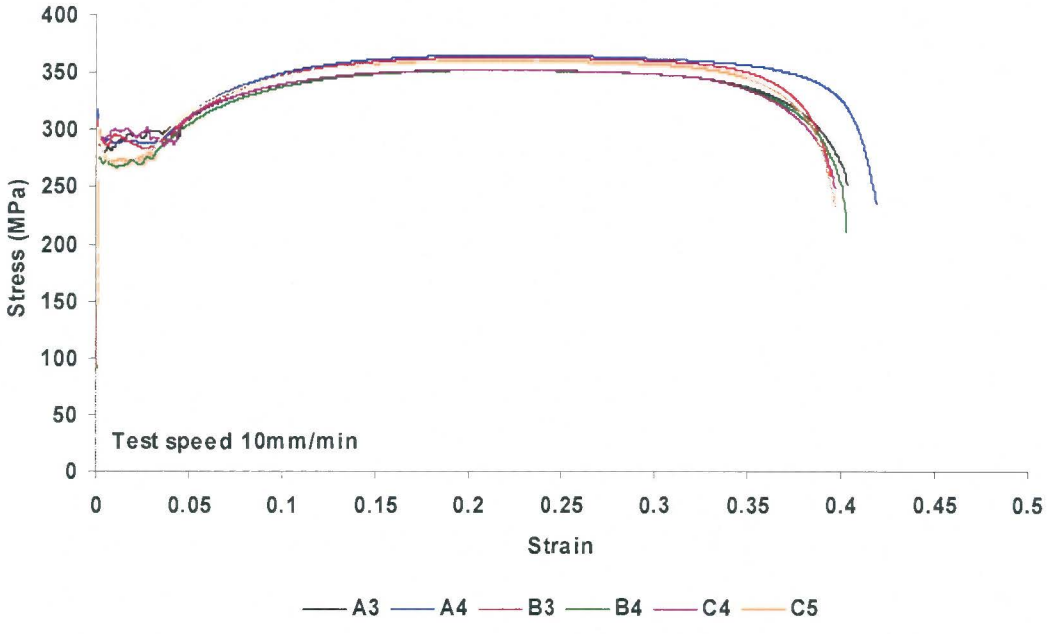

Figure 3.8: Graph of Stress versus Strain for strain rate $4.17 \times 10^{-3} s^{-1}$

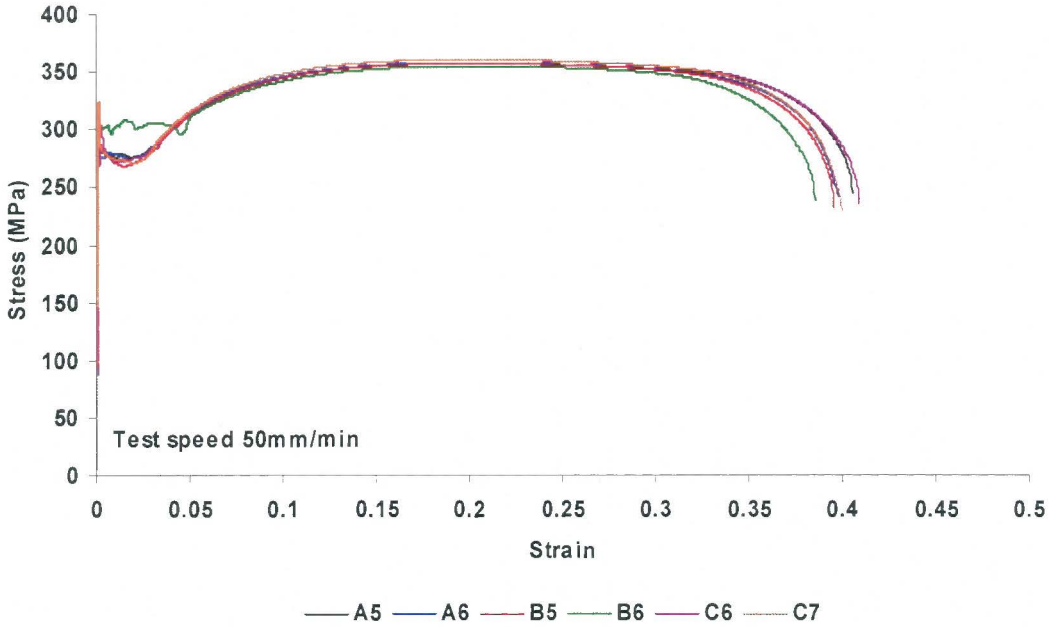

Figure 3.9: Graph of Stress versus Strain for strain rate $2.08 \times 10^{-2} s^{-1}$

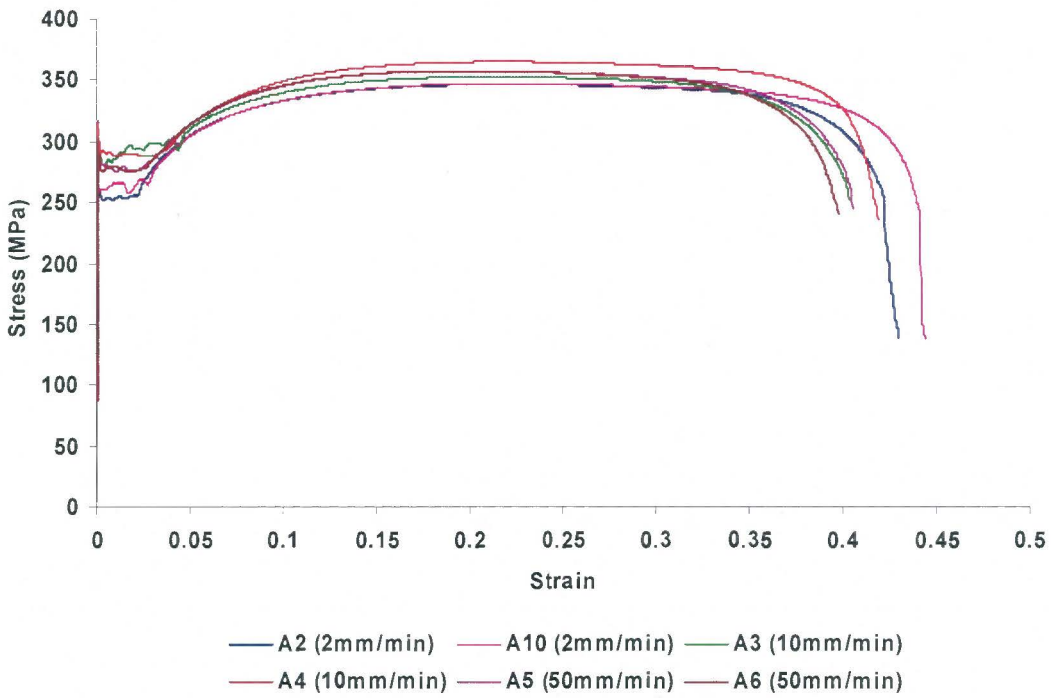

Figure 3.10: Graph of Stress versus Strain at different cross-head speeds for Sheet A

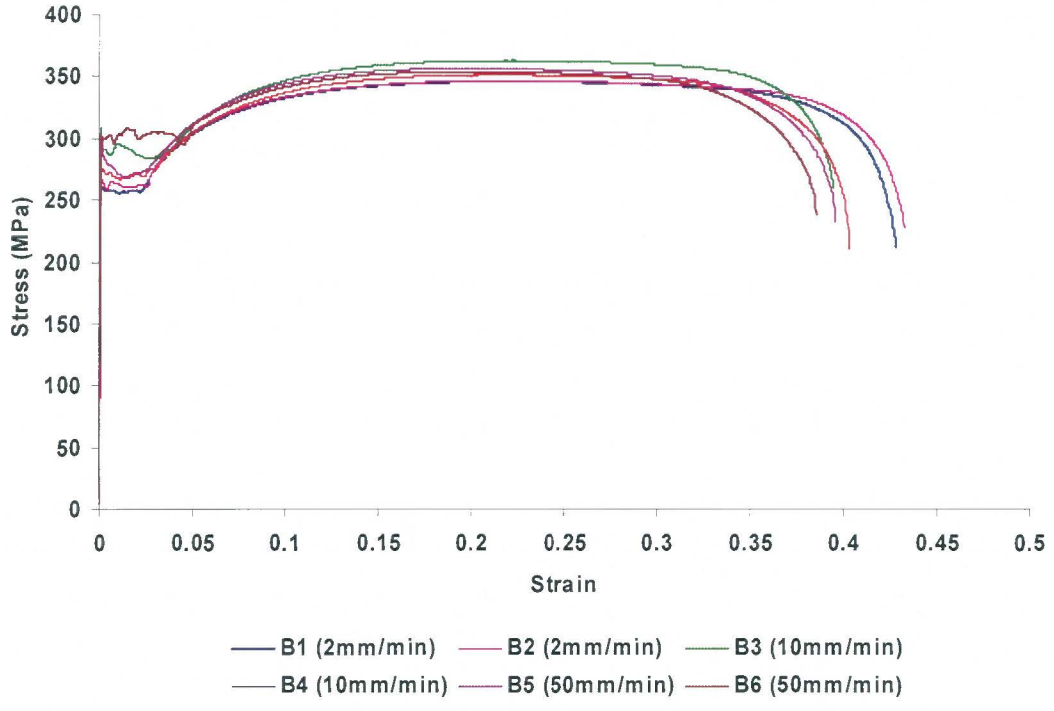

Figure 3.11: Graph of Stress versus Strain at different cross-head speeds for Sheet B

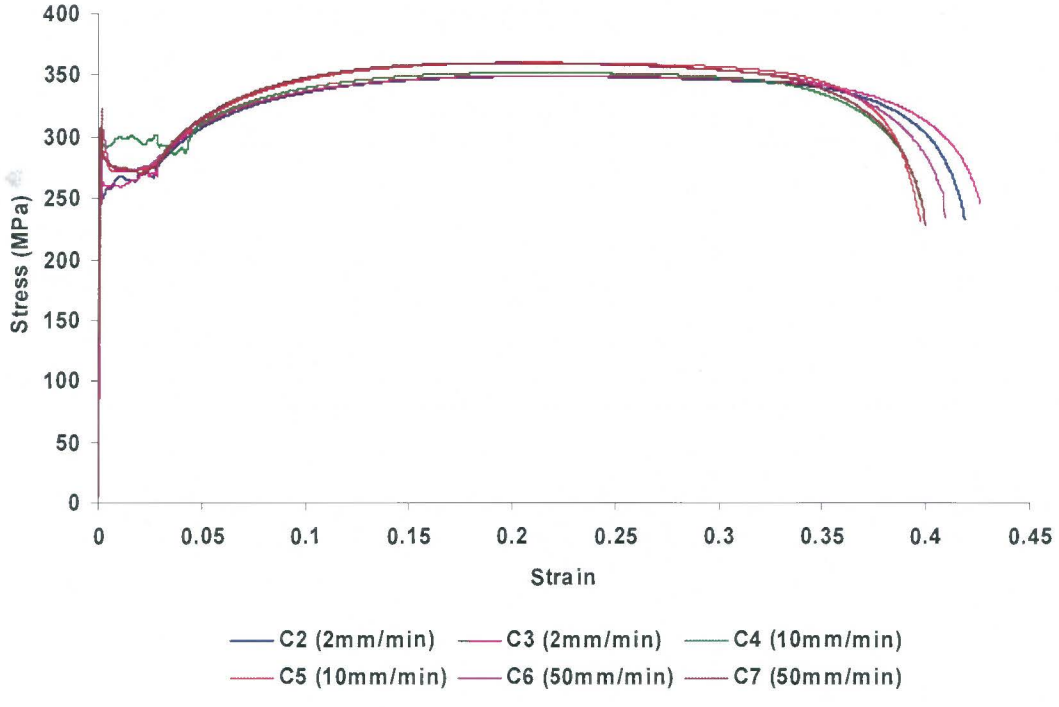

Figure 3.12: Graph of Stress versus Strain at different cross-head speeds for Sheet C

3.3 Blast loading

Plastic explosive PE4 is used to provide the blast load on test specimens. PE4 is a combination of RDX and Lithium grease (Wharton et al [38]).

Table 3.3: Composition and material characteristics of PE4, [38]

RDX and Lithium grease	88% RDX and 12% Lithium grease
Density	1.6 (gcm^{-3})
$TNT_{equivalent}$	130% (by ballistic mortar tests)
Detonation velocity	8200 (ms^{-1})

The PE4 is shaped into a disc of diameter 34mm and placed onto a 13mm thick polystyrene pad as shown in Figure 3.13. The diameter of the pad is identical to the diameter (110mm) of the recess machined at end of the tubes. A 1g leader of explosive is used to attach the detonator to the main charge, as shown in Figure 3.14. Thus the total mass of explosive is the sum of the disc and the 1g leader. The inclusive charge masses used in this investigation are 4g, 5g, 7g, 9g, 11g, 13g and 15g. The different loading scenarios implemented to ascertain the possible effects of using the polystyrene pad as a stand-off buffer to prevent spalling is discussed in detail in Section 3.3.1.

A summary of experimental details is given in Table 3.4.

Table 3.4: Summary of experimental details

Test parameters	**Details**
Plate thickness	1.9mm
Plate diameter	106mm
Stand-off distance (tube lengths)	25mm, 30mm, 40mm, 50mm, 75mm, 100mm, 150mm, 200mm, 250mm and 300mm
Charge diameter	34mm
Charge mass	4g, 5g, 7g, 9g, 11g, 13g and 15g

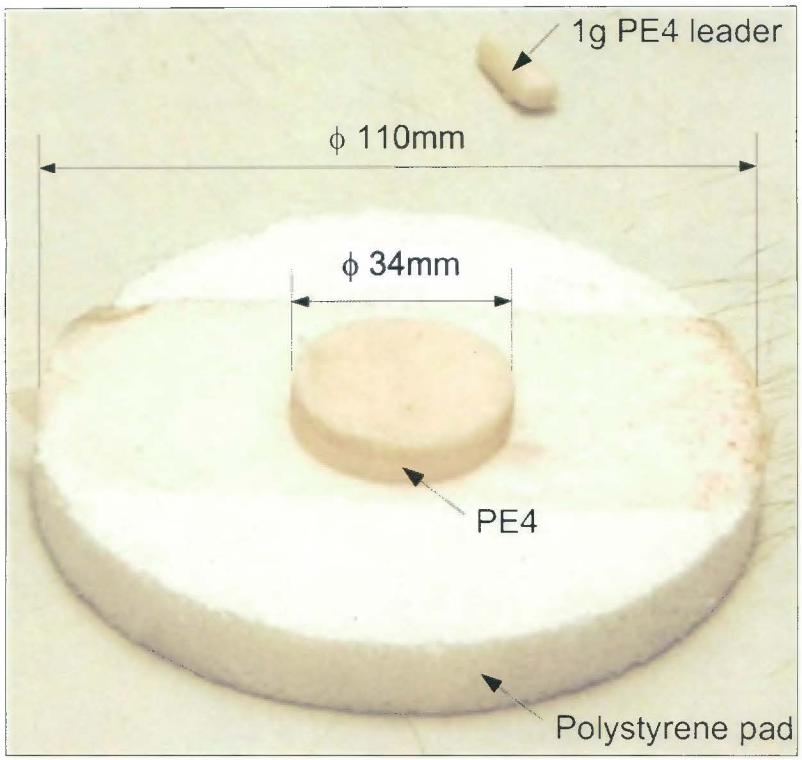

Figure 3.13: Photograph of disc shaped PE4 explosive of diameter 34mm attached to a circular polystyrene pad of diameter 110mm and thickness of 13mm

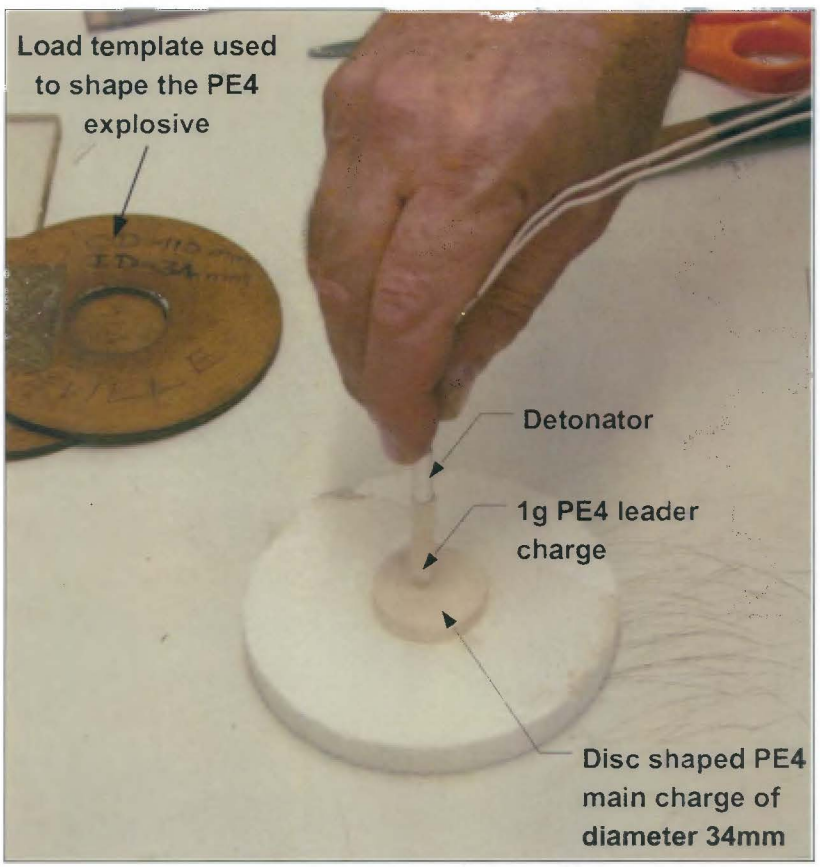

Figure 3.14: Photograph of disc shaped PE4 explosive with 1g leader attached to the detonator

3.3.1 Different blast loading conditions

Nurick and Martin [2] report on various materials (for example, sponge rubber and neoprene) used to separate the explosive charge and the test plate to prevent spallation. They also report an experimental investigation conducted by Jones, Uran and Tekin (1970) on fully clamped rectangular plates. A significant result of this work was that the type of attenuator, i.e. foam or neoprene, did not appear to influence the outcome of the tests, except that the impulsive velocity varied according to the attenuator used [2]. Langdon [39] suggests research into the possible effects of using polystyrene to separate the explosive and plate on measured impulse and plate deformation. Hence different loading conditions are used in this investigation as shown in Figure 3.15 and classified as follows,

- ***Loading condition 1 (LC-1)*** – The plastic explosive is attached to a 13mm thick polystyrene pad using a strip of double sided tape and the pad is pushed into place on the end of a tube. Stand off distance is varied using different lengths of tube. This arrangement is shown in Figure 3.15(a).

- ***Loading condition 2 (LC-2)*** – Double sided tape is used to secure the plastic explosive at one end of the tube, as shown in Figure 3.15(b).
  Note: *No polystyrene is used.*

- ***Loading condition 3 (LC-3)*** – Double sided tape is used to secure the plastic explosive at one end of the tube. A 13mm polystyrene pad is placed directly against the test specimen as shown in Figure 3.15(c).

- ***Loading condition 4 (LC-4)*** – this method has been widely used by Nurick et al [6 - 8]. In this case the plastic explosive is mounted on the polystyrene pad using double sided tape and placed directly against the test specimen as shown in Figure 3.15(d).

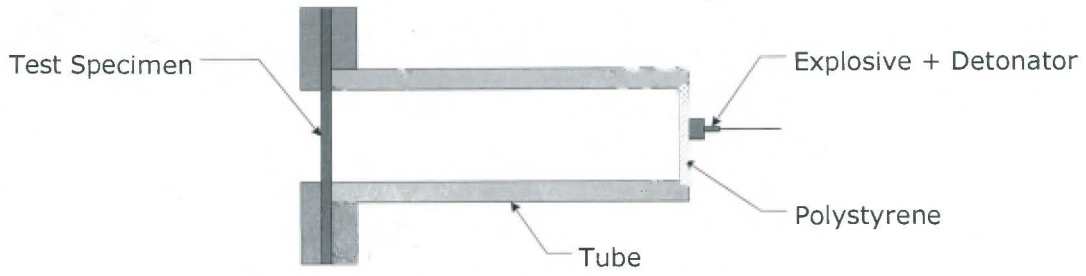

(a) Loading Condition 1 (LC-1)

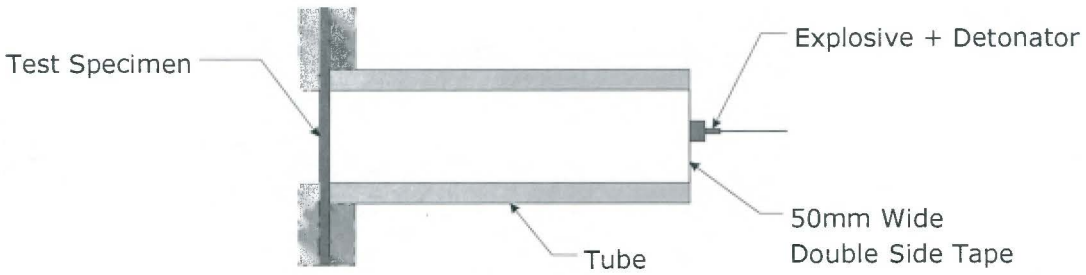

(b) Loading Condition 2 (LC-2)

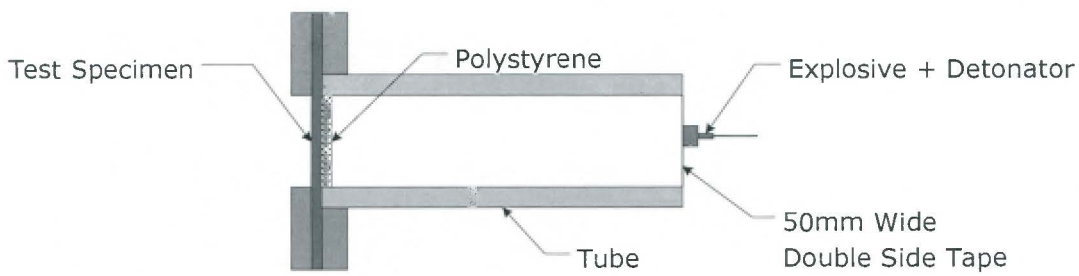

(c) Loading Condition 3 (LC-3)

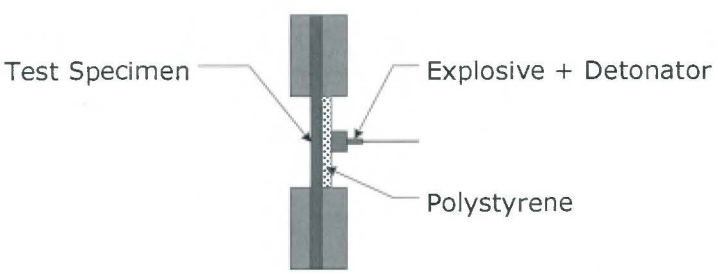

(d) Loading Condition 4 (LC-4)

Figure 3.15: Different loading conditions used in experiments

3.4 Experimental measurements

For the experiments the following measurements are required and measured:

- The impulse imparted on to each test specimen measured from the pendulum displacement
- Mid-point deflection of each test specimen is measured using a digital height gauge as shown in Figure 3.16

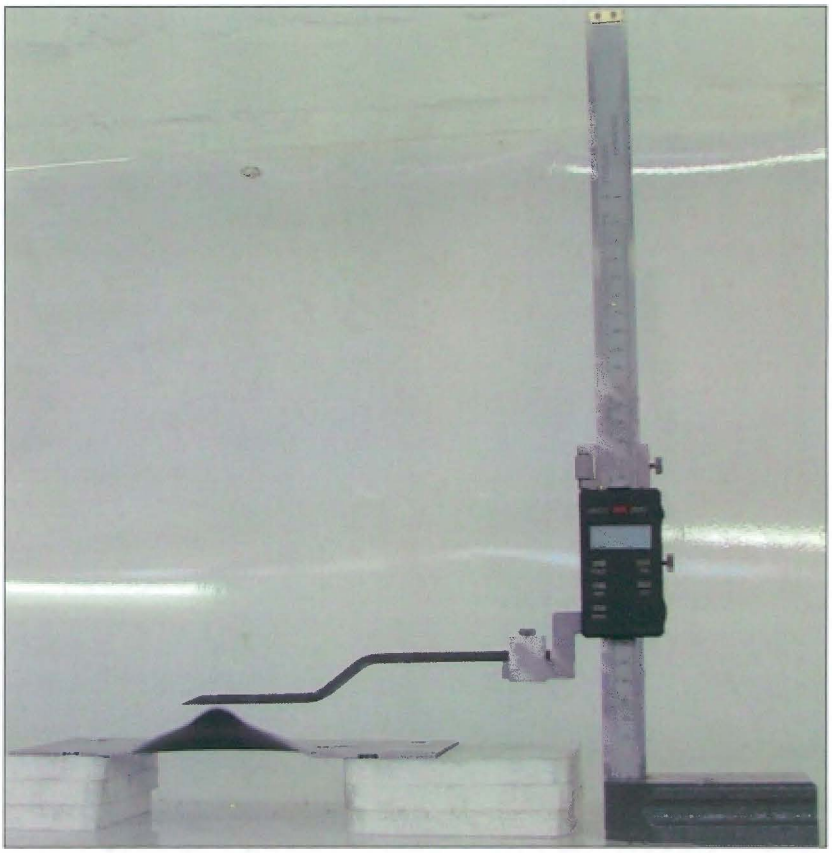

Figure 3.16: Photograph of height gauge used to measure the final mid-point deflection of a test specimen after a test

4 Experimental results

This chapter describes the results and observations from blast tests on clamped circular plates at varying stand-off distances for loading conditions LC-1, LC-2, LC-3 and LC-4. The measured test data is presented in Section 4.4. Chapter 5 discusses the results in more detail.

4.1 General plate deformation

In most cases Mode I type failure on the plates (large inelastic deformation) was observed. The plate profiles differ according to the distance between the plastic explosive and the test specimens. In cases with stand-off distances ranging from 100mm to 300mm, the plate profile resembled a uniform dome shape as shown in Figures 4.1. In cases of shorter stand-off distances ranging from 13mm to 40mm the plate profile resembled a smaller inner dome atop a larger global dome as shown in Figure 4.2.

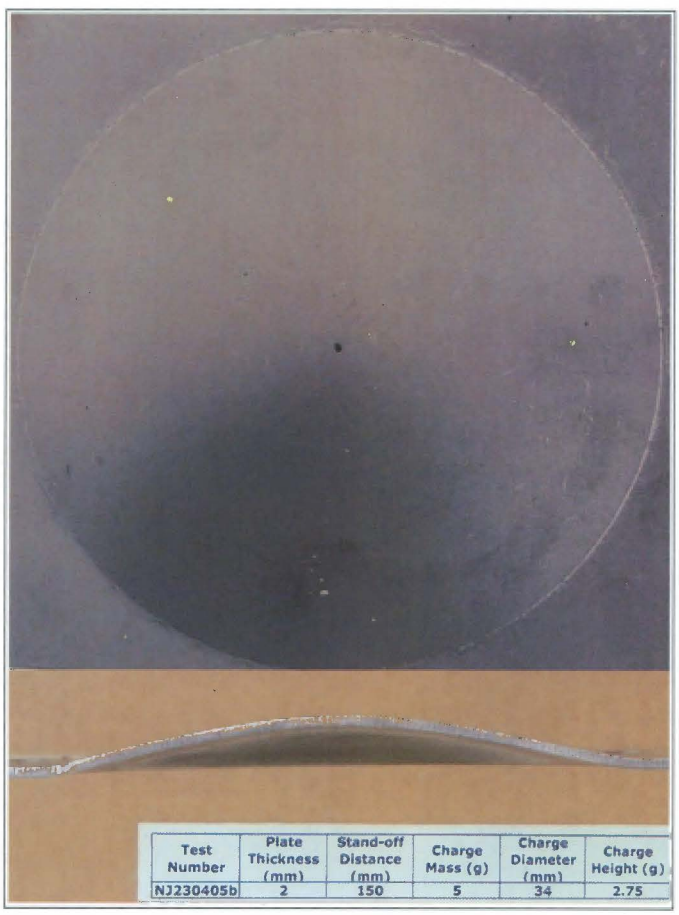

Figure 4.1: Photograph of plate profile showing large global dome. Plate number NJ230405b, I = 12.03Ns, S = 150mm

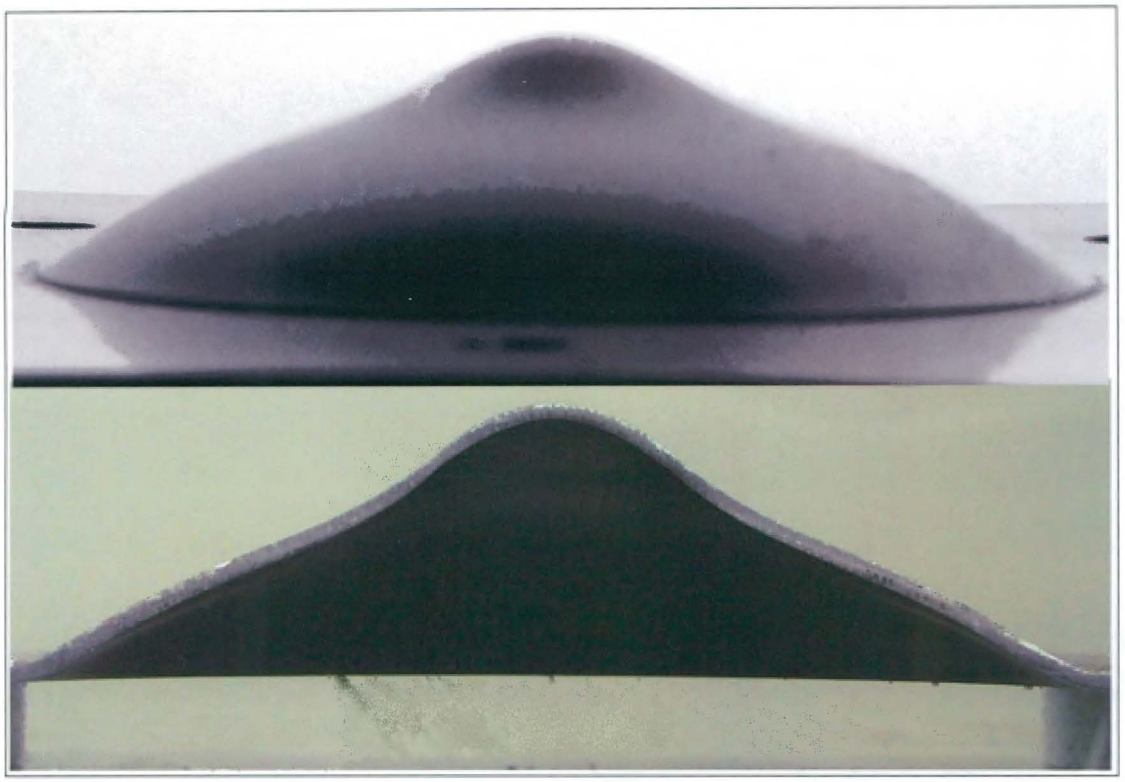

Figure 4.2: Photograph of typical plate profile for smaller stand off distances (13mm to 40mm) Plate number NJ250405c, I =12.44Ns, S = 13mm

The change in plate profile at different stand-off distances is shown in Figures 4.3 – 4.5 for charge masses 4g, 7g and 9g respectively. The plate profiles change from dish shape (large global dome) at stand-off distances ranging from 300mm to 100mm. An inner dome atop a global dome is observed for stand-off distances ranging from 40mm to 13mm. The plate profile at stand-off distance 50mm and 75mm exhibit an increase in deformation near the boundary, but the deformation does not show an inner dome near the centre of the plate. The measured mid point deflections for stand off distances 75mm, 100mm, 150mm, 200mm, 250mm and 300mm show little variation. This is shown in Figures 4.3 – 4.5 by the closed packed nature of the bottom five plates.

Figure 4.3: Photograph of sequential layout of test specimens for increasing stand-off distance for constant charge mass, 5g
(Plate numbers top to bottom - NJ250405b, NJ160405g, NJ160405a, NJ150405a, NJ090405a, NJ020705b, NJ080405a, NJ230405c, NJ050405a, NJ290305f and NJ210405a)

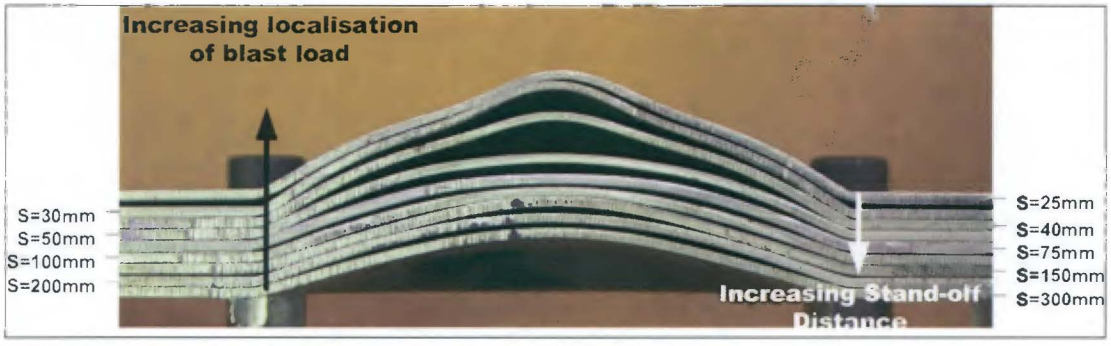

Figure 4.4: Sequential layout of test specimens for increasing stand-off distance for constant charge mass, 7g
(Plate numbers top to bottom - NJ160405h, NJ150405b, NJ090405b, NJ020705c, NJ080405b, NJ230405d, NJ050405b and NJ210405d)

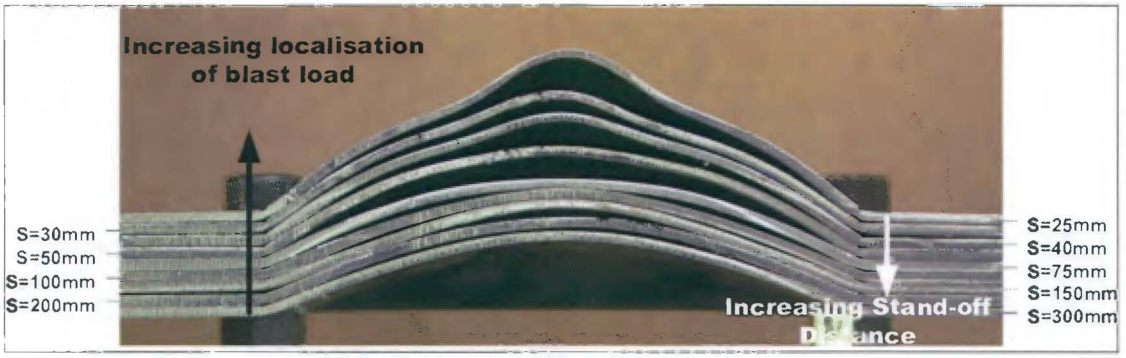

Figure 4.5: Sequential layout of test specimens for increasing stand-off distance for constant charge mass, 9g
(Plate numbers top to bottom - NJ160405i, NJ160405d, NJ150405c, NJ040705a, NJ080405c, NJ060405c, NJ050405c and NJ310305c)

4.2 Effect of different loading conditions

Polystyrene has been used extensively in experiments reported by Nurick et al [2 – 8, 25, 27 – 31]. It is used primarily as a stand-off buffer to prevent spalling. Nurick and Martin [2] report an experimental investigation conducted by Jones et al (1970) on rectangular plates subjected to blast loading. The results indicated that, the type of stand-off buffer used (for example, neoprene or foam) does not appear to influence the outcome of the tests. However, it was deemed necessary to ascertain if polystyrene had any observable effect on plate deformation and impulse [39] using the different loading conditions outlined in Section 3.3.1.

Figures 4.6, 4.7 and 4.8 show the loaded side of the plates for load conditions LC-1, LC-2 and LC-3 respectively. The reader is reminded of the different loading conditions as shown in Figure 3.15. The loaded side of a test plate subjected to load condition LC-1 shows an even coating of black soot on the surface of the plate as shown in Figure 4.6. The charge mass was kept constant and the polystyrene was replaced with double sided tape (LC-2). The loaded side had significantly less black soot as seen for the previous load condition (LC-1). The plate surface was visible and covered with a thin coating of semi-transparent soot which can be easily wiped away as shown in Figure 4.7. Following the test pattern described previously, charge mass was maintained and a 13mm thick polystyrene pad was placed directly against the plate. Thus the explosive charge was separated from the polystyrene by the distance of the tube (LC-3). After the test, residue of the polystyrene was visible on the loaded side of the test plate as shown in Figure 4.8 and a close up of the residue is shown in Figure 4.9. The cross-sectional view of plates subjected to LC-1, LC-2 and LC-3 for charge mass of 5g and 7g are shown in Figures 4.10 and 4.11 respectively.

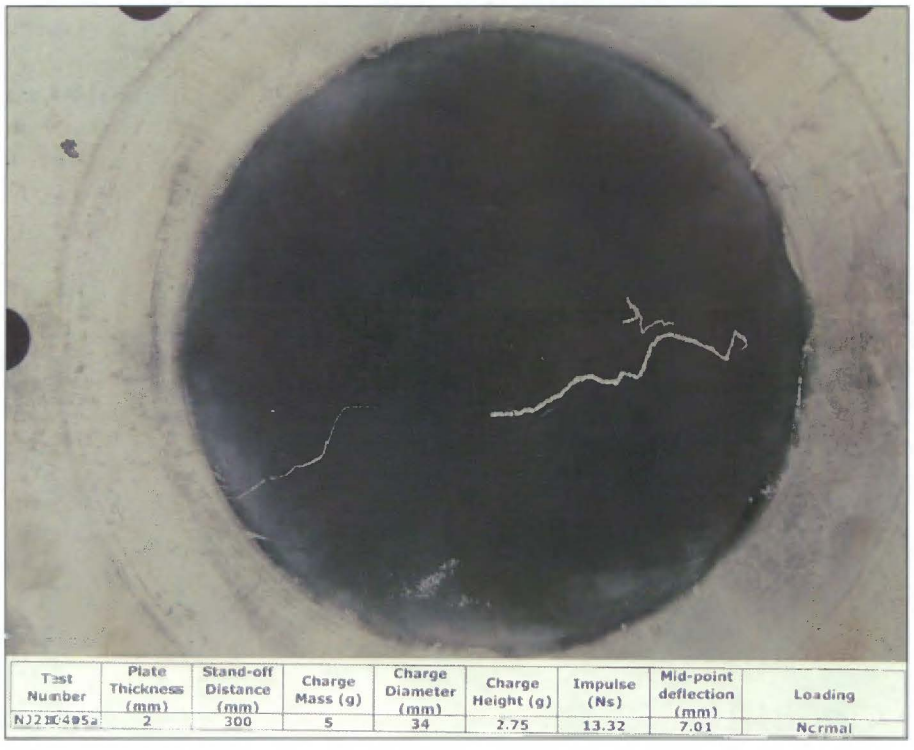

Test Number	Plate Thickness (mm)	Stand-off Distance (mm)	Charge Mass (g)	Charge Diameter (mm)	Charge Height (g)	Impulse (Ns)	Mid-point deflection (mm)	Loading
NJ21C405a	2	300	5	34	2.75	13.32	7.01	Normal

Figure 4.6: Photograph of black soot observed for test plate subjected to load condition LC-1
Test plate Number NJ210405a, S = 300mm, I = 13.32Ns and Mid-point deflection = 7.01mm

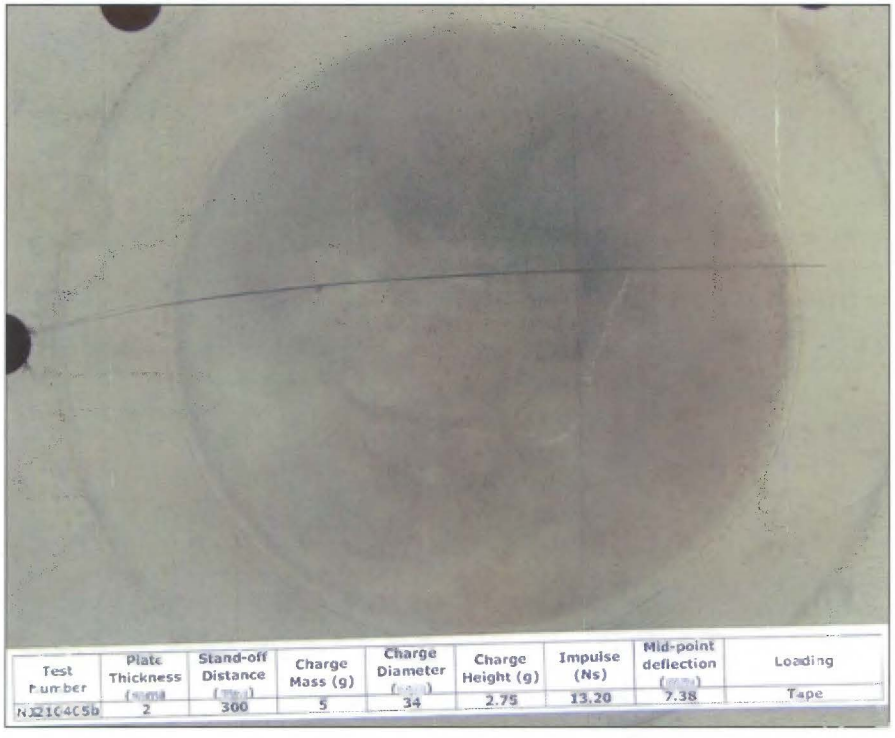

Test Number	Plate Thickness (mm)	Stand-off Distance (mm)	Charge Mass (g)	Charge Diameter (mm)	Charge Height (g)	Impulse (Ns)	Mid-point deflection (mm)	Loading
NJ21C405b	2	300	5	34	2.75	13.20	7.38	Tape

Figure 4.7: Photograph of translucent soot observed for test plate subjected to load condition LC-2
Test plate Number NJ210405b, S=300mm, I=13.20Ns and Mid-point deflection = 7.38mm

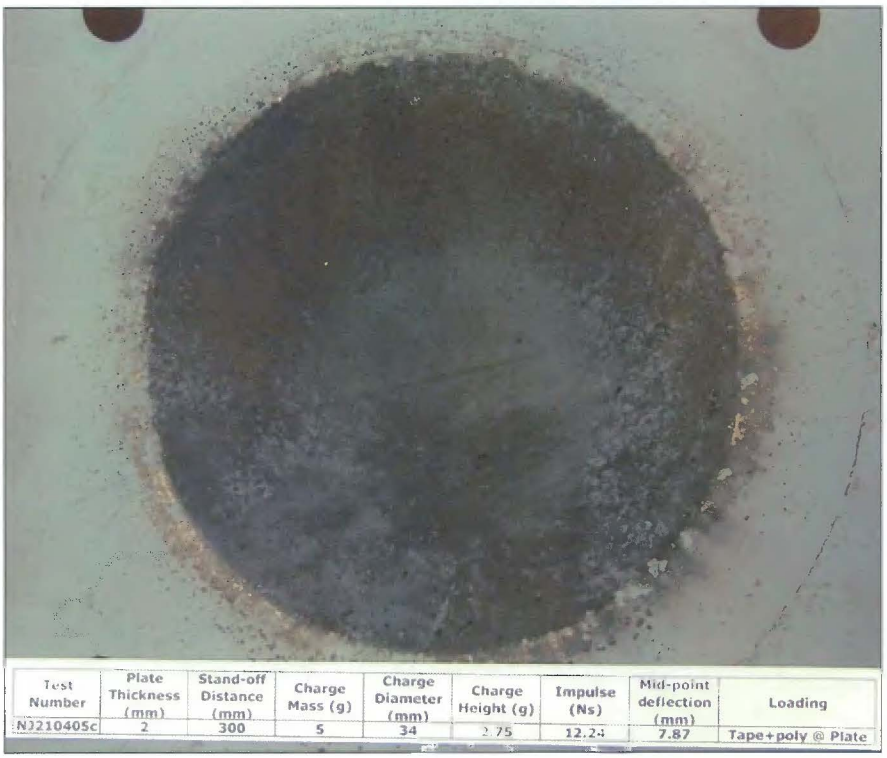

Test Number	Plate Thickness (mm)	Stand-off Distance (mm)	Charge Mass (g)	Charge Diameter (mm)	Charge Height (g)	Impulse (Ns)	Mid-point deflection (mm)	Loading
NJ210405c	2	300	5	34	2.75	12.24	7.87	Tape+poly @ Plate

Figure 4.8: Photograph of polystyrene residue visible for test plate subjected to load condition LC-3
Test plate Number NJ210405c, S = 300mm, I = 12.24Ns and Mid-point deflection = 7.87mm

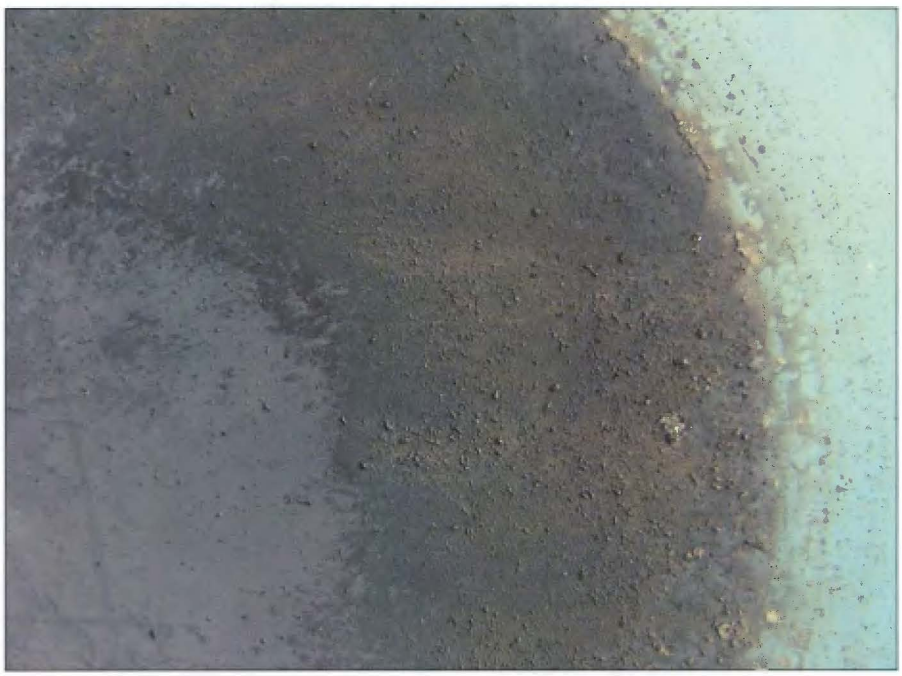

Figure 4.9: Photograph showing a close up view of the polystyrene residue visible for test plate (NJ210405c) subjected to load condition LC-3

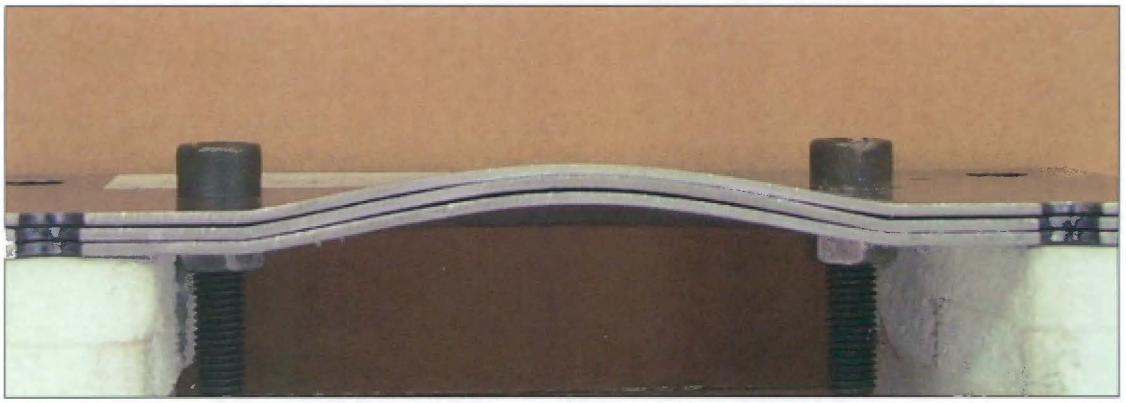

Figure 4.10: Photograph of plate profile for test plate subjected to same charge mass (5g) but different load conditions (LC-1, LC-2 and LC-3) Test plate Numbers, NJ210405a, NJ210405b, NJ210405c

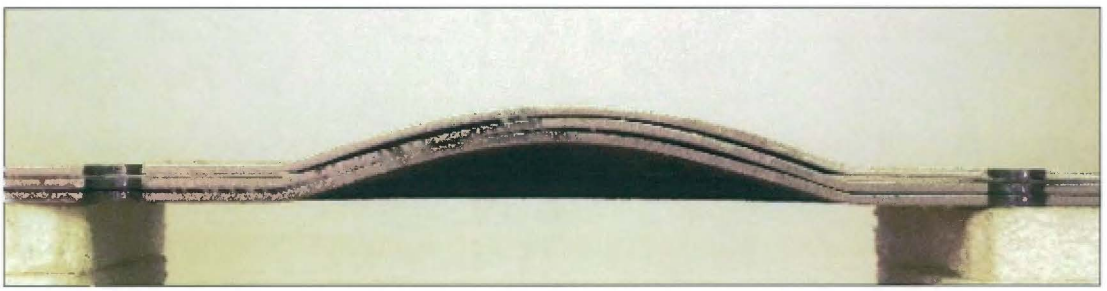

Figure 4.11: Photograph of plate profile for test plate subjected to same charge mass (7g) but different load conditions (LC-1, LC-2 and LC-3) Test plate Numbers, NJ220405c, NJ220405e, NJ220405f

4.3 Burn diameter phenomenon

A circular ring referred to as the "burn diameter" is observed on the loaded side of the test specimens. This has been observed by Nurick et al [6 - 8]. The burn diameter is observed for stand-off distances ranging from 13mm up to 75mm (Figure 4.12). In experiments with stand-off distances ranging from 100mm to 300mm an even coating of soot is observed as shown in Figure 4.13.

Burn diameter is visible after cleaning the soot from the test specimens with turpentine as shown in Figure 4.14. In cases where a uniform coating of soot was observed no visible burn diameter was observed.

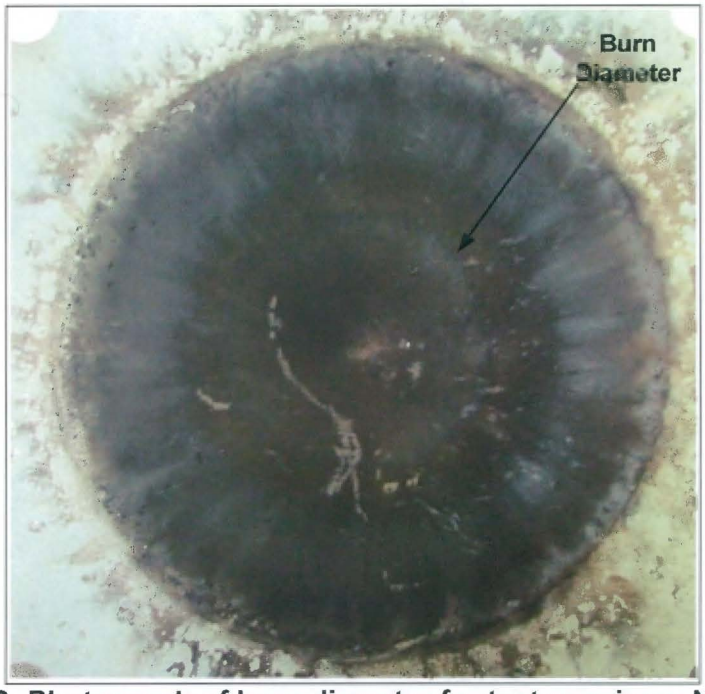

Figure 4.12: Photograph of burn diameter for test specimen NJ180405a, S = 13mm, charge mass 5g, I = 10.99Ns, Load condition LC-1

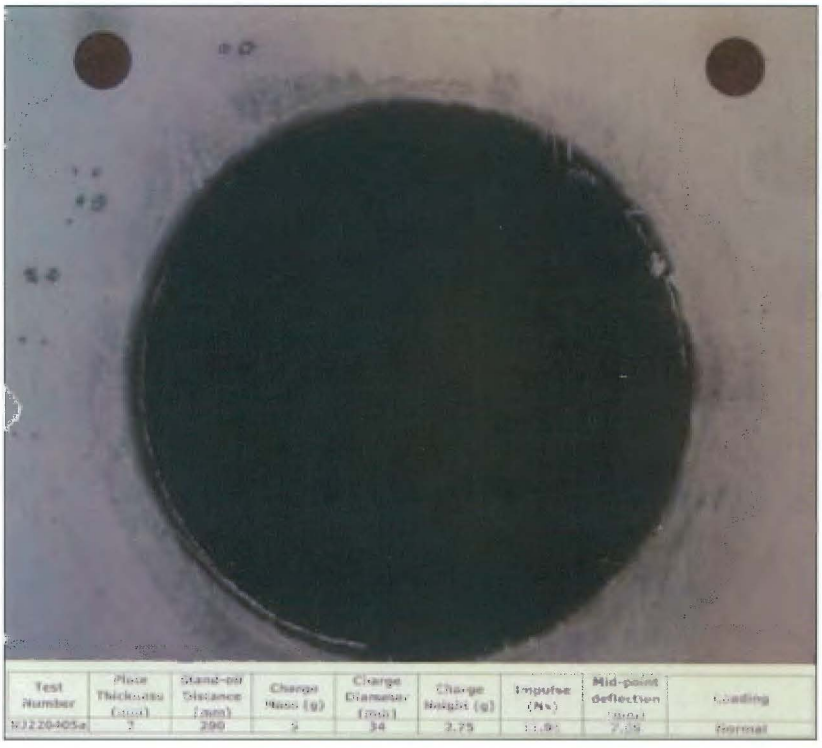

Figure 4.13: Photograph of uniform coat of soot, no visible indication of burn diameter for test specimen NJ220405a,S = 200mm, charge mass 5g, I = 11.91Ns, Load condition LC-1

Figure 4.14: Photograph of burn diameter for test specimen NJ150405c, S = 40mm, charge mass 9g, I = 17.97Ns, Load condition LC-1

4.4 Thinning

Thinning is observed in both the central area and at the boundary of the test specimens.

4.4.1 Thinning in the central region

Thinning in the central area, as shown in Figure 4.15, is a function of the distance between the test specimen and the plastic explosive. It is observed at higher impulses for stand-off distances ranging from 13mm to 40mm. An inner dome atop a larger global dome is observed within this range. Thinning coincides with the inflection diameter which demarcates the boundary between the larger global dome and the inner dome characterised by the sharp increase in gradient of the plate profile. This is similar to plate behaviour observed in localised blast loading tests, Nurick et al [6 - 8].

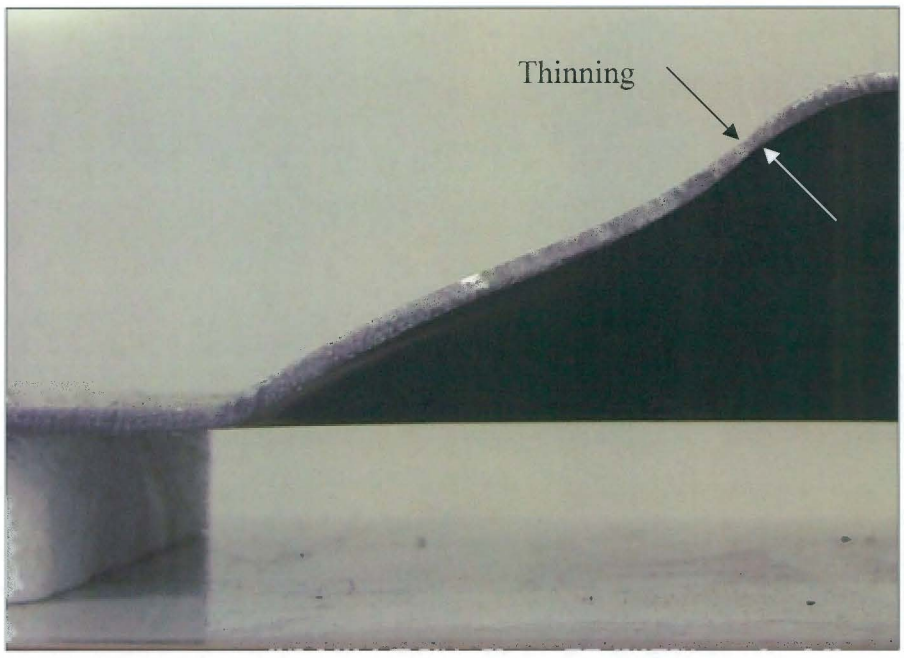

Figure 4.15: Photograph of thinning at the central area of the plate for test specimen NJ250405c, charge mass 6g, I =12.44Ns, S = 13mm

4.4.2 Thinning at the boundary

Thinning at the boundary is observed at stand-off distances ranging from 25mm to 300mm using the tubes provided the impulse was sufficiently high. Mode Ib, (necking around the entire boundary of the plate) was most prevalent. The thinning mechanism observed can be described as a sharp indentation due to the sharp edge of the clamping plate with stretching and thinning occurring thereafter [3] as shown in Figure 4.16.

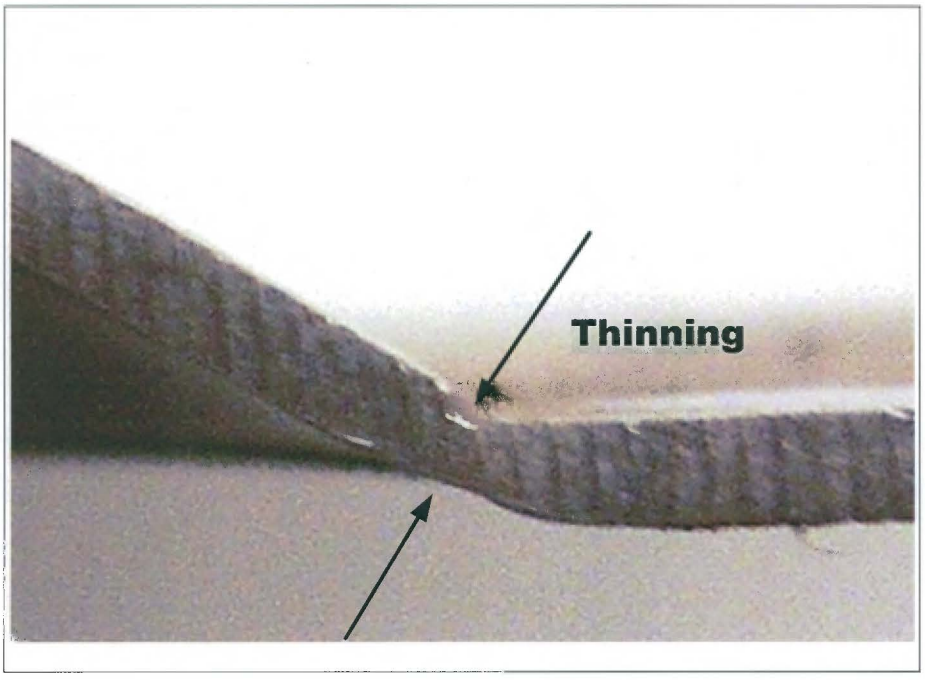

Figure 4.16: Photograph of thinning at the boundary for test specimen NJ290305g, charge mass = 15.5g, I =33.47Ns, S = 250mm

4.4.3 Tearing at the boundary

The central deformation of the test specimen increases with increasing impulse. Tearing occurs once a certain threshold impulse has been achieved. However this impulse is dependent on plate thickness. Partial tearing (Mode II*) along the boundary, as shown in Figure 4.17, was observed at stand off distances of 250mm and 150mm at impulse values of 32.1Ns and 32.44Ns respectively. However, at stand-off distance of 25mm the test plate exhibited partial tearing at the boundary and thinning in the central area of the plate at an impulse of 17.2Ns as shown in Figure 4.18. Complete tearing at the boundary was observed only in two cases at stand-off distances of 50mm and 250mm at impulses of 21.17Ns and 29.92Ns respectively, as shown in Figure 4.19. Thus, the results indicate that tearing occurs at lower impulses for smaller stand-off distances due to the severity of the blast load as the charge is moved closer to the plate.

It should be noted that the purpose of this investigation is to establish the relationship between stand-off distance and large inelastic deformation (Mode I). However, partial tearing (Mode II*) and complete tearing (Mode II) occurred during tests done to establish the limits of charge masses that could be used.

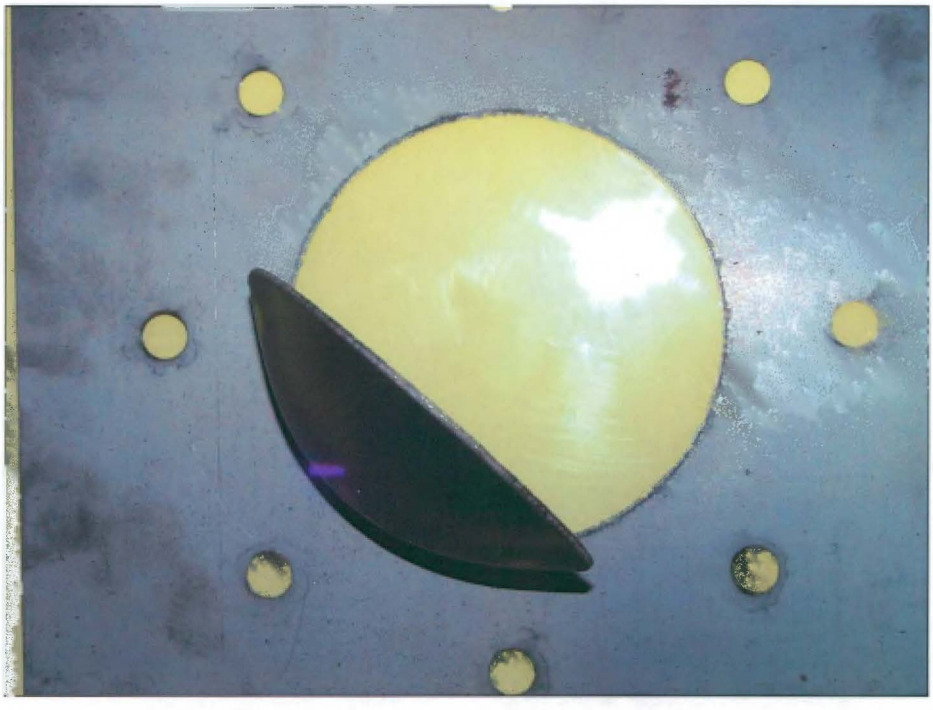

Figure 4.17: Photograph of partial tearing at the boundary of test specimen NJ060405f, charge mass 15g, I = 32.44Ns, S = 150mm

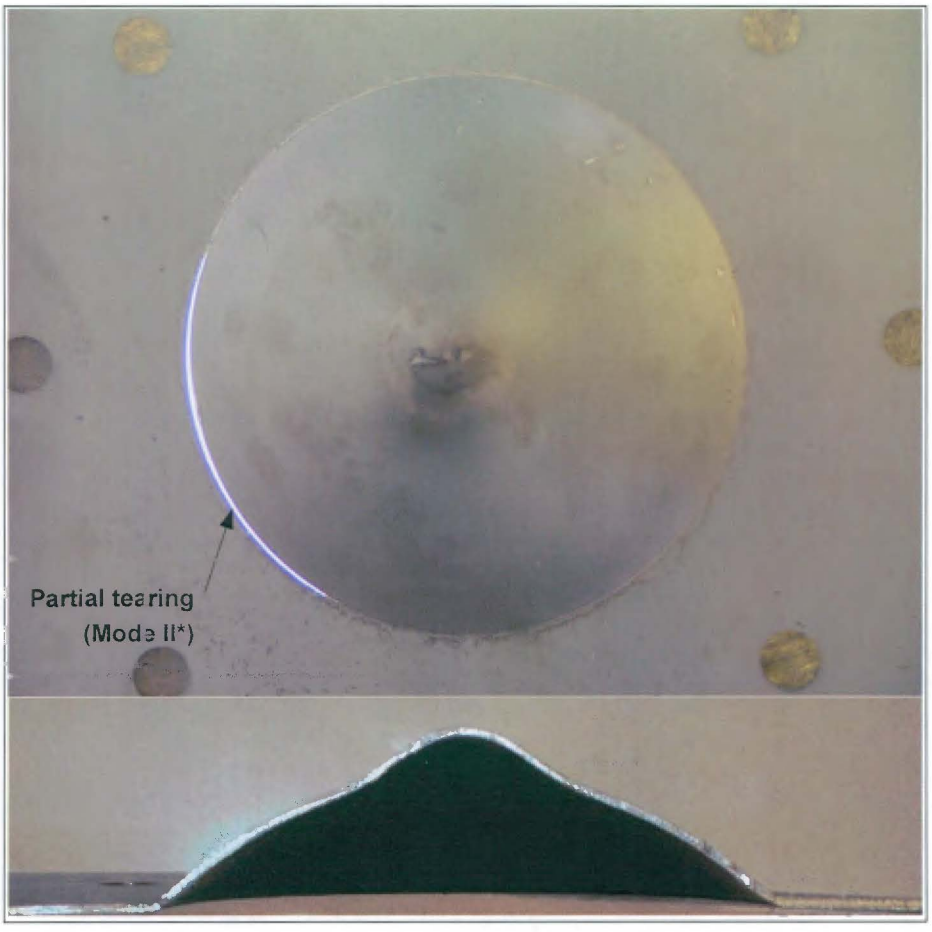

Figure 4.18: Photograph of partial tearing at the boundary with thinning at the central area of the plate of test specimen NJ160405i, charge mass 9g, I = 17.2Ns, S = 25mm

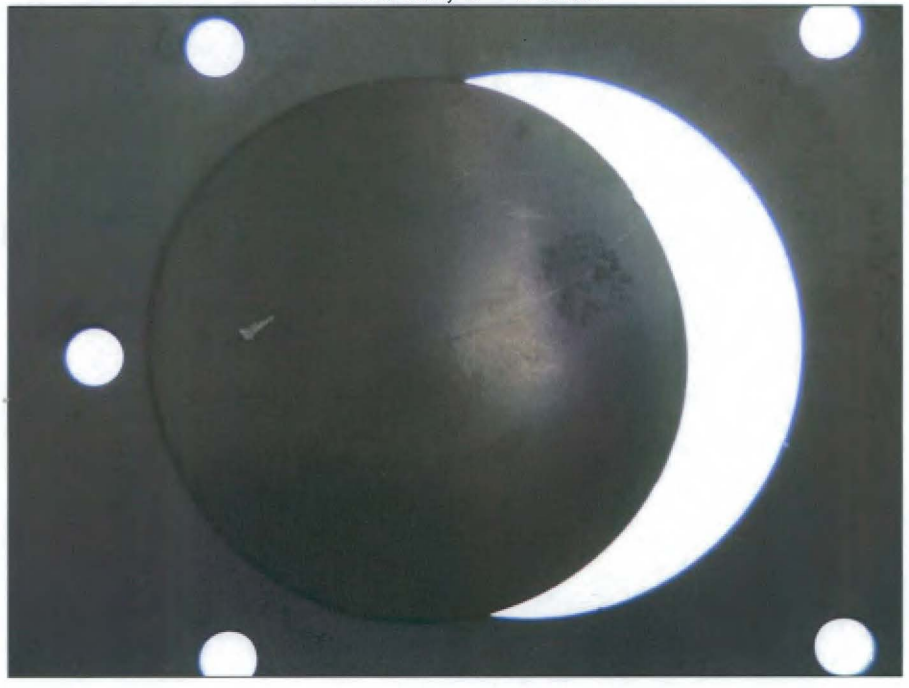

Figure 4.19: Photograph of complete tensile tearing at the boundary of test specimen NJ090405d, charge mass 11g, I = 21.17Ns, S = 50mm

4.5 Experimental results

The experimental data are presented in Table 4.1. The test plates are labelled according to the date of the test and the order in which the test were conducted. For example NJ – denotes author's initials, 250405 – date (25th April 2005), a – 1st test of the day.

The charge mass listed include the 1g leader charge attached to detonator, for example 5g equals to (4+1)g. The reader is referred to Figure 4.4 for description of the different loading conditions used.

Table 4.1: Experimental results

Test Number	Plate Thickness (mm)	Stand-off Distance (mm)	Charge Mass (g)	Charge Diameter (mm)	Charge Height (mm)	Impulse (Ns)	Mid-point deflection (mm)	Mid-point deflection - Plate thickness Ratio	Burn Diameter(mm)	Mode of Failure	Loading condition
NJ180405a	1.9	13	5	34	2.75	10.99	22.21	11.69	47.52	Mode I	LC-1
NJ250405a	1.9	13	4	34	2.07	8.65	18.35	9.66	45.81	Mode I	LC-4
NJ250405b	1.9	13	5	34	2.75	10.99	22.54	11.86	48.26	Mode I	LC-4
NJ250405c	1.9	13	6	34	3.44	12.44	26.45	13.92	49.61	Mode Itc	LC-4
NJ160405f	1.9	25	4	34	2.07	8.68	14.78	7.78	50.38	Mode I	LC-1
NJ160405g	1.9	25	5	34	2.75	10.33	17.34	9.12	55.08	Mode I	LC-1
NJ160405h	1.9	25	7	34	4.13	14.02	21.67	11.40	61.96	Mode Ib	LC-1
NJ160405l	1.9	25	9	34	5.51	17.20	28.10	14.79	62.06	Mode II*+Mode Itc	LC-1
NJ160405a	1.9	30	5	34	2.75	10.51	15.57	8.19	60.05	Mode I	LC-1
NJ160405b	1.9	30	7	34	4.13	14.32	22.77	11.98	63.63	Mode Ib	LC-1
NJ160405c	1.9	30	8	34	4.82	15.90	24.23	12.75	62.48	Mode Ib	LC-1
NJ160405d	1.9	30	9	34	5.51	17.16	23.80	12.53	67.10	Mode Ib	LC-1
NJ160405e	1.9	30	4	34	2.07	8.43	12.64	6.65	55.32	Mode I	LC-1
NJ150405a	1.9	40	5	34	2.75	11.40	12.34	6.50	68.35	Mode I	LC-1
NJ150405b	1.9	40	7	34	4.13	14.37	19.00	10.00	66.57	Mode Ib	LC-1
NJ150405c	1.9	40	9	34	5.51	17.97	22.26	11.71	73.38	Mode Ib	LC-1
NJ150405d	1.9	40	8	34	4.82	16.21	19.61	10.32	64.44	Mode Ib	LC-1
NJ150405e	1.9	40	4	34	2.07	8.51	10.71	5.63	61.59	Mode I	LC-1
NJ300405a	1.9	50	4	34	2.07	9.11	8.39	4.41	62.74	Mode I	LC-1
NJ090405a	1.9	50	5	34	2.75	10.59	9.84	5.18	68.44	Mode I	LC-1
NJ090405b	1.9	50	7	34	4.13	14.11	13.26	6.98	74.62	Mode Ib	LC-1
NJ090405c	1.9	50	9	34	5.51	17.94	18.12	9.54	77.36	Mode Ib	LC-1
NJ090405d	1.9	50	11	34	6.88	21.17	21.58	11.36	-	Mode II	LC-1

Test Number	Plate Thickness (mm)	Stand-off Distance (mm)	Charge Mass (g)	Charge Diameter (mm)	Charge Height (mm)	Impulse (Ns)	Mid-point deflection (mm)	Mid-point deflection - Plate thickness Ratio	Burn Diameter(mm)	Mode of Failure	Loading condition
NJ020705a	1.9	75	4	34	2.07	9.10	6.65	3.50	-	Mode I	LC-1
NJ020705b	1.9	75	5	34	2.75	11.33	8.28	4.36	-	Mode I	LC-1
NJ020705b	1.9	75	7	34	4.13	14.64	11.64	6.12	-	Mode I	LC-1
NJ040705a	1.9	75	9	34	5.51	17.68	13.85	7.29	-	Mode I	LC-1
NJ040705b	1.9	75	11	34	6.88	19.91	16.60	8.73	-	Mode Ib	LC-1
NJ300405b	1.9	100	4	34	2.07	9.57	5.92	3.12	-	Mode I	LC-1
NJ080405a	1.9	100	5	34	2.75	10.79	8.05	4.24	-	Mode I	LC-1
NJ080405b	1.9	100	7	34	4.13	14.76	11.66	6.13	-	Mode I	LC-1
NJ080405c	1.9	100	9	34	5.51	17.97	14.48	7.62	-	Mode I	LC-1
NJ080405d	1.9	100	11	34	6.88	21.86	17.03	8.96	-	Mode I	LC-1
NJ080405e	1.9	100	13	34	8.26	25.36	19.79	10.42	-	Mode Ib	LC-1
NJ060405a	1.9	150	5	34	2.75	11.83	8.31	4.37	-	Mode I	LC-1
NJ060405b	1.9	150	7	34	4.13	16.15	11.61	6.11	-	Mode I	LC-1
NJ060405c	1.9	150	9	34	5.51	19.00	14.37	7.56	-	Mode I	LC-1
NJ060405d	1.9	150	11	34	6.88	25.19	17.18	9.04	-	Mode I	LC-1
NJ060405e	1.9	150	13	34	8.26	28.73	20.05	10.55	-	Mode Ib	LC-1
NJ060405f	1.9	150	15	34	9.64	32.44	-	-	-	Mode II*	LC-1
NJ230405a	1.9	150	5	34	2.75	11.47	7.83	4.12	-	Mode I	LC-1
NJ230405b	1.9	150	5	34	2.75	12.03	8.50	4.47	-	Mode I	LC-2
NJ230405c	1.9	150	5	34	2.75	10.56	7.87	4.14	-	Mode I	LC-3
NJ230405d	1.9	150	7	34	4.13	15.30	11.76	6.19	-	Mode I	LC-1
NJ230405e	1.9	150	7	34	4.13	15.11	12.18	6.41	-	Mode I	LC-2
NJ230405f	1.9	150	7	34	4.13	15.30	12.28	6.46	-	Mode I	LC-3

Test Number	Plate Thickness (mm)	Stand-off Distance (mm)	Charge Mass (g)	Charge Diameter (mm)	Charge Height (mm)	Impulse (Ns)	Mid-point deflection (mm)	Mid-point deflection - Plate thickness Ratio	Burn Diameter(mm)	Mode of Failure	Loading condition
NJ300405c	1.9	200	4	34	2.07	9.64	5.96	3.14	-	Mode I	LC-1
NJ050405a	1.9	200	5	34	2.75	13.06	7.96	4.20	-	Mode I	LC-1
NJ050405b	1.9	200	7	34	4.13	17.35	11.29	5.94	-	Mode I	LC-1
NJ050405c	1.9	200	9	34	5.51	22.41	13.55	7.13	-	Mode I	LC-1
NJ050405d	1.9	200	11	34	6.88	25.18	16.05	8.44	-	Mode Ib	LC-1
NJ050405e	1.9	200	13	34	8.26	30.69	18.55	9.76	-	Mode Ib	LC-1
NJ050405f	1.9	200	15	34	9.64	31.67	20.01	10.53	-	Mode Ib	LC-1
NJ220405a	1.9	200	5	34	2.75	11.91	7.65	4.03	-	Mode I	LC-1
NJ220405b	1.9	200	5	34	2.75	11.67	7.82	4.12	-	Mode I	LC-2
NJ220405c	1.9	200	7	34	4.13	16.18	10.72	5.64	-	Mode I	LC-1
NJ220405d	1.9	200	5	34	2.75	11.38	8.07	4.25	-	Mode I	LC-3
NJ220405e	1.9	200	7	34	4.13	15.66	11.38	5.99	-	Mode I	LC-2
NJ220405f	1.9	200	7	34	4.13	15.26	11.14	5.86	-	Mode I	LC-3
NJ220405g	1.9	200	7	34	4.13	14.85	11.77	6.20	-	Mode I	LC-3
NJ290305a	1.9	250	11	34	6.88	24.05	15.30	8.05	-	Mode Ib	LC-1
NJ290305b	1.9	250	13	34	8.26	26.33	17.03	8.96	-	Mode Ib	LC-1
NJ290305c	1.9	250	15	34	9.64	30.24	18.92	9.96	-	Mode Ib	LC-1
NJ290305d	1.9	250	17	34	11.01	29.92	-	-	-	Mode II	LC-1
NJ290305e	1.9	250	16	34	10.33	32.10	-	-	-	Mode II*	LC-1
NJ290305f	1.9	250	5	34	2.75	11.85	7.37	3.88	-	Mode I	LC-1
NJ290305g	1.9	250	15.5	34	9.98	33.47	19.53	10.28	-	Mode Ib	LC-1

Test Number	Plate Thickness (mm)	Stand-off Distance (mm)	Charge Mass (g)	Charge Diameter (mm)	Charge Height (mm)	Impulse (Ns)	Mid-point deflection (mm)	Mid-point deflection - Plate thickness Ratio	Burn Diameter(mm)	Mode of Failure	Loading condition
NJ310305a	1.9	300	5	34	2.75	14.95	7.32	3.85	-	Mode I	LC-1
NJ310305b	1.9	300	11	34	6.88	24.82	14.97	7.88	-	Mode I	LC-1
NJ310305c	1.9	300	9	34	5.51	21.63	13.06	6.87	-	Mode I	LC-1
NJ310305d	1.9	300	13	34	8.26	30.24	18.17	9.56	-	Mode Ib	LC-1
NJ310305e	1.9	300	15	34	9.64	33.03	18.98	9.99	-	Mode Ib	LC-1
NJ210405a	1.9	300	5	34	2.75	13.32	7.01	3.69	-	Mode I	LC-1
NJ210405b	1.9	300	5	34	2.75	13.20	7.38	3.88	-	Mode I	LC-2
NJ210405c	1.9	300	5	34	2.75	12.24	7.87	4.14	-	Mode I	LC-3
NJ210405d	1.9	300	7	34	4.13	16.74	10.43	5.49	-	Mode I	LC-1
NJ210405e	1.9	300	7	34	4.13	16.30	10.27	5.41	-	Mode I	LC-2
NJ210405f	1.9	300	7	34	4.13	15.65	10.41	5.48	-	Mode I	LC-3
NJ300405d	1.9	300	4	34	2.07	10.96	5.66	2.98	-	Mode I	LC-1

5 Analysis of experimental results

This chapter examines the relationship between experimental input parameters such as mass of explosive, stand off distances and loading conditions to measured results, namely impulse and plate mid-point deflection.

5.1 Relationship between impulse and charge mass

The impulse increases for increasing charge mass and is independent of plate response. A similar trend has been reported by Nurick et al [8]. The impulses for all charge masses used in experiments are shown in Figure 5.1. A descriptive statistical analysis of the data shown in Figure 5.1 is conducted using Microsoft office EXCEL Data Analysis tool to determine the confidence interval of the best fit curve through the data points. The analysis indicates that impulse for a given charge mass will be within ±1.31Ns with a 90% confidence. Similarly, impulse will be with ±2.69Ns of the same best fit curve with a 99.9% confidence.

The regularity of the explosive can be illustrated by plotting mass of explosive to impulse ratio versus charge height. The data fall within a range of 0.4 and 0.6 as shown in Figure 5.2 in agreement with results reported by Nurick et al [6, 8].

A closer scrutiny of Figure 5.1 indicates a relationship between impulse and stand-off distance. The graph of impulse versus charge mass showing data points for stand-off distance ranging from 13mm to 50mm grouped together and subsequent stand-off distances ranging from 75mm to 300mm plotted individually is shown in Figure 5.3. It is evident that impulses measured at stand-off distance ranging from 13mm to 50mm, for a given charge mass, are less than the impulses measured (for the same charge mass) at a stand-off distance of 300mm. The relationship between impulse and stand-off distance is discussed in detail in the following Section 5.2.

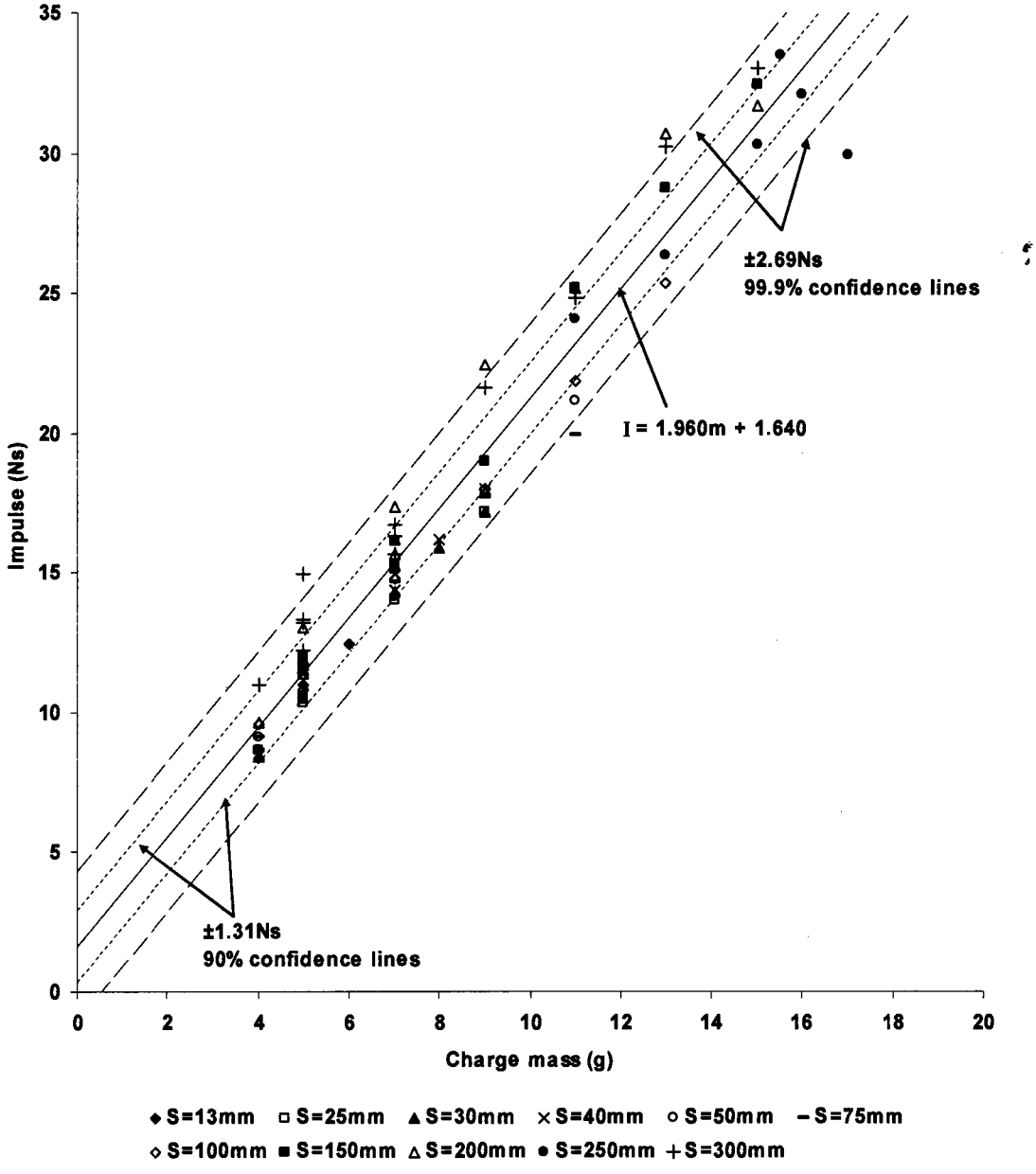

Figure 5.1: Graph of impulse versus charge mass for all tests

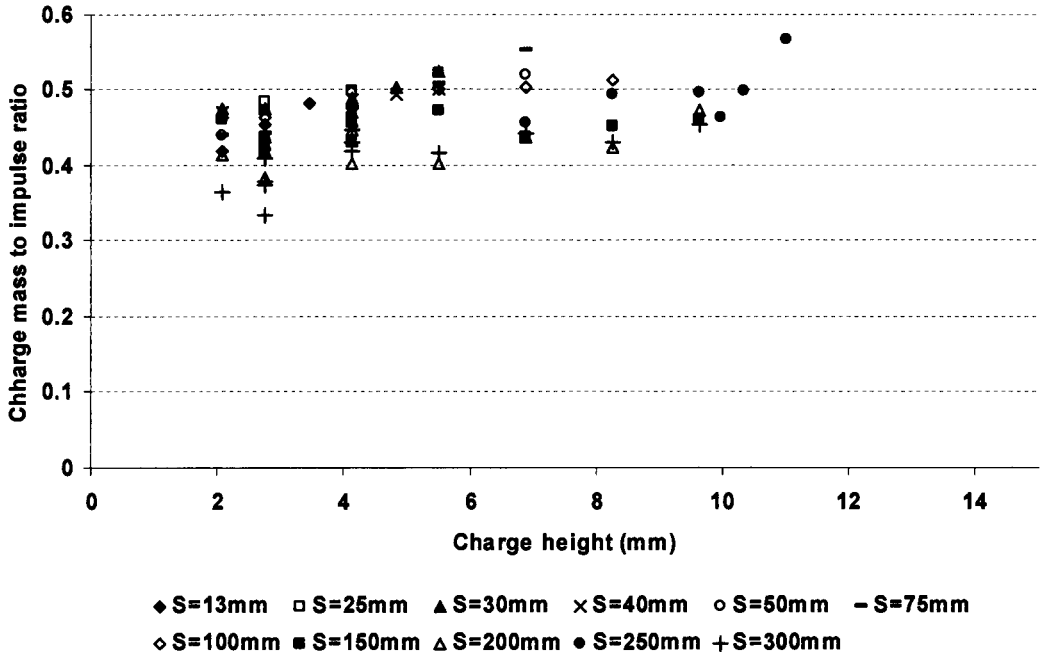

Figure 5.2: Graph of charge mass to impulse ratio versus charge height

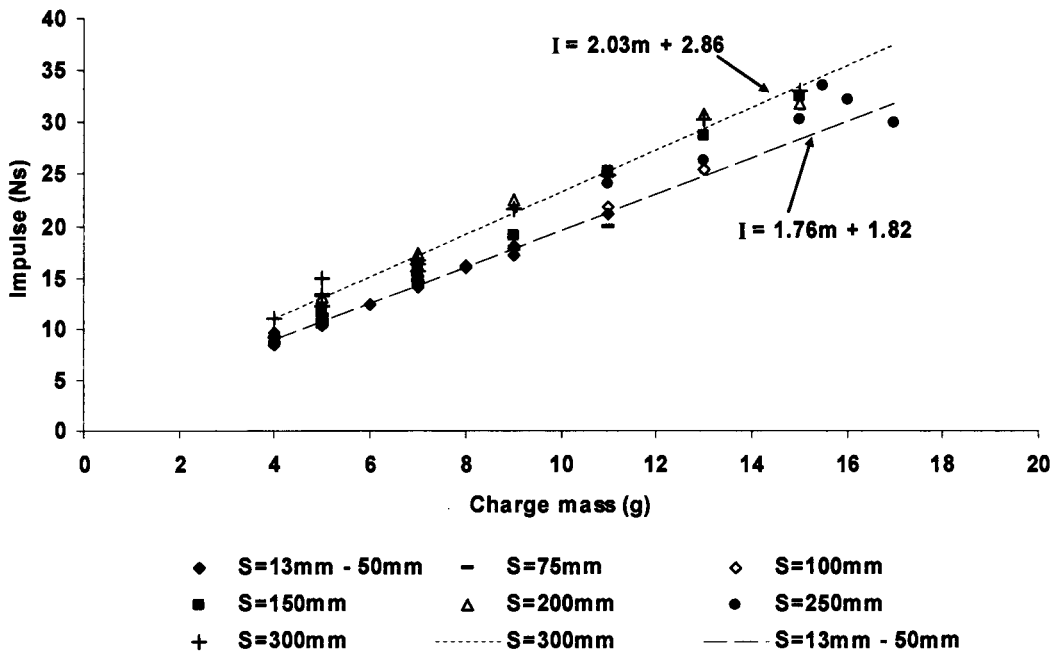

Figure 5.3: Graph of impulse versus charge mass showing the lower and upper bound in impulse due to the influence of stand-off distance

5.2 Relationship between impulse and stand-off distance

The impulses measured for a given charge mass at different stand-off distance ranging from 13mm to 300mm are shown in Figure 5.4. The data points show a gradual increase in impulse with increasing stand-off distance. The scatter in the experimental data is significantly greater for the larger charge masses 9g, 11g, 13g and 15g compared to the experimental data for charge masses 4g, 5g and 7g.

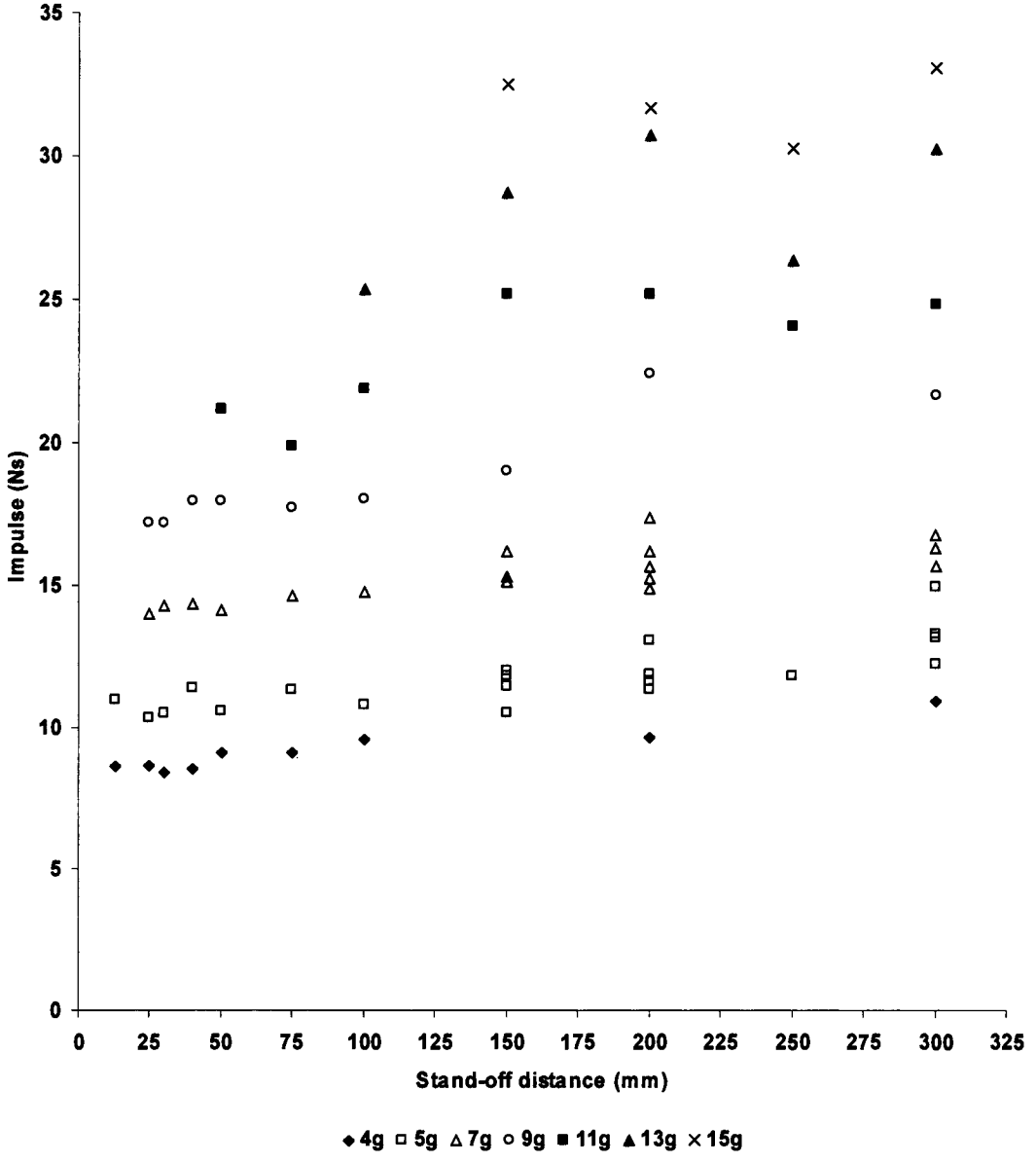

Figure 5.4: Graph of impulse versus stand-off distance for all charge masses

Best fit curves drawn through the data points for the different charge masses (4g, 5g, 7g, 9g, 11g, 13g and 15g) are shown in Figure 5.5 and Figure 5.6.

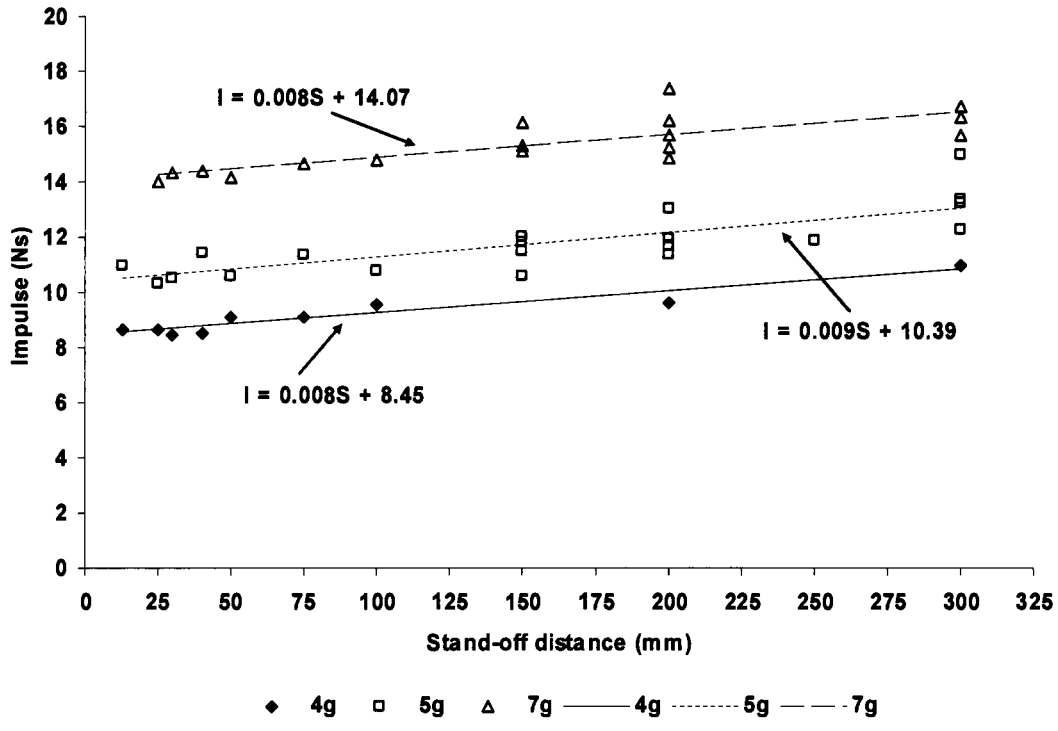

Figure 5.5: Graph of Impulse versus stand-off distance for charge masses 4g, 5g and 7g

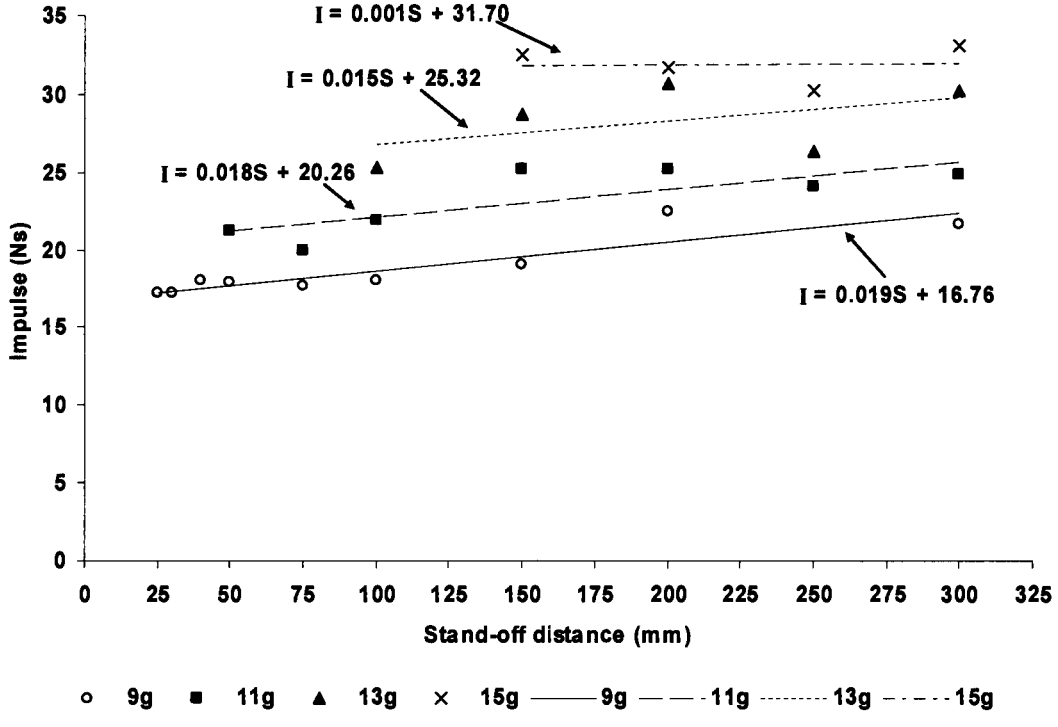

Figure 5.6: Graph of Impulse versus stand-off distance for charge masses 9g, 11g, 13g and 15g

The results show two groupings in terms of gradients of best fit curves shown in Figure 5.5 and Figure 5.6. Charge masses 4g, 5g, and 7g have comparable gradients of 0.008, 0.009 and 0.008 respectively. Whilst charge masses 9g, 11g and 13g have similar gradients of 0.019, 0.018 and 0.015. The difference in gradients of the two grouping indicates that the rate of increase in impulse with increasing stand-off distance is dependent on charge mass, with the charge masses 9g, 11g and 13g showing larger variation in impulse as compared to charge masses 4g, 5g, and 7g.

The gradual increase in impulse with increasing stand-off distance is illustrated by considering the equation of the best fit curve through the data points for charge mass 5g.

$$I = 0.009S + 10.39 \qquad \text{(eq. 5.1)}$$

The impulse calculated using equation (5.1) at stand-off distance of 13mm is equal to 10.51Ns (10.99Ns) (measured values in brackets). Similarly, at stand-off distance of 75mm, the impulse is equal to 11.06Ns (11.33Ns). The difference between the two calculated impulse values is a 5% increase at a stand-off distance of 75mm. In the case of stand-off distance 300mm, the impulse calculated using equation (5.1) is 13.09Ns (13.32Ns). The percentage increase in impulse from stand-off distance of 13mm to 300mm is equal to 20%.

The gradual increase in impulse for a given charge mass, as stand-off distance increases, is further illustrated by using the equations of the best fit curves shown in Figure 5.5 and Figure 5.6 to estimate the values of impulse (for charge masses 4g, 5g, 7g, 9g, 11g and 13g) at zero stand-off distance. This is done so as to establish a lower bound in impulse for any given charge mass with respect to stand-off distance. The calculated impulse values are plotted in the graph of impulse versus charge mass as shown in Figure 5.7. The results show an increase in impulse as stand-off distance increases for a given charge mass. The best fit curve through the data points for zero stand-off distance forms a lower bound, while the best fit curve through the data points for stand-off distance 300mm form an upper bound. The impulse values for stand-off distance ranging from 13mm to 250mm fall within the bounding best fit curves as shown in Figure 5.7.

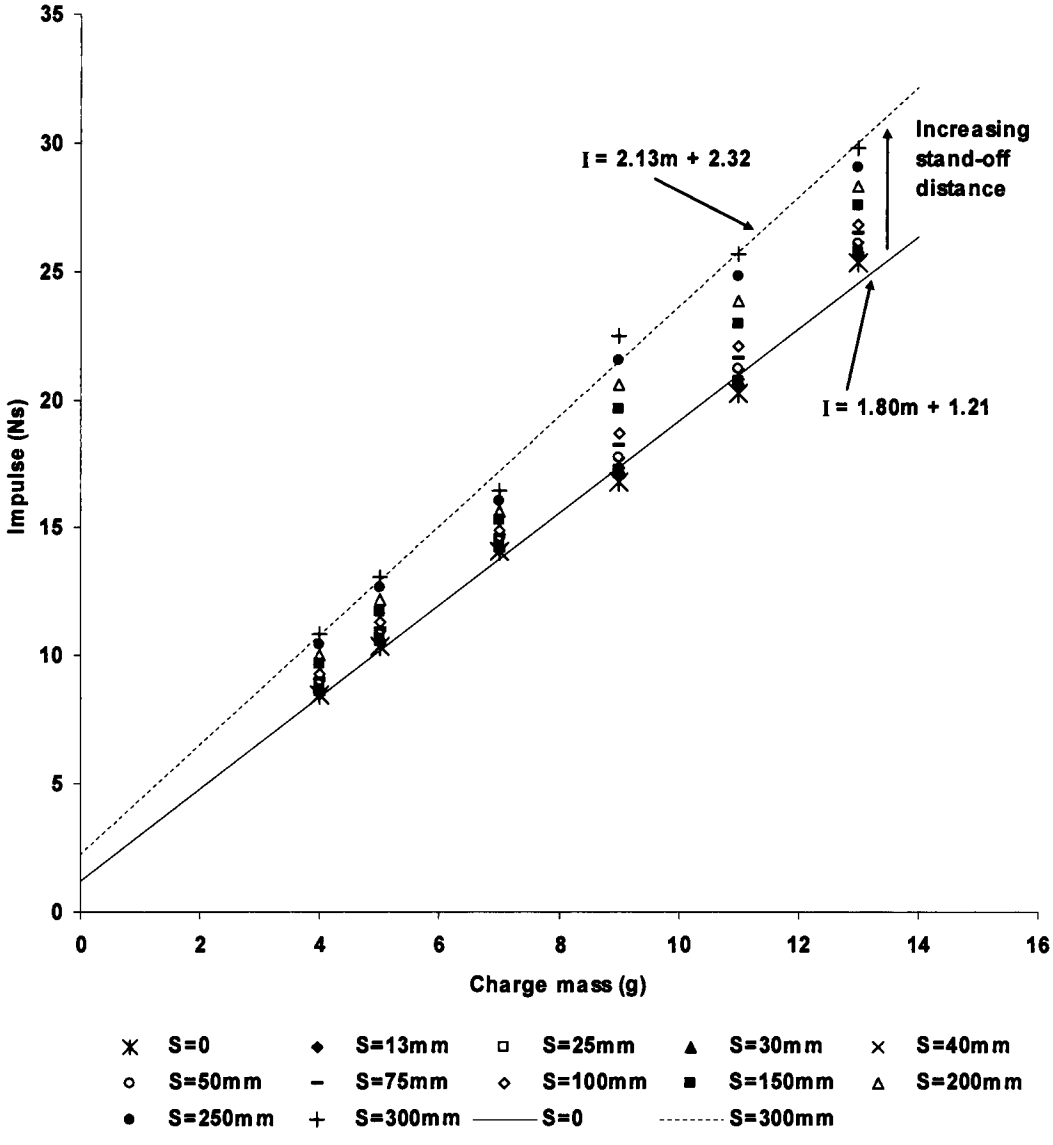

Figure 5.7: Graph of impulse versus charge mass for stand-off distances ranging from zero to 300mm calculated using the equations of the best fit curves shown in Figure 5.5 and Figure 5.6

The percentage increases in measured impulse from the closest stand-off distance to the furthest distance for different charge masses used is given in Table 5.1.

The confidence intervals of the best fit curves through the data points for charge masses 4g, 5g and 7g shown in Figure 5.5 indicate that measured impulses will be within ±0.50Ns, ±0.43Ns and ±0.38Ns respectively with 90% confidence. In the case of charge masses 9g, 11g, 13g and 15g the variation in impulse with changing stand-off distance is within ±1.19Ns, ±1.59, ±2.24 and ±1.42 of the best fit curves through the data points respectively (Figure 5.6) with a 90% confidence level.

Table 5.1: Statistical variation of impulse for different charge masses

Charge Mass (g)	Stand-off distance range	No of tests	90% confidence	Variation in impulse (Ns)		% difference
				Impulse at S=closest	Impulse at S=300mm	
4	13mm – 300mm	9	±0.50Ns	8.65	10.96	21
5	13mm – 300mm	21	±0.43Ns	10.99	14.95	27
7	25mm – 300mm	18	±0.38Ns	14.02	16.74	16
9	25mm – 300mm	9	±1.19Ns	17.20	21.63	21
11	50mm – 300mm	7	±1.59Ns	21.17	24.82	15
13	100mm – 300mm	5	±2.24Ns	25.36	30.24	16
15	150mm – 300mm	4	±1.42Ns	32.44	33.03	2

5.3 Relationship between mid-point deflection and stand-off distance

The measured mid-point deflection for a given charge mass decreases for increasing stand-off distance as shown in Figure 5.8. The trends observed from Figure 5.8 concur with information reported by Akus and Yildirim [11] for experiments on square plates subjected to blast loads at different stand-off distances and varying charge masses.

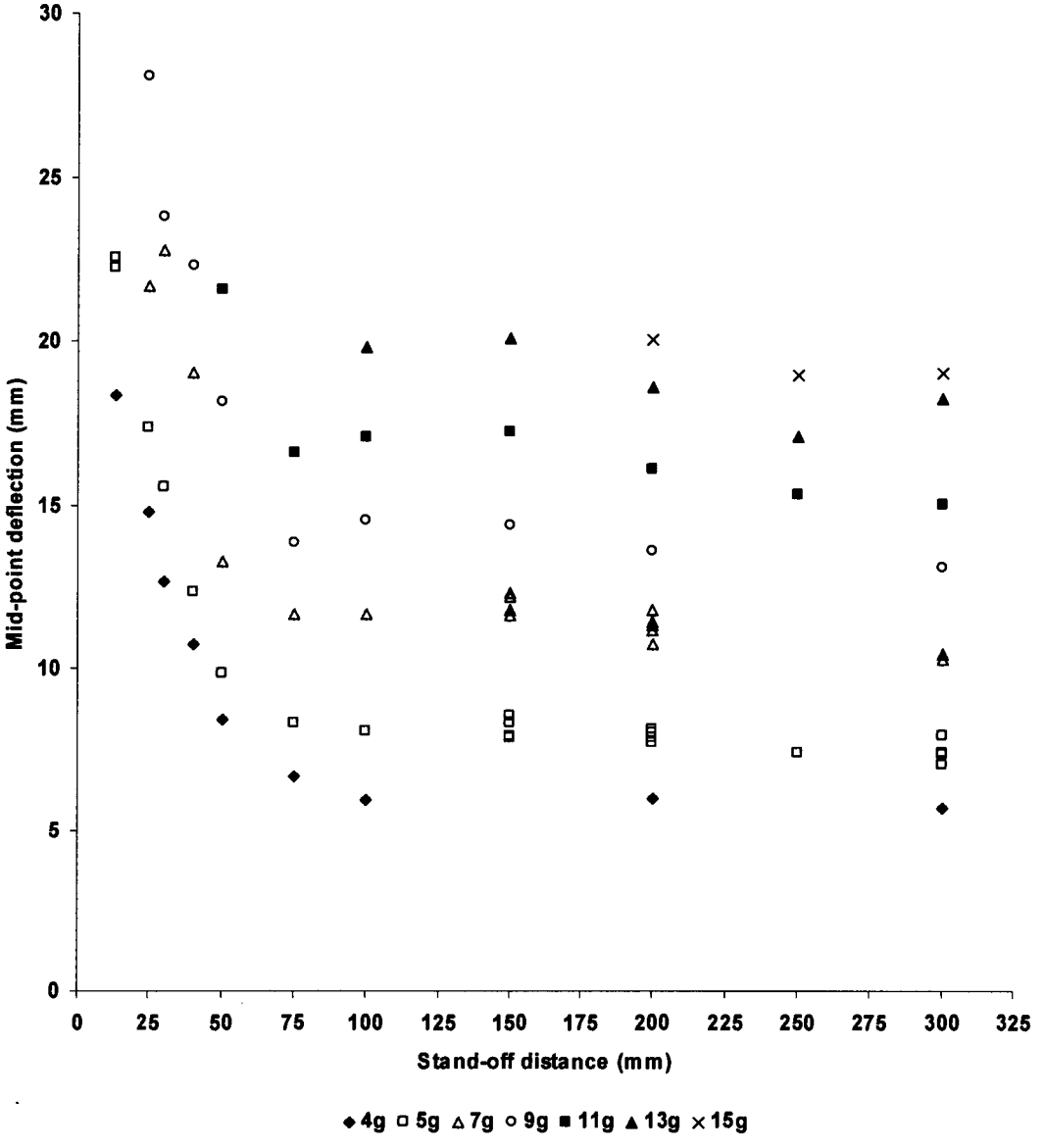

Figure 5.8: Graph of mid-point deflection versus stand-off distance

The results show a sharp decrease in mid-point deflection for stand-off distances ranging from 13mm to 50mm for a specific charge mass. The difference in mid-point deflection with respect to stand-off distance is given in Table 5.2 for charge masses 4g, 5g, 7g and 9g. The results illustrate increasing difference in mid-point deflection measured at stand-off distances of 25mm and 50mm for increasing charge mass. The percentage difference in mid-point deflection between stand-off distances 25mm and 50mm is 43%, 43%, 39% and 36% for charge masses 4g, 5g, 7g and 9g respectively. This means that mid-point deflection decreases by 57%, 57%, 61% and 64% for charge masses 4g, 5g, 7g and 9g respectively as stand-off distance is increased from 25mm to 50mm.

Alternatively, the results show that mid-point deflection increases rapidly with decreasing stand-off distance ranging from 50mm to 13mm and increasing charge mass.

Table 5.2: Variation in measured mid-point deflection for stand-off distance ranging from 25mm to 50mm for different charge masses

Charge Mass (g)	Range of stand-off distance (mm)	Range of mid-point deflection (mm)		Difference in mid-point deflection (mm)	% difference in mid-point deflection
		S=25mm	S=50mm	(S=25mm - S=50mm)	
4	25 - 50	14.78	8.39	6.39	43
5	25 - 50	17.34	9.84	7.50	43
7	25 - 50	21.67	13.26	8.41	39
9	25 - 50	28.10	18.12	9.98	36

The mid-point deflections are similar in magnitude for stand-off distances ranging from 75mm to 300mm. The maximum and minimum mid-point deflection for different charge mass for stand-off distances ranging from 75mm – 300mm is given in Table 5.3. The confidence intervals of the data points for charge masses 4g, 5g, 7g, 9g, 11g, 13g and 15g for stand-off range of 75mm to 300mm is presented in Table 5.3. The results show that there is a 90% probability that the mid-point deflection will be within approximately ±1mm of the best fit curves through the data points as shown in Figure 5.9. Nevertheless, the mid-point deflection decreases gradually with increasing stand-off distance as indicated by the gradients of the best fit curves. The decrease in mid-point deflection is least evident for charge mass 4g, as indicated by the magnitude of the gradient of the best fit curve of -0.003. Whilst, for charge mass of 15g the magnitude of the gradient of the best fit curve of -0.01, indicates that mid-

point deflection asymptotes earlier for the smaller charge masses compared to larger charge masses.

Table 5.3: Variation in measured mid-point deflection for stand-off distance ranging from 75mm to 300mm for different charge masses

Charge Mass (g)	No. data points	Range of stand-off distance (mm)	90% confidence level	Range of mid-point deflection (mm)		Difference in mid-point deflection (mm)	% difference in mid-point deflection
			(mm)	max	min	(max - min)	
4	4	75 - 300	±0.50	6.65	5.66	0.99	15
5	15	75 - 300	±0.19	8.50	7.01	1.49	18
7	14	75 - 300	±0.31	12.28	10.27	2.01	16
9	5	75 - 300	±0.56	14.48	13.06	1.42	10
11	6	75 - 300	±0.75	17.18	14.97	2.21	13
13	5	100 - 300	±1.18	20.05	17.03	3.02	15
15	3	200 - 300	±1.03	20.01	18.92	1.09	6

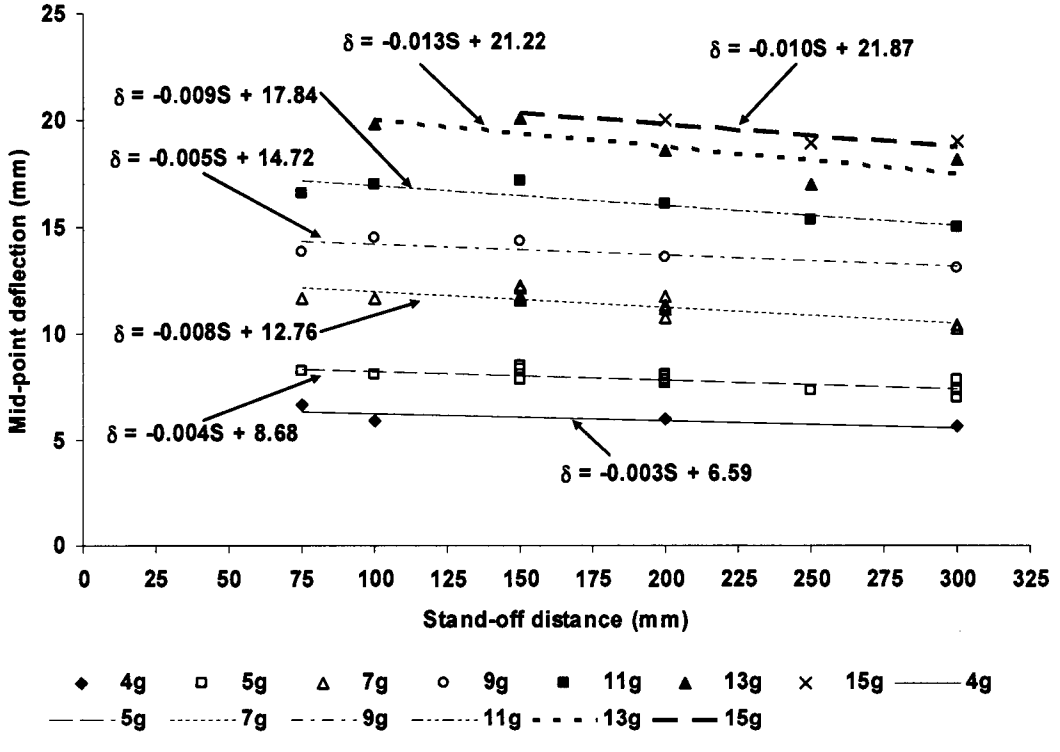

Figure 5.9: Graph of mid-point deflection versus stand-off distance, for charge masses 4g, 5g, 7g, 9g, 11g, 13g and 15g, and stand-off distance ranging from 75mm to 300mm

The experimental data shown in Figure 5.9 plotted in terms of mid-point deflection – thickness ratio and stand-off distance is shown in Figure 5.10. Analyses of the data points show that the variation of mid-point deflection – thickness ratio is within ±1 mid-point deflection – thickness ratio of the best fit curves through the data points

with 90% confidence level. The statistical variation in mid-point deflection - thickness ratio for different charge masses is given in Table 5.4 for stand-off distance ranging from 75mm to 300mm.

Table 5.4: Variation in mid-point deflection – thickness ratio for different charge masses at stand-off distances ranging from 75mm to 300mm with 90% confidence level

Charge mass (g)	Stand-off distance range (mm)	Variation in mid-point – thickness ratio
4	75 - 300	±0.26
5	75 - 300	±0.10
7	75 - 300	±0.16
9	75 - 300	±0.29
11	75 - 300	±0.39
13	75 - 300	±0.62
15	75 - 300	±0.54

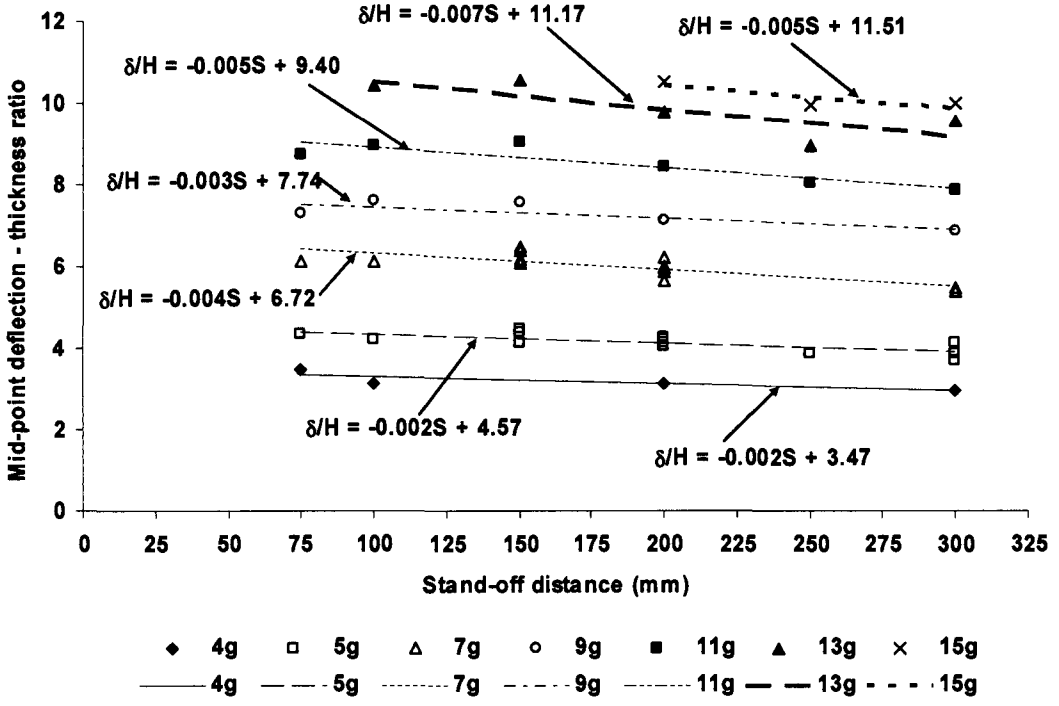

Figure 5.10: Graph of mid-point deflection – thickness ratio versus stand-off distance, for charge masses 4g, 5g, 7g, 9g, 11g, 13g and 15g, and stand-off distance ranging from 75mm to 300mm

5.4 Relationship between stand-off distance and loading condition

The distinction between the two loading conditions (namely, localised and uniform) is in accordance with the guide reported by Marchand and Alfawakhiri [33]. They propose that the loading can be assumed to be uniformly distributed over the structure if the stand-off distance is greater than one-half of the largest dimension of the structure. In the experiments described herein the plate diameter is the largest dimension. Hence uniform loading conditions should occur for stand-off distances greater than the half plate diameter (53mm). This is confirmed by the observation of large global dome for stand-off distance ranging from 100mm to 300mm as shown in Figure 5.11 to Figure 5.13. This form of deformation has been reported by Nurick et al [3, 5, 9] for uniformly loaded plates using concentric rings of explosive.

In the case of closer stand-off distances ranging from 13mm to 40mm the plate profiles show an inner dome atop a larger global dome as shown in Figure 5.11 to Figure 5.13. This concurs with similar observations reported by Nurick et al [6 - 8] for circular and quadrangular plates subjected to localised blast loads. The other notable feature observed that is unique to localised loading is burn diameter. This feature has been reported for localised loading of circular and quadrangular plates by Nurick et al [6 - 8]. This phenomenon has not been reported for uniform loading.

At stand-off distances of 50mm and 75mm the plate profile exhibits a transition phase between uniform and localised loading. The plate response at these stand-off distances exhibit aspects of localised and uniform loading. The plate profiles show a large global dome similar to that observed for stand-off distance ranging from 100mm to 300mm. However, the top of the dome is "flatter" than that observed at the larger stand-off distances as shown in Figure 5.11 and Figure 5.12 for charge masses 5g and 7g respectively. The profiles also show increased deformation on the plate closer towards the boundary similar to that observed at the stand-off distances ranging from 13mm to 40mm. Burn diameters are also observed on the loaded side of the plate for stand-off distance 50mm and 75mm

It should be noted that for charge mass 9g the plate profile at stand-off distance of 50mm show the emergence of an inner dome as shown in Figure 5.13 along with increased deformation closer to the boundary. At stand-off distance of 75mm the plate profile exhibits a "flatter" global dome with increased deformation closer to the boundary similar to that observed for charge masses 5g and 7g.

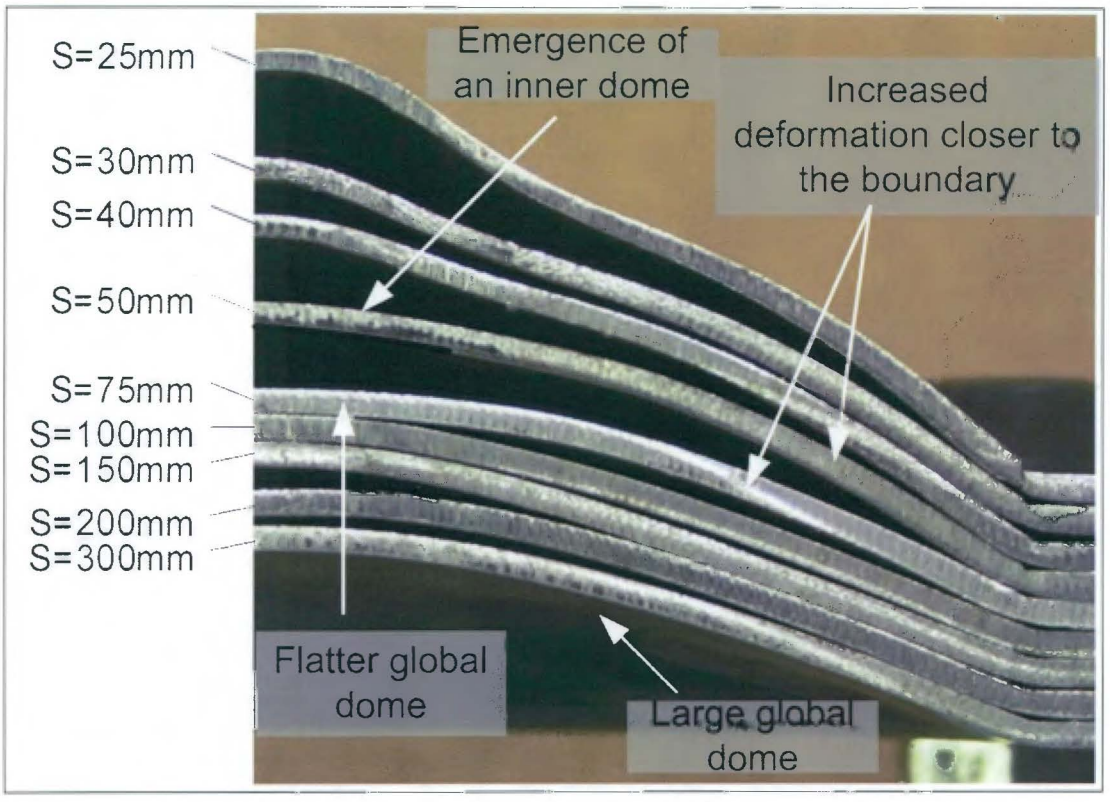

Figure 5.13: Photograph of plate profiles at different stand-off distances for charge mass 9g

The above mentioned observations indicate that classification of localised and uniform loading conditions is a function of stand-off distance and charge mass.

In other words, the emergence of a "flatter" global dome in conjunction with increased deformation closer to the boundary as well as the appearance of the burn diameter mark the transition to localised loading as the charge is moved nearer to the plate for a given charge mass.

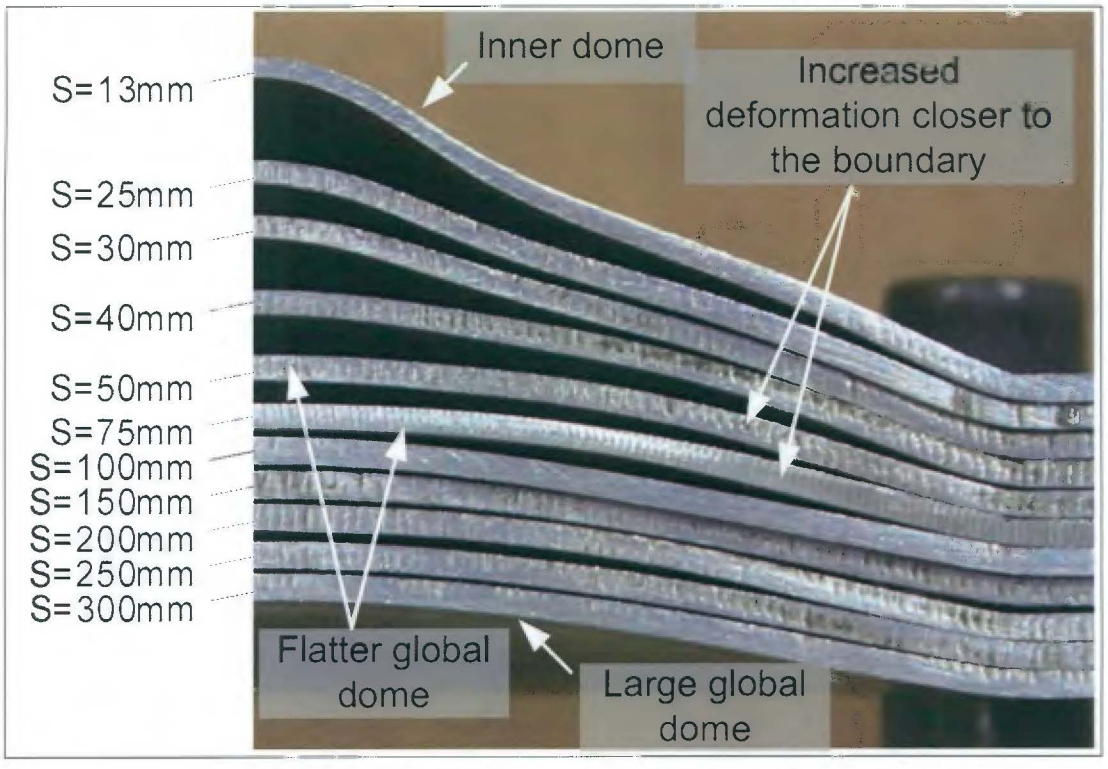

Figure 5.11: Photograph of plate profiles at different stand-off distances for charge mass 5g

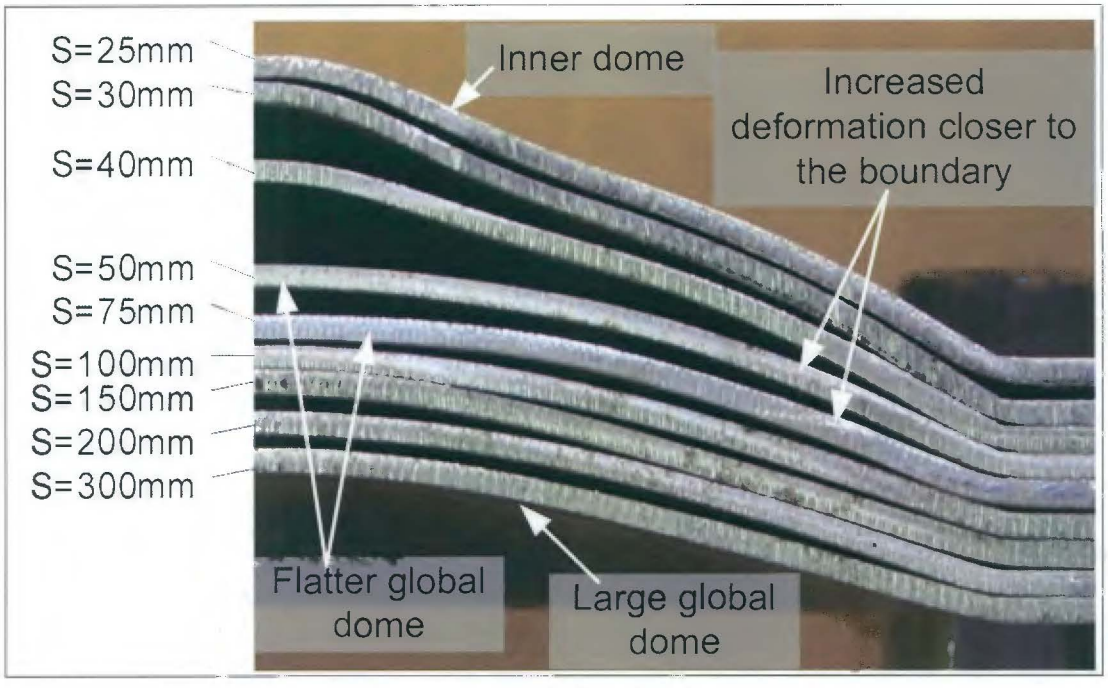

Figure 5.12: Photograph of plate profiles at different stand-off distances for charge mass 7g

5.5 Relationship between plate mid-point deflection and impulse

The mid-point deflection increases with increasing charge mass for a given stand-off distance as shown in Figure 5.14. The trends show increasing mid-point deflection for a given charge mass as it is moved closer to the test plate. The results indicate that for the larger stand-off distances (75mm to 300mm) the mid-point deflection does not vary appreciably for a specific charge mass as shown by the grouping of data points as compared to significant increase in mid-point deflection for stand-off distances ranging from (13mm to 50mm) This behaviour concurs with results reported by Akus and Yildirim [11] for square plates subjected to blast loads of varying charge masses and stand-off distances.

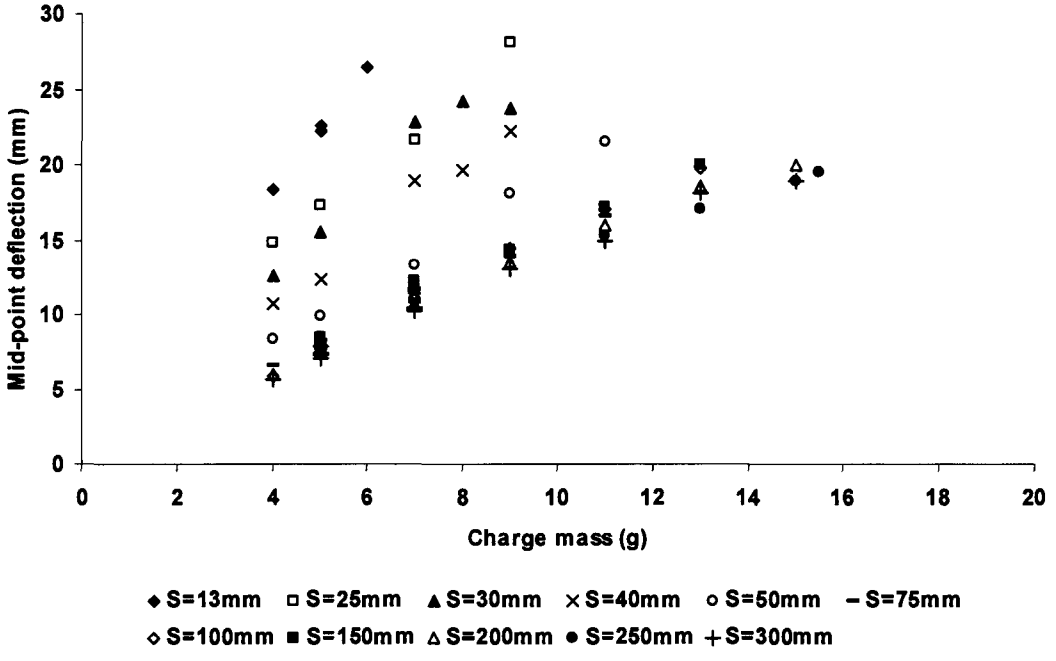

Figure 5.14: Graph of mid-point deflection versus charge mass for different stand-off distances

The graph of impulse versus mid-point deflection for different stand-off distances shows similar trends as shown in Figure 5.15. The results indicate a steep rise in mid-point deflection at stand-off distance of 13mm for increasing impulse. The mid-point deflections for subsequent stand-off distances ranging from 25mm to 300mm become progressively less pronounced for increasing impulse.

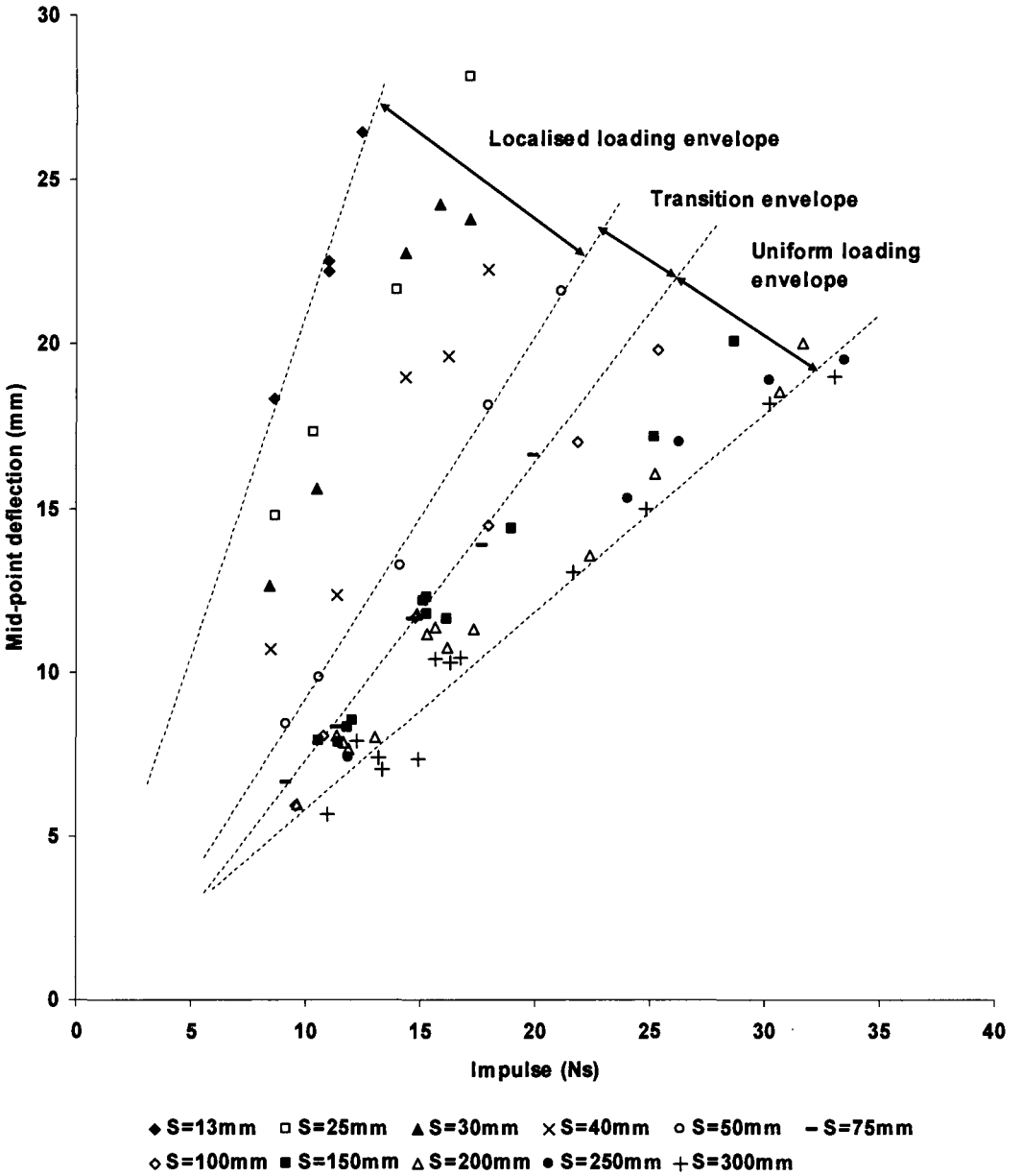

Figure 5.15: Graph of mid-point deflection versus impulse for different stand-off distances

The data plotted in Figure 5.15 show a bounding envelope formed by stand-off distance range of 13mm to 50mm. The loading within this region is said to be localised with plate deformations showing an inner dome atop a global dome as show in Figure 5.11 – Figure 5.13 in Section 5.4. The stand-off distance of 50mm forms the lower bound of localised loading. A transition envelope bounded by stand-off distances 50mm and 75mm describe a range where plate deformation exhibit aspects of both localised and uniform loading, namely large global dome associated with uniform loading and increased deformation closer to the plate boundary as well as burn diameter, both of which are associated with localised loading. The loading condition within the envelope bounded by stand-off distances 75mm and 300mm is said to be uniform loading. The plate deformation observed within this range is that of large global dome as shown in Figure 5.11 – Figure 5.13 in Section 5.4. The stand-off distance of 75mm forms the upper bound of uniform loading envelope before the onset of localised loading as the charge is moved closer to the plate.

The graph of mid-point deflection versus impulse for the different charge masses is shown in Figure 5.16. The data points for charge masses 4g, 5g, 7g and 9g that fall within the localised loading envelope show steep decrease in mid-point deflection with increasing stand-off distance for a given charge mass. The data points for the same charge masses that fall within the uniform loading envelope show that mid-point deflection are similar but the corresponding impulses increases. The trends observed in Figure 5.16 show that similar impulse is measured for stand-off distances ranging from 13mm to 50mm whilst a gradual increase is evident for stand-off distances between 75mm and 300mm along with decreasing mid-point deflection.

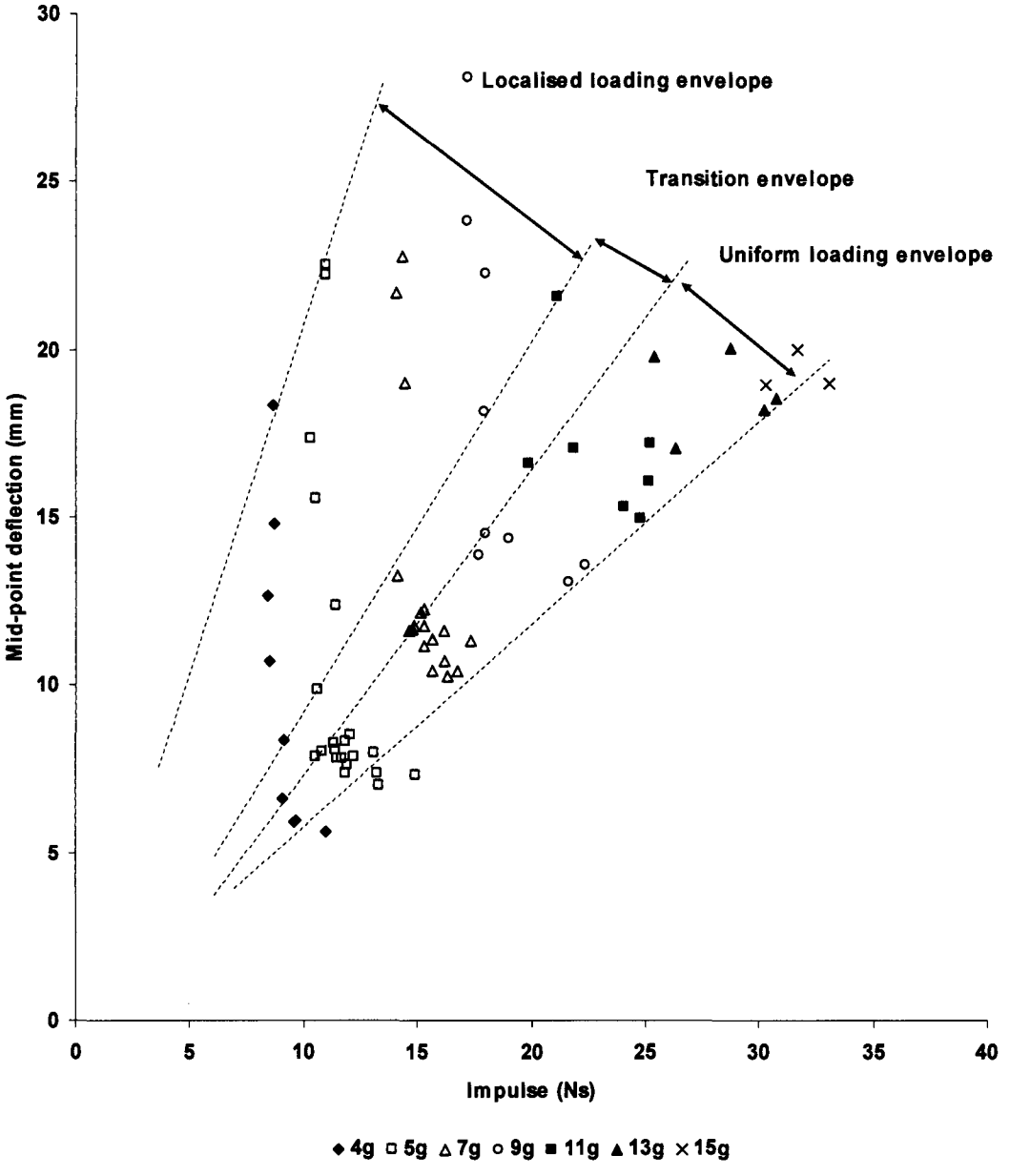

Figure 5.16: Graph of mid-point deflection versus impulse for different charge masses

The data points bounded within the uniform loading envelope as shown in Figure 5.15 for stand-off distances ranging from 75mm to 300m are shown in Figure 5.17. The results show that within this loading envelope there is a distinction with respect to stand-off distance illustrated by the changing gradient of the best fit curves through the data points. The gradients for stand-off distances 200mm, 250mm and 300mm are the same with a value close to 0.60. The implication being, for a given charge mass, similar plate responses can be expected for stand-off distances greater than 200mm. However, for stand-off distances 75mm, 100mm and 150mm the values of gradients are 0.91, 0.85 and 0.67 respectively. The decreasing gradient with increasing stand-off distance is further evidence that plate mid-point deflection is sensitive to position of the charge with respect to the test plate.

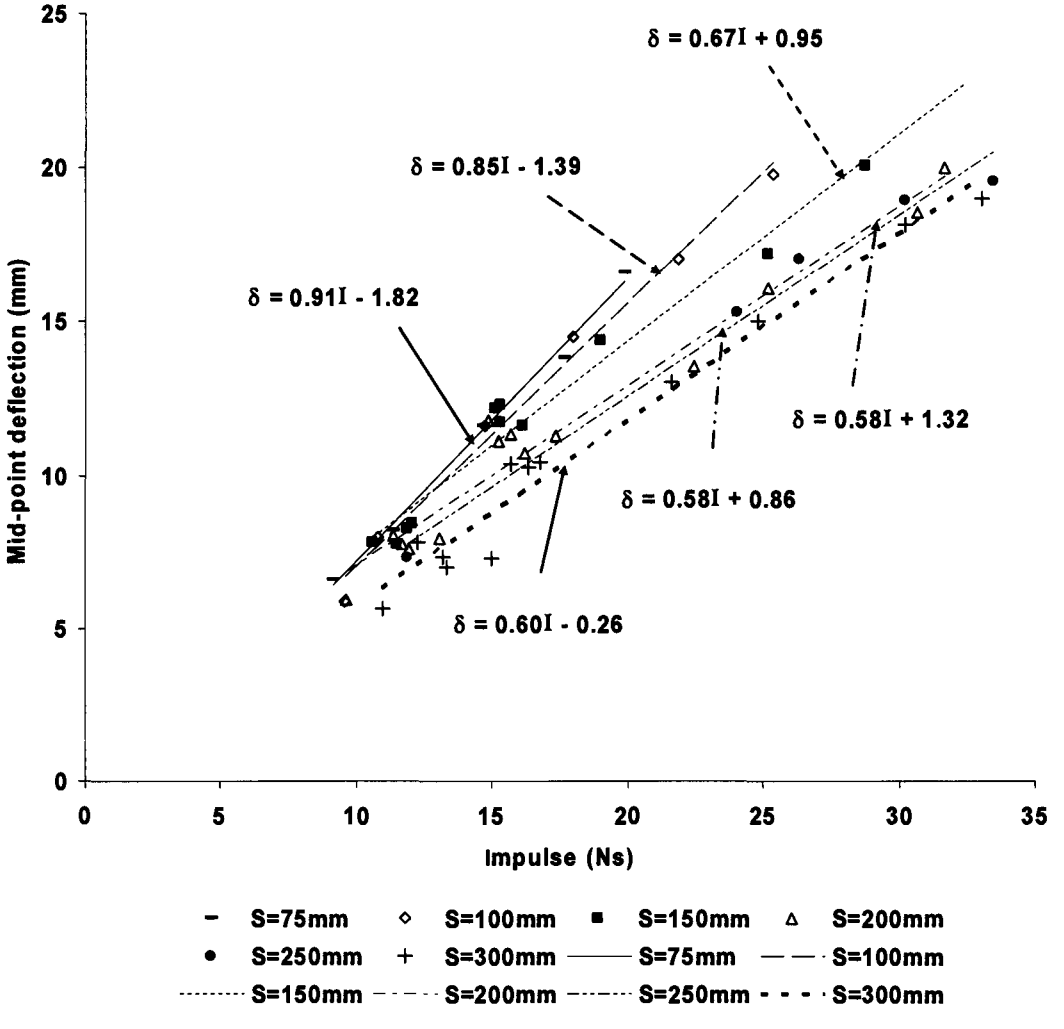

Figure 5.17: Graph of mid-point deflection versus impulse for stand-off distances ranging from 75mm to 300mm

The data points bounded within the localised loading envelope as shown in Figure 5.15 for stand-off distances ranging from 13mm to 50mm are shown in Figure 5.18. The gradients of the best fit curves through the data points show considerable variation with respect to stand-off distance. The gradient of the best fit curves have values of 2.08, 1.52, 1.41, 1.29 and 1.12 for stand-off distances 13mm, 25mm, 30mm, 40mm and 50mm respectively. The variation in values of the gradients for stand-off distances of 13mm and 50mm is approximately a factor of 2. This means that for a charge mass of 5g the mid-point deflection at 13mm will be approximately twice that at 50mm. For example, the mid-point deflection for a charge mass of 5g at stand-off distance of 13mm is 22.21mm for test number NJ180405a and the corresponding mid-point deflection at stand-off distance of 50mm is 9.84mm for test number NJ090405a. Similarly, the variation of gradients between stand-off distances of 13mm and 300mm is approximately a factor of 3. The mid-point deflection for charge mass 5g at stand-off distance 300mm is 7.01mm for test number NJ210405a which is approximately three time lower than the mid-point deflection measured at stand-off distance of 13mm.

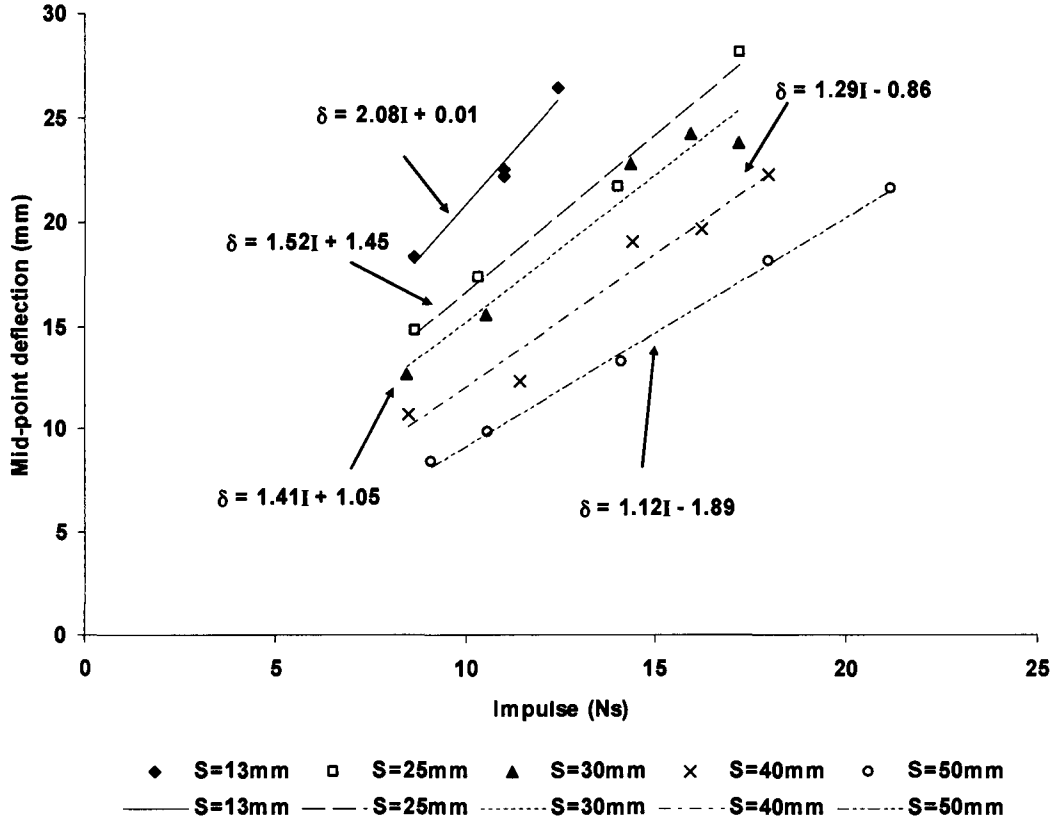

Figure 5.18: Graph of mid-point deflection versus Impulse for stand-off distances ranging from 13mm to 50mm

5.6 Effect of polystyrene on impulse and mid-point deflection

The effect of using polystyrene pads as a method of securing the plastic explosive and preventing spalling of the test specimens is reported in this section.
Details of the different loading conditions used are explained in detail in Section 3.3. The results indicate negligible influence on impulse and plate mid-point deflection. Two charge masses were used on three stand-off distances (150mm, 200mm and 300mm). The experimental results form the tests for the different loading conditions are given in Table 5.5.

The data given Table 5.5 are plotted in the graph of mid-point deflection – thickness ratio versus dimensionless impulse ϕ_{cs} as shown in Figure 5.19. The results show variation in mid-point deflection is less than ±1 deflection – thickness ratio and all the data points fall within the ±1 confidence lines of the empirical prediction equation (2.55).
***Note**: derivation of dimensionless impulse ϕ_{cs} is discussed in detail in Section 5.8.1.1.*

The measured impulses for loading conditions LC-1, LC-2 and LC-3, in general, show less than 5% variation on the average impulse value for a given charge mass and stand-off distance. The impulse measured for test number NJ230405c shows the largest variation from the average impulse value for that particular charge mass and stand-off distance. The variation in measured impulse (10.56Ns) from the average impulse value of 11.35Ns is 7%. This translates to a difference in impulse of 0.8Ns from the average impulse value.

Table 5.5: Experimental data for investigation into the influence of polystyrene as a stand-off buffer

Test number	Loading condition	Charge mass (g)	Stand-off distance (mm)	Impulse (Ns)	% variation in impulse from average	Mid-point deflection (mm)	% variation in mid-point deflection from average
NJ230405a	LC-1	5	150	11.47	1.0	7.83	3.0
NJ230405b	LC-2	5	150	12.03	6.0	8.50	5.4
NJ230405c	LC-3	5	150	10.56	7.0	7.87	2.4
			Average	**11.35**	**Average**	**8.07**	
NJ230405d	LC-1	7	150	15.30	0.4	11.76	2.6
NJ230405e	LC-2	7	150	15.11	0.8	12.18	0.9
NJ230405f	LC-3	7	150	15.30	0.4	12.28	1.7
			Average	**15.24**	**Average**	**12.07**	
NJ220405a	LC-1	5	200	11.91	2.2	7.65	2.5
NJ220405b	LC-2	5	200	11.67	0.1	7.82	0.3
NJ220405d	LC-3	5	200	11.38	2.3	8.07	2.8
			Average	**11.65**	**Average**	**7.85**	
NJ220405c	LC-1	7	200	16.18	3.1	10.72	3.2
NJ220405e	LC-2	7	200	15.66	0.3	11.38	2.7
NJ220405f	LC-3	7	200	15.26	2.8	11.14	0.6
			Average	**15.70**	**Average**	**11.08**	
NJ210405a	LC-1	5	300	13.32	3.1	7.01	5.6
NJ210405b	LC-2	5	300	13.20	2.2	7.38	0.5
NJ210405c	LC-3	5	300	12.24	5.3	7.87	6.1
			Average	**12.92**	**Average**	**7.42**	
NJ210405d	LC-1	7	300	16.74	3.1	10.43	0.6
NJ210405e	LC-2	7	300	16.30	0.4	10.27	0.9
NJ210405f	LC-3	7	300	15.65	3.6	10.41	0.4
			Average	**16.23**	**Average**	**10.37**	

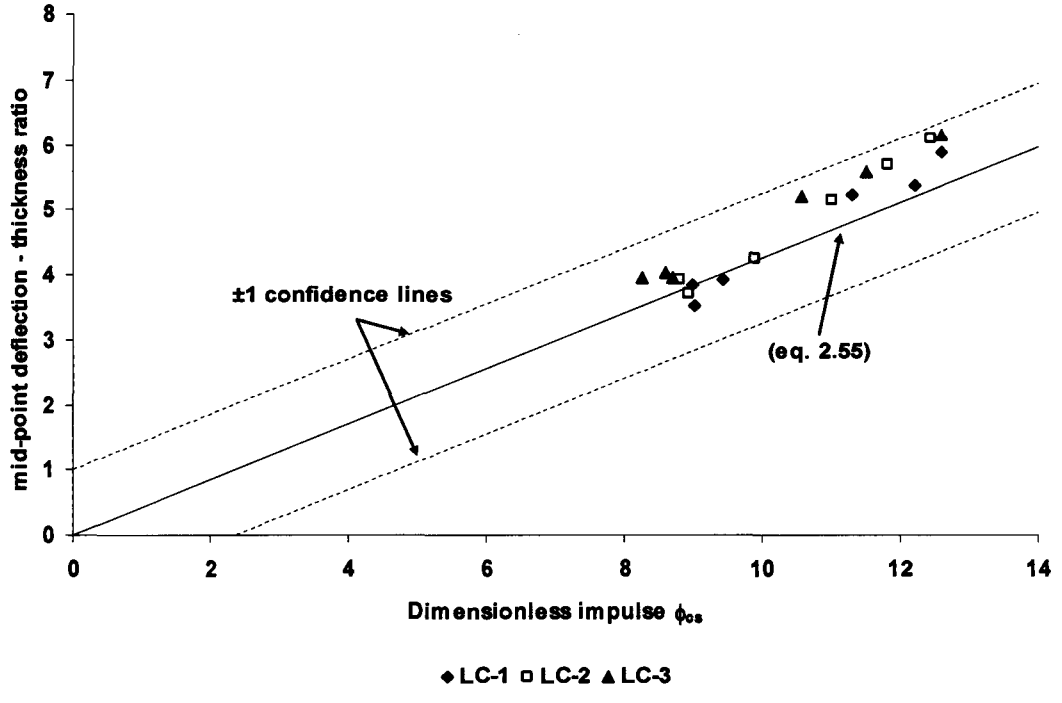

Figure 5.19: Graph of mid-point deflection - thickness ratio versus dimensionless impulse ϕ_{cs} for data given in Table 5.5

5.7 Relationship between stand-off distance and burn diameter

The circular discolouration observed on the loaded side of a test plate, as discussed in Section 4.3, is referred to as the burn diameter. This phenomenon is observed at stand-off distances ranging from 13mm to 75mm as shown in Figure 5.20 and Figure 5.21. The burn diameter is well defined for stand-off distances 13mm, 25mm, 30mm and 40mm. However at stand-off distances of 50mm and 75mm the burn diameter begins to blur around the edges and loses its form. For stand-off distances greater than 75mm (100mm – 300mm) the burn diameter is no longer visually discernable as the plate is covered with an even coating of black soot. The burn diameter is also not visible after removing the black soot.

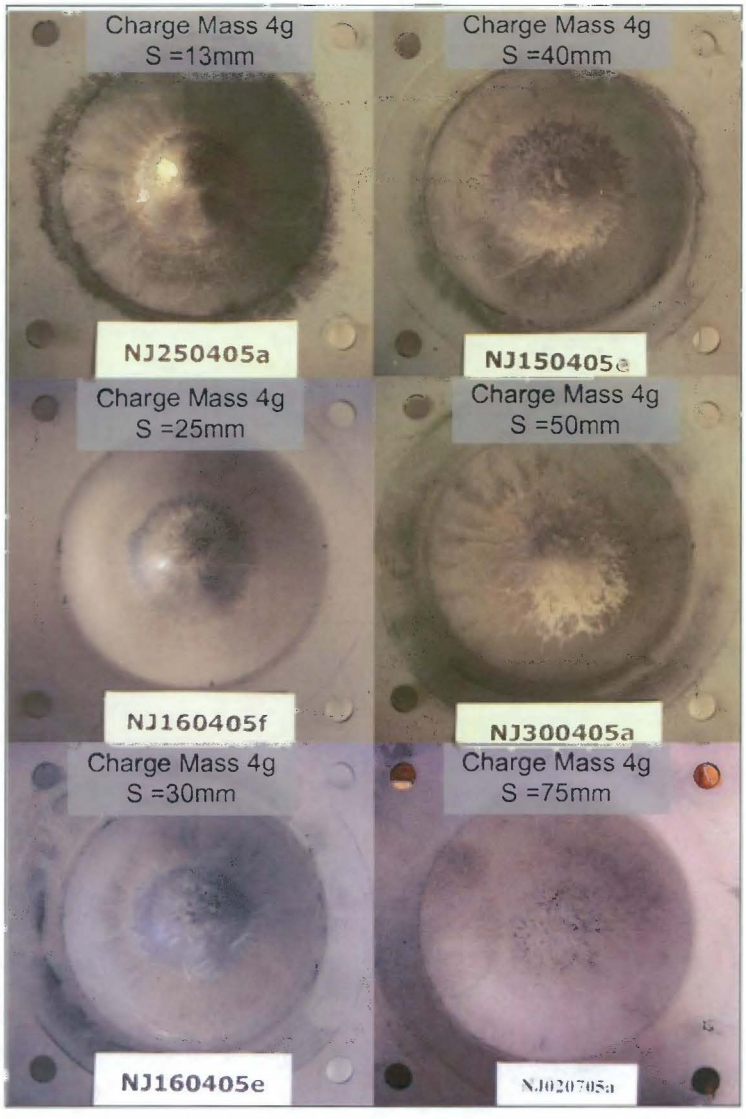

Figure 5.20: Photograph of burn diameters for charge mass 4g at different stand-off distances ranging from 13mm to 75mm
(Plate number: NJ250405a, NJ160405f, NJ160405e, NJ150405e, NJ300405a, NJ020705a)

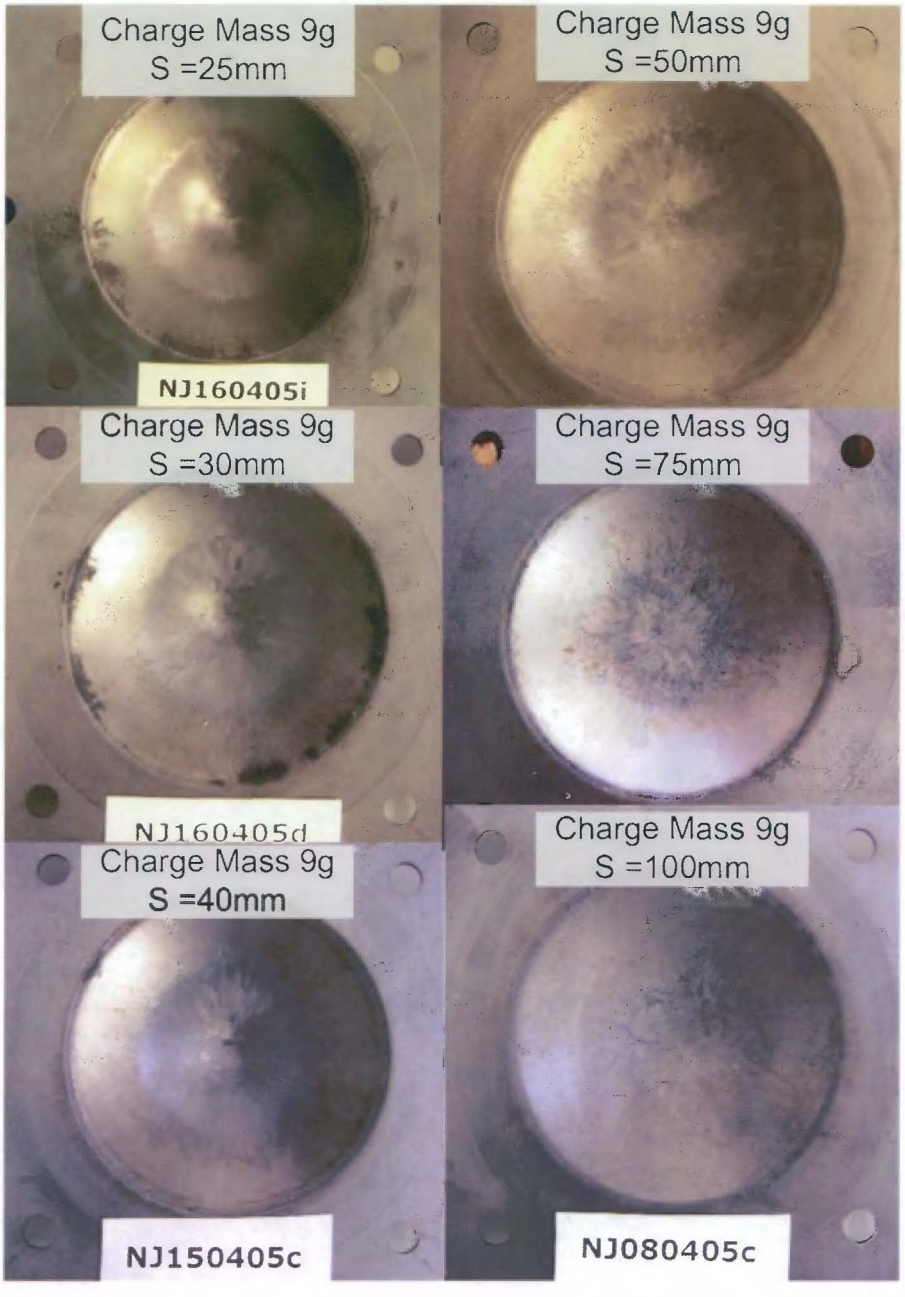

Figure 5.21: Photograph of burn diameters for charge mass 9g at different stand-off distances ranging from 25mm to 100mm
(Plate number: NJ160405i, NJ160405d, NJ150405c, NJ090405c, NJ040705a)

The burn diameter increases with increasing stand-off distance ranging from 13mm to 50mm. At stand-off distance of 75mm the burn diameter loses its form as mentioned earlier and it becomes difficult to judge its boundary. Hence the burn diameter at stand-off distance 75mm is not measured. The graph of burn diameter versus stand-off distance is shown in Figure 5.22. The results show that burn diameter is always larger than charge diameter.

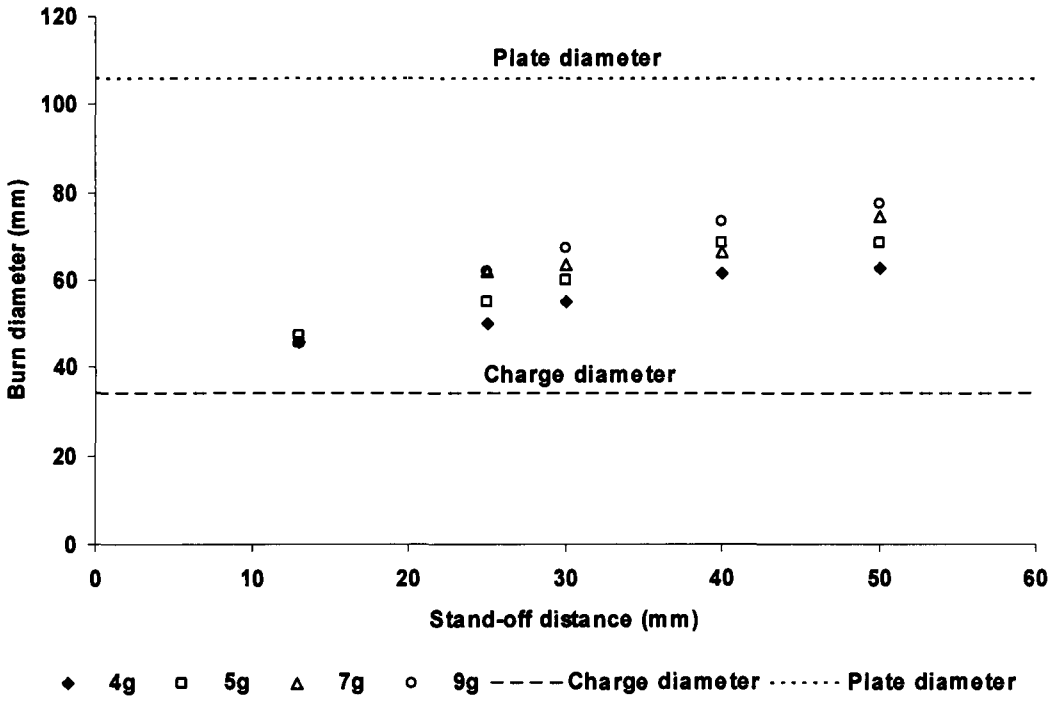

Figure 5.22: Graph of burn radius versus stand-off distance

5.8 Theoretical analysis

Empirical and theoretical analysis is carried out in this section. Empirical analysis using dimensionless impulse parameter developed by Nurick and Martin [2] is reported. Analytical predictions are provided using Jones damage number [34]. Strain energy analysis using methodology presented by Ezra [35] and Duffey [36].

5.8.1 Nurick and Martin dimensionless impulse, ϕ_c

Nurick and Martin [2] proposed a dimensionless impulse parameter ϕ_c and an empirical equation (2.55) for predicting large inelastic deformation (Mode I) of fully clamped circular plate subjected to blast loads. The dimensionless impulse parameter ϕ_c (equation (2.50a)) is implemented for case where the blast load is applied over the entire plate area. Equation (2.50b) is implemented for cases where the blast load is focused and the plate is said to be subjected to localised loading.

$$\phi_c = \frac{I}{\pi R H^2 (\rho\sigma_0)^{1/2}} \quad \text{(Uniform loading)} \qquad \text{(Recall eq. 2.50a)}$$

$$\phi_c = \frac{I\left(1+\ln\frac{R}{R_0}\right)}{\pi R H^2 (\rho\sigma_0)^{1/2}} \quad \text{(Localised loading)} \qquad \text{(Recall eq. 2.50b)}$$

The dimensionless impulse parameter ϕ_c (eq. 2.50a) plotted in Figure 5.23 is implemented under the assumption of uniform load distribution over the entire plate for all stand-off distance. The empirical relationship proposed by Nurick and Martin [2] (equation (2.55)) to predict mid-point deflection is represented by the solid line in Figure 5.23.

$$\frac{\delta}{H} = 0.425\phi_c \qquad \text{(Recall eq. 2.55)}$$

The data points for stand-off distances 13mm to 40mm fall above the empirical line, whilst for stand-off distances between 75mm to 300mm fall below. At stand-off distance of 50mm the data points fall within the ±1 mid-point deflection – thickness ratio confidence lines.

The graph of mid-point deflection – thickness ratio versus dimensionless impulse parameter ϕ_c (eq. 2.50a) as shown in Figure 5.23 illustrates the influence of stand-off distance on plate deformation.

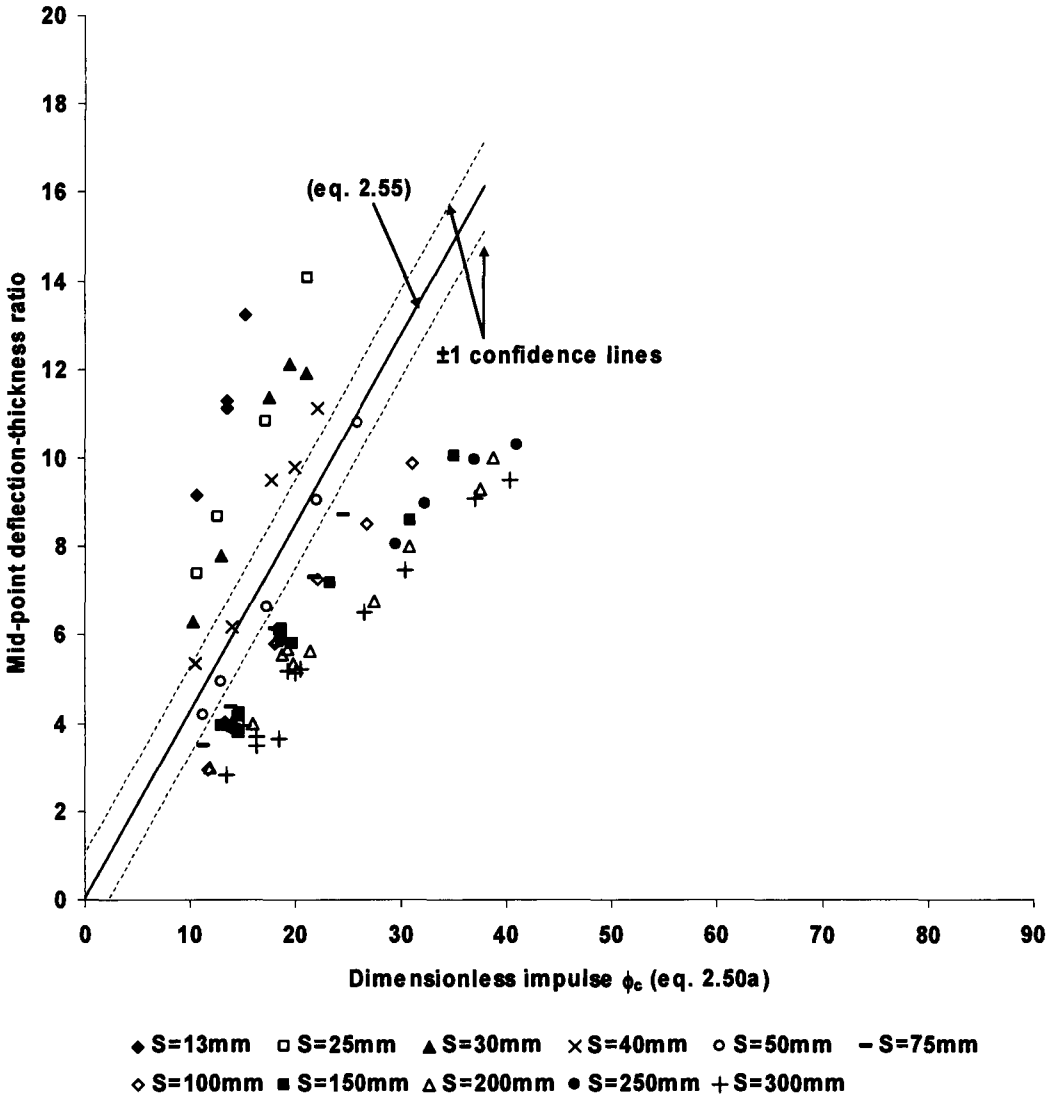

Figure 5.23: Graph of mid-point deflection – thickness ratio versus dimensionless impulse ϕ_c (eq. 2.50a) - assuming uniform loading

In the case of assuming localised loading for all stand-off distances, the graph of mid-point deflection – thickness ratio versus dimensionless impulse ϕ_c (eq. 2.50b) show data points for stand-off distances ranging from 25mm to 300mm falling below the empirical relationship proposed by Nurick and Martin [2] , as shown in Figure 5.24. The data points for stand-off distance 13mm, (LC-4, as shown in Figure 3.15), fall within the ±1 confidence lines. This behaviour is a validation of the current series of experiments as the data correlates with published experimental results reported by Nurick et al [6, 7] for localised blast loading of circular plates using loading condition LC-4.

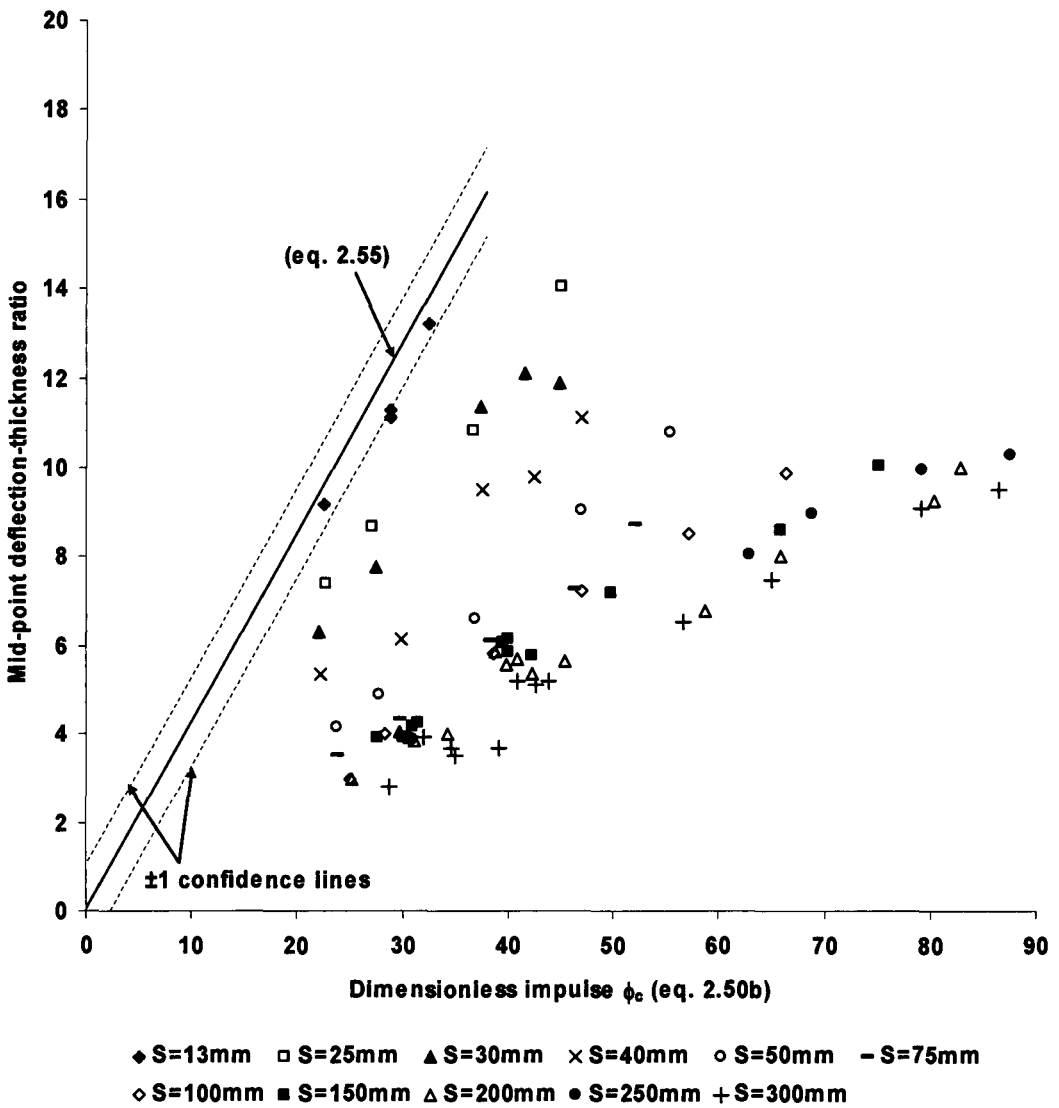

Figure 5.24: Graph of mid-point deflection – thickness ratio versus dimensionless impulse ϕ_c (eq. 2.50b)

5.8.1.1 *Modified Nurick and Martin dimensionless impulse*

In order to account for the effect of stand-off distance on plate response, a stand-off distance parameter ς_S is introduced. The parameter is a function of stand-off distance and charge radius and is written as,

$$\zeta_S = \left(1 + \ln\left(\frac{S}{R_o}\right)\right) \qquad \text{(eq. 5.2)}$$

Where, S – stand-off distance, R_o – charge radius

The new loading parameter is incorporated into dimensionless impulse ϕ_c for localised loading (equation (2.50b)) as follows,

$$\phi_c = \frac{I\left(1 + \ln\left(\frac{R}{R_o}\right)\right)}{\pi R H^2 (\rho\sigma_0)^{1/2}} \times \frac{1}{\varsigma_S} \qquad \text{(eq. 5.3)}$$

Hence equation (2.50b) is rewritten as

$$\phi_{cS} = \frac{I\gamma}{\pi R H^2 (\rho\sigma_0)^{1/2}} \qquad \text{(eq. 5.4)}$$

Where, ϕ_{cS} – modified dimensionless impulse and

$$\gamma = \frac{\left(1 + \ln\left(\frac{R}{R_0}\right)\right)}{\left(1 + \ln\left(\frac{S}{R_0}\right)\right)} \qquad \text{(eq. 5.5)}$$

In cases where the charge radius is greater than stand-off distance (R_o > S), equation (2.50b) is used unchanged. The stand-off distance parameter ς_S is only incorporated into equation (2.50b) in cases where the charge radius is less than the stand-off distance (R_o < S). The two different loading parameter criteria are shown in Figure 5.25.

The two loading parameter criteria are written as follows,

Case 1: $R_0 \geq S$

$$\gamma = \varsigma = \left(1 + \ln\left(\frac{R}{R_0}\right)\right) \qquad \text{(eq. 5.5a)}$$

Case 2: $R_0 < S$

$$\gamma = \frac{\varsigma}{\varsigma_S} = \frac{\left(1 + \ln\left(\frac{R}{R_0}\right)\right)}{\left(1 + \ln\left(\frac{S}{R_0}\right)\right)} \qquad \text{(eq. 5.5b)}$$

Where, γ, is new loading parameter, incorporating charge (R_o – charge radius) and plate (R – plate radius) geometry and stand-off distance (S).

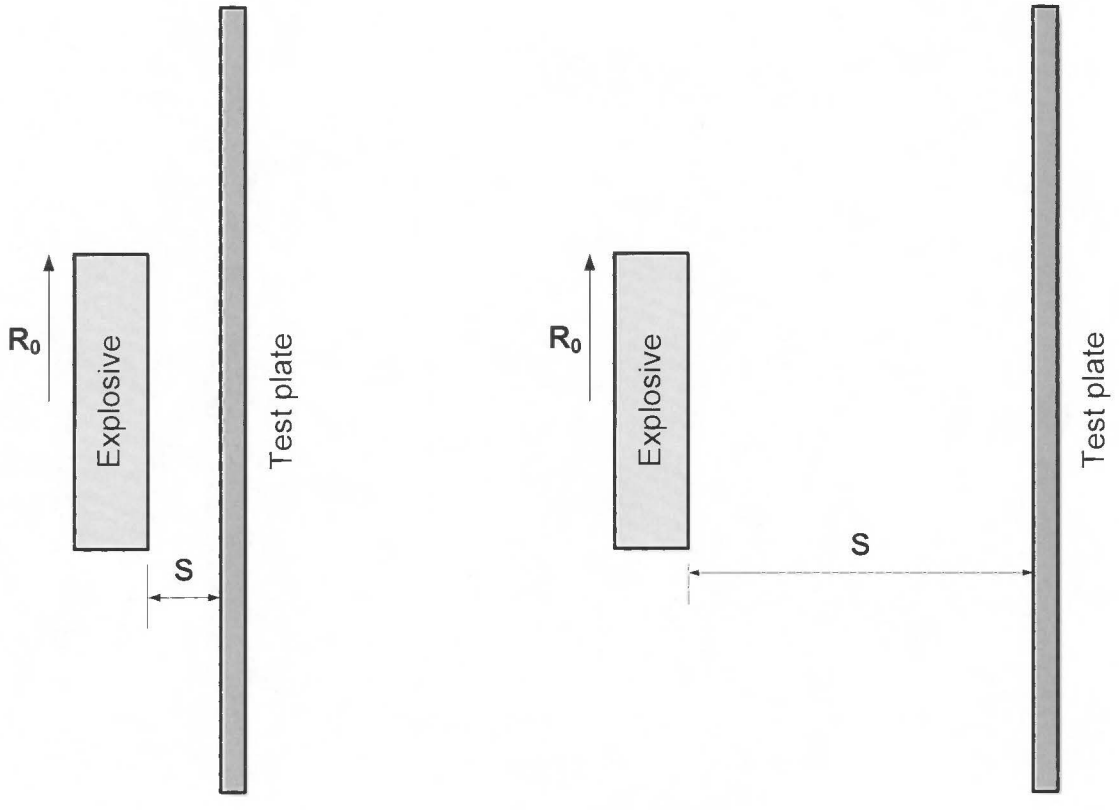

(a) Case 1 **(b) Case 2**

Figure 5.25: Schematic showing the two loading parameter criteria (a) case 1 – $R_0 \geq S$ and (b) case 2 – $R_0 < S$

In the experiments described herein, stand-off distance 13mm is less than the charge radius (17mm). Thus equation (2.50b) is used in its unmodified form. The results show data points falling within the ±1 confidence lines of equation (2.55), as shown in

Figure 5.24. In the case of stand-off distances ranging from 25mm to 300mm, the modified dimensionless impulse is calculated.

The graph of mid-point deflection – thickness ratio versus modified dimensionless impulse (ϕ_{cs}) is shown in Figure 5.26. A total of 79 experiments were conducted in this investigation and all the data points are plotted in the graph shown in Figure 5.26. The data points fall within the ±1 mid-point deflection – thickness ratio confidence lines of equation (2.55) with 95% confidence.

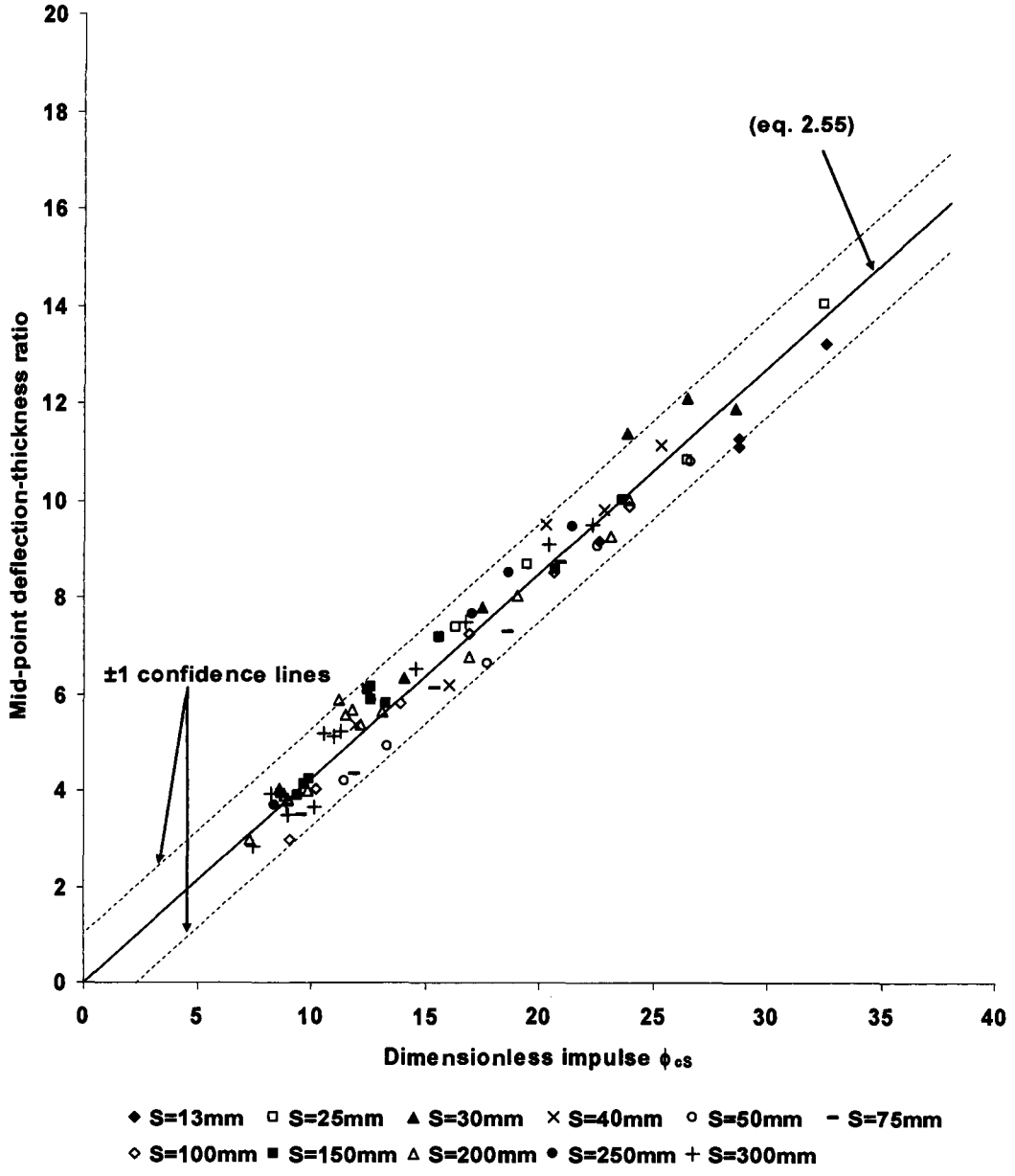

Figure 5.26: Graph of mid-point deflection – thickness ratio versus modified dimensionless impulse ϕ_{cs}

5.8.2 Jones damage number

The graph of mid-point deflection – thickness ratio versus Jones damage number λ (equation (2.35)) is shown in Figure 5.27.

$$\lambda = \frac{4I^2}{\pi^2 R^2 H^4 \rho \sigma_o} \qquad \text{(Recall eq. 2.35)}$$

Where, I – impulse, R – plate radius, H – plate thickness, ρ – plate density and σ_o – static yield stress

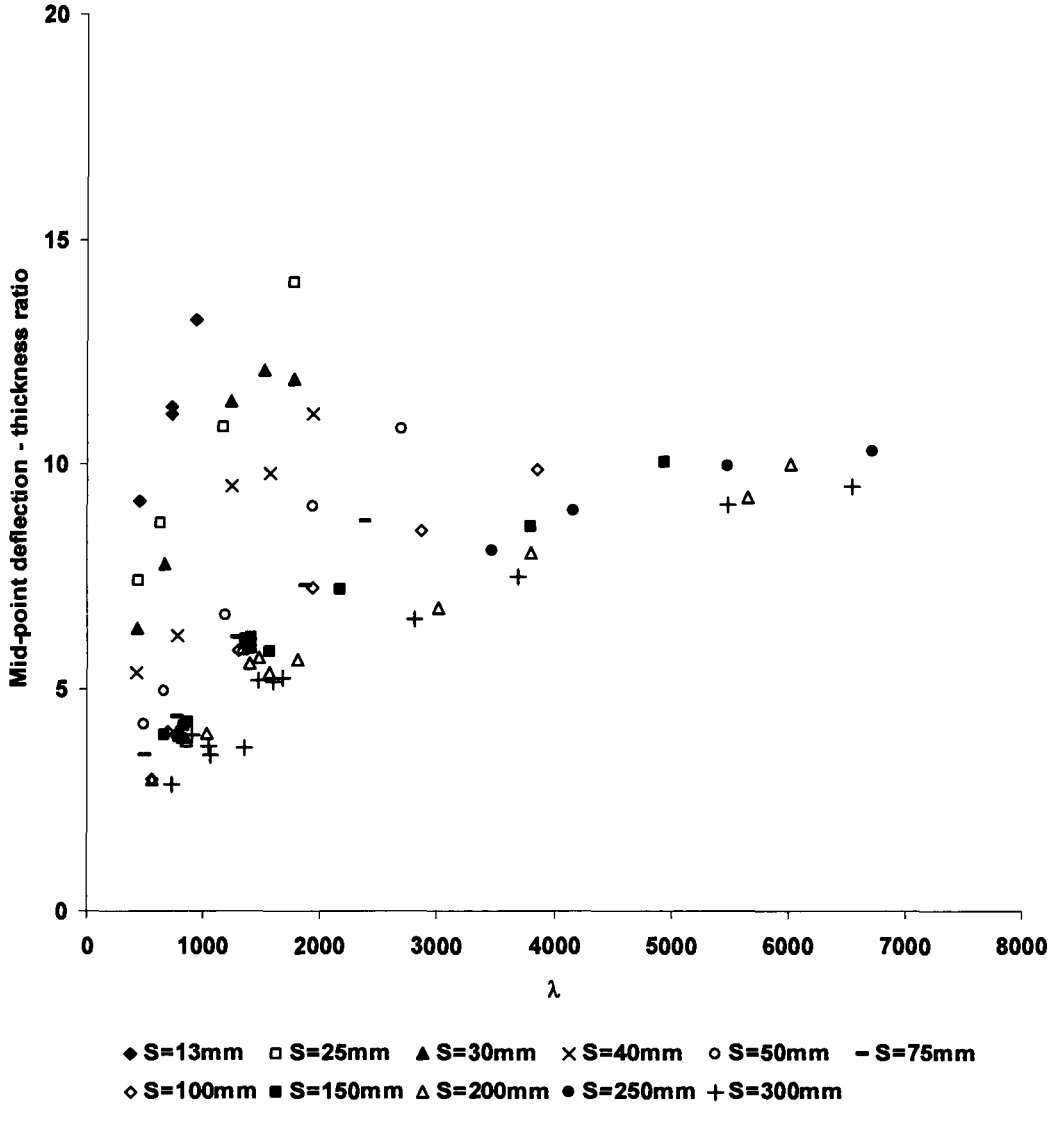

Figure 5.27: Graph of mid-point deflection – thickness ratio versus Jones damage number λ

The analysis is based on the assumption of uniform loading across the loaded side of the test specimen. The distinct separation of the data points for stand-off distances ranging from 13mm to 50mm is due to increased load localisation as the charge is

moved closer to the test plate. The grouping of data points for stand-off distances ranging from 75mm to 300mm represent the uniform loading envelop discussed in Section 5.5 whereby variation in plate mid-point deflection is within ±1 deflection – thickness ratio for a given charge mass. The best fit curve through the data points is shown in Figure 5.28. The equation of the best fit curve is given by,

$$\frac{\delta}{H} = 0.16\lambda^{0.48} \qquad \text{(eq. 5.6)}$$

Where, δ - mid-point deflection

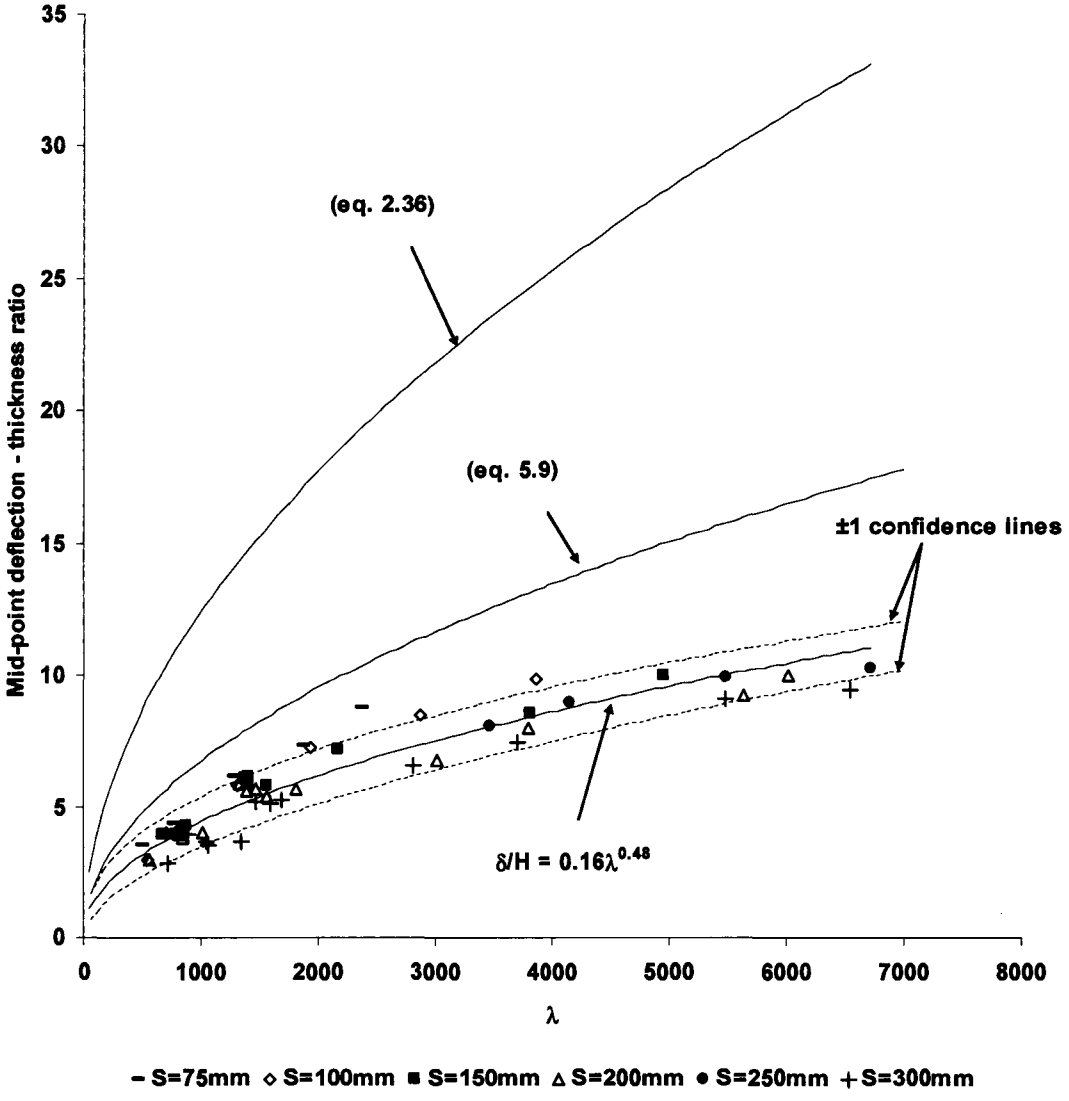

Figure 5.28: Graph of mid-point deflection – thickness ratio versus Jones damage number for stand-off distances 75mm – 300mm

The analytical solution reported by Jones [34] for predicting plate mid-point deflection of fully clamped circular plates subjected to uniformly distributed impulsive loads is given by equation (2.36)

$$\delta/H = \frac{\left(1 + 2\lambda/3\right)^{1/2} - 1}{2} \qquad \text{(Recall eq. 2.36)}$$

The analytical prediction is shown in Figure 5.28 for stand-off distance ranging from 75mm to 300mm. The predicted mid-point deflection – thickness ratios are significantly higher than the measured data. This is attributed to the effect of stand-off distance on load distribution and strain rate sensitivity of plate material. The effect of stand-off distance and strain rate sensitivity of mild steel on plate response is incorporated into Jones damage number in Sections 5.8.2.2 and 5.8.2.3 respectively.

5.8.2.1 Relationship between Jones damage number and Nurick and Martin dimensionless impulse parameter

Jones damage number is given by equation (2.35) and can be rewritten as follows,

$$\lambda = \frac{4I^2}{\pi^2 R^2 H^4 \rho\sigma_o} = 4\left[\frac{I}{\pi R H^2 (\rho\sigma_0)^{1/2}}\right]^2 = 4\phi_c^{\,2} \qquad \text{(eq. 5.7)}$$

Where, ϕ_c - Nurick and Martin dimensionless impulse (equation (2.50a))

From the relationship between Jones damage number and Nurick and Martin dimensionless impulse parameter (equation (5.7)). The empirical relationship given by equation (2.55) can be rewritten as follows,

$$\frac{\delta}{H} = 0.425\phi_c = 0.425\left(\frac{\lambda}{4}\right)^{1/2} \qquad \text{(eq. 5.8)}$$

Therefore,

$$\frac{\delta}{H} = 0.213\lambda^{1/2} \qquad \text{(eq. 5.9)}$$

The graph of mid-point deflection – thickness ratio versus Jones damage number (equation (2.35)) show that equation (5.9) over estimates mid-point deflection for stand-off distances ranging from 75mm to 300mm as shown in Figure 5.28. This is due to the fact that the effects of different stand-off distances between test plate and explosive are not taken into account. Modification to Jones damage number to account for stand-off distance is discussed in Section 5.8.2.2.

5.8.2.2 *Modification to Jones damage number*

Jones damage number λ in it current form does not consider the effect of stand-off distance as shown in the previous section. Hence a modification to the damage number is introduced in the form of a loading parameter γ. This parameter is incorporated into Jones damage number based on the relationship between Jones damage number and Nurick and Martin dimensionless impulse parameter.

Based on the relationship given by equation (5.7), the loading parameter γ (equation (5.5)) is incorporated into Jones damage number as follows,

$$\lambda\gamma^2 = 4\phi_c{}^2\gamma^2 = 4(\phi_c\gamma)^2 = 4\phi_{cS}{}^2 \qquad \text{(eq. 5.10)}$$

Therefore, modified Jones damage number is written as

$$\lambda_S = \lambda\gamma^2 = \frac{4I^2\gamma^2}{\pi^2 R^2 H^4 \rho\sigma_o} \qquad \text{(eq. 5.11)}$$

The analytical solution proposed by Jones [34] (eq. 2.36) is rewritten as

$$\delta/H = \frac{\left(1 + 2\lambda_S/3\right)^{1/2} - 1}{2} \qquad \text{(eq. 5.12)}$$

The empirical prediction based on equation (2.55) proposed by Nurick and Martin [2] is rewritten as follows

$$\frac{\delta}{H} = 0.213\lambda_S{}^{1/2} \qquad \text{(eq. 5.13)}$$

The experimental data is re-plotted for mid-point deflection – thickness ratio versus modified Jones damage number λ_S. The experimental results, analytical prediction using equation (5.12) and empirical prediction (equation (5.13) based on equation (2.55) proposed by Nurick and Martin [2] are shown in Figure 5.29. It is evident that by incorporating a simple loading parameter, γ, into Jones damage number and re-plotting the data show satisfactory correlation between the empirical prediction (equation (5.13)) and experimental results.

It should be noted that the same loading parameter criteria set out in Section 5.8.1.1 is applied to modified Jones damage number. The effect of stand-off distance is only taken into consideration in cases where the load radius is less than the stand-off distance ($R_0 < S$).

The predicted mid-point deflection calculated using equation (5.12) significantly over estimates the plate deformations. This is due to the fact that the analytical solution does not take strain rate sensitivity of mild steel into account. Whilst the empirical equation (equation 5.9) based on the relationship proposed by Nurick and Martin

(equation 2.55) is derived from experimental data obtained from blast loaded mild steel plates that strain harden at high strain rates. The modification to Jones damage number to account for strain rate sensitive mild steel is discussed in Section 5.8.2.3. The best fit curve through experimental data for stand-off distance ranging from 75mm to 300mm shown in Figure 5.28 fall below the empirical prediction (equation (5.13)) and analytical prediction (equation (5.12)).

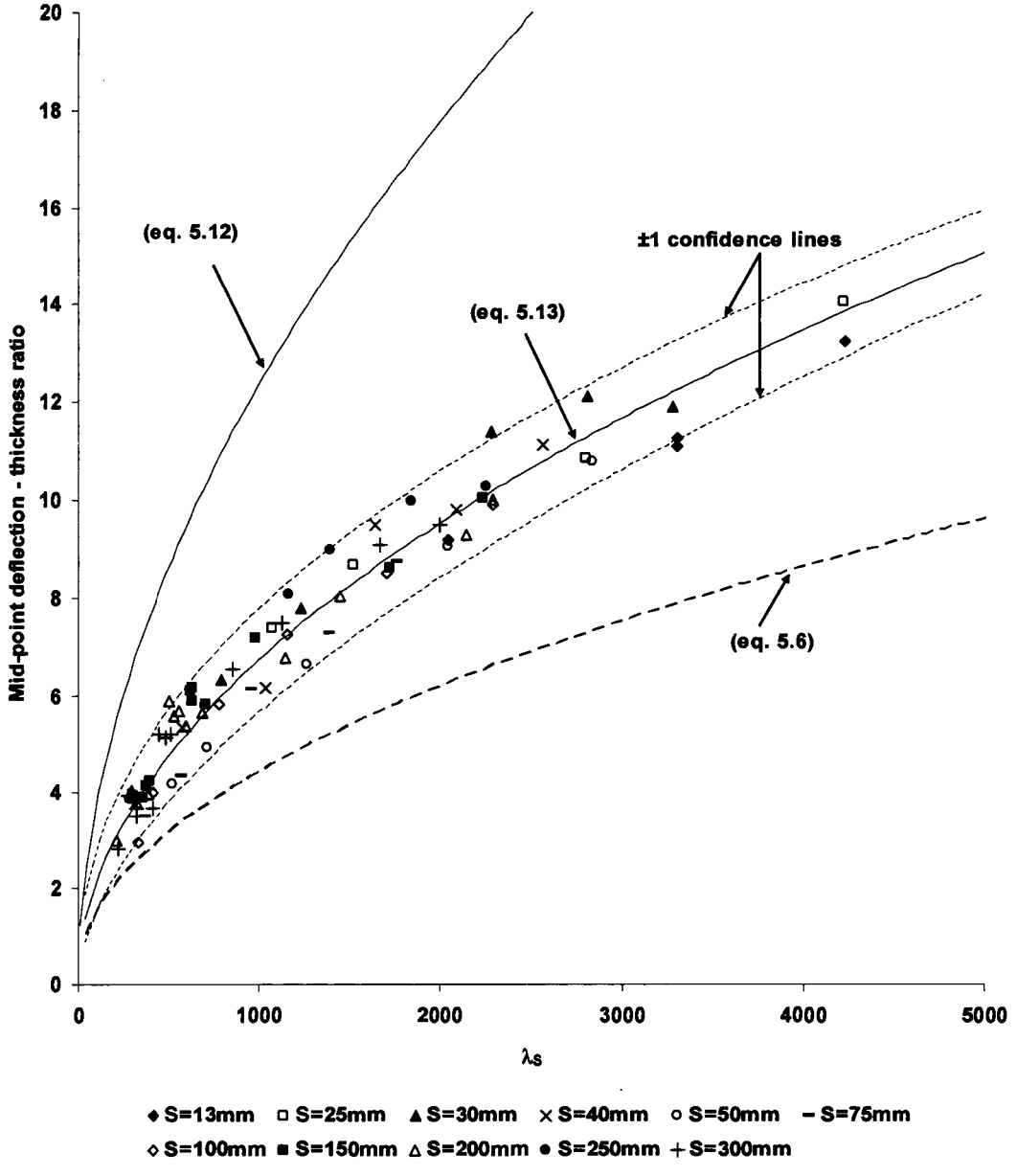

Figure 5.29: Graph of mid-point deflection – thickness ratio versus modified Jones damage number λ_S

5.8.2.3 *Incorporating strain rate sensitivity of mild steel into Jones damage number*

The strain rate sensitivity of mild steel plates subjected to blast loads was highlighted in Section 5.8.2.2. The analytical solution proposed by Jones [34] overestimates the mid-point deflection – thickness ratio for all test conducted in this investigation. However, it has been shown that by incorporating a loading parameter, γ, into Jones damage number, λ, all the data points converge onto a single line as shown in Figure 5.29 for all stand-off distances.

Jones [34] proposes replacing the static yield σ_o with the dynamic yield stress σ_o^1 to account for material strain rate sensitivity. Hence Jones damage equation λ (equation (2.35)) is rewritten as follows,

$$\lambda = \frac{4I^2}{\pi^2 R^2 H^4 \sigma_0^1 \rho} \qquad \text{(eq. 5.14)}$$

The dynamic yield stress σ_o^1 is given by

$$\sigma_0^1 = n\sigma_0 \qquad \text{(eq. 5.15)}$$

Where

$$n = 1 + \left\{ \frac{V_o \delta}{3\sqrt{2}\,\dot{\varepsilon}_0 R^2} \right\}^{1/\eta} \qquad \text{(eq. 5.16)}$$

$\dot{\varepsilon}_0$ = 40.4 and $\eta = 5$ are material constants for mild steel [34]

The static yield stress σ_o is determined from tensile tests performed on samples from each sheet of mild steel used to prepare the test specimens. The results of the tensile test are presented in Section 3.2.

If equation (2.36) is substituted into equation (5.16) to eliminate deflection δ, then

$$n = 1 + \left[\frac{V_0 H \left[\left(1 + \frac{2\lambda}{3} \right)^{1/2} - 1 \right]}{6\sqrt{2}\,\dot{\varepsilon}_0 R^2} \right]^{1/\eta} \qquad \text{(eq. 5.17)}$$

Where $V_0 = \frac{I}{\pi R^2 H \rho}$ and $\lambda = \frac{4I^2}{\pi^2 R^2 H^4 \sigma_0 \rho}$

Hence the dynamic yield stress σ_o^1 is determined using equations (5.17) and (5.15). The graph of dynamic yield stress σ_o^1 versus impulse for all tests conducted in this investigation using charge masses 4g, 5g, 7g, 9g, 11g, 13g and 15g are plotted in Figure 5.30. The graph shows that the dynamic yield stress increases with increasing impulse. The equation of the best fit curve through the data points is given by,

$$\sigma_0^1 = 304 I^{0.25} \qquad \text{(eq. 5.18)}$$

Symonds and Wierzbicki [37] propose an iterative process to determine dynamic yield stress σ_o^1 as discussed in Section 2.5.3.1.

$$\frac{0.05365 I^2}{R^5 H^2 \sqrt{\rho^3 \sigma_o^1}} = 40.4 \left[\frac{\sigma_0^1}{\sigma_0} - 1 \right]^5 \qquad \text{(Recall eq. 2.86)}$$

Where, R – plate radius, H – plate thickness, I – impulse, ρ – plate density, σ_o – static yield stress and σ_o^1 – dynamic yield stress

Equation (2.86) can be rewritten for the experimental set up used in this investigation as follows,

Plate radius – 53mm, Plate thickness – 1.9mm, Plate density – 7691kg/m^3 and σ_o – 240MPa

$$\frac{0.05365 I^2}{0.053^5 \times 0.0019^2 \sqrt{7691^3 \sigma_o^1}} = 40.4 \left[\frac{\sigma_0^1}{\sigma_0} - 1 \right]^5$$

Thus

$$\frac{52687.67 I^2}{\sqrt{\sigma_0^1}} = 40.4 \left[\frac{\sigma_0^1}{\sigma_0} - 1 \right]^5 \qquad \text{(eq. 5.19)}$$

The graph of dynamic yield stress σ_o^1 (equation (5.19)) versus impulse for tests conducted using charge masses 4g, 5g, 7g, 9g, 11g, 13g and 15g is shown in Figure 5.30. The equation of the best fit curve through the data points is given by,

$$\sigma_0^1 = 334 I^{0.24} \qquad \text{(eq. 5.20)}$$

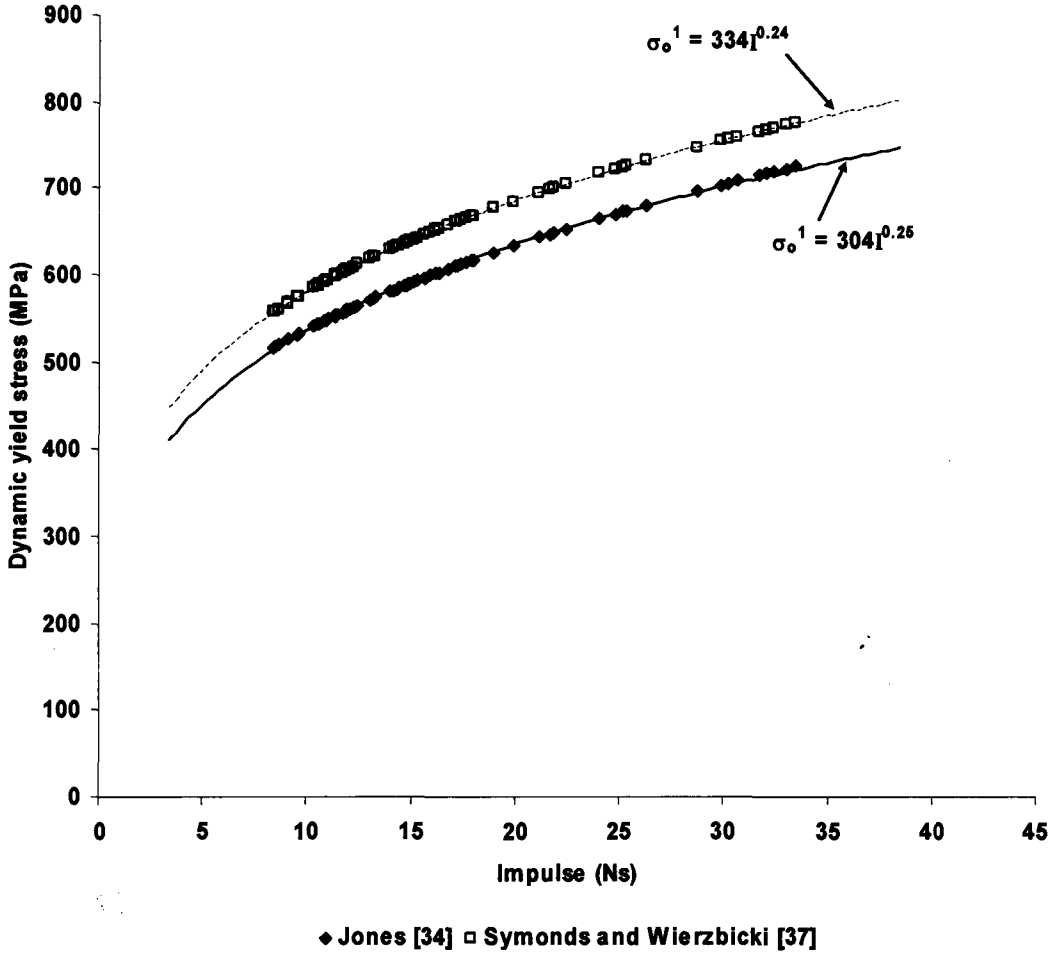

Figure 5.30: Graph of dynamic yield stress versus impulse using equations (5.15) and (5.19)

The dynamic yield stress σ_o^1 determined using the methodology proposed by Jones [34] is less than that determined using the iterative process proposed by Symonds and Wierzbicki [37] for any given impulse. A comparison of the influence of the two methodology on analytical predictions using equation (2.36) and Jones damage number λ (equation (5.14) is shown in Figure 5.31. The analysis indicates no difference in predicted mid-point deflection. Hence either methodology to determine dynamic yield stress is applicable. In this report the iterative methodology proposed by Symonds and Wierzbicki [37] is used.

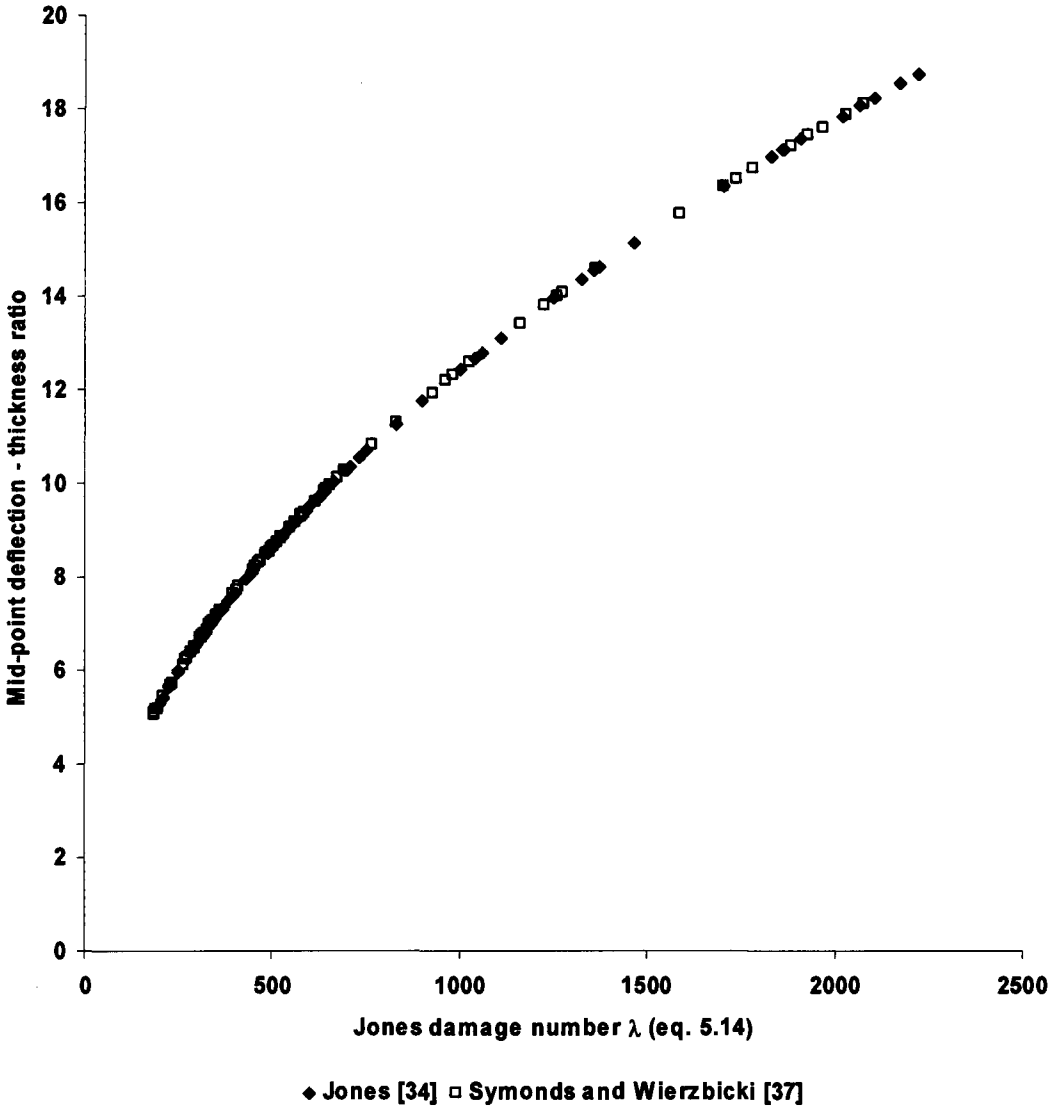

Figure 5.31: Graph of mid-point deflection - thickness ratio versus Jones damage number λ ((equation (5.14)) comparing analytical predictions (equation (2.36)) using dynamic yield stress using equations (5.15) and (5.19)

The dynamic yield stress σ_o^1 given by equation (5.20) is substituted into equation (5.11). The modified Jones damage number is given by

$$\lambda_S^{\,1} = \frac{4I^2\gamma^2}{\pi^2 R^2 H^4 \rho\left(334I^{0.24}\right)} = \frac{0.012I^{1.76}\gamma^2}{\pi^2 R^2 H^4 \rho}$$

$$\lambda_S^{\,1} = \frac{0.012I^{1.76}\gamma^2}{\pi^2 R^2 H^4 \rho} \qquad \text{(eq. 5.21)}$$

Hence the analytical prediction equation (2.36) is rewritten as follows,

$$\delta/H = \frac{\left(1 + 2\lambda_S^{\,1}/3\right)^{1/2} - 1}{2} \qquad \text{(eq. 5.22)}$$

The experimental data is plotted in the graph of mid-point deflection – thickness ratio versus modified Jones damage number λ_S^1 as shown in Figure 5.32. The experimental results show satisfactory correlation with the analytical solution given by equation (5.22). It should be noted that experimental results for stand-off distance 13mm fall outside the ±1 confidence lines. The analysis indicate that by incorporating dynamic yield stress to account for strain rate sensitivity of mild steel, the analytical solution (equation (5.22)) agrees satisfactorily with predictions determined using modified empirical prediction proposed by Nurick and Martin (equation (5.13)).

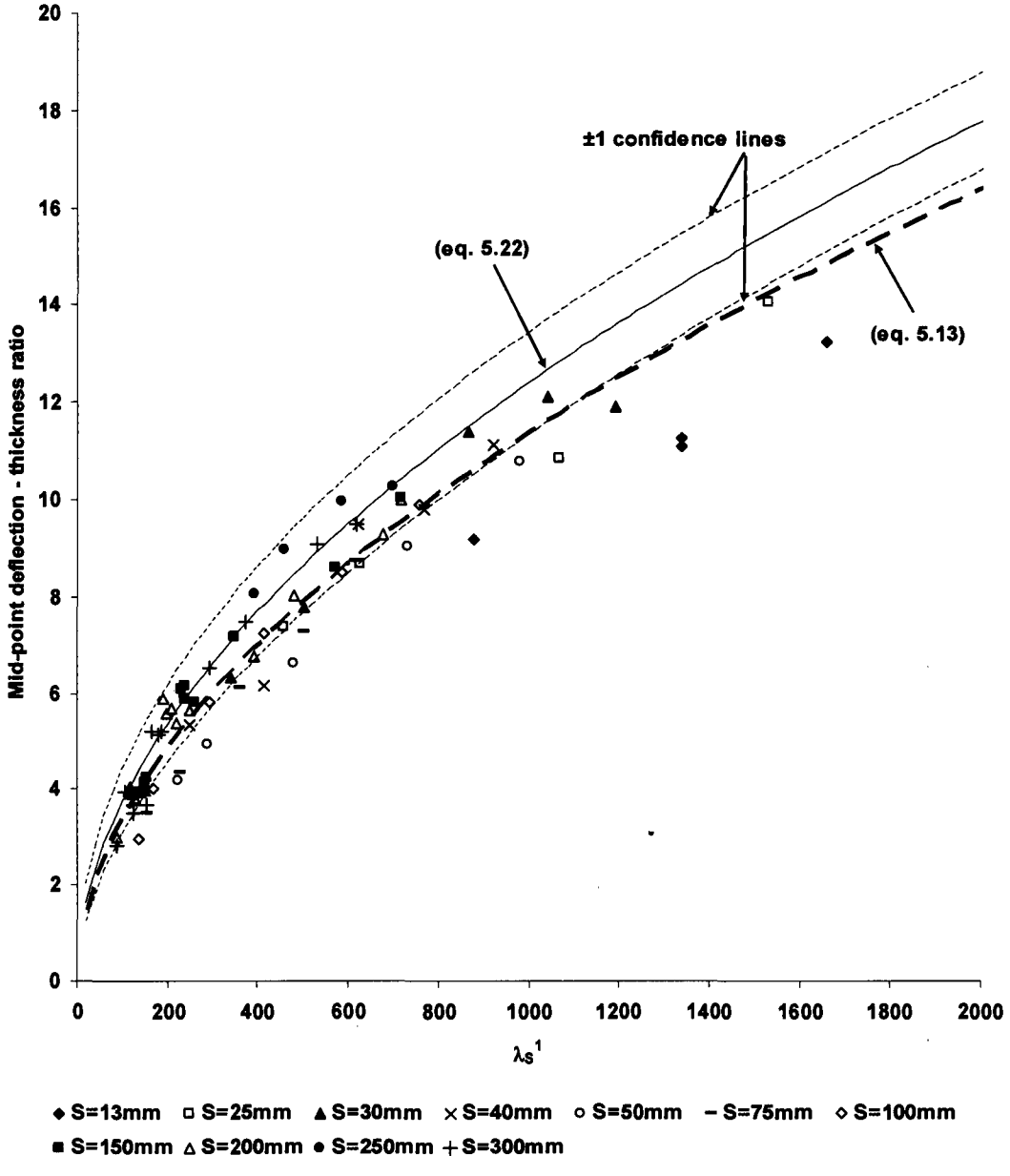

Figure 5.32: Graph of mid-point deflection – thickness ratio versus modified Jones damage number λ_S^1

5.8.3 Strain energy analysis

The strain energy analysis outlined in Section 2.5 is used to predict the mid-point deflections for a given charge mass for varying stand-off distance. The results are compared with measured mid-point deflections.

The strain energy relationships outlined in Section 2.5 are based on the following assumption that the shape of the deformed plate is that of a uniform global dome.

The methodology outlined by Ezra [35] takes into account strain hardening of mild steel and the equation for deformation strain energy is given as

$$U_{def} = \frac{\pi}{4} D^2 H_o \frac{K}{n+1} \left\{ \ln\left[1 + 4\left(\frac{\delta}{D}\right)^2 \right] \right\}^{n+1} \qquad \text{(Recall eq. 2.81)}$$

Alternatively for non-strain hardening material the plate is assumed to exhibit rigid-plastic material behaviour. Hence the plate undergoes negligible deformation until the yield point is reached and subsequently flows plastically without further increase in stress in the material. For this case the deformation strain energy is given by

$$U_{def} = \frac{\pi}{4} D^2 H_o \sigma_o \ln\left[1 + 4\left(\frac{\delta}{D}\right)^2 \right] \qquad \text{(Recall eq. 2.82)}$$

Duffey [36] uses similar energy method for rigid-plastic material behaviour of plates subjected to impulsive loading. The deformed shape of the plate is described by shape functions. Teeling-Smith and Nurick [5] used the shape function proposed by Duffey [36],

$$w = \delta \cos\left(\frac{\pi r}{2R}\right) \qquad \text{(Recall eq. 2.83)}$$

The deformation strain energy for plate deformation described by equation (2.83) is given by

$$U_{def} = \frac{\pi^3 H \sigma_0^1 \delta^2}{4\left(1 - v + v^2\right)^{1/2}} \left(\frac{1}{4} + \frac{1}{\pi^2}\right) \qquad \text{(Recall eq. 2.85)}$$

It should be noted that the plate profile described by equation (2.83) is a large global dome similar to that observed on uniformly loaded plates and concurs with experimental results [5].

The deformation strain energy calculated using equations (2.82) and (2.85) will be approximately the same, as the two equations are based on the assumption of rigid-

plastic material behaviour with constant yield stress and plate profile after deformation of a large global dome.

Deformation strain energy given by equations (2.82) and (2.85) does not consider strain hardening. The test plate material used in this investigation is mild steel, which strain hardens at high strain rates. Teeling-Smith and Nurick [5] used dynamic yield stress to account for strain hardening of mild steel. The dynamic yield stress is determined using the iterative process proposed by Symonds and Wierzbicki [37] (equation (2.86)). The results obtained from the analysis relating impulse and dynamic yield stress in Section 5.8.2.3 is also used in the strain energy analysis. The dynamic yield stress determined using the iterative method is incorporated into the deformation strain energy equations (2.82) and (2.85).

The strain energy equations (2.81), (2.82) and (2.85) are used to predict the mid-point deflection of plates subjected to impulsive loading at different stand-off distance. In the case of impulsive loading the duration of the load is significantly lower than the natural period of the structure. Hence the blast produces an instantaneous velocity change on the plate. As a result the plate gains kinetic energy (input energy) which is converted to deformation strain energy, U_{def}. Thus for Mode I type failure the following energy balance is stated [5],

$$E_{input} = U_{def} \qquad \text{(Recall eq. 2.87)}$$

The relationship between impulse and input energy is given by

$$E_{input} = \frac{I^2}{2\pi R^2 H \rho} \qquad \text{(Recall eq. 2.93)}$$

The relationship between input energy (equation 2.93) and stand-off distance is shown in Figure 5.33 for charge masses 4g, 5g, 7g and 9g. The results show that input energy is similar for all stand-off distances. Hence according to equation (2.87) the deformation strain energy is similar for a given charge mass at all stand-off distances. Thus implying that plate deformation should be the same at all stand-off distances for a given charge mass. This is contrary to the experimental results that show that plate mid-point deflection decreases with increasing stand-off distance. Therefore deformation strain energy cannot be similar for all stand-off distances. A modification to the input energy equation (2.93) is introduced in Section 5.8.3.1 to account for the portion of total energy released by a given charge mass that is applied on the plate with respect to different stand-off distances.

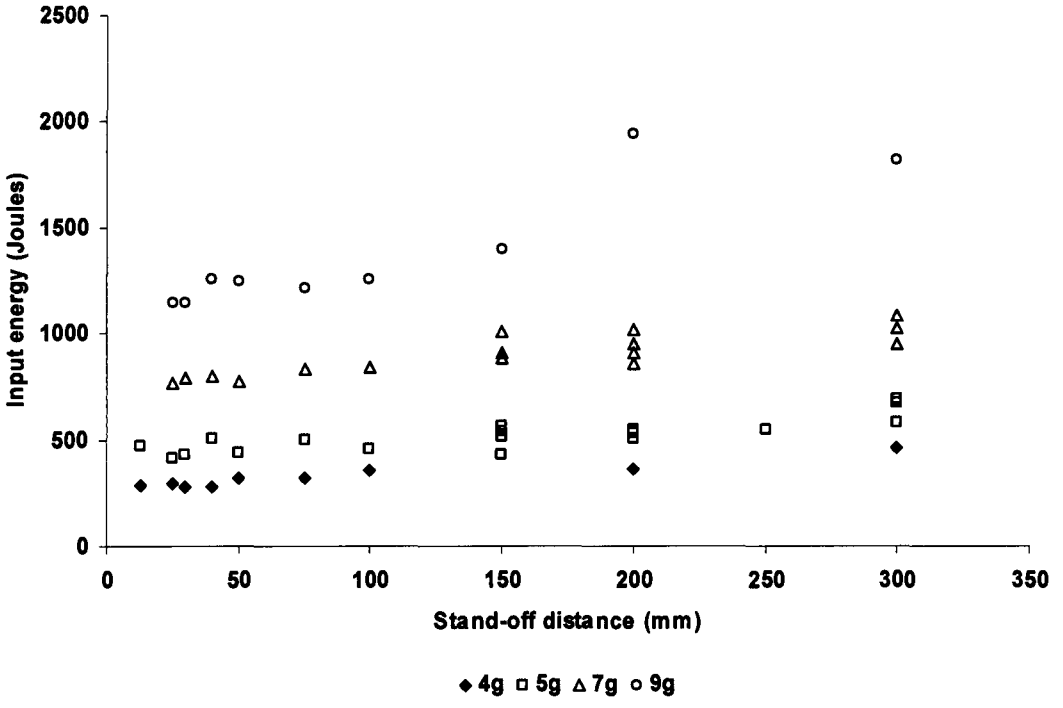

Figure 5.33: Graph of input energy versus stand-off distance

5.8.3.1 Modified input energy

The effect of loading condition is important in determining the input energy. The loading parameter γ (equation (5.5)) introduced in Section 5.8.1.1 is incorporated into equation (2.93). It should be noted that the loading parameter is used in strain energy analysis based on the loading parameter criteria set out in Section 5.8.1.1, regarding the effect of stand-off distance being incorporated into loading parameter, γ, only in cases where the load radius is less than stand-off distance.

The loading parameter is incorporated into the input energy equation (2.93) as follows,

$$E_{input} = \gamma^2 \left(\frac{I^2}{2\pi R^2 H \rho} \right) \qquad \text{(eq. 5.23)}$$

Note: γ^2 is used instead of γ, as better correlation between predicted mid-point deflection and experimental results is achieved using the former as shown in Section 5.8.3.2

The graph of modified input energy (equation 5.23) versus stand-off distance is shown in Figure 5.34. It can be seen that input energy varies with stand-off distance similar to the relationship between mid-point deflection and stand-off distance as shown in Section 5.3.

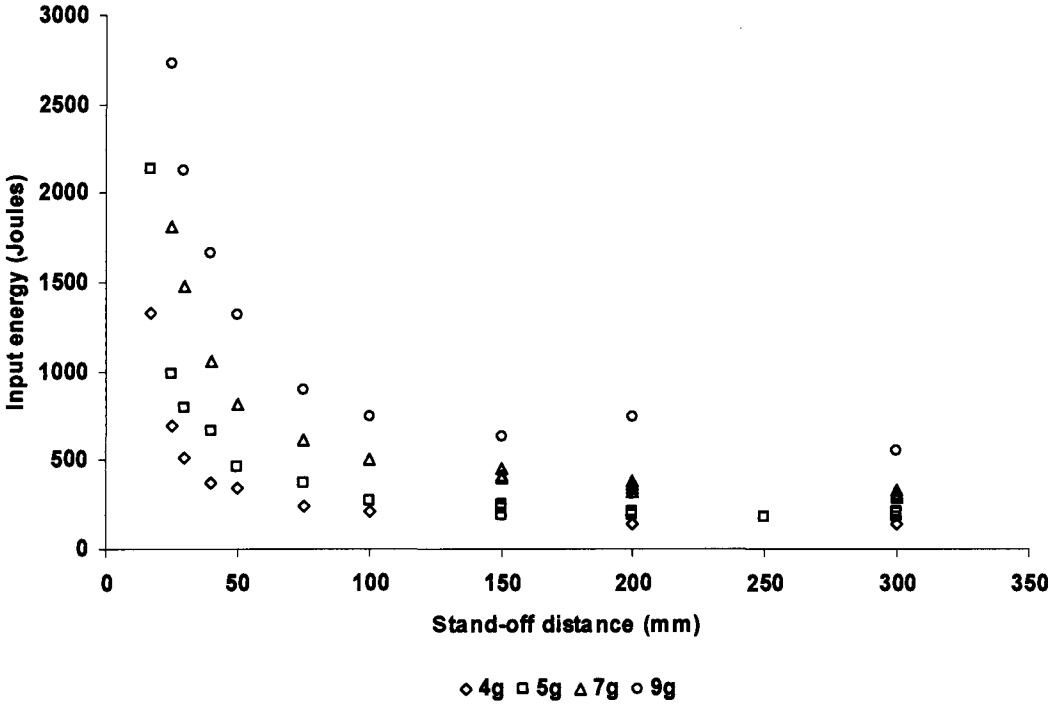

Figure 5.34: Graph of modified energy input versus stand-off distance

The input energy calculated using equation (5.23) is larger than the value obtained using equation (2.93) for the closer stand-off distances (13mm to 50mm) as shown in Figure 5.35 for charge mass 5g. This is required to account for the difference between the observed plate profile of an inner dome atop a global dome and the assumed deformed shape of a uniform global dome for stand-off distances ranging from 13mm to 40mm. The deformation strain energy equations (2.81), (2.82) and (2.85) overestimate the deformation energy required for a given mid-point deflection at stand-off distances where an inner dome is observed. The comparison between measured plate profiles and assumed deformed shape using equation (2.83) are shown in Figure 5.36 – Figure 5.39 for a selection of test plates for charge mass of 5g.

For stand-off distances ranging from 75mm to 300mm the input energy calculated using equation (5.23) is lower than that obtained from equation (2.93) for increasing stand-off distances.

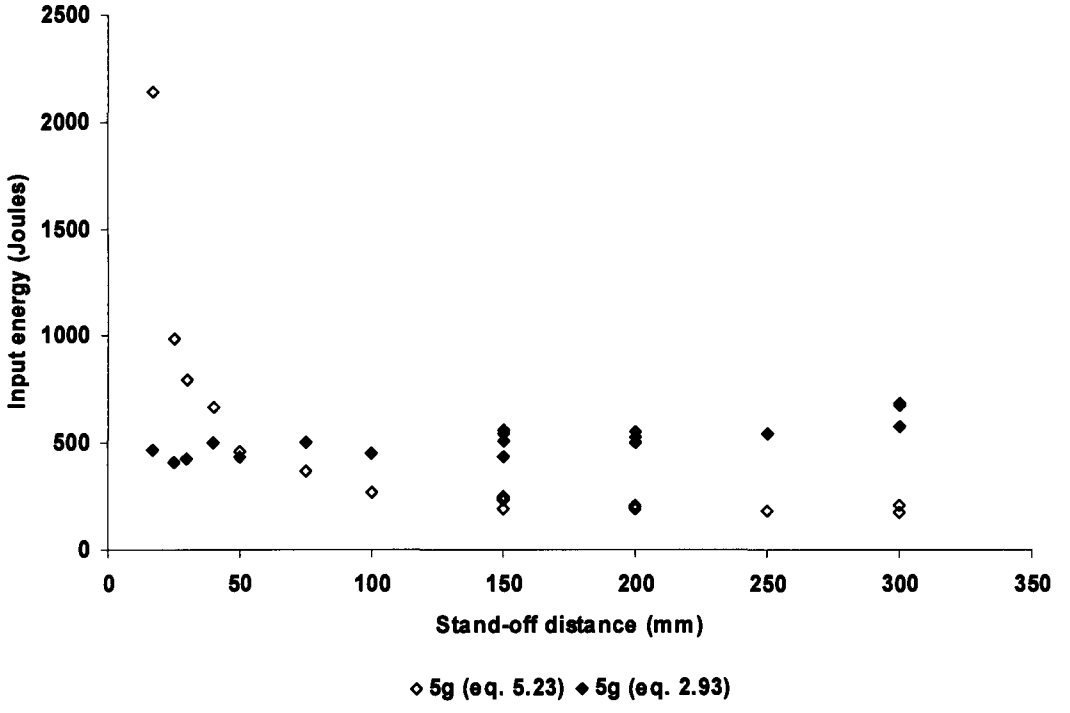

Figure 5.35: Graph of input energy versus stand-off distance comparing the equations (5.23) and (2.93)

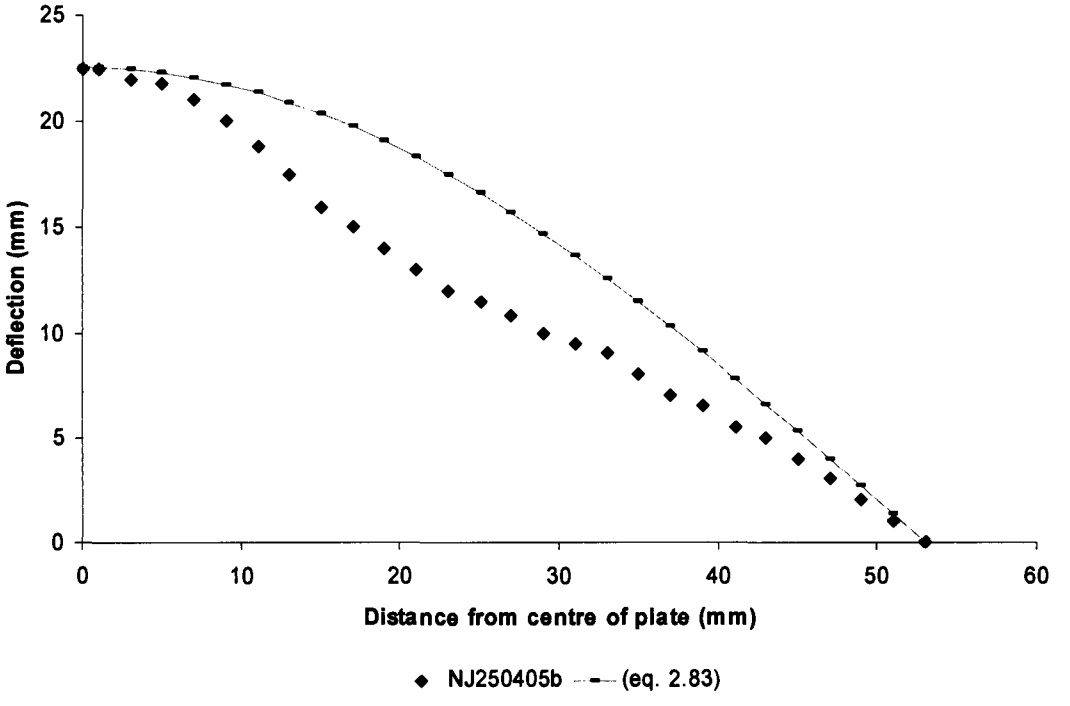

Figure 5.36: Cross-section plate profile for test plate NJ250405b charge mass 5g, stand-off distance 13mm

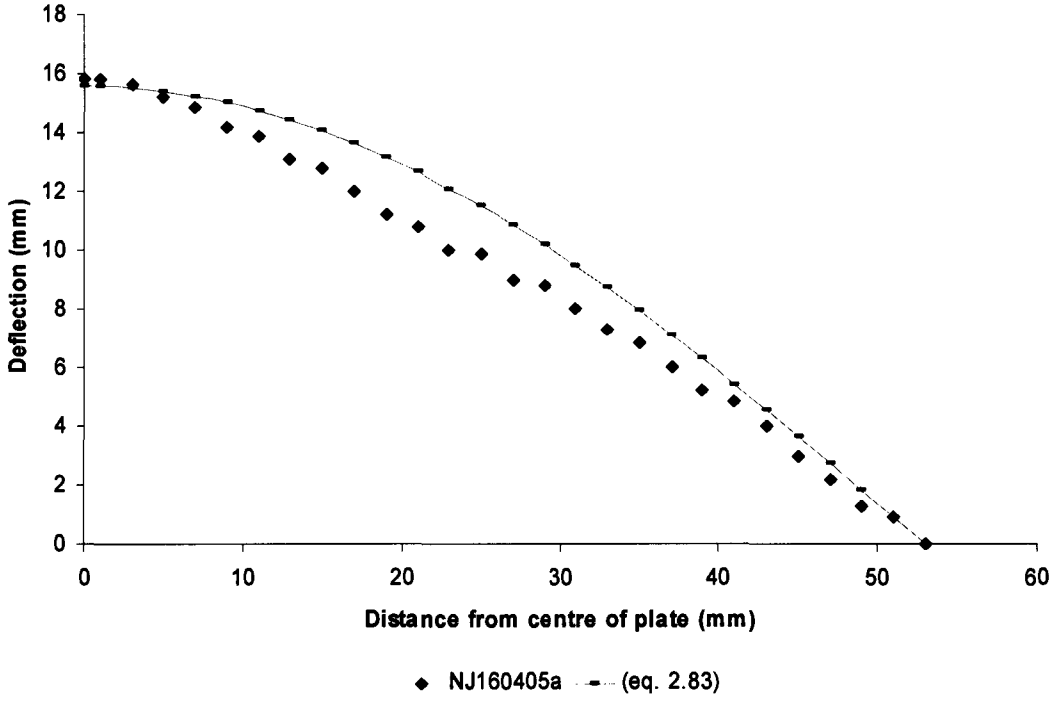

Figure 5.37: Cross-section plate profile for test plate NJ160405a charge mass 5g, stand-off distance 30mm

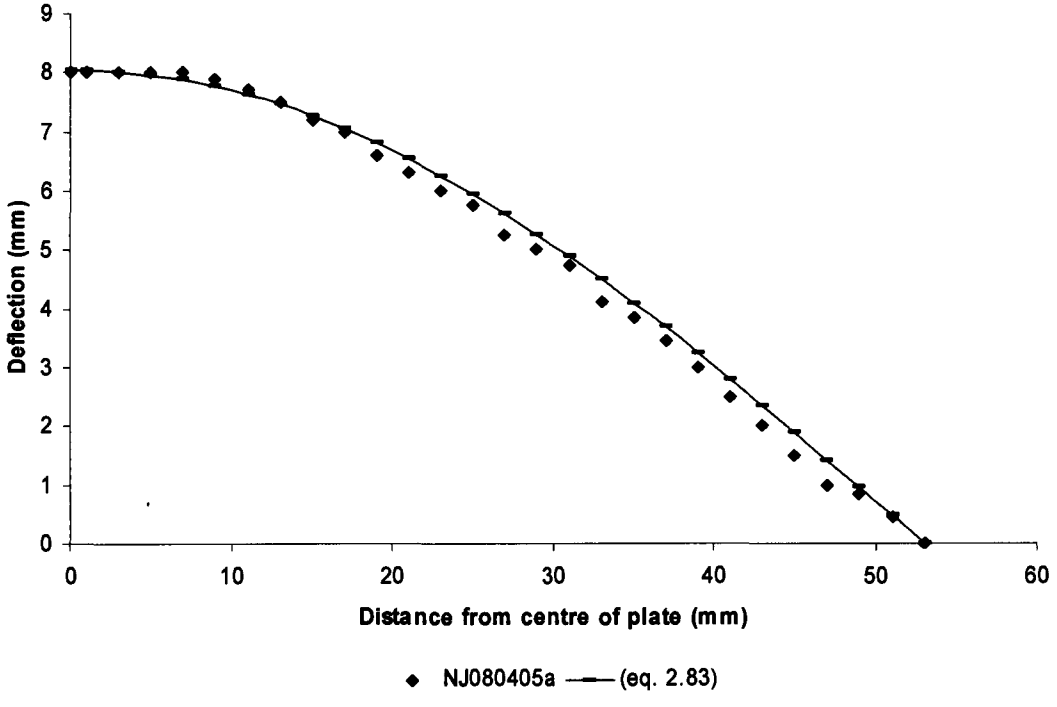

Figure 5.38: Cross-section plate profile for test plate NJ080405b charge mass 5g, stand-off distance 100mm

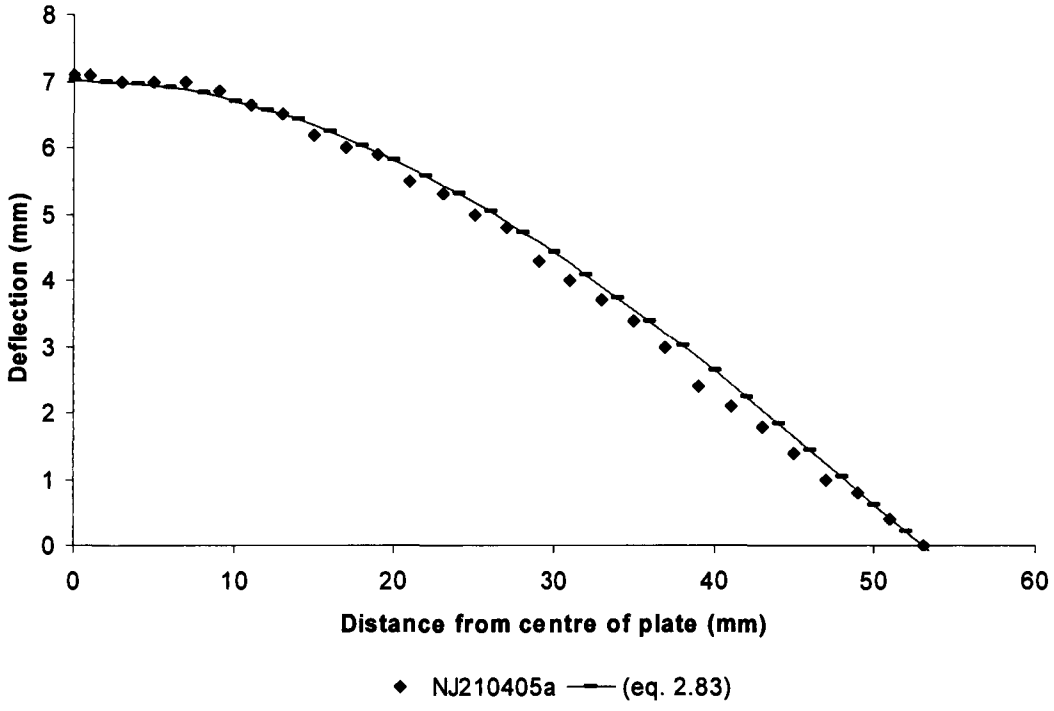

Figure 5.39: Cross-section plate profile for test plate NJ210405a charge mass 5g, stand-off distance 300mm

5.8.3.2 Determining Mid-point deflection using Deformation Energy Analysis

The mid-point deflection is determined using equations (2.81), (2.82) and (2.85). The input energy is calculated using equation (5.23) for a given impulse. The dynamic yield stress determined using equation (5.20) is used in equations (2.82) and (2.85). The results for charge masses 4g, 5g, 7g and 9g are shown in Figure 5.40 – Figure 5.43.

The mid-point deflections determined using strain energy analysis (equations (2.82) and (2.85)) shows good correlation experimental data.

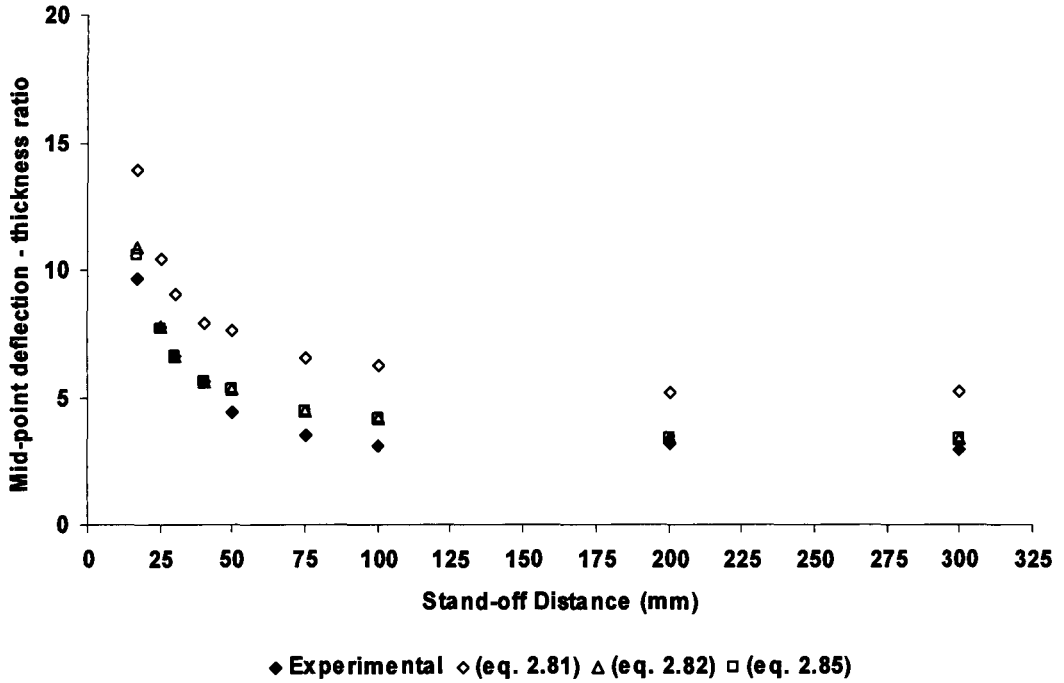

Figure 5.40: Graph of mid-point deflection – thickness ratio versus stand-off distance for charge mass 4g

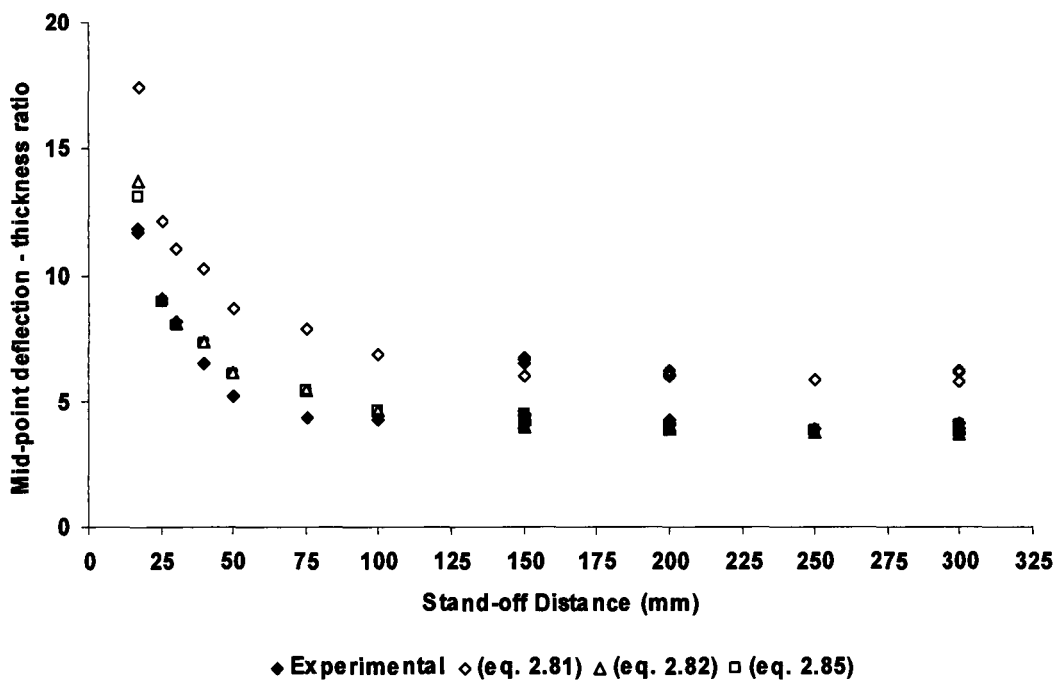

Figure 5.41: Graph of mid-point deflection – thickness ratio versus stand-off distance for charge mass 5g

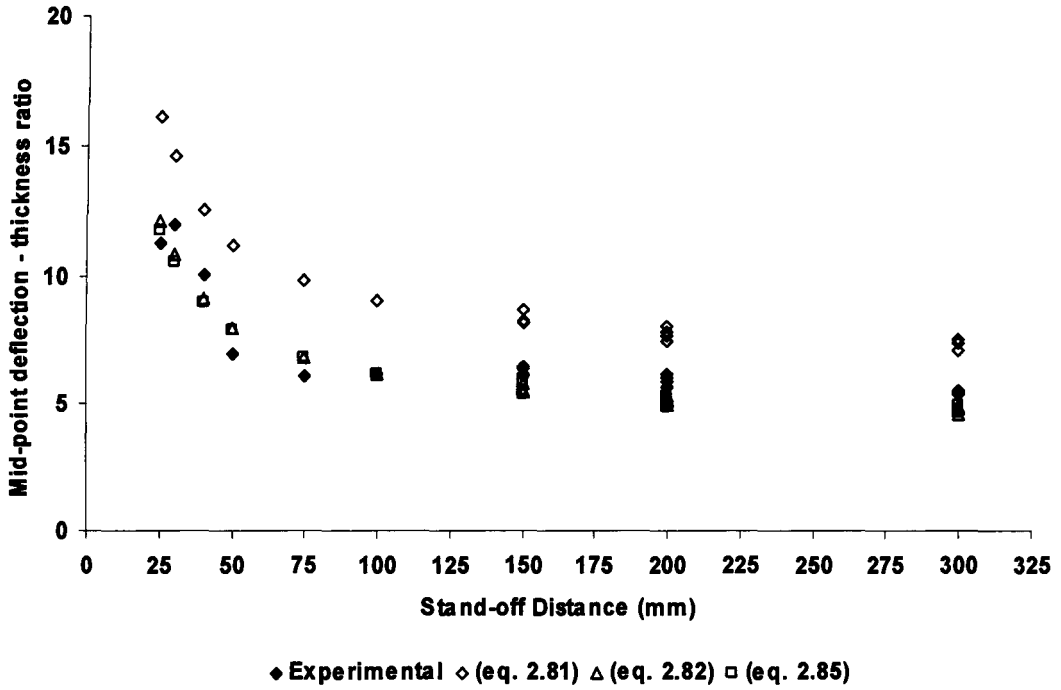

Figure 5.42: Graph of mid-point deflection – thickness ratio versus stand-off distance for charge mass 7g

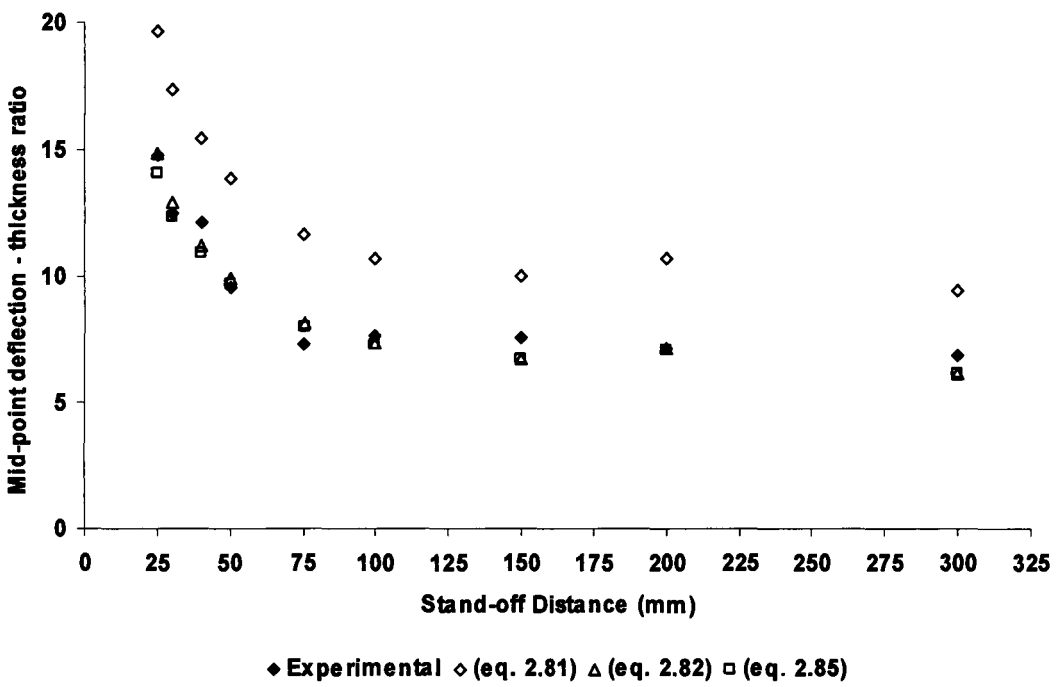

Figure 5.43: Graph of mid-point deflection – thickness ratio versus stand-off distance for charge mass 9g

6 Conclusions

Deformation of circular plates subjected to localised blast loads at varying stand-off distances using tubes was investigated. The effect of using polystyrene pads as a buffer between the explosive charge and test plate was also investigated. Based on the finding of these investigations, the following conclusions are drawn:

Effect of stand-off distance on impulse

The impulse measured using the ballistic pendulum varies with increasing stand-off distance. The change in impulse exhibits a gradual increase over the range of stand-off distance used in this investigation. The variation between the impulses measured for a given charge mass at stand-off distance 13mm compared to stand-off distance 300mm is approximately 20%.

Effect of stand-off distance on mid-point deflection

The mid-point deflections decrease significantly as stand-off distance increases from 13mm to 50mm for a given charge mass. For stand-off distances ranging from 75mm to 300mm the mid-point deflections are similar for a given charge mass.

Effect of stand-off distance on plate deformation profile and loading condition

The deformed plate profile varies with changing stand-off distances. An inner dome atop a global dome is observed at closer stand-off distances ranging from 13mm to 40mm indicating localised loading. The appearance of an inner dome atop a global dome concurs with experimental results reported by Nurick and Radford [6] and Chung Kim Yuen and Nurick [7] for circular plates subjected to localised blast loads.
At stand-off distances greater than plate radius (53mm) ranging from 100mm to 300mm the deformed profile of the plate is that of a large global dome associated with uniform loading. The large global dome observed concur with experimental results reported by Teeling-Smith and Nurick [5] for uniformly loaded circular plates.
A transition from localised blast load to a uniform load is apparent. The transition occurs at stand-off distances of 50mm and 75mm. At the transition phase the plate exhibits aspects of uniform and localised loading with "flatter" dome shaped deformation with increased deformation near the boundary and the appearance of the burn diameter.

Effect of stand-off distance on modes of failure

The failure modes observed were predominantly large inelastic deformation (Mode I), with thinning at the central area (Mode Itc) and plate boundary (Mode Ib). However, thinning at the central area of the plate is only observed for stand-off distances ranging from 13mm to 40mm. At stand-off distances ranging from 50mm to 300mm only thinning at the boundary is observed for increasing impulse. Further increases in impulse at larger stand-off distances (50mm – 300mm) results in partial tearing (Mode II*) followed by complete tearing at the boundary (Mode II).

Burn diameter and stand-off distance

Distinct discolouration (referred to as burn diameter), observed on the loaded side of the plate for localised blast load, was observed for stand-off distances ranging from 13mm to 75mm. Furthermore the results show that burn diameter increases with increasing stand-off distance up to 50mm for a given charge mass. At a stand-off distance of 75mm the burn diameter is visible but not clearly defined. For stand-off distance ranging from 100mm to 300mm, the plate is covered with an even coating of black soot.

Effect of polystyrene on impulse and plate deformation

Tests were conducted using loading conditions LC-1, LC-2 and LC-3 to determine the effect of polystyrene on plate deformation and impulse. The test were conducted at three different stand-off distances (150mm, 200mm and 300mm) with two charge masses (5g and 7g). The results show negligible effect on plate deformation and impulse, concurring with findings by Jones et al (1970) reported by Nurick and Martin [2]. The plate deformations are within ±1 mid-point deflection to thickness ratio for a given stand-off distance and charge mass. The variation in impulse for LC-1, LC-2 and LC-3 is generally less than 5% of the average impulse for a given charge mass at a particular stand-off distance. This translates to a difference of 0.7Ns between the measured impulse of 12.24Ns and the average impulse value of 12.92Ns for charge mass 5g.

Analytical and empirical predictions

A new loading parameter γ (equation 5.5) written as function of charge radius, plate radius and stand-off distance is incorporated into the Nurick and Martin dimensionless impulse parameter ϕ_c (equation 2.50a). The results are plotted in the graph of mid-point deflection – thickness ratio versus modified Nurick and Martin

damage number. The experimental data fall within the ±1 deflection – thickness ratio confidence lines of the empirically derived equation (2.55) proposed by Nurick and Martin [2] for predicting mid-point deflection with 95% confidence. The same loading parameter, γ, is applied to Jones damage number to account for the effect of stand-off distance. The analytical solution proposed by Jones [34] with the modified Jones damage number λ_S (equation (5.12)) over predicts the mid-point deflections. The strain rate sensitivity of mild steel plates used in this investigation is incorporated into modified Jones damage number λ_S (equation (5.12)) as proposed by Jones [34]. The static yield stress is replaced by the dynamic yield stress that increases with increasing impulse. The resulting Jones damage number λ_s^1 accounts for strain rate sensitivity of mild steel and the experimental results show satisfactory correlation with the analytical solution proposed by Jones [34] incorporating modified Jones damage number λ_s^1 (equation (5.22)).

The strain energy analysis produced satisfactory results in predicting mid-point deflection. However, using this methodology requires that the input energy is calculated accurately. The inclusion of the loading parameter, γ, (same as that incorporated into Nurick and Martin dimensionless impulse parameter and Jones damage number) in the input energy equation (2.93) accounted for energy required for deformation for the different stand-off distance.

7 Recommendations

As a result of the findings and conclusions of this research work, the following recommendations are made:

- The effect of different tube diameters should be investigated in order to ascertain possible influence of tube length to diameter ratio on loading conditions and plate deformation.

- The effect of stand-off distance on different plate thickness should be investigated.

- Further tests using different charge diameter to height ratios should be investigated to ascertain if there is a particular stand-off distance where charge mass influences plate deformation rather than charge geometry.

- It is recommended that the pressure – time history at different stand-off distance be measured in order to relate plate mid-point deflection to blast load pressure.

- The influence of the tubes used to vary the stand-off distances on blast load pressure – time history and spatial distribution should be investigated using finite element modelling.

- The influence of different thicknesses and density of polystyrene pads on impulse and plate deformation should be further investigated.

References

1. NURICK, GN and MARTIN, JB, Deformations of thin plates subjected to impulsive loading - a review; Part I - Theoretical consideration, International journal of impact engineering. Vol. 8 (2), pp 159 - 170, 1989.
2. NURICK, GN and MARTIN, JB, Deformation of thin plates subjected to impulsive loading - a review; Part II - Experimental studies, International journal of impact engineering. Vol. 8 (2), pp 170 - 186, 1989.
3. NURICK, GN GELMAN, ME and MARSHALL, NS, Tearing of blast loaded plates with clamped boundary conditions, International journal of impact engineering. Vol. 18 (7 - 8), pp 803 - 827, 1996.
4. NURICK, GN and SHAVE, GC, The deformation and tearing of thin square plates subjected to impulsive loads - an experimental study, International journal of impact engineering. Vol. 18 (1), pp 99 - 116, 1996.
5. TEELING-SMITH, RG and NURICK, GN, The deformation and tearing of circular plates subjected to impulsive loads, International journal of impact engineering. Vol. 11 (1), pp 77 - 92, 1991.
6. NURICK, GN and RADFORD, AM, Deformation and tearing of clamped circular plates subjected to localised central blast loads, Recent developments in computational and applied mechanics: a volume in honour of John B. Martin, International centre for numerical methods in engineering (CIMNE), Barcelona, Spain, pp 276 – 301, 1997.
7. CHUNG KIM YUEN, S and NURICK, GN, The significance of the thickness of a plate when subjected to localised blast loads. Proceedings of 16th international symposium military aspects of blast and shock (MABS16) Oxford, UK, pp 491 - 499, 2000.
8. JACOB, N, CHUNG KIM YUEN, S, BONORCHIS, D, NURICK, GN, DESAI, SA, and TAIT, D. Quadrangular plates subjected to localised blast loads - an insight into scaling. International journal of impact engineering, Vol. 30 (8 - 9), pp 1179 - 1208, 2004.
9. THOMAS, BM, and NURICK, GN, The effect of boundary conditions on thin plates subjected to impulsive loads, Plasticity 1995 - The 5th international symposium on plasticity and its current application. Osaka, Japan, pp 85 - 88, 1995.

10. JACINTO, AC, AMBROSINI, RD and DANESI, RF, Experimental and computational analysis of plates under air blast loading, International journal of impact engineering, Vol. 25 pp 927 - 947, 2001.
11. AKUS, Y. and YILDIRIM, OR, Effects of changing explosion distance and explosive mass on deformation of shock loaded square plates, 11th International conference on machine design and production, Antalya, Turkey, 2004.
12. KINNEY, KF, Explosive shocks in air, The Macmillan company, 1962
13. The Steel construction institute, The effects of simplification of the explosion pressure-time history, British gas research and technology, OTI-92599(BRI), 1992.
14. BAKER, WE, Explosions in air, University of Texas, Austin, 1973
15. Structures to resist the effects of accidental explosions, TM5-1300, NAVFAC P-397, AFR 88-22, 1990
16. RINEHART, JS and PEARSON, P, Explosive working of metals, Pergamon press, 1963
17. COOPER, PW and KUROWSKI, SR, Introduction to the technology of explosives, WILEY-VCH, 1996.
18. SMITH, PD and HETHERINGTON, JG, Blast and ballistic loading of Structures, Butterworth and Heinemann, 1994.
19. ESPARZA, ED, Blast measurement and equivalency for spherical charges at small scaled distances, International journal of impact engineering, Vol. 4 (1), pp 23 - 40, 1986.
20. STOFFEL, M, SCHMIDT, R and WEICHERT, D, Shock wave loaded plates, International journal of solids and structures, Vol. 38, pp 7659 - 7680, 2001.
21. KOSING, OE and SKEWS, BW, An investigation of high-speed forming of circular plates in a liquid shock tube, International journal of impact engineering, Vol. 21 (9), pp 801 - 816, 1998.
22. BJERKETVEDT, D, BAKKE, JR and van WINGERDEN, K, Gas explosion handbook, Journal of hazardous material, Vol. 52, pp 1 - 150, 1997.
23. BELTMAN, WM and SHEPHERD, JE, Linear elastic response of tubes to internal detonation loading, Journal of sound and vibration, Vol. 252 (4), pp 617 - 655, 2002.
24. LANGDON, GS, Failure of corrugated panels and supports under blast loading: experimental, analytical and numerical studies, PhD. Thesis, University of Liverpool, 2003.

25. NURICK, GN and MARTIN, JB, The measurement of the response of clamped circular plates to impulsive loading, 3rd Institute of physics conference on mechanical properties at high rates of strain, Oxford, Ser. No. 70, pp. 495 - 501, 1984.
26. SCHLEYER, GK, HSU, SS, WHITE, MD and BIRCH, RS, Pulse pressure loading of clamped mild steel plates, International journal of impact engineering, Vol. 28, pp 223 - 247, 2003.
27. NURICK, GN and CONOLLY, AG, Response of clamped single and double stiffened rectangular plates subjected to blast loads. 3rd International conference on structures under shock and impact, Madrid, Spain, pp 207 - 220, 1994.
28. NURICK, GN and LUMPP, DM, Deflection and tearing of clamped stiffened circular plates subjected to uniform impulsive blast loads, 4th International conference on structures under shock and impact, Computational mechanics publications, Southampton, Boston, pp 393 - 404, 1996.
29. NURICK, GN, OLSON, MD, FAGNAN, JR and Levin A, Deformation and tearing of blast-loaded stiffened square plates, International journal of impact engineering, Vol. 16 (2), pp 273 - 291, 1995.
30. CHUNG KIM YUEN, S and NURICK, GN, Experimental and numerical studies on the response of quadrangular stiffened plates - Part I: uniform blast loading, International journal of impact engineering, Vol. 31 (1), pp 55 - 83, 2005.
31. LANGDON, GS, CHUNG KIM YUEN, S and NURICK, GN, Experimental and numerical studies on the response of quadrangular stiffened plates - Part II: localised blast loading, International journal of impact engineering, Vol. 31 (1), pp 85 - 111, 2005.
32. MENKES, SB and OPAT, HJ, Tearing and shear failure in explosively loaded clamped beams, Experimental mechanics, No. 13, pp 480 - 486, 1973.
33. MARCHAND, KA and ALFAWAKHIRI, F, Blast and progressive collapse - Facts for steel buildings, No. 2, American institute of steel construction, Inc, 2004.
34. JONES, N, Structural impact, Cambridge University Press, Cambridge UK, 1989.
35. EZRA, AA, Principles and practice of explosive metal working, Garden city press, 1973.

36. DUFFEY, TA, The large deflection dynamic response of clamped circular plates subjected to explosive loading, Sandia laboratories research report, SC-RR-67-532, 1967.

37. SYMONDS, PS and WIERZBICKI, T, Membrane mode solution for impulsively loaded circular plates, Journal of applied mechanics, Vol. 46, pp 58 - 64, 1979.

38. WHARTON, RK, FORMBY, SA and MERRIFIELD, R, Air-blast TNT equivalence for a range of commercial blasting explosives, Journal of hazardous materials, A79, pp 31 - 39, 2000.

39. LANGDON, GS, Private communication.

Appendix A: Ballistic pendulum

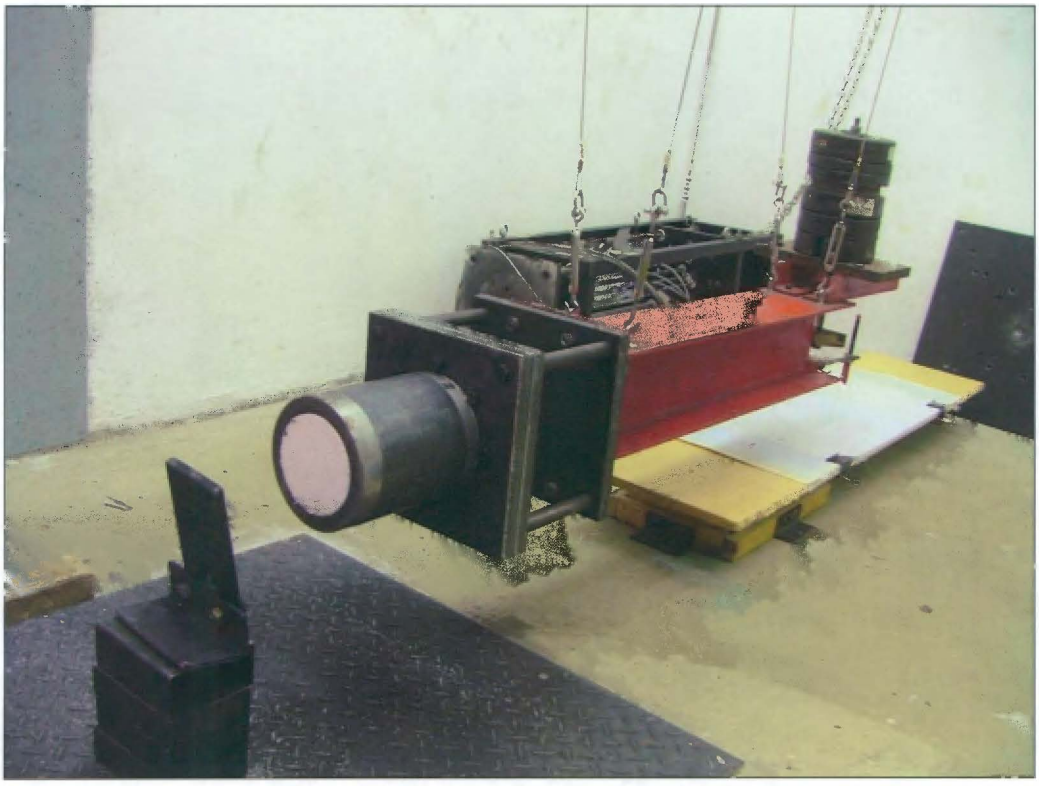

Figure A1: Ballistic pendulum

The initial amplitude recorded on the paper is directly proportional to the impulse applied to the test plate.

By assuming viscous damping the equation of motion of the pendulum is

$$\ddot{X} + 2\beta\dot{X} + \omega_n{}^2 X = 0 \qquad \text{(eq, A1)}$$

Where, $\beta = \frac{C}{2M}$, $\omega_n = \frac{2\pi}{T}$ and $\omega_d = \left(\omega_n{}^2 - \beta^2\right)^{1/2}$

C is the damping coefficient; M is the total mass of the pendulum (test rig, I - beam and counterbalances) and T is the natural period of the pendulum.

The solution to equation (A1) is given by

$$X = \frac{e^{-\beta t}\dot{x}_0 \sin(\omega_d t)}{\omega_d} \qquad \text{(eq. A2)}$$

Where $\dot{x}_0$ is the initial velocity of the pendulum.

Now let x_1 be the horizontal displacement at t = $\frac{T}{4}$

And x_2 be the horizontal displacement at t = $\frac{3T}{4}$

Substituting these values into equation (A2) gives

$$x_1 = \frac{\dot{x}_0 T}{2\pi} e^{(-1/4)\beta.T} \qquad \text{(eq. A3)}$$

And

$$x_2 = \frac{\dot{x}_0 T}{2\pi} e^{(-3/4)\beta.T} \qquad \text{(eq. A4)}$$

Hence dividing x_1 by x_2

$$\frac{x_1}{x_2} = e^{(1/2)\beta.T} \qquad \text{(eq. A5)}$$

The damping constant is given by

$$\beta = \frac{2}{T} \ln\left(\frac{x_1}{x_2}\right) \qquad \text{(eq. A5)}$$

From equation (A3)

$$\dot{x}_0 = \frac{2\pi}{T} x_1 e^{(0.25\beta.T)} \qquad \text{(eq. A6)}$$

Hence the Impulse can be calculated and is given by

$$I = M\dot{x}_0 \qquad \text{(eq. A7)}$$

The natural period of the pendulum, T is determined by averaging the time taken for a number of oscillations of the ballistic pendulum. The damping constant is determined for each test using equation (A5). The forward (x_1) and backward (x_2) displacements of the pendulum are calculated from measurements taken from the lines drawn on the tracing paper by the recording pen.

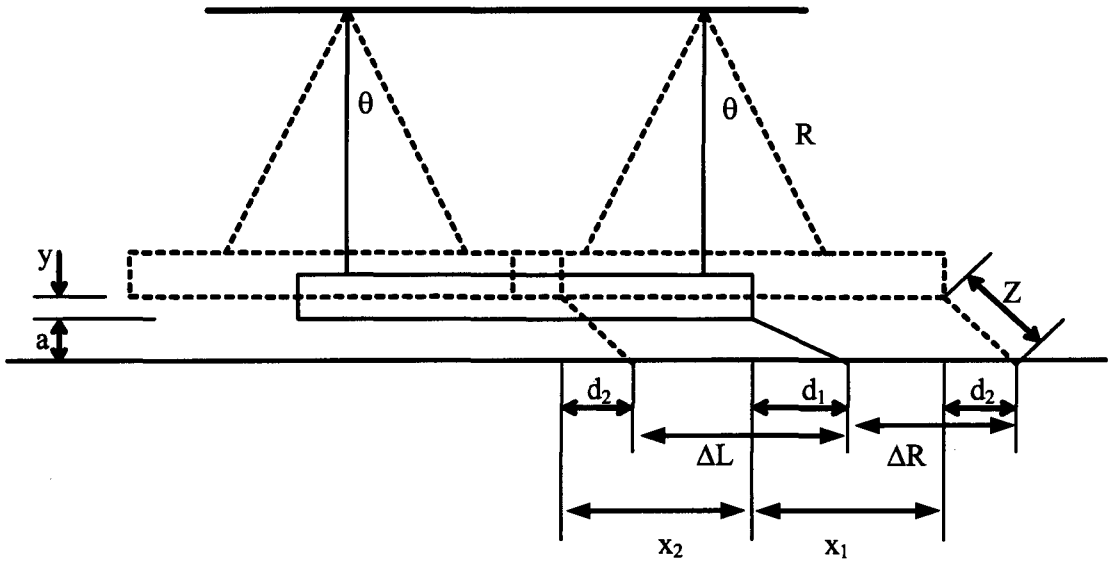

Figure A2: Ballistic pendulum geometry

It should be noted that the distance moved by the pendulum is not the same distance as that recorded by the pen on the paper as shown in Figure A2. The true displacement of the pendulum is determined using the following method

The horizontal distance from the end of the I-beam to the tip of the pen when the pendulum is stationary is given by

$$d_1 = \sqrt{(Z^2 - a^2)} \qquad \text{(eq. A8)}$$

At maximum amplitude of the oscillation the horizontal distance between the end of the I-beam and recording pen decreases, the new distance d_2 is given by

$$d_2 = \sqrt{Z^2 - (a+y)^2} \qquad \text{(eq. A9)}$$

For small angles

$$x_1 = R\theta \text{ and } y = \frac{R\theta^2}{2}$$

Hence

$$y = \frac{x_1^2}{2R} \qquad \text{(eq. A10)}$$

Substituting equation (A10) into equation (A9)

$$d_2 = \left[Z^2 - \left(a + \left(\frac{x_1^2}{2R} \right) \right)^2 \right]^{1/2} \qquad \text{(eq. A11)}$$

From Figure A2,

$$x_1 = \Delta R + d_1 - d_2 \qquad \text{(eq. A12)}$$

And

$$x_2 = \Delta L - d_1 + d_2 \qquad \text{(eq. A13)}$$

Substituting equations (A8) and (A11) into equations (A12) and (A13), the true forward (x_1) and backward (x_2) displacements of the pendulum is given by

$$x_1 = \Delta R + \left(Z^2 - a^2\right)^{1/2} - \left[Z^2 - \left[a + \frac{x_1^2}{2R}\right]^2\right]^{1/2} \qquad \text{(eq, A14)}$$

And

$$x_2 = \Delta L - \left(Z^2 - a^2\right)^{1/2} + \left[Z^2 - \left[a + \frac{x_1^2}{2R}\right]^2\right]^{1/2} \qquad \text{(eq. A15)}$$

ΔL, ΔR, Z, a, and R are measured and as a result x_1 and x_2 can be calculated.

The details of the ballistic pendulum are given in Tables A1 and A2.

Total mass of system

Total mass of pendulum = Front (test rig mass) + Back (counter balance mass) + mass of I-beam.

No tube

- Front (test rig mass) = B + D + E + G
- Back (counter balance mass) = (n x H) + (n x I) + (n x S) + K

With tubes

- Front (test rig mass) = B + E + F + G + appropriate tube mass
- Back (counter balance mass) = (n x H) + (n x I) + (n x S) + K

Table A1: Ballistic pendulum data

	Time Period (T)	3.41s
	R	2.92m
	Z	0.21m
	a	0.14m
	Masses (kg)	
A	Pendulum I-Beam	25.22
B	Back Plate + Spacers+ Bolts	10.66
C	2 clamp Plates (with out tube)	15.28
D	1 Clamp Plate	7.66
E	1 Clamp Plate	7.62
F	Threaded clamp Plate	6.32
G	Test plate	0.87
	Counter balancing masses (kg)	
H	Large (L)	4.54
I	Medium (M)	2.26
J	Small (S)	1.00
K	Fittings + Last block	6.30
	Tubes masses (kg)	
L	25mm	1.6
M	30mm	1.88
N	40mm	2.64
O	50mm	3.36
P	75mm	5.20
Q	100mm	7.00
R	150mm	10.34
S	200mm	13.88
T	250mm	17.24
U	300mm	20.70

Table A2: Detailed list of masses for different stand-off distances

Stand-off distance (mm)	Front - test rig mass (kg)	Back - counter balance mass configuration	Back - counter balance mass (kg)	Total mass of pendulum (kg)
13 - no tube	26.81	4L+1M	26.72	78.75
25	27.07	4L+1M	26.72	79.01
30	27.35	4L+1M+1S	27.72	80.29
40	28.11	4L+1M+1S	27.72	81.05
50	28.83	4L+1M+2S	28.72	82.77
75	30.67	4L+2M+1S	29.98	85.87
100	32.47	6L	33.54	91.23
150	35.81	6L	33.54	94.57
200	39.35	6L+2M+1S	39.06	103.63
250	42.71	6L+2M+2S	40.06	107.99
300	46.17	6L+2M+2S	40.06	111.45

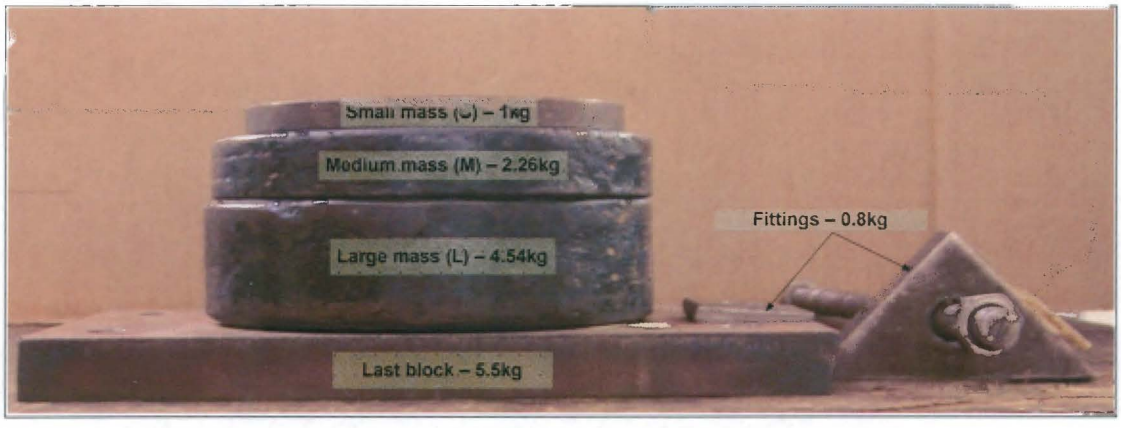

Figure A3: Different counter balance masses

Appendix B: Drawings

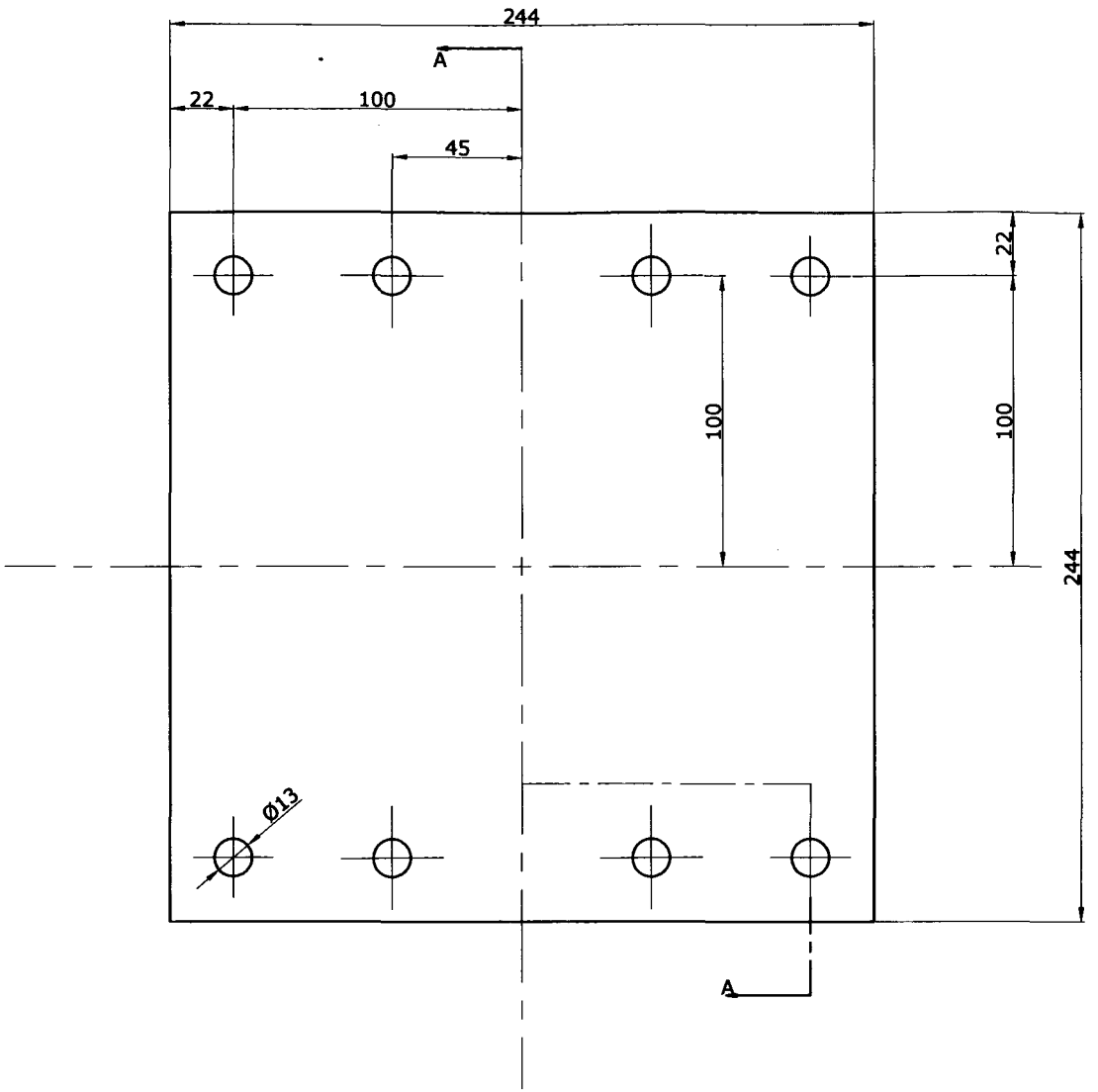

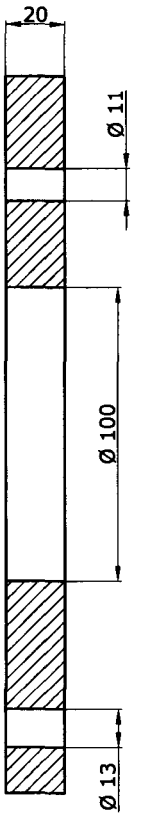

Section A-A

Material: Mild Steel	
Quantity: 1	
All measurement in millimeters	
Title: Back Plate	
	University Of Cape Town

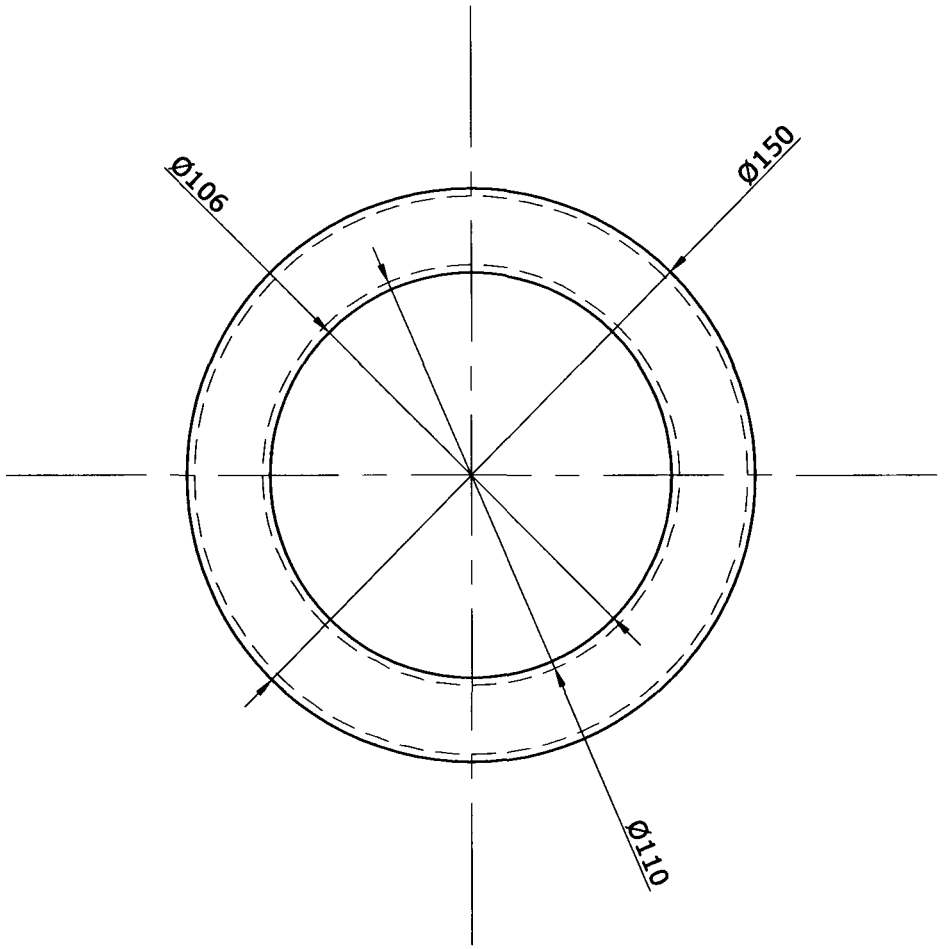

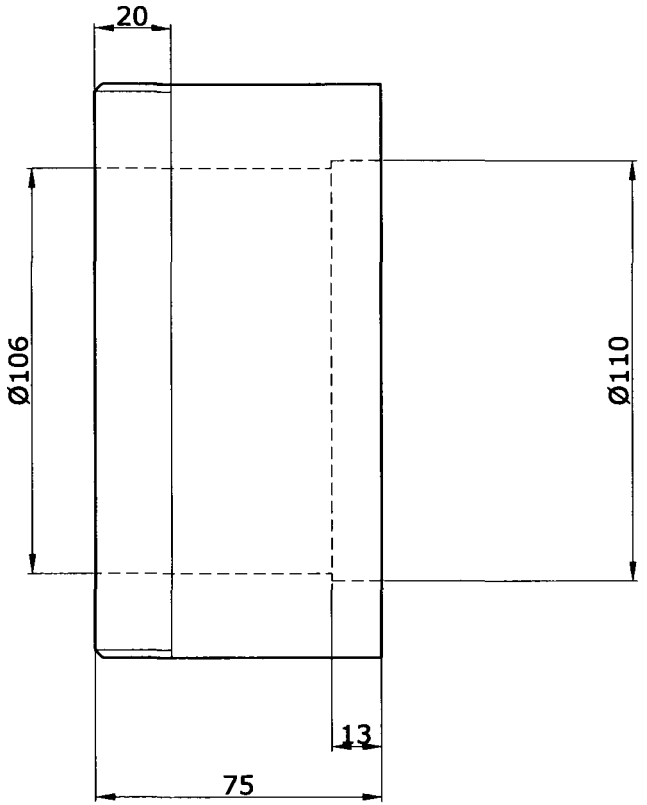

Required blast tube lengths - 25mm, 30mm, 40mm, 50mm, 75mm, 100mm, 150mm, 200mm, 250mm, 300mm

Material: Mild steel
Quantity: 1
All measurement in millimeters
Title: Tube
University Of Cape Town

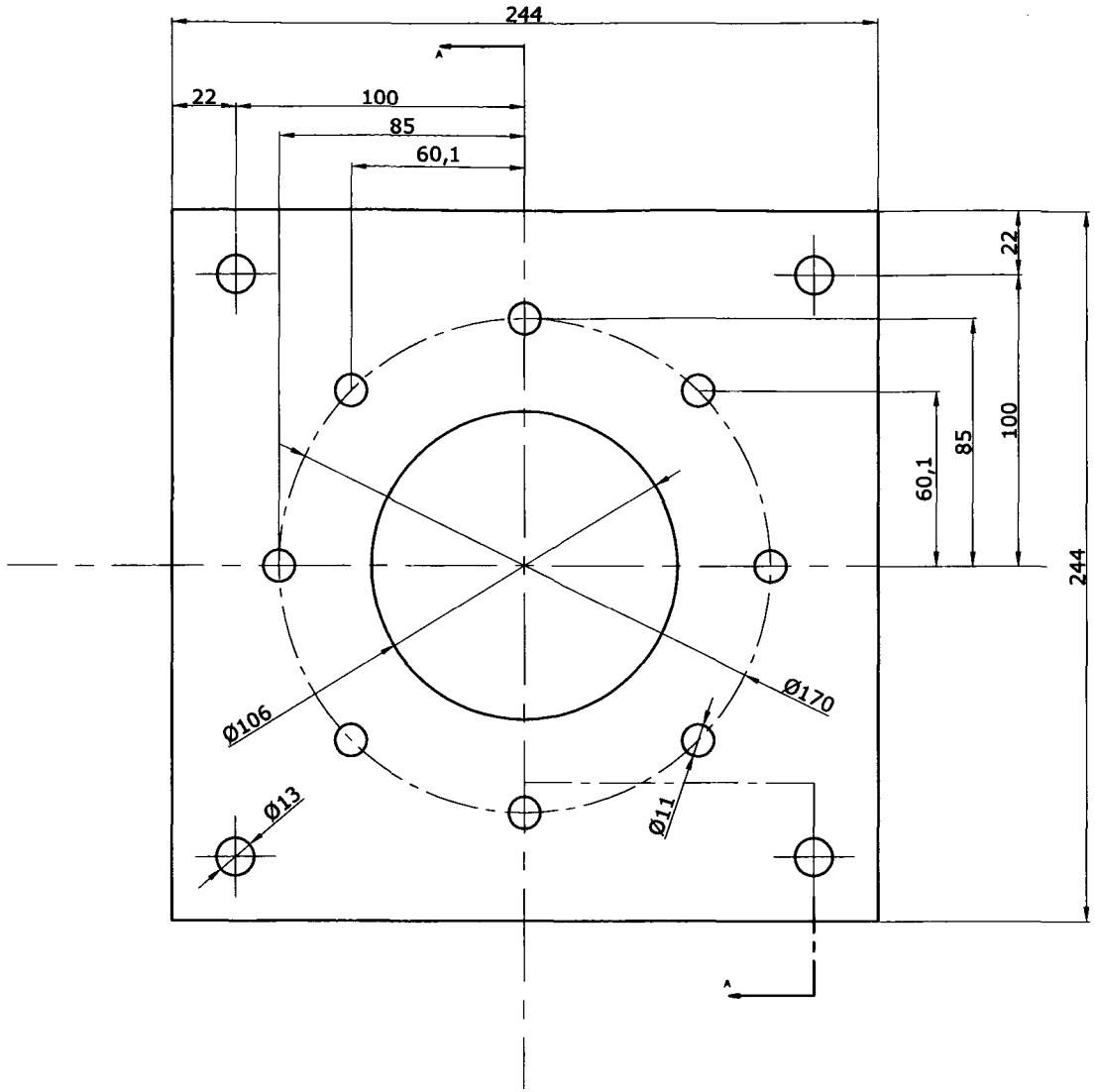

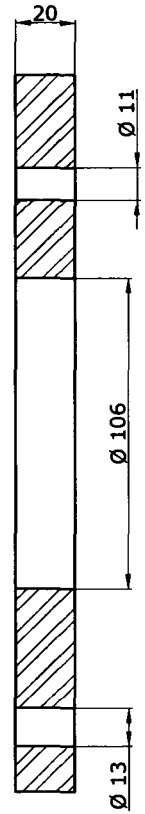

Section A-A

Quantity 1

Material:	Mild Steel
Quantity:	1
All measurement in millimeters	
Title: Dia 106mm Clamp Plate	

University Of Cape Town

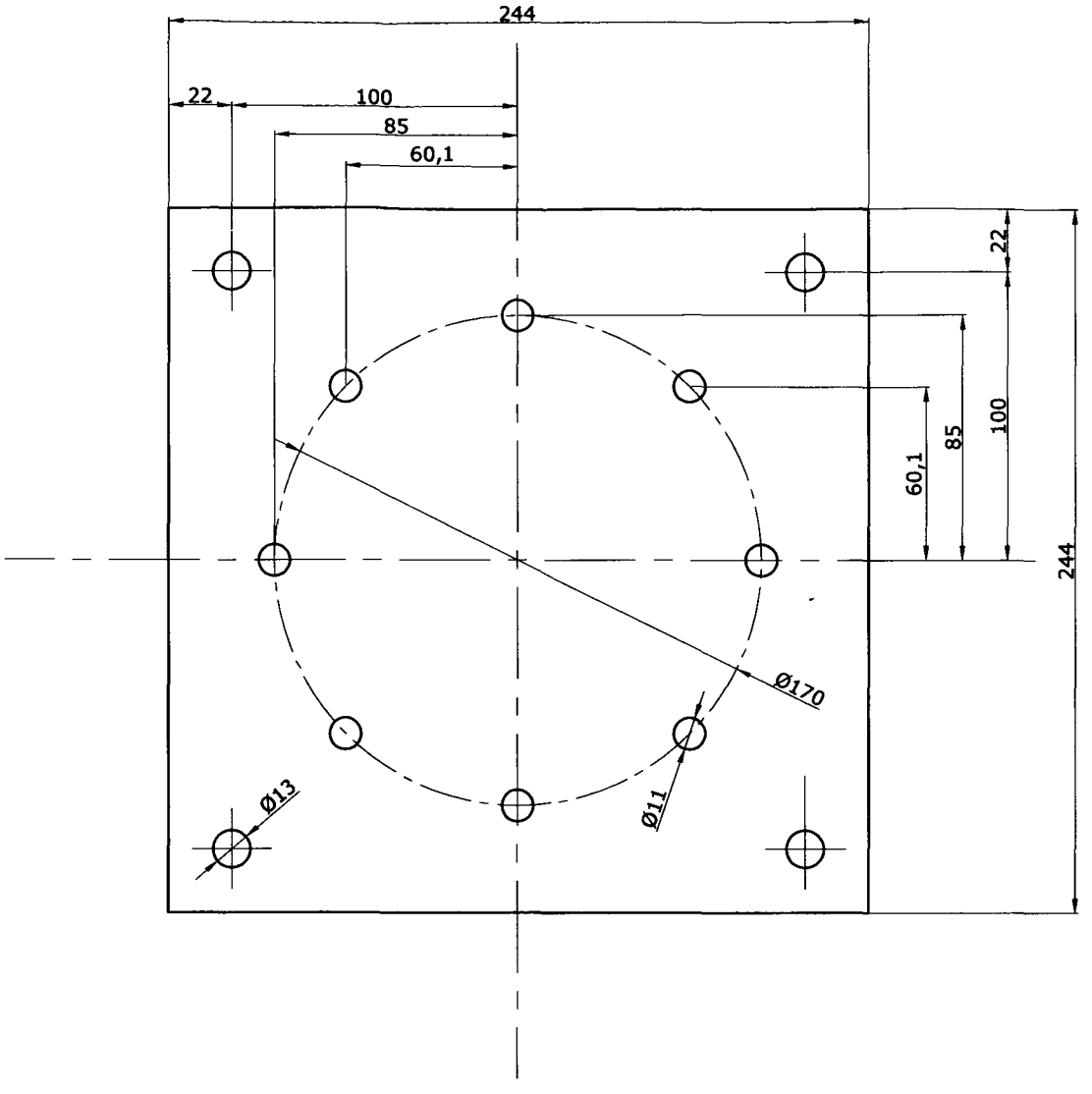

Required thickness: 2.0mm

Quantity 80

Material: Mild Steel	
Quantity:	
All measurement in millimeters	
Title: Test Plates	
University Of Cape Town	